NASA-CP-10019

Thermal Barrier Coatings

Workshop

NASA Lewis Research Center
Cleveland, Ohio

May 21-22, 1985

Abstracts
and Figures

CONTENTS

SESSION IV - NONDESTRUCTIVE AND ANALYTICAL ASSESSMENT

SESSION V - COATING DEVELOPMENT

SESSION VI - ALTERNATIVE APPLICATIONS

DEVELOPMENT OF THERMOMECHANICAL LIFE PREDICTION MODELS FOR THERMAL BARRIER COATINGS

T.E. Strangman
Garrett Turbine Engine Company
Pheonix, Arizona 85010

Thermal barrier coatings (TBCs) for turbine airfoils in high-performance engines represent an advanced materials technology with both performance and durability benefits. The foremost TBC benefit is the reduction of heat transferred into air-cooled components. To achieve these benefits, however, the TBC system must be reliable. Mechanistic thermomechanical and thermochemical life models and statistically significant design data are therefore required for the reliable exploitation of TBC benefits on gas turbine airfoils. Garrett's NASA-Host Program (NAS3-23945) is designed to fulfill these requirements.

This program focuses on predicting the lives of two types of strain-tolerant and oxidation-resistant TBC systems that are produced by commercial coating suppliers to the gas turbine industry. The plasma-sprayed TBC system, composed of a low-pressure plasma-spray (LPPS) applied oxidation resistant NiCrAlY bond coating and an air-plasma-sprayed yttria (8 percent) partially stabilized zirconia insulative layer, is applied by both Chromalloy (Orangeburg, New York) and Klock (Manchester, Connecticut). The second type of TBC is applied by the electron beam-physical vapor deposition (EB-PVD) process by Temescal (Berkeley, California).

Thermomechanical life models are being tailored to predict TBC strain tolerance in terms of materials (zirconia thickness, NiCrAlY roughness), engine (component temperature, applied strains) and mission (time at temperature) parameters. Continuum and fracture mechanics approaches and statistical methods are being evaluated to develop tensile and compressive strain functions required to drive a mission analysis capable thermomechanical life model for TBCs. Results of initial testing to calibrate these life models will be presented.

GARRETT'S TBC LIFE PREDICTION STRATEGY IS COMPREHENSIVE

- COMMERCIAL FIXED-PROCESS TBC SYSTEMS
- MISSION-ANALYSIS CAPABLE LIFE MODELS
- AFFORDABLE TESTS TO CALIBRATE MODELS
- RAPID TBC LIFE COMPUTATION APPROACHES
- NDE FEASIBILITY
- ITERATIVE TFE731 TURBOFAN ENGINE TESTS TO VALIDATE LIFE ANALYSIS

Figure 1.

LIFE PREDICTION MODELS ARE BEING DEVELOPED FOR PLASMA-SPRAYED AND EB-PVD TBC SYSTEMS

PLASMA SPRAY	ELECTRON BEAM — PHYSICAL VAPOR DEPOSITION
APS Y_2O_3 (8%) STABILIZED ZrO_2	EB-PVD Y_2O_3 (20%) STABILIZED ZrO_2
LPPS Ni-31Cr-11Al-0.5Y	EB-PVD Ni-23Co-18Cr-11Al-0.3Y
MAR-M 247 SUPERALLOY	MAR-M 247 SUPERALLOY
• CHROMALLOY • KLOCK	• TEMESCAL

Figure 2.

MISSION ANALYSIS CAPABLE LIFE MODELS ARE BEING DEVELOPED FOR OPERATIVE TBC FAILURE MODES

- ZIRCONIA SPALLING
- BOND COATING OXIDATION
- MOLTEN SALT FILM DAMAGE
- CARBON PARTICLE EROSION

Figure 3.

FAILURES IN TBC ARE MECHANICALLY INDUCED

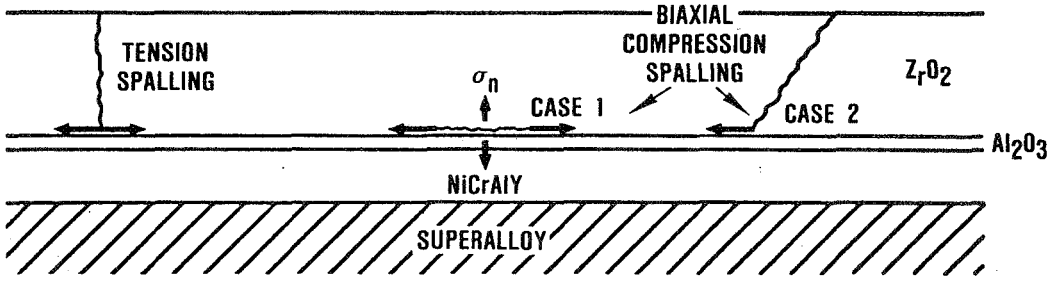

- STRESS INTENSITY AT TIP OF CRACK

  $K \sim C\ E\ \varepsilon_A\ t^n$

  $\varepsilon_A = \varepsilon_\alpha + \varepsilon_T + \varepsilon_R + \varepsilon_C + \varepsilon_S + \varepsilon_{PT}$

  E = ELASTIC MODULUS

- STRAIN-TOLERANT TBC: $E \rightarrow 0$

  OXIDATION OF NiCrAlY AND ADHESION OF Al_2O_3 SCALE GOVERN TBC LIFE

Figure 4.

A MISSION ANALYSIS CAPABLE THERMOMECHANICAL MODEL PREDICTS TBC LIFE AS A FUNCTION OF ENGINE, MISSION, AND MATERIALS PARAMETERS

CRITICAL PARAMETERS

ENGINE

- COMPONENT TEMPERATURE
- THERMAL STRAINS
- CENTRIFUGAL STRAINS
- TURBINE PRESSURE
  - SALT DEPOSITION

MISSION

- POWER REQUIREMENTS
  - LEVEL
  - DURATION
- ALTITUDE
  - SALT DEPOSITION

MATERIALS SYSTEM

- $\varepsilon_\alpha + \varepsilon_R + \varepsilon_S + \varepsilon_{PT}$
- ELASTIC MODULUS
- K_{IC}, σ_f
- BOND COATING ROUGHNESS
- OXIDATION RATE
- THERMAL CONDUCTIVITY
- THERMAL EXPANSION

Figure 5.

FRACTURE MECHANICS AND STATISTICAL APPROACHES CAN POTENTIALLY ESTABLISH SPALLING STRAIN LIMITS FOR TBCs

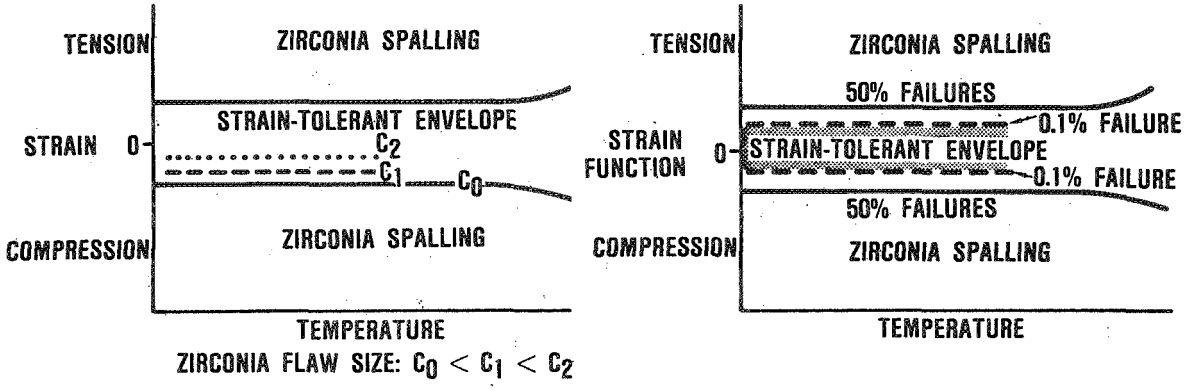

Figure 6.

THERMOMECHANICAL TBC LIFE MODEL IS CALIBRATED WITH AFFORDABLE TESTS

- COHESIVE (INTERFACIAL) STRENGTH AND TOUGHNESS

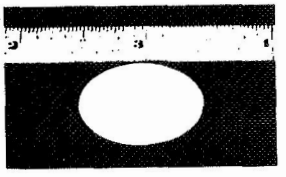

$\sigma_f, K_{IC} = F$ { TEMPERATURE; TIME; NiCrAlY ROUGHNESS; $\varepsilon_R, \varepsilon_S, \varepsilon_{PT}$

- TENSILE AND COMPRESSIVE SPALLING STRAINS

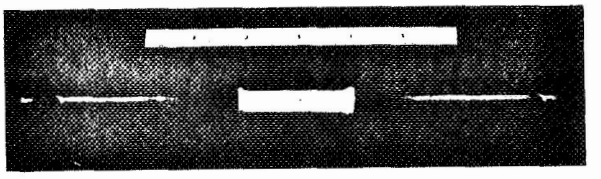

$\varepsilon_{SPALL} = F$ { MODULUS; ZIRCONIA THICKNESS; TEMPERATURE; K_{IC}, σ_f, C; SALT DEPOSITION

Figure 7.

COHESIVE AND INTERFACIAL TOUGHNESS OF TBC SYSTEM CAN BE QUANTIFIED WITH MODIFIED BOND STRENGTH TEST

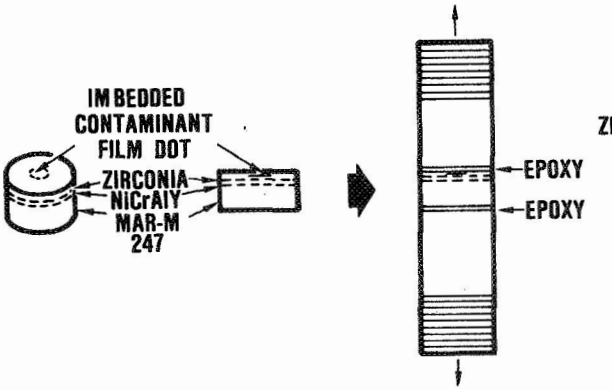

COHESIVE (INTERFACIAL) TOUGHNESS TEST

$K_{IC} = 2/\sqrt{\pi}\ \sigma_F \sqrt{C/2}$

FRACTURE SURFACE

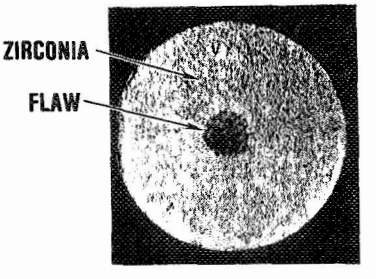

K_{IC} = 0.46 MPa $\sqrt{m}$
AS-COATED CHROMALLOY
PLASMA-SPRAYED TBC

Figure 8.

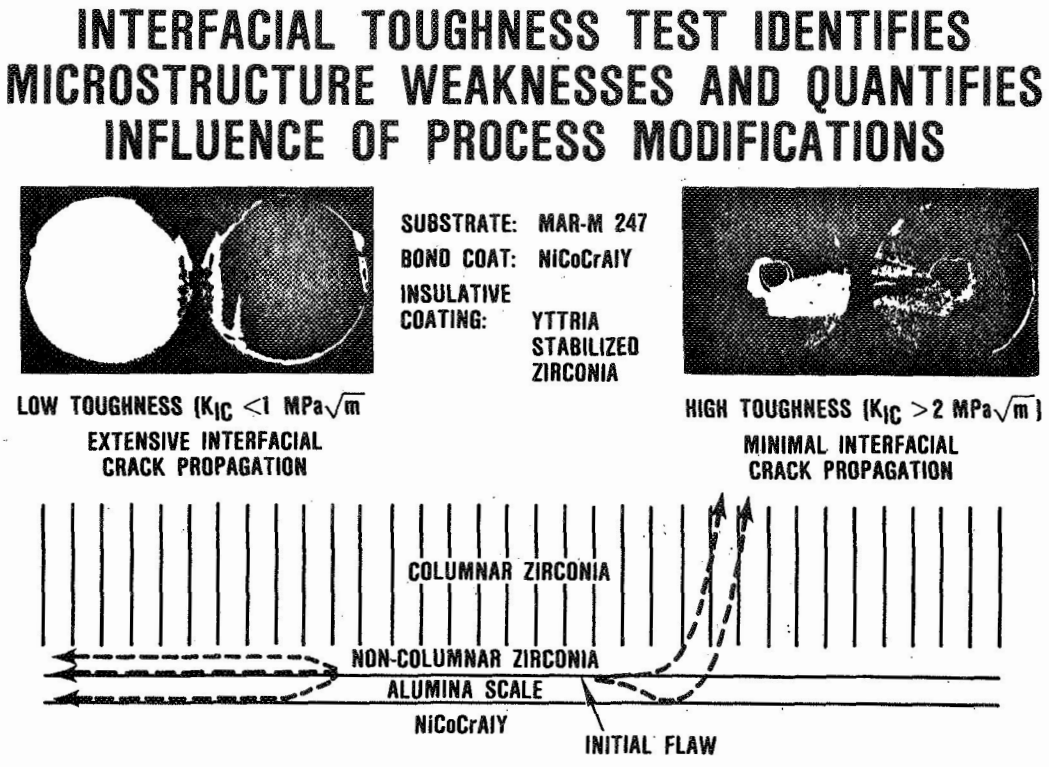

Figure 9.

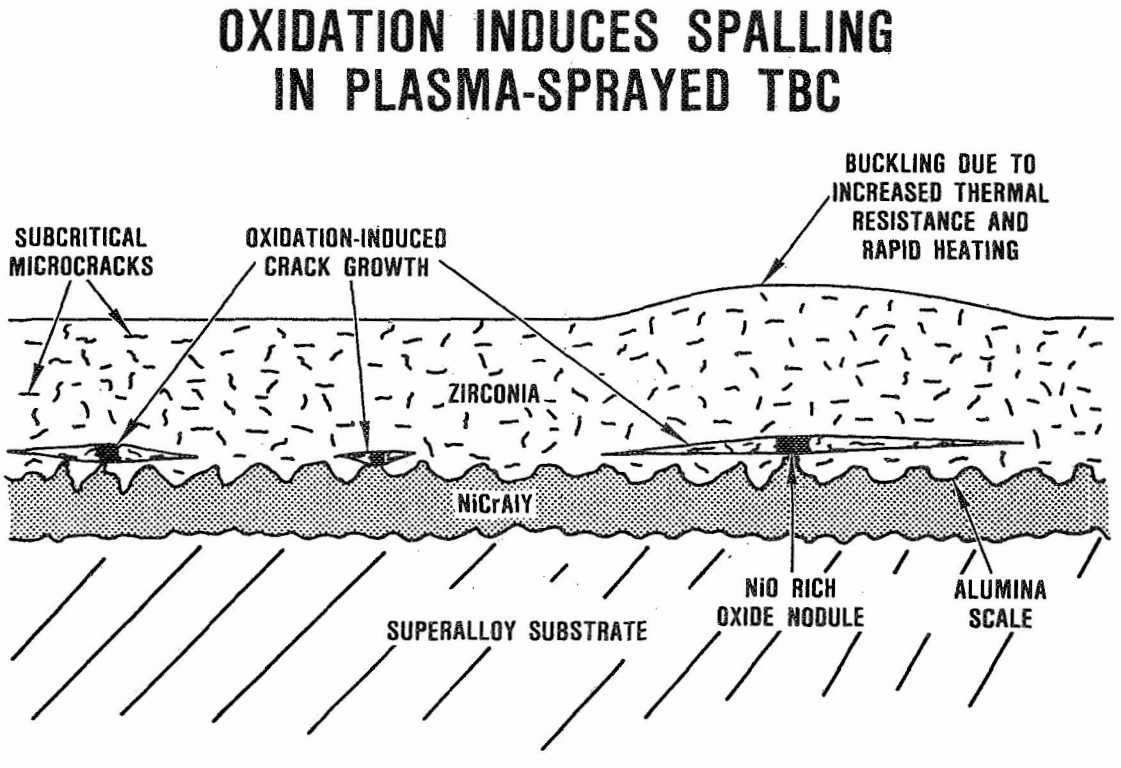

Figure 10.

ENVIRONMENTAL FACTORS (OXIDATION AND SALT DEPOSITS) REDUCE TBC SPALLING STRAIN LIMITS

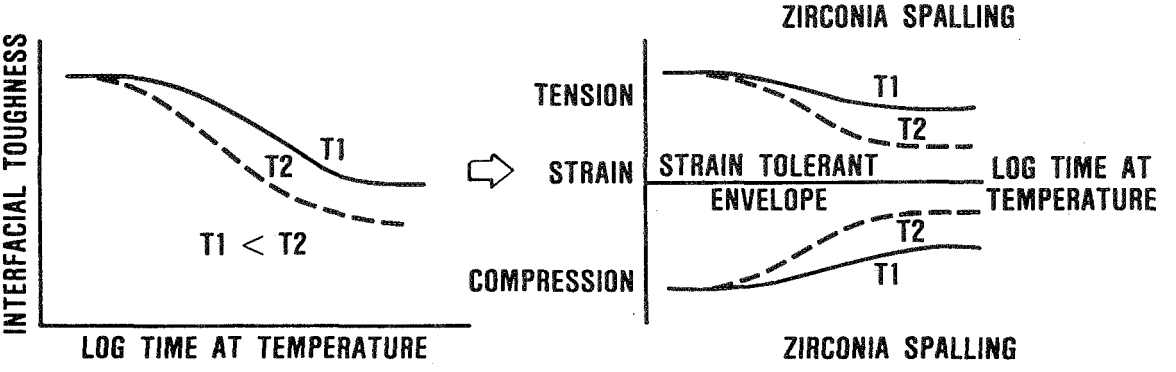

Figure 11.

SUMMARY

- THERMOMECHANICAL MODEL IS BEING DESIGNED TO PREDICT TBC LIFE AS A FUNCTION OF ENGINE, MISSION, AND MATERIALS PARAMETERS
- LIFE MODEL IS BEING CALIBRATED FOR COMMERCIALLY APPLIED PLASMA-SPRAYED (CHROMALLOY, KLOCK) AND EB-PVD (TEMESCAL) TBCs
- AFFORDABLE TESTS HAVE BEEN DEVELOPED TO CALIBRATE THERMOMECHANICAL TBC LIFE MODELS

Figure 12.

MECHANISMS OF THERMAL BARRIER COATING DEGRADATION AND FAILURE

J.T. DeMasi and K.D. Sheffler
Pratt & Whitney Aircraft
East Hartford, Connecticut 06108

This presentation describes the objectives and initial results of a Thermal Barrier Coating (TBC) Life Prediction Model Development Program. The goals of this program, which is sponsored in part by NASA under the HOST (Hot Section Technology) Program, are to:

- o Identify and understand TBC failure modes
- o Generate quantitative TBC life data
- o Develop and verify a TBC life prediction model

The coating being studied on this program is a two layer thermal barrier system incorporating a nominal ten mil outer layer of seven percent yttria partially stabilized zirconia plasma deposited over an inner layer of highly oxidation resistant low pressure plasma sprayed NiCoCrAlY bond coating. This coating currently is in flight service on turbine vane platforms in the JT-9D and PW2037 engines and is bill-of-material on turbine vane airfoils in the advanced PW4000 and IAE V2500 engines.

Effort currently is in progress on the first task of this program, which involves the identification and understanding of TBC failure modes. Five modes of coating damage were considered in this study:

- o Thermomechanical ceramic failure
- o Oxidative bond coat failure
- o Hot corrosion
- o Foreign Object Damage (FOD)
- o Erosion

An initial review of experimental and flight service components indicates that the predominant mode of TBC failure involves thermomechanical spallation of the ceramic coating layer. This ceramic spallation involves the formation of a dominant crack in the ceramic coating parallel to and closely adjacent to the metal-ceramic interface.

Initial results from a laboratory test program designed to study the influence of various "driving forces" such as temperature, thermal cycle frequency, environment, coating thickness, etc. on ceramic coating spalling life appears to confirm the hypothesis initially proposed by Miller (Ref. 1). This hypothesis suggests that bond coat oxidation damage at the metal-ceramic interface contributes significantly to thermomechanical cracking in the ceramic layer. Low cycle rate furnace testing in air and in argon clearly shows a dramatic increase of spalling life in the non-oxidizing environment. At lower

temperatures, on the order of 2000°F, elevated temperature pre-exposure of TBC specimens in air causes a proportionate reduction of cyclic thermal spalling life, whereas pre-exposure in argon does not. At higher temperatures, on the order of 2100°F, it appears that additional degradation mode(s) may be operative. Future activity will be devoted to confirming this observation and to identification of additional TBC degradation mode(s).

Ref. 1 R.A. Miller "An Oxidation Model for Thermal Barrier Coating Life", J. Am. Ceramic Soc. 67 8 517-521 (1984).

HOST PROGRAM GOALS

- → IDENTIFY/UNDERSTAND FAILURE MODES
- GENERATE QUANTITATIVE FAILURE DATA
- DEVELOP AND VERIFY LIFE PREDICTION MODEL

Figure 1.

PWA 264 TWO LAYER THERMAL BARRIER COATING

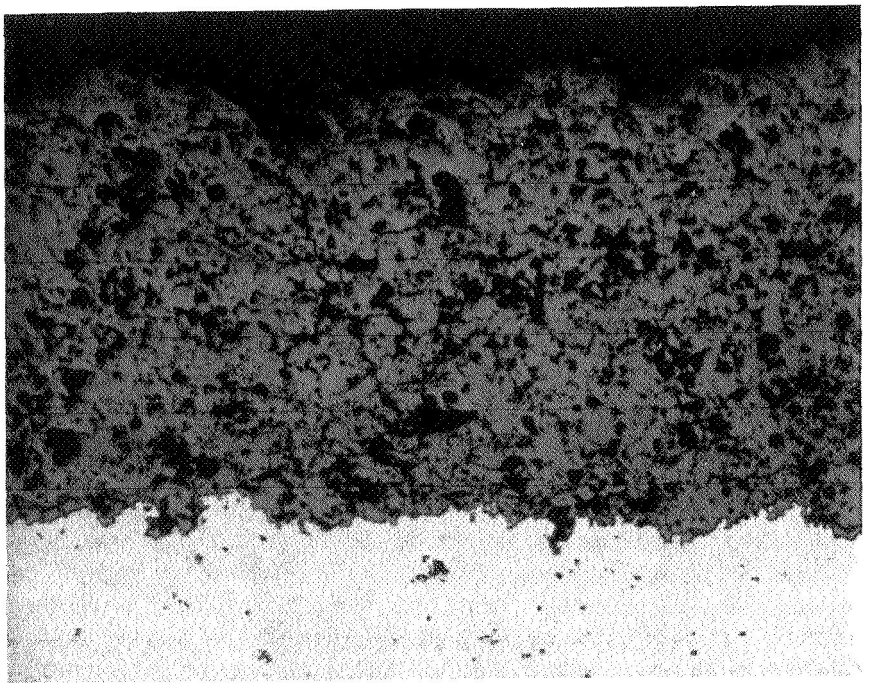

- PLASMA DEPOSITED YTTRIA PARTIALLY STABILIZED ZIRCONIA
  - CONTROLLED POROSITY, MICROCRACKING
- INCORPORATES RESIDUAL STRESS CONTROL
  - COOL WORKPIECE DURING APPLICATION
- LOW PRESSURE CHAMBER SPRAY BOND COAT
  - OXIDATION RESISTANT MCrAlY COMPOSITION

Figure 2.

POTENTIAL TBC FAILURE MODES

- THERMOMECHANICAL FAILURE OF CERAMIC
- OXIDATIVE FAILURE OF BOND COAT
- HOT CORROSION
- FOD
- EROSION

Figure 3.

TYPICAL THERMAL BARRIER COATING FAILURE MODE

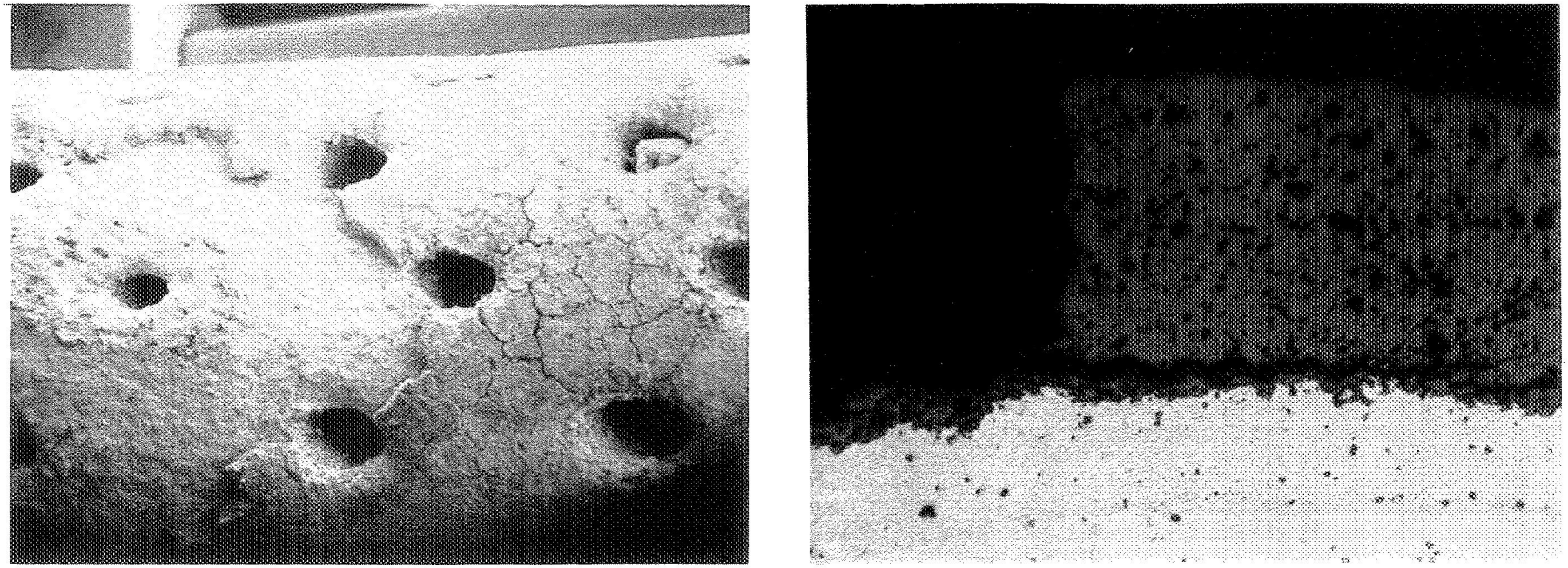

Figure 4.

BOND COAT OXIDATION FAILURE

Figure 5.

HOT CORROSION FAILURE OBSERVED ONLY AT HIGH SALT LEVEL (35 PPM)

- NOT OBSERVED TO DATE IN FLIGHT SERVICE

35 PPM

10 PPM

Figure 6.

COATING FOD IS NOT COMPONENT LIFE LIMITING

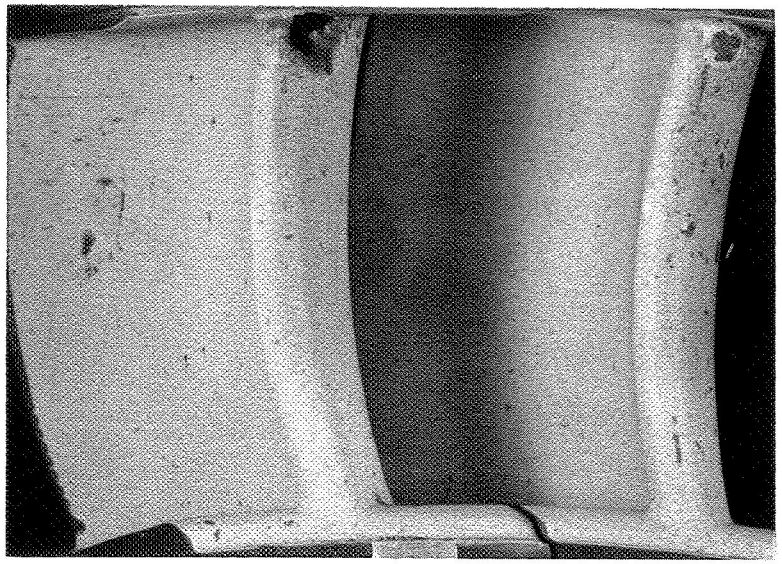

TURBINE VANE LEADING EDGE

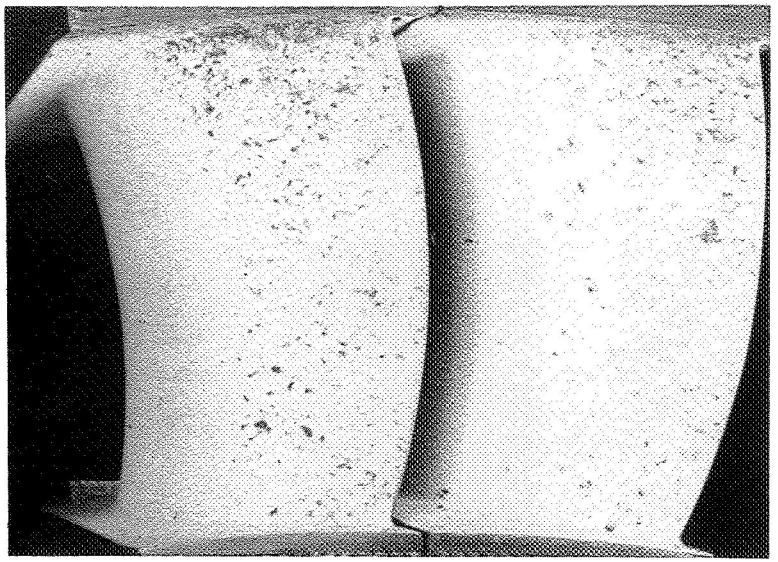

TURBINE VANE TRAILING EDGE

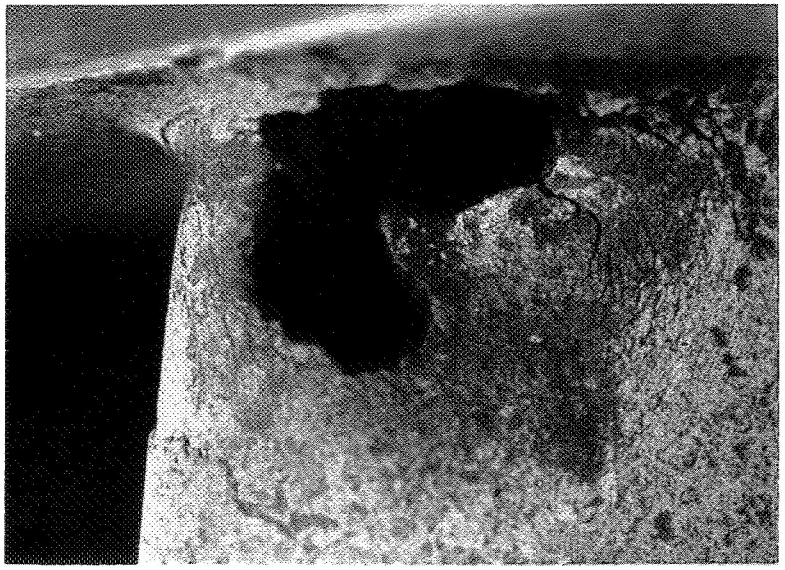

"DAMAGED COATING"

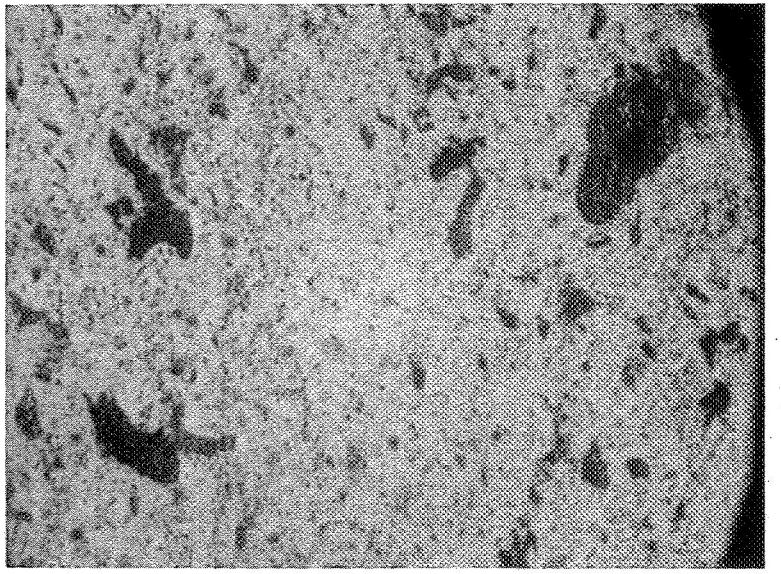

METAL SMEARED ON INTACT COATING

Figure 7.

EROSION

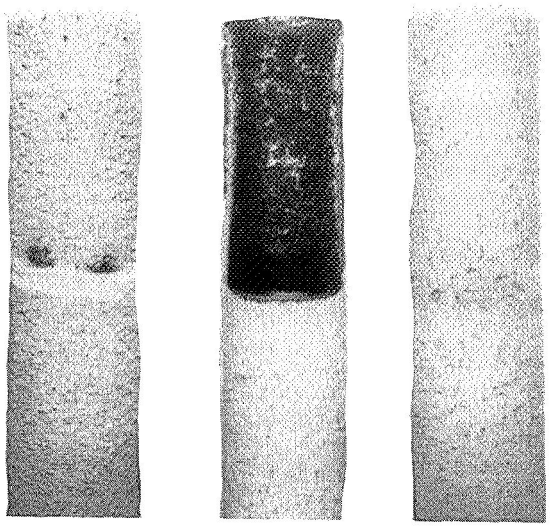

8-10 mils
20% Y_2O_3-ZrO_2

1-3 mils
$ZrSiO_4$

8-10 mils
6% Y_2O_3-ZrO_2

NOT FOUND SO FAR ON ENGINE COMPONENTS

- 21% MgO-ZrO_2 COMBUSTORS
  (20 YEARS EXPERIENCE)
- 7% Y_2O_3 - ZrO_2 TURBINE COMPONENTS
  (3 YEARS EXPERINECE)

Figure 8.

PREDOMINANT ENGINE FAILURE MODE IS TIME/CYCLE DEPENDENT

CERAMIC CRACKING NEAR METAL INTERFACE

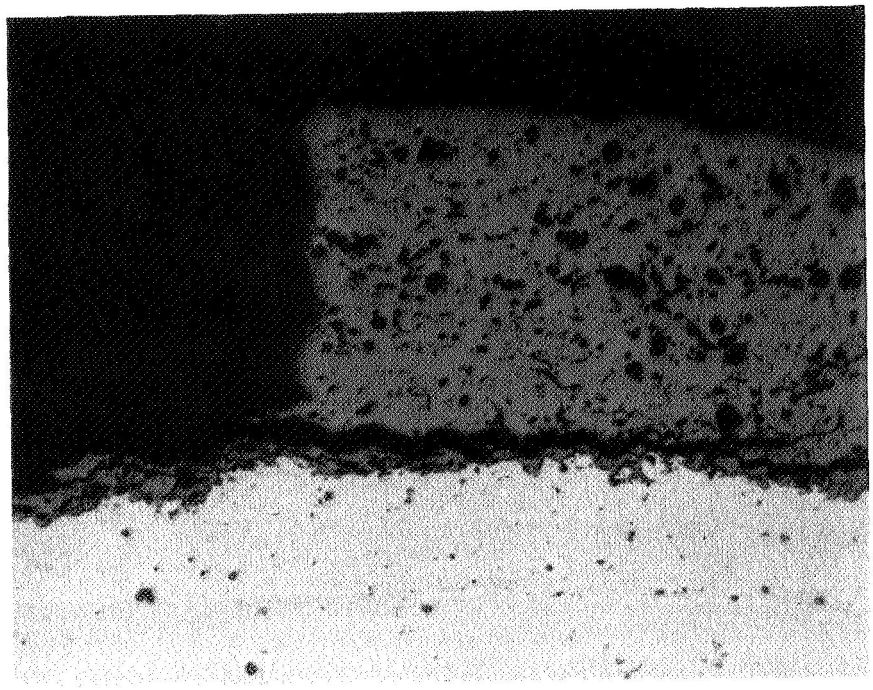

Figure 9.

EFFECTS WHICH MIGHT CONTRIBUTE TO EXPOSURE (TIME/TEMP./CYCLING) DEPENDENT CERAMIC CRACKING

- SUBCRITICAL CRACK PROPOGATION
- EXPOSURE DEPENDENT CERAMIC STRESS INCREASE
  - PHYSICAL ALTERATIONS AT INTERFACE (MILLER OXIDATION MODEL)
    - INTERFACE THICKNESS (SCALE) GROWTH
    - INTERFACE TOPOLOGY CHANGES
  - RESIDUAL STRESS ALTERATION (TOWARD COMPRESSION)
    - CERAMIC "DIMENSIONAL" CHANGES E.G. SINTERING (PROBABLY GOES TOWARD TENSION)
    - BOND COAT RELAXATION
    - SUBSTRATE RELAXATION/DIMENSIONAL CHANGES
  - REDUCED CERAMIC "STRAIN TOLERANCE" (MODULUS INCREASE)
    - SINTERING
  - PHASE INSTABILITIES (INCREASED MONCLINIC)
- EXPOSURE DEPENDENT CERAMIC STRENGTH DECREASE
  - PHASE CONTENT/DISTRIBUTION
  - SOLUTE DISTRIBUTION

Figure 10.

HOST PROGRAM APPROACH TASK 1 - ASSESS PREDOMINANT FAILURE MECHANISMS

- "STATIC" FAILURE TESTS
  - AIR
  - ARGON
- CLEAN FUEL CYCLIC BURNER RIG TESTS
  - BASELINE COATING (10 MILS)
  - VARY THICKNESS (5, 15 MILS)
  - PRE-EXPOSED SPECIMENS (AIR, ARGON)
  - VARIOUS TEMPERATURES, CYCLE RATES, TRANSIENTS
- CYCLIC HOT CORROSION TESTS
- FRACTIONAL EXPOSURE TESTS
- PHYSICAL/MECHANICAL PROPERTIES
  - BULK CERAMIC
  - BULK METALLIC

Figure 11.

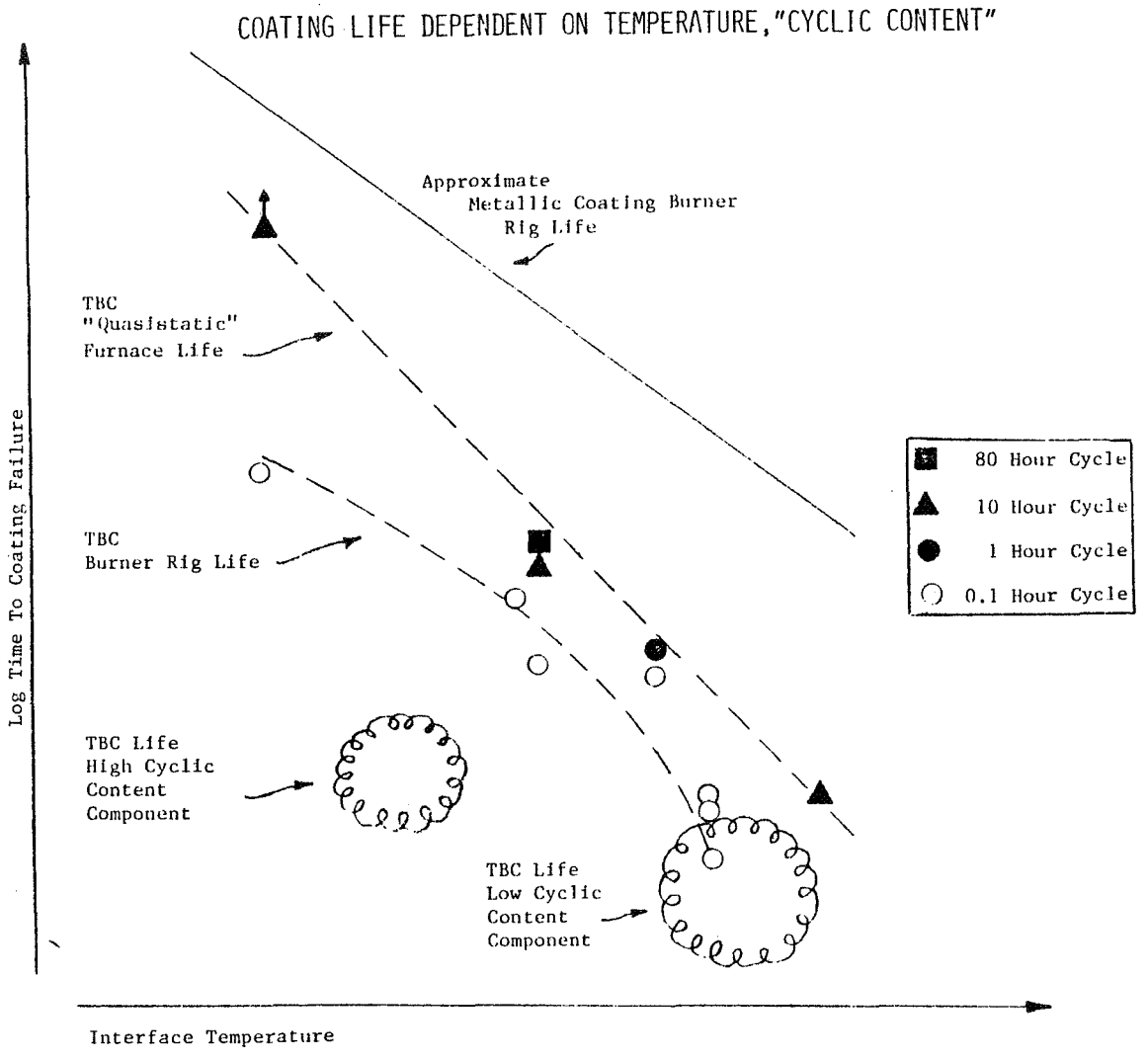
COATING LIFE DEPENDENT ON TEMPERATURE,"CYCLIC CONTENT"
Approximate
Metallic Coating Burner
Rig Life
TBC
"Quasistatic"
Furnace Life
TBC
Burner Rig Life
TBC Life
High Cyclic
Content
Component
TBC Life
Low Cyclic
Content
Component
80 Hour Cycle
10 Hour Cycle
1 Hour Cycle
0.1 Hour Cycle
Log Time To Coating Failure
Interface Temperature

Figure 12.

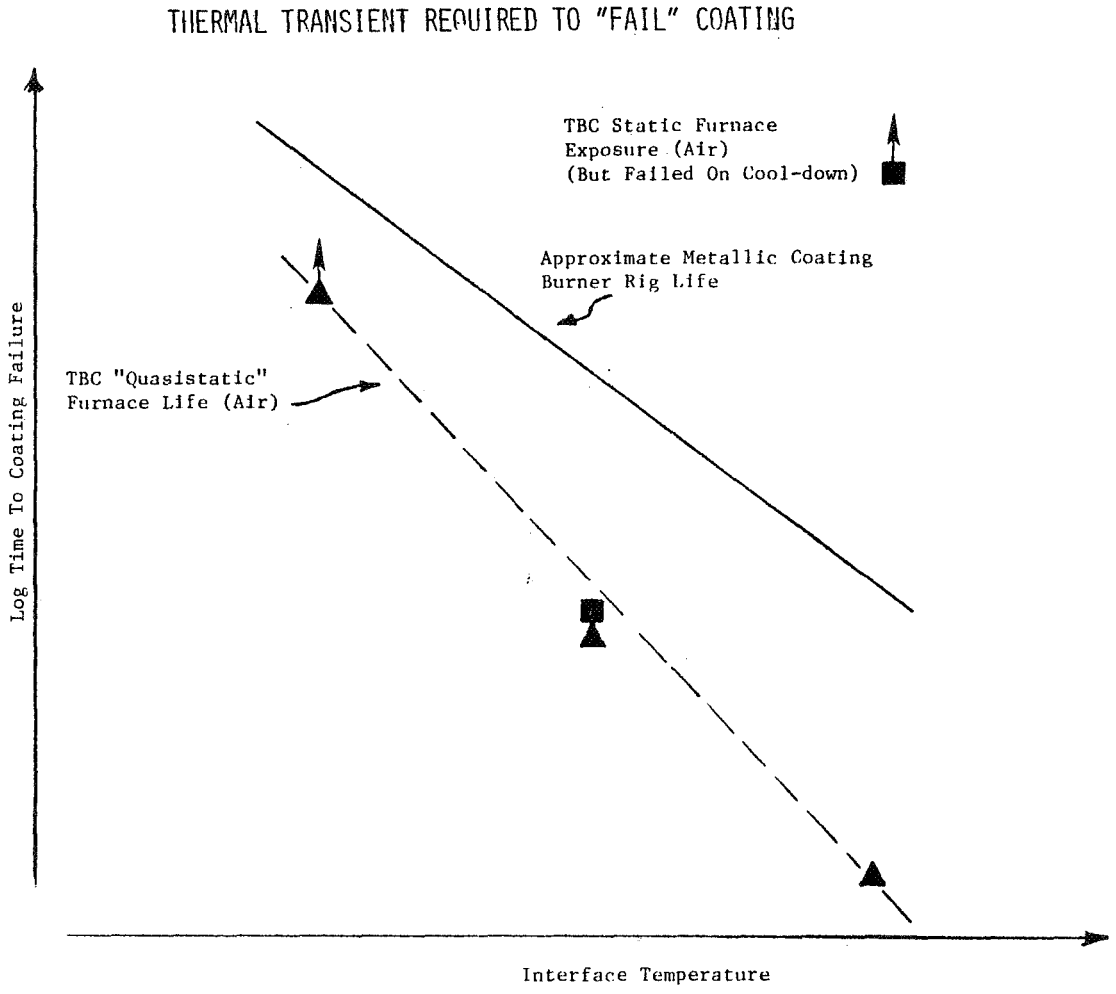
THERMAL TRANSIENT REQUIRED TO "FAIL" COATING
TBC Static Furnace
Exposure (Air)
(But Failed On Cool-down)
Approximate Metallic Coating
Burner Rig Life
TBC "Quasistatic"
Furnace Life (Air)
Log Time To Coating Failure
Interface Temperature

Figure 13.

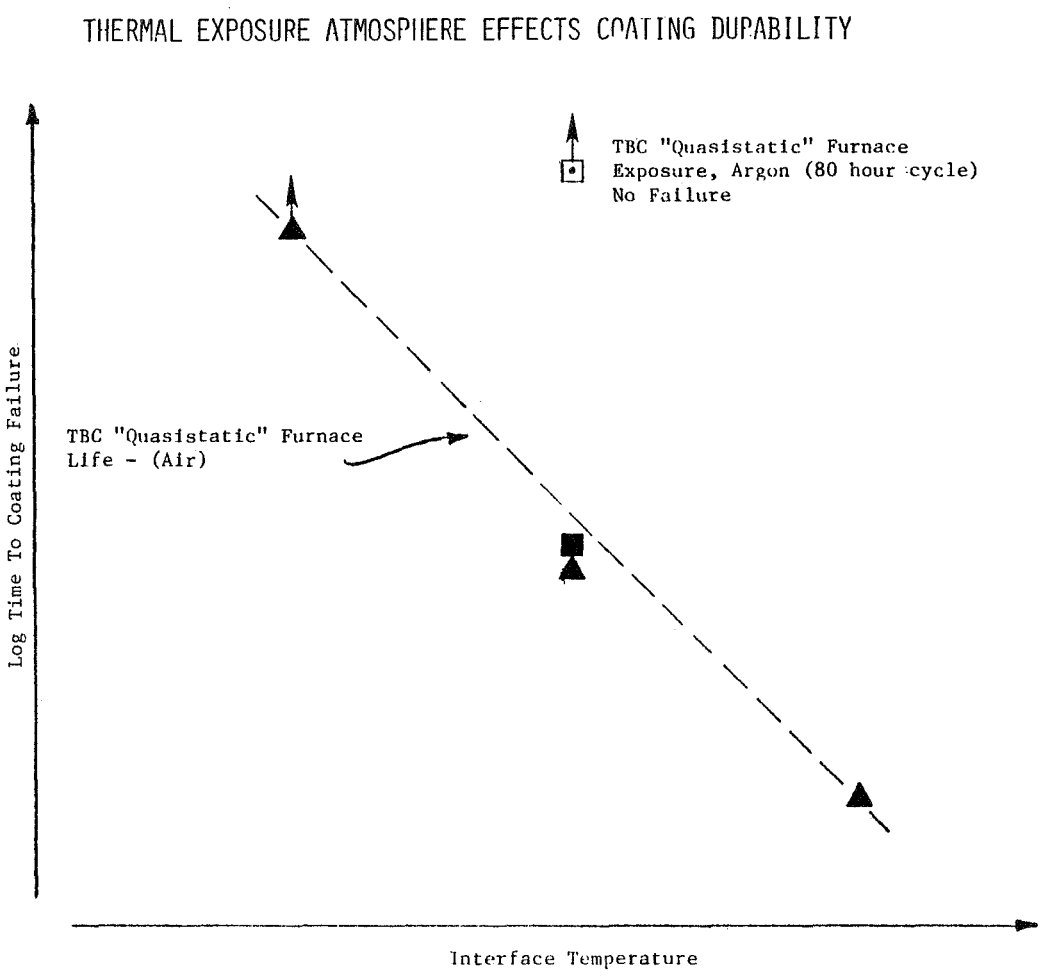
THERMAL EXPOSURE ATMOSPHERE EFFECTS COATING DURABILITY
TBC "Quasistatic" Furnace
Exposure, Argon (80 hour cycle)
No Failure
TBC "Quasistatic" Furnace
Life - (Air)
Log Time To Coating Failure
Interface Temperature

Figure 14.

COATINGS SURVIVE EXTENDED FURNACE EXPOSURE IN ARGON

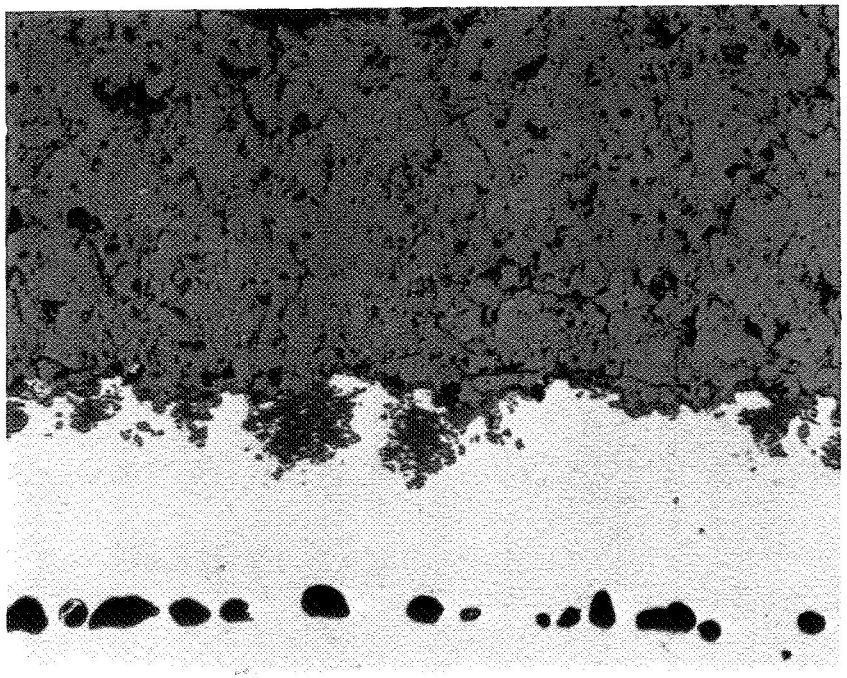

ARGON

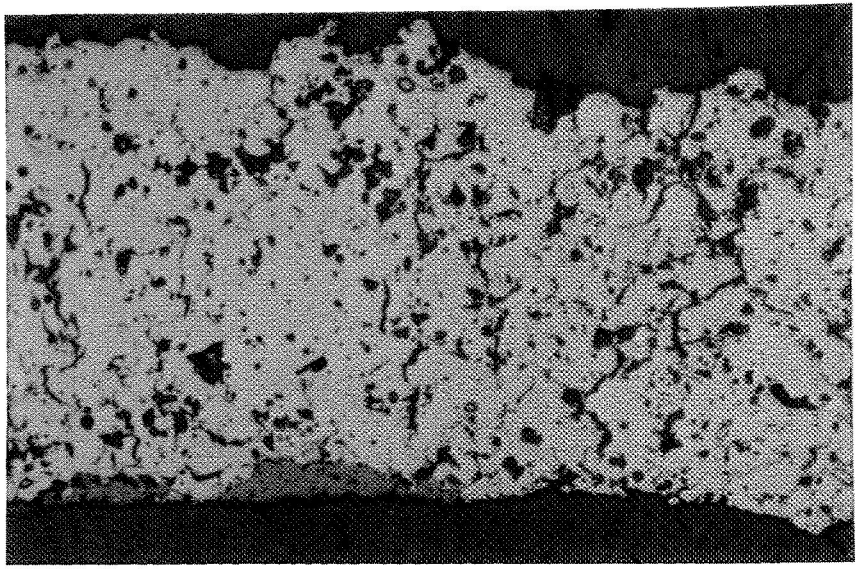

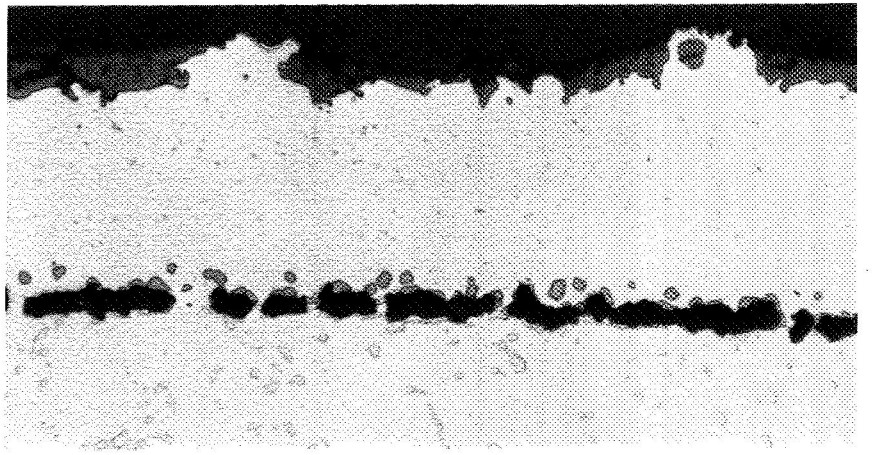

AIR

Figure 15.

AIR PRE-EXPOSURE DEGRADES CYCLIC LIFE

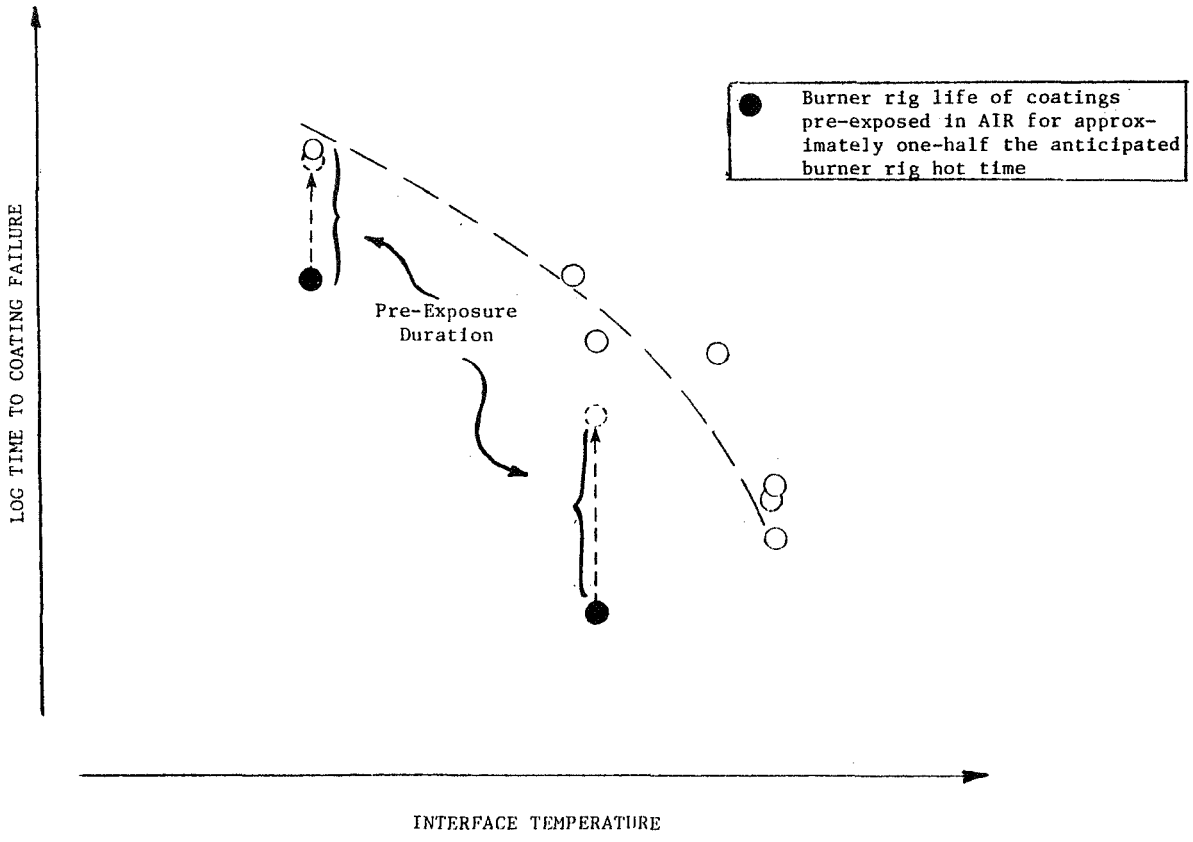

Figure 16.

"INERT" PRE-EXPOSURE EFFECT, APPEARS TO BE TEMPERATURE DEPENDENT

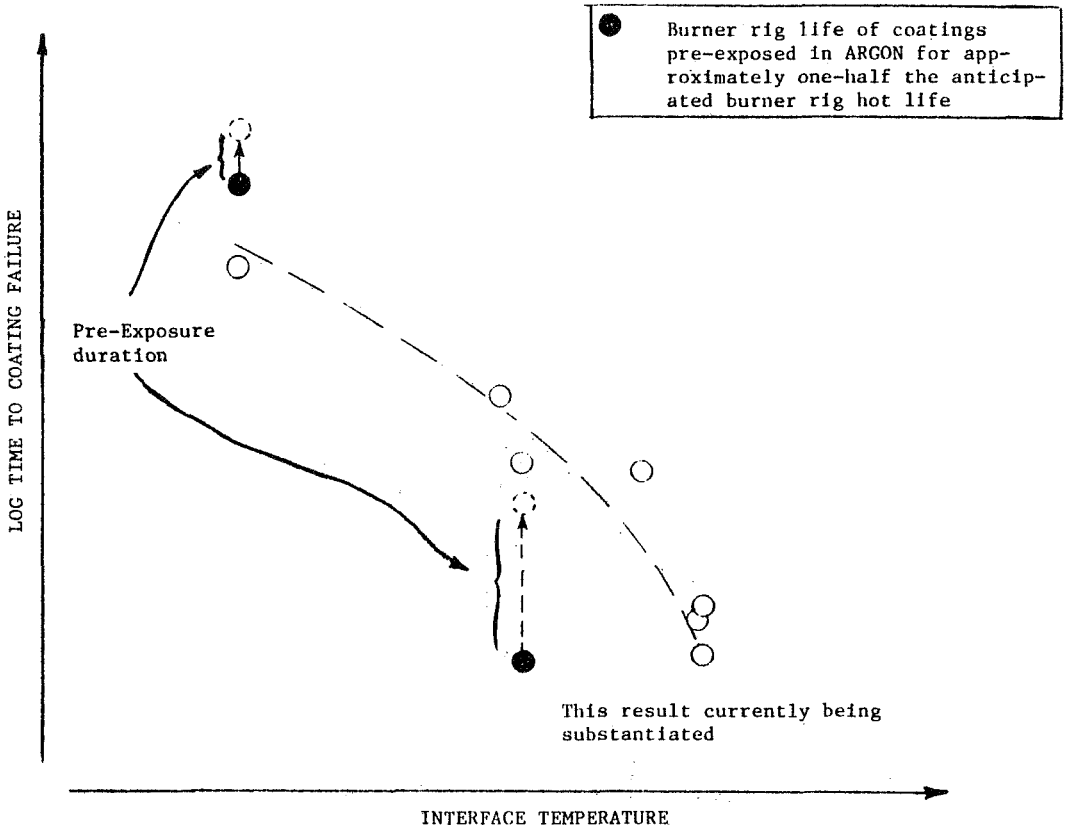

Figure 17.

MICROSTRUCTURAL VARIATIONS FOR PRE-TEST THERMAL EXPOSURE ATMOSPHERES

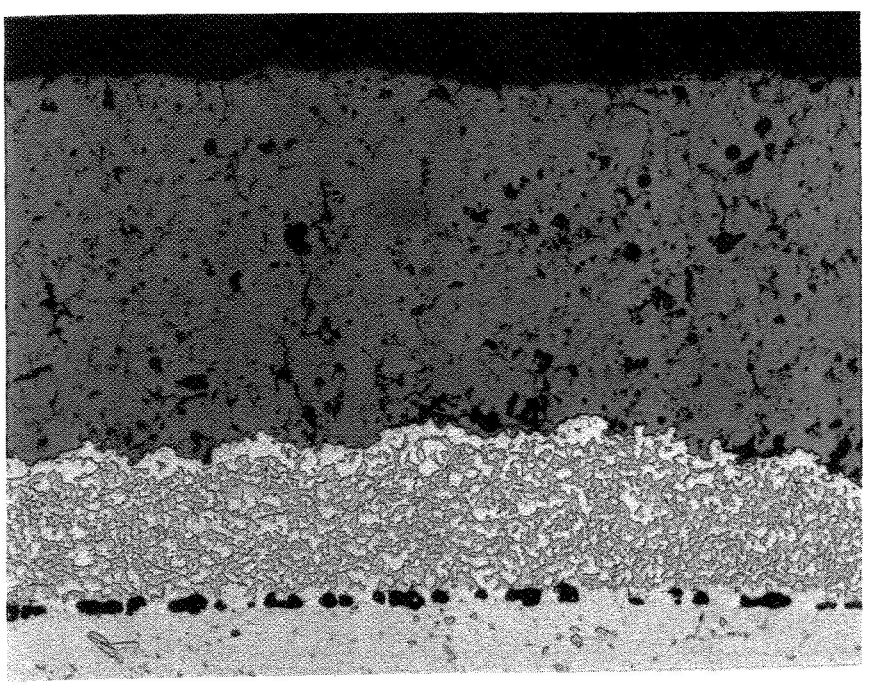

ARGON

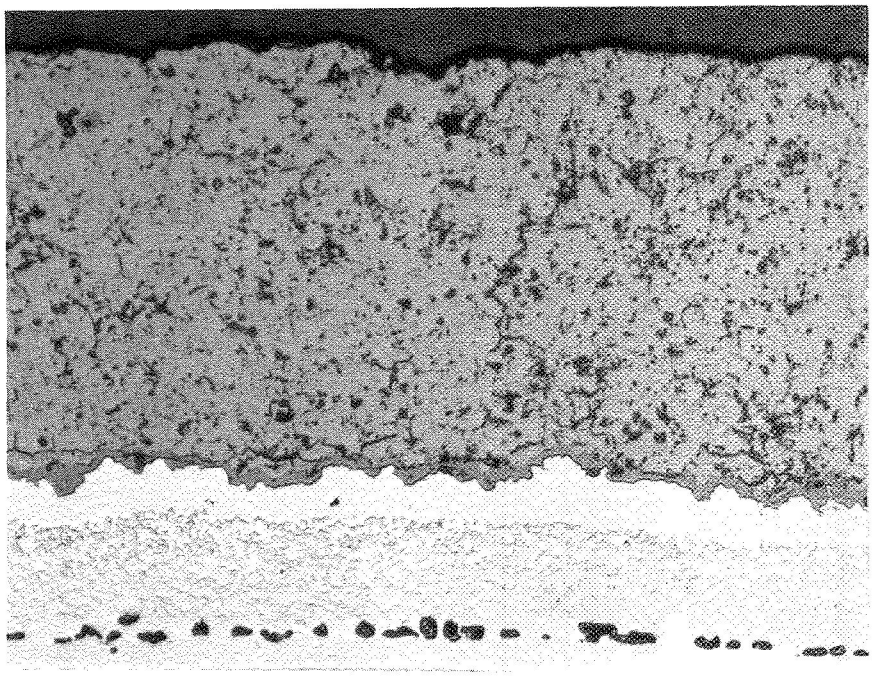

AIR

Figure 18.

CERAMIC THICKNESS AFFECTS DURABILITY

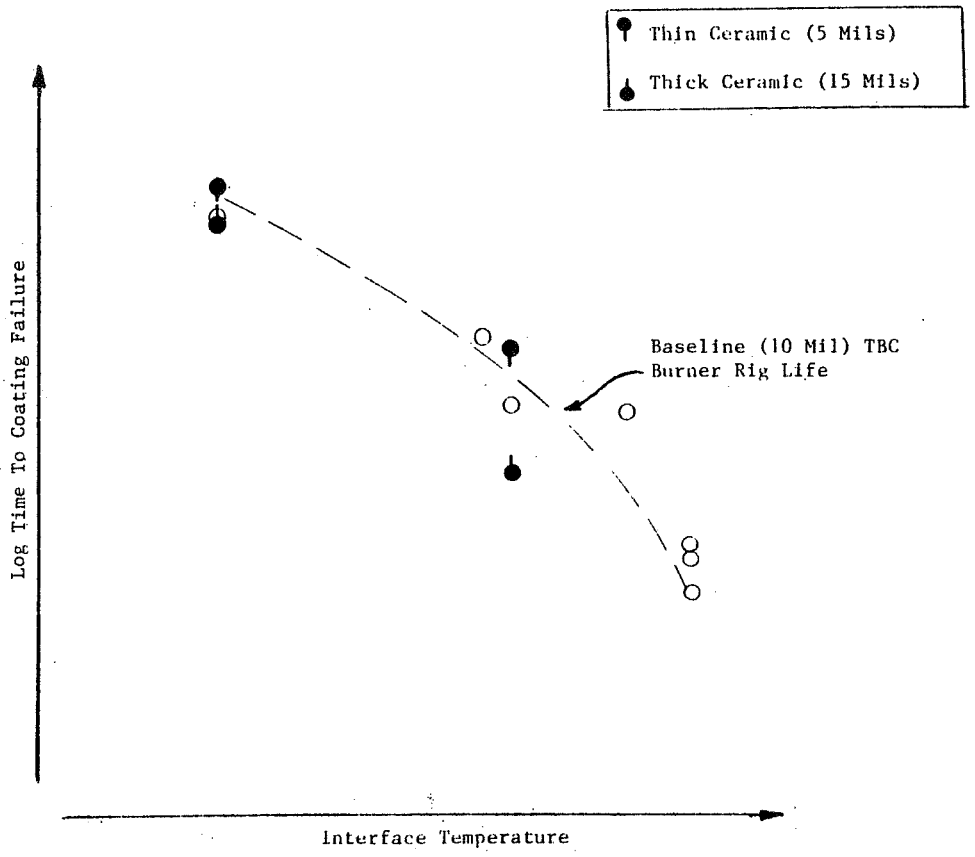

Figure 19.

SUMMARY

- PREDOMINANT FAILURE MODE; THERMOMECHANICAL CERAMIC SPALLATION NEAR INTERFACE.
- COATING LIFE DEPENDENT ON TEMPERATURE, "CYCLIC CONTENT".
  - THERMAL TRANSIENT REQUIRED TO SPALL COATING
- LONG TIME THERMAL EXPOSURE ATMOSPHERE AFFECTS COATING DURABILITY.
  - INERT ENVIRONMENT LIMITS COATING DEGRADATION
  - PRE-TEST INERT EXPOSURE EFFECT MAY BE TEMPERATURE DEPENDENT
- CERAMIC THICKNESS AFFECTS DURABILITY.
  - THIN COATINGS HAVE INCREASED LIFE
- SECONDARY FAILURE MODE; THERMOCHEMICAL (CYCLIC HOT CORROSION).
  - GENERALLY NOT OBSERVED
  - CORRODENT LEVEL THRESHOLD LIMIT ESTABLISHED IN LABORATORY

Figure 20.

KEY ISSUES TO BE ADDRESSED

- CONTINUED MICROANALYTICAL INTERPRETATION OF RESULTS.
- "PROGRESSIVE" OR "SINGLE EVENT" FAILURE (SUBCRITICAL CRACK PROPAGATION).
- NEAR INTERFACE STRESS MODELING IS CRITICAL TO UNDERSTANDING AND PREDICTION.

Figure 21.

A PERFORMANCE AND RELIABILITY MODEL FOR THERMAL BARRIER COATINGS

A. P. Batakis
Solar Turbines Incorporated
San Diego, California 92138

A modeling technique for predicting the performance and reliability of TBC's is being developed at Solar Turbines Incorporated. The concept combines experimental coating property data with finite element analyses to predict the thermal and mechanical behavior of coating systems in service. A key feature of Solar's approach is the use of a four point flexure test to estimate coating strength distributions and to predict coating failure probability.

This model has been used to evaluate the effect of physical variations on coating performance in high heat flux rocket engine applications for NASA. Current work, promoted by Caterpillar Tractor Company for diesel engine applications, is being conducted to measure coating strength as a function of temperature, and future work will document strength degradation with time at temperature. Solar's interest lies in the application of TBC's to gas turbine engine components.

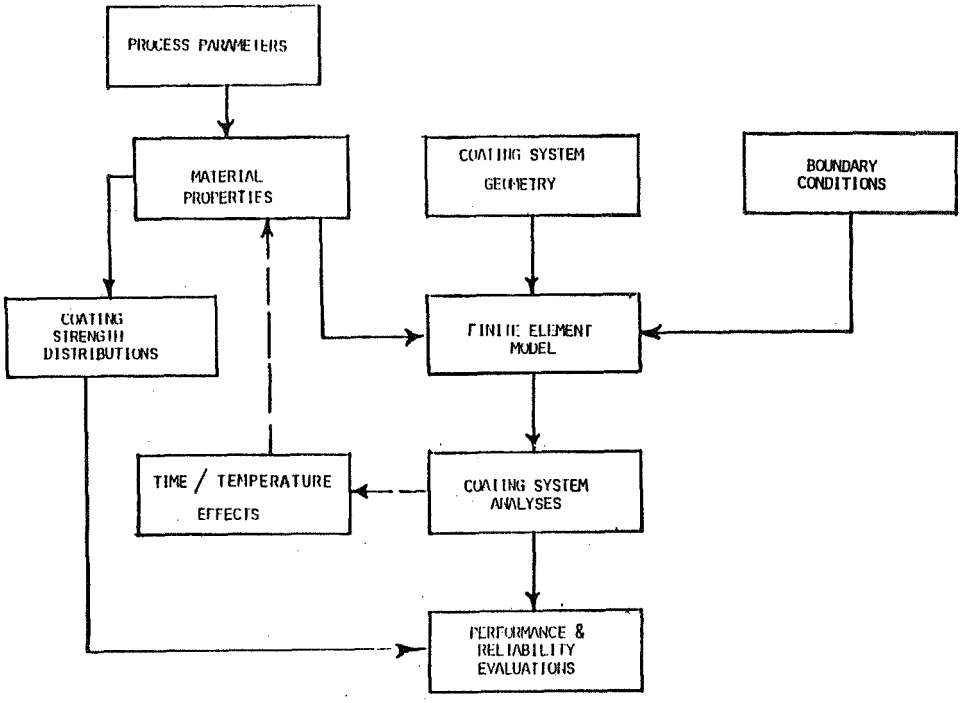

Figure 1. - TBC model development.

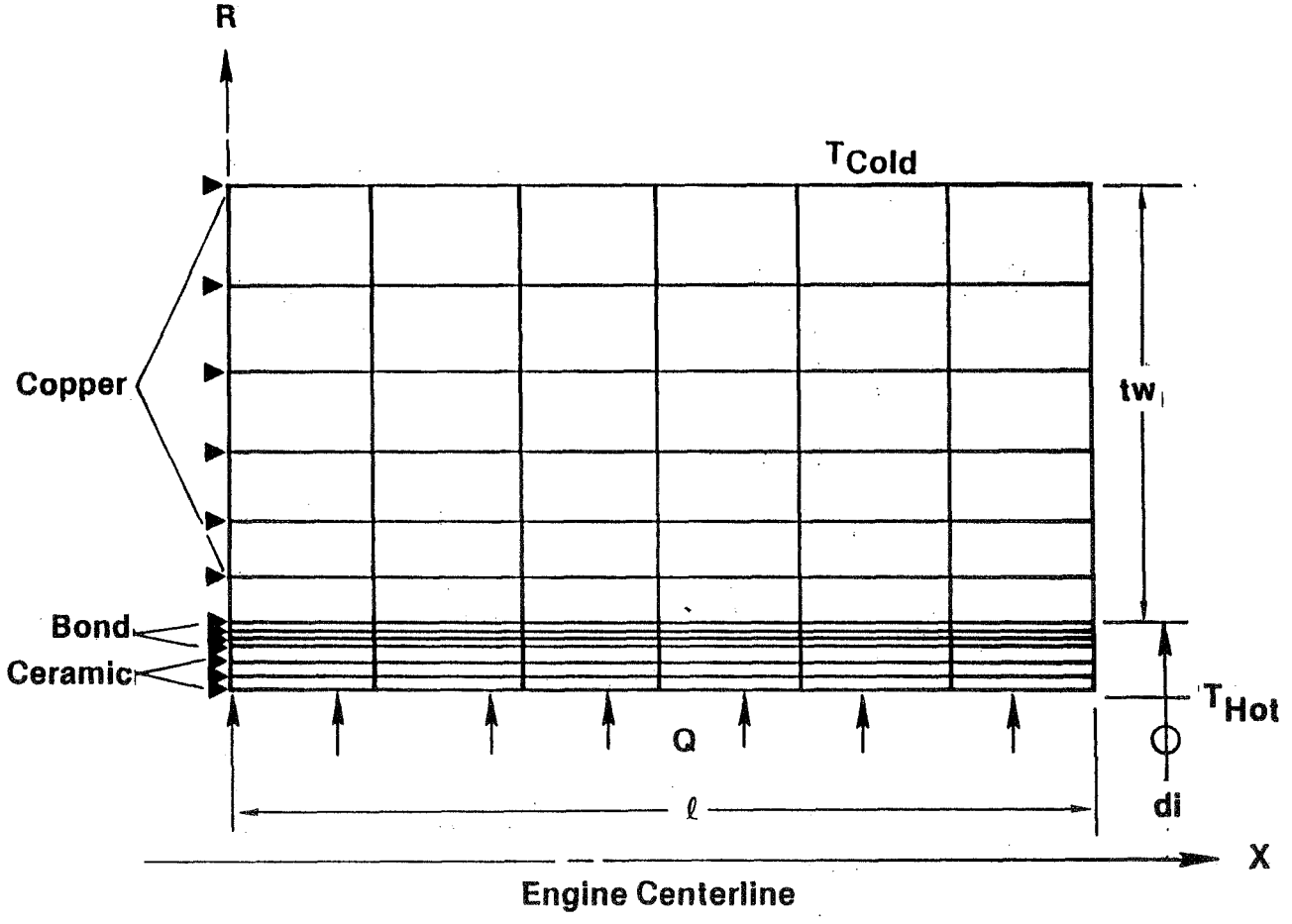

Figure 2. - Two-dimensional finite-element model of simulated rocket chamber wall.

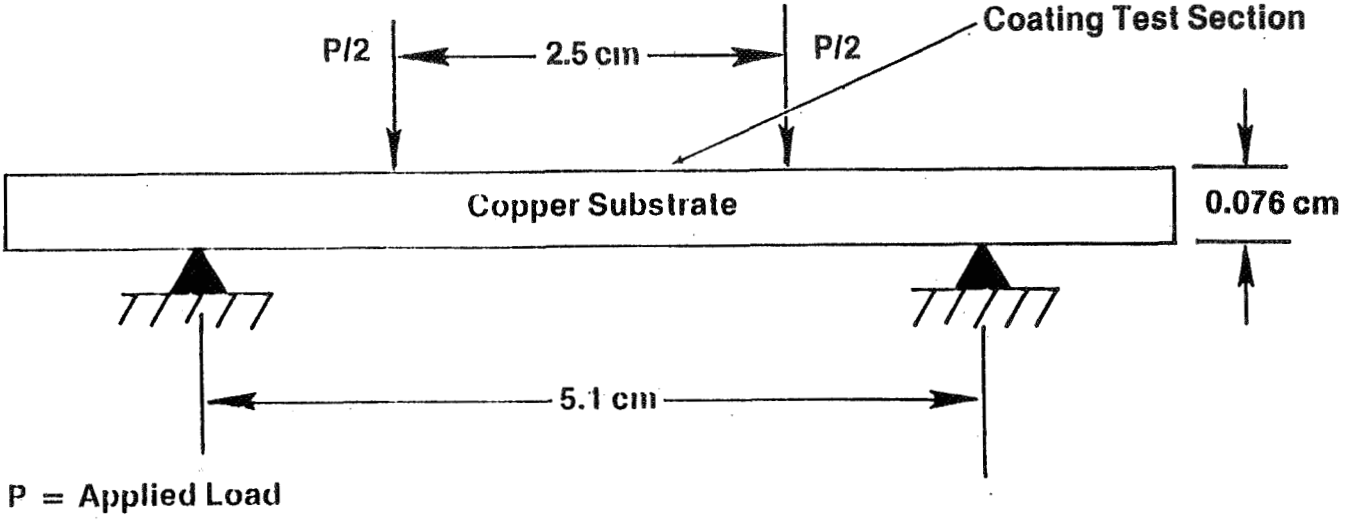

Figure 3. - Schematic of four point flexure test.

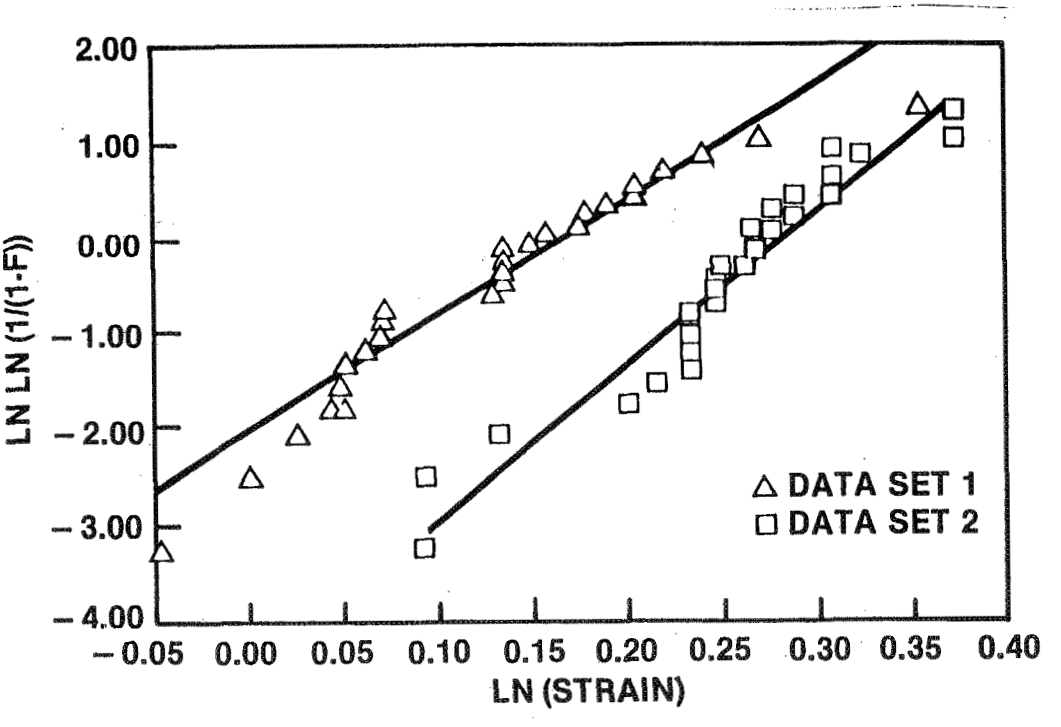

Figure 4. - Coating strength Weibull plots.

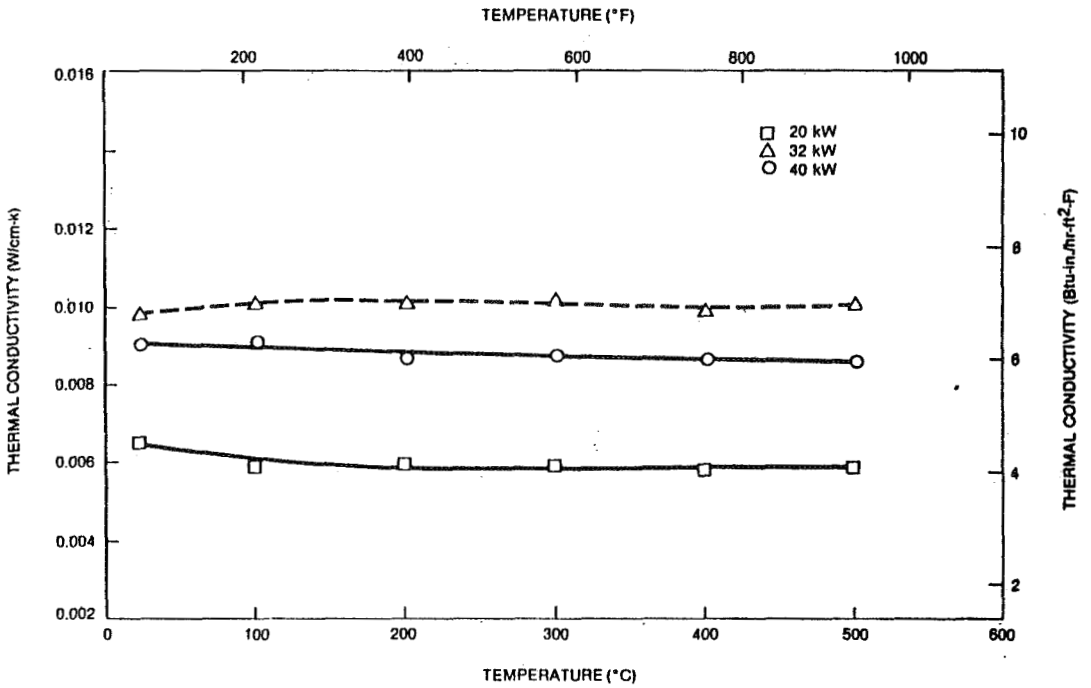

Figure 5. - Thermal conductivity of $ZrO_2Y_2O_3$ layers.

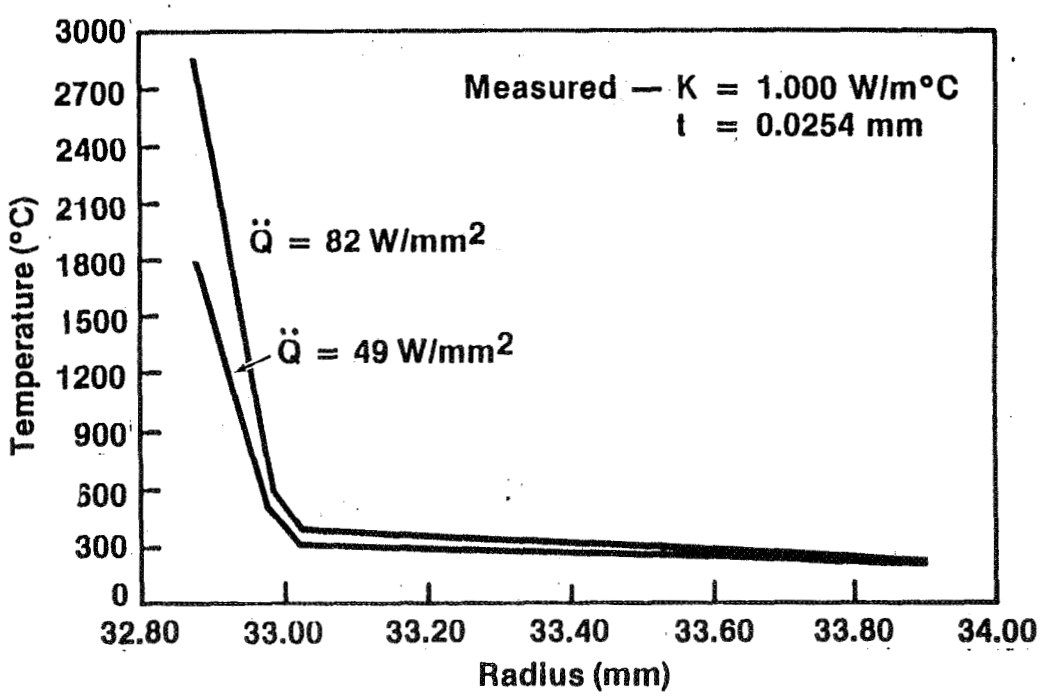

Figure 6. - Predicted coating temperature profile.

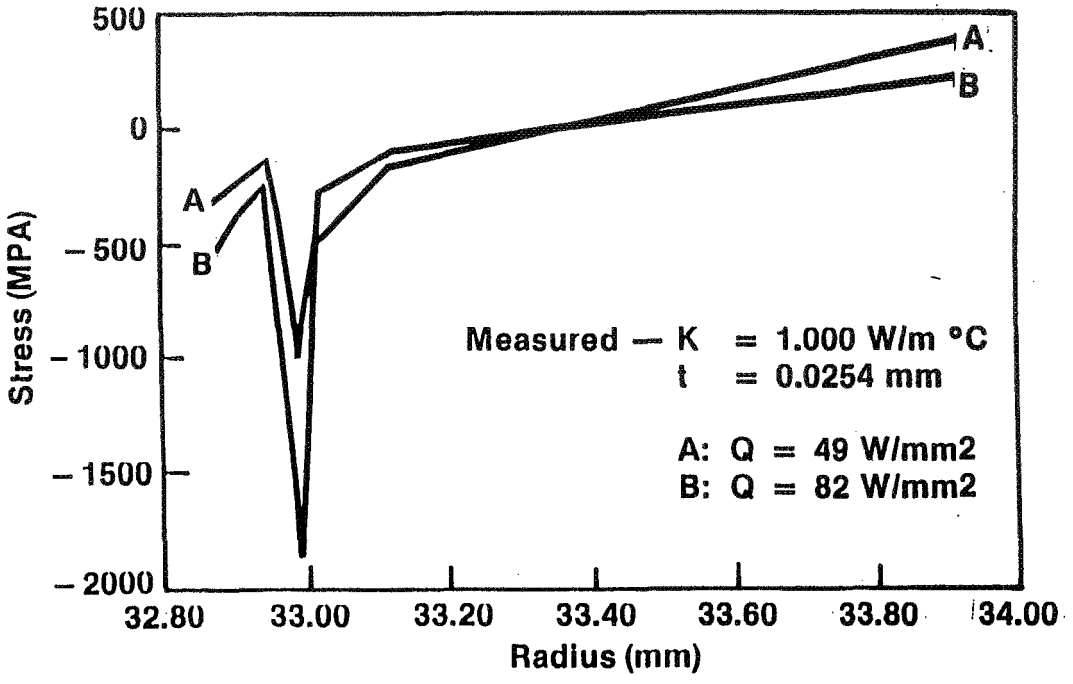

Figure 7. - Predicted hoop and axial coating stress profile.

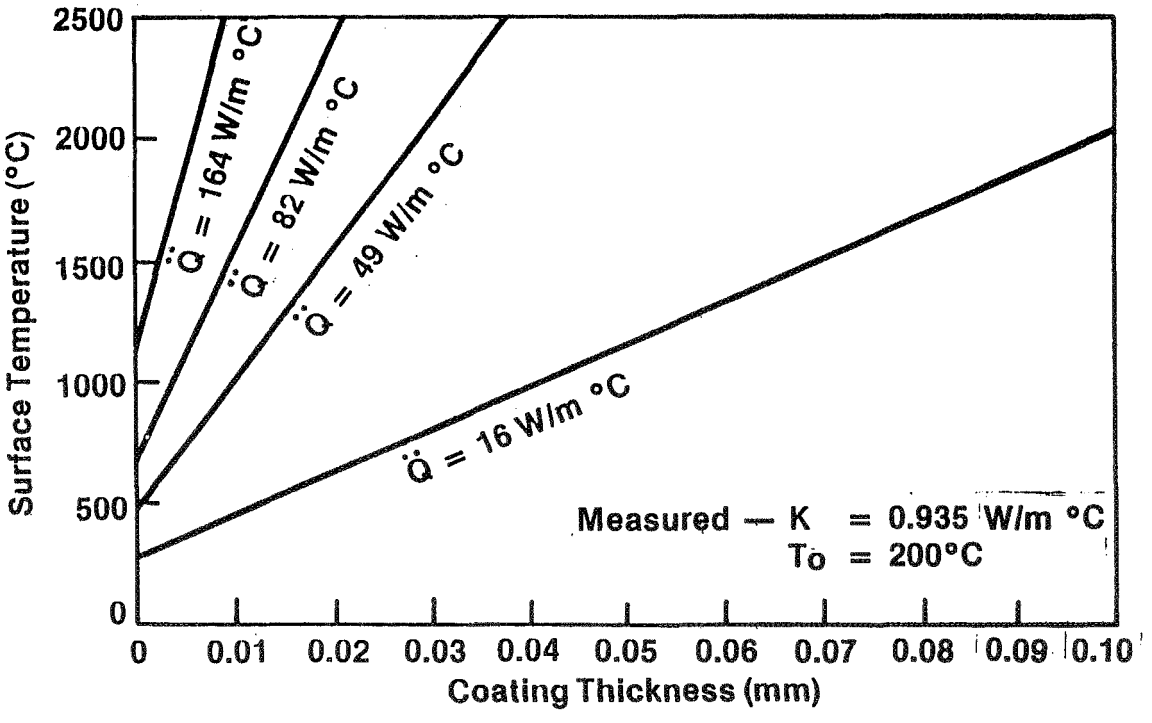

Figure 8. - Coating surface temperature vs. coating thickness.

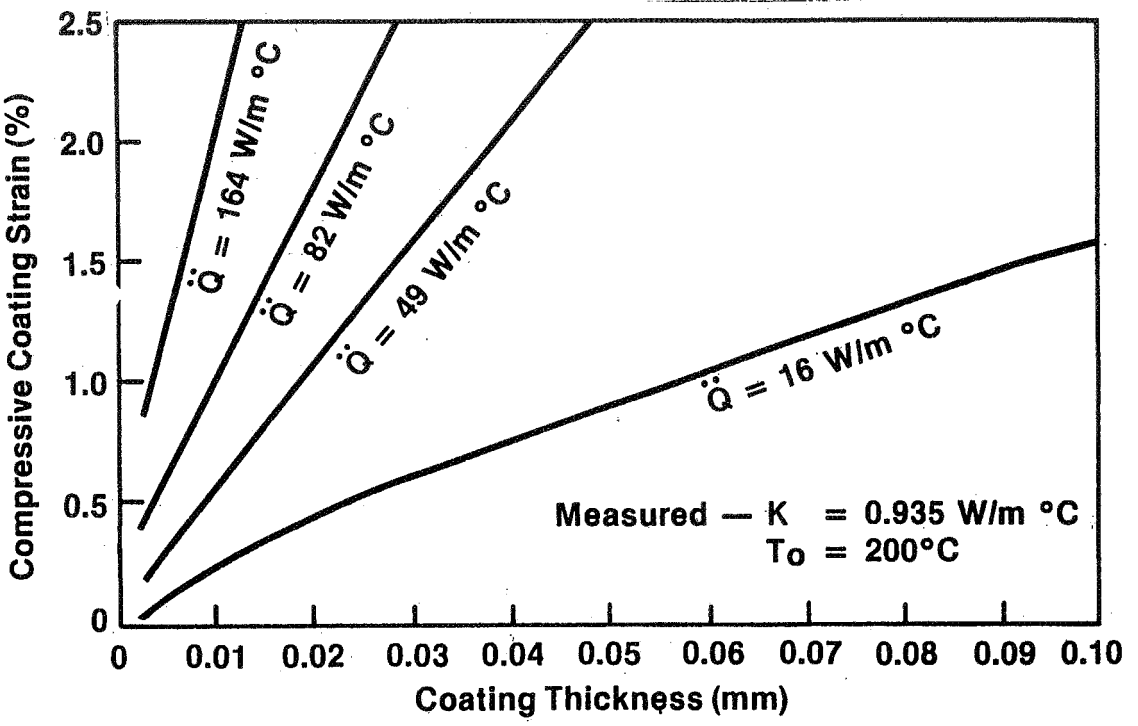

Figure 9. - Coating strain vs. coating thickness for various heat fluxes.

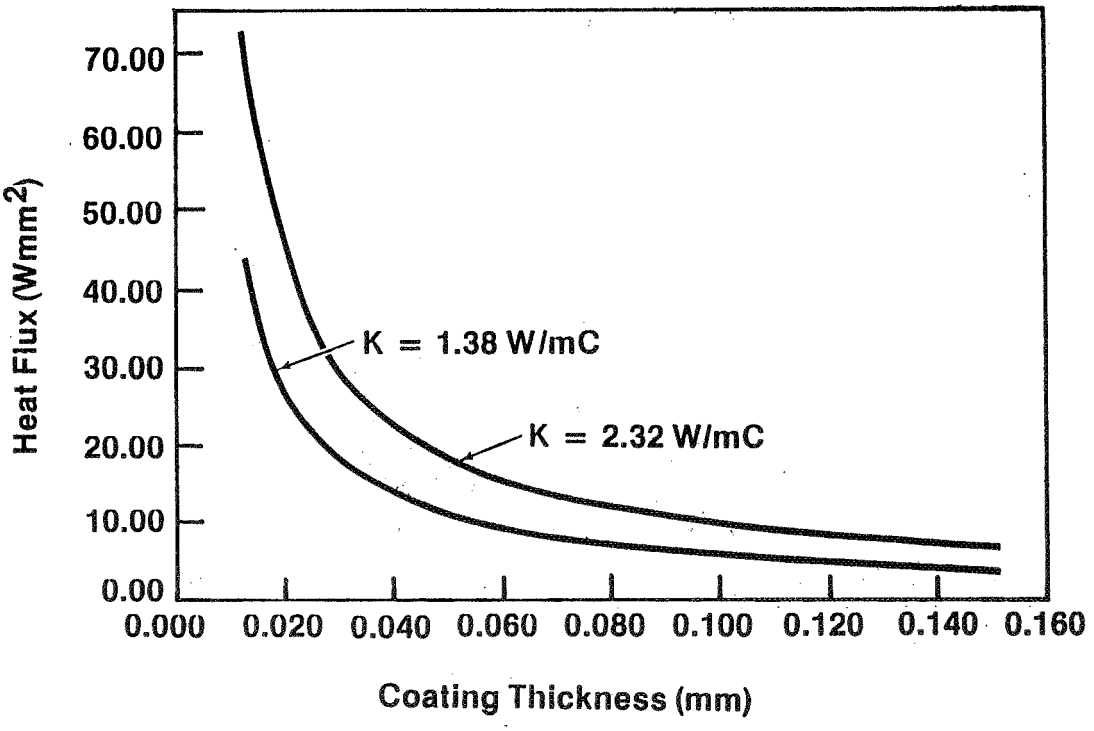

Figure 10. - Maximum heat flux vs. coating thickness for 95% survival probability.

THE EFFECT OF OXIDATION ON THE HIGH HEAT FLUX BEHAVIOR OF A THERMAL BARRIER COATING

Robert A. Miller
NASA Lewis Research Center
Cleveland, Ohio 44135

The effect of oxidation on the high heat flux behavior of a thermal barrier coating has been evaluated by cyclically exposing preoxidized specimens to a 3000°C nitrogen plasma. The thermal barrier coatings consisted of a 0.025 cm layer of air-plasma-sprayed ZrO_2-7%Y_2O_3 and a 0.012 cm layer of low pressure-plasma-sprayed NiCoCrAlY applied over 0.13 cm diameter B1900+Hf cylindrical substrates. A gradient of 800°C is produced across the ceramic layer in each 0.5 second exposure. This is much more severe than the gradient encountered on a gas turbine engine. Prior to exposure, the specimens were preoxidized at 1200°C for times from 0 to 20 hours.

These coatings were found to be tolerant to the high heat flux plasma flame for all but the most severe preoxidations. However, life degraded rapidly for preoxidation times in excess of 15 hours at 1200°C. A log-log plot of cycles-to-failure vs. estimated oxidative weight gain yield a straight or nearly straight line, and this line could be rationalized using an oxidation-based model that had been developed previously for low heat flux applications.

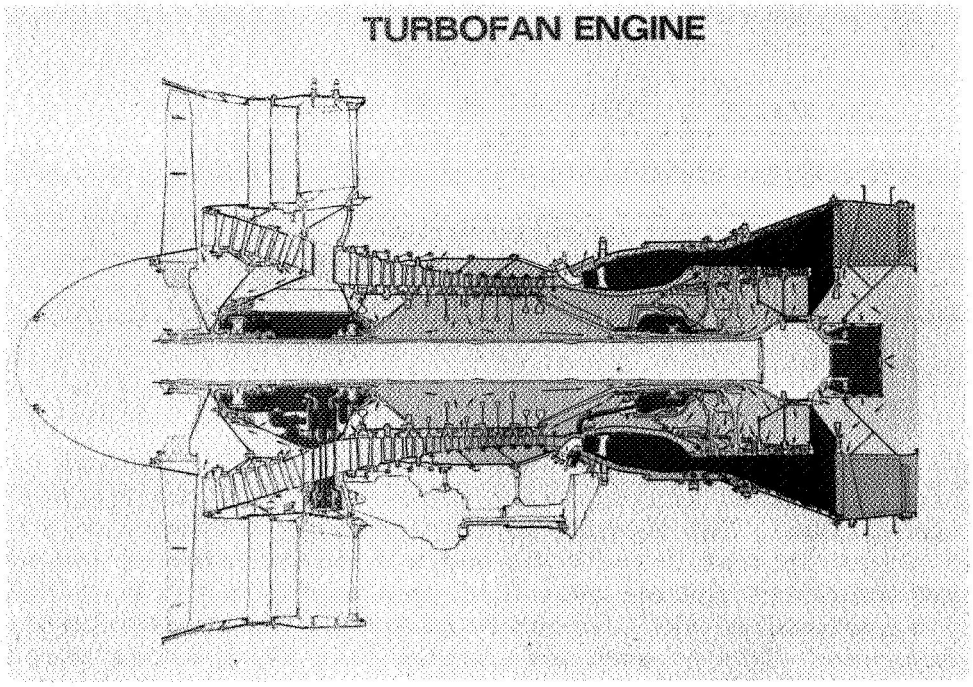

Figure 1.

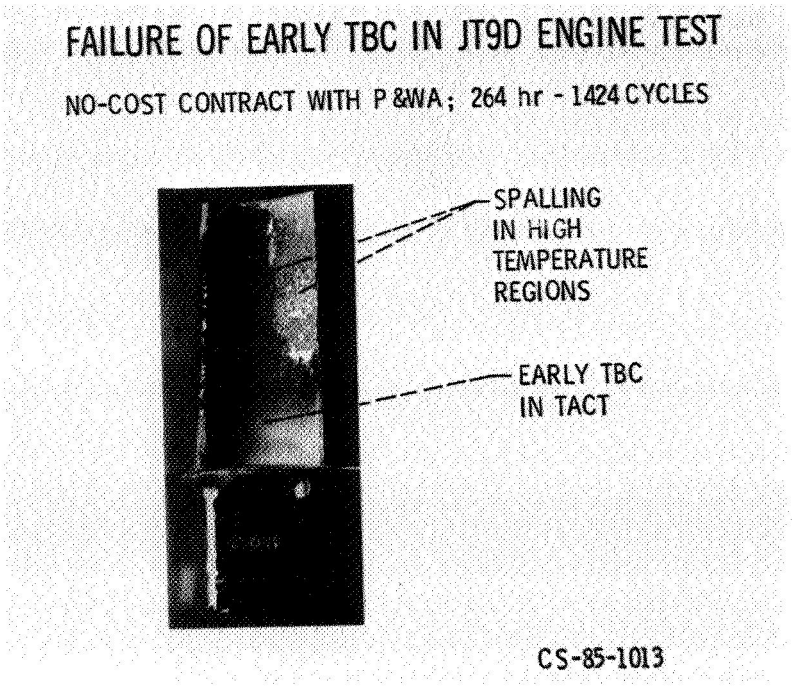

Figure 2.

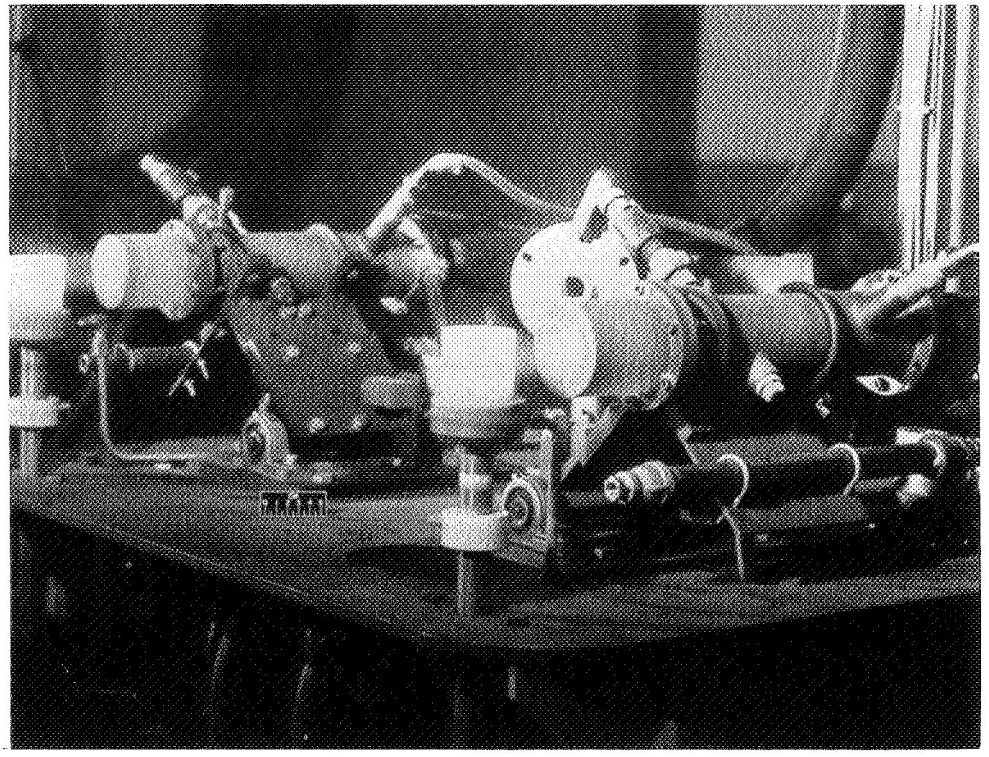

Figure 3.

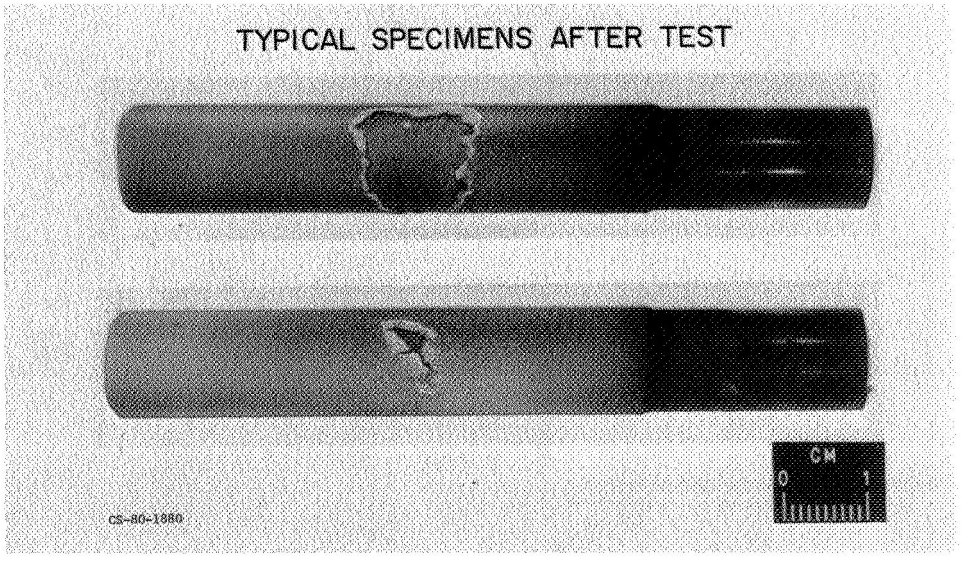

Figure 4.

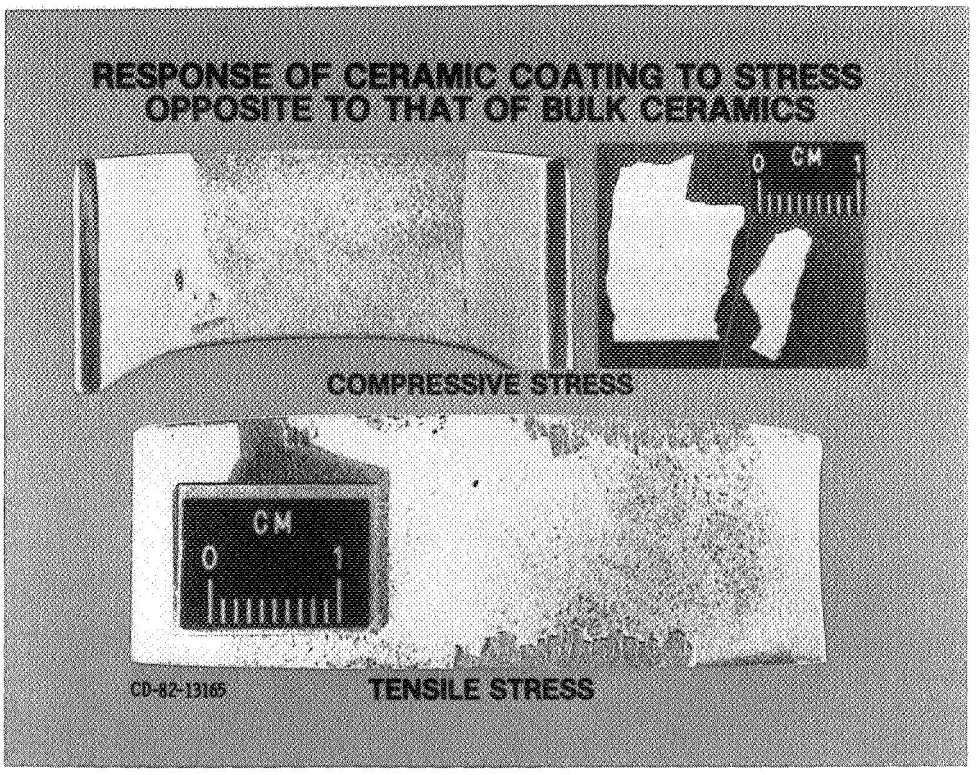

Figure 5.

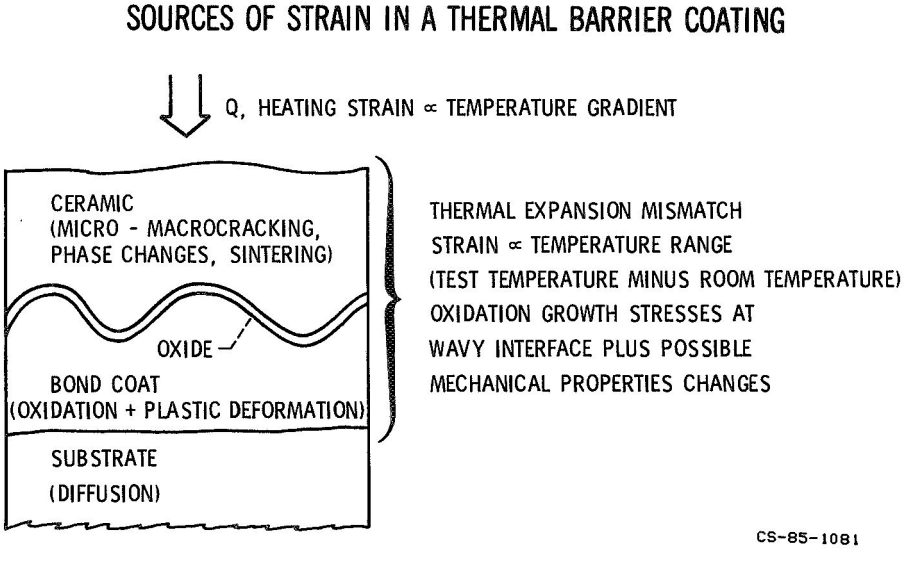

Figure 6.

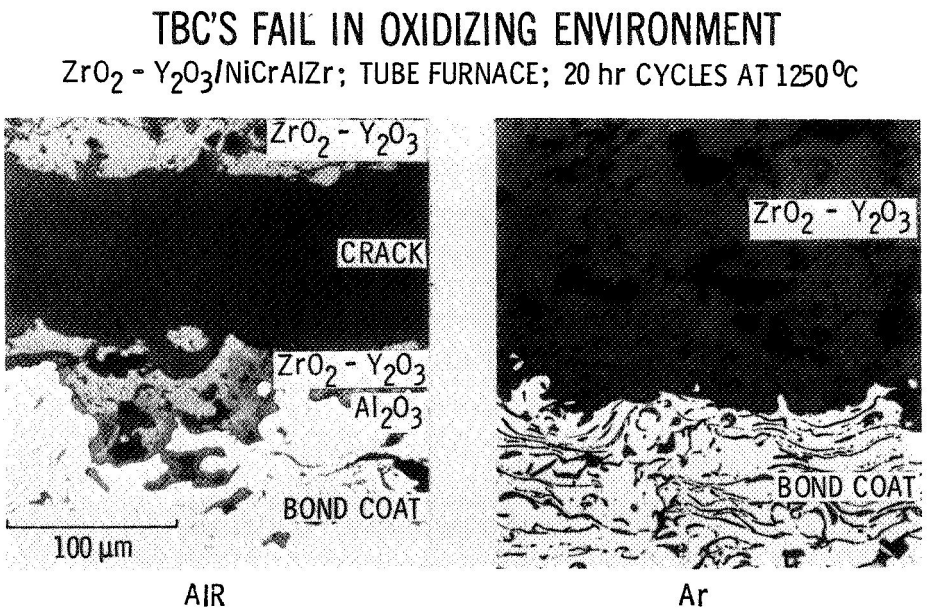

Figure 7.

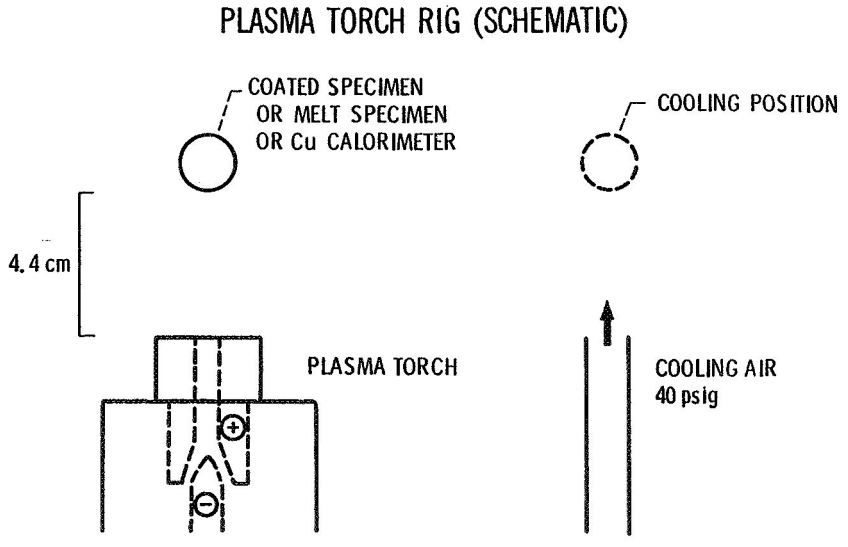

Figure 8.

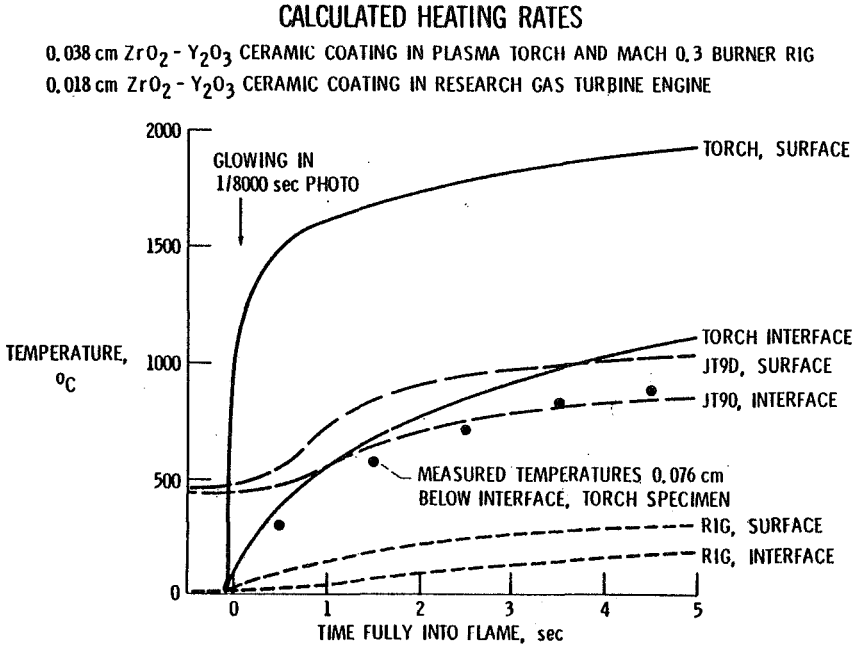

Figure 9.

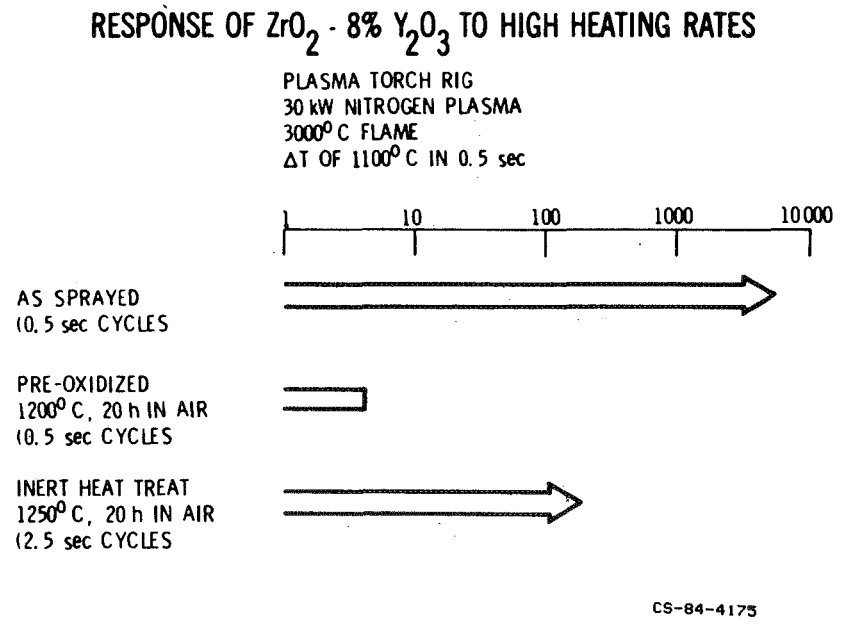

Figure 10.

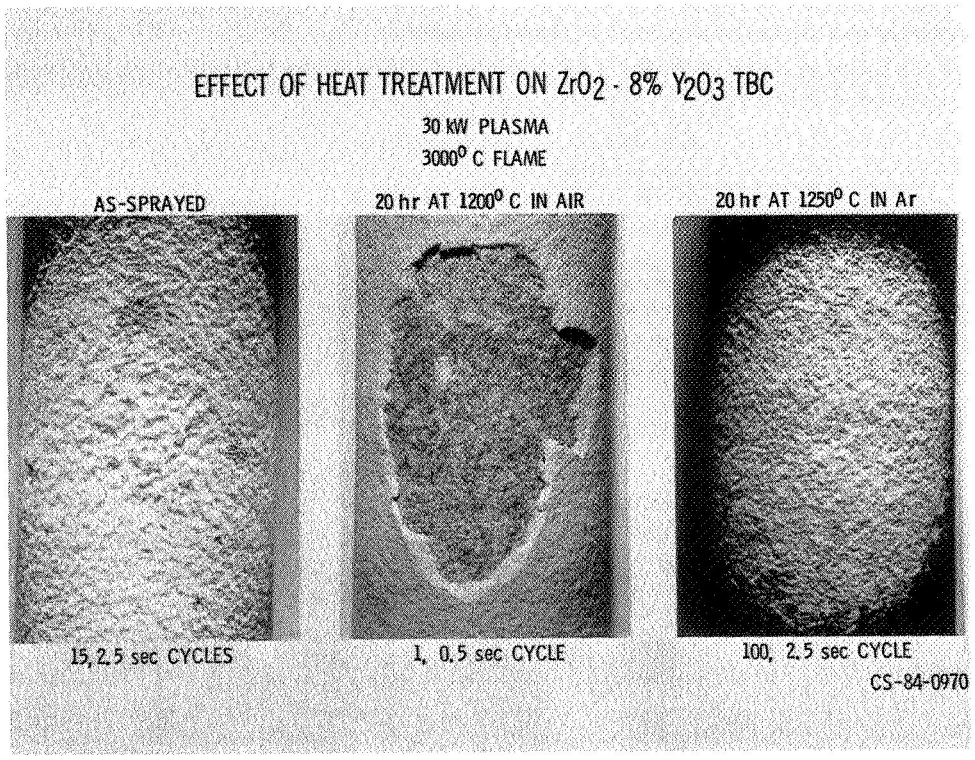

Figure 11.

THE STORY SO FAR -

- AS - SPRAYED 0.04 cm ZrO_2 - 8% Y_2O_3 TBCs TOLERATE LOCALIZED HIGH HEAT FLUX GREATER THAN EXPECTED IN GAS TURBINE ENGINE
- HIGH HEAT FLUX LIFE MAY BE SEVERLY DEGRADED BY PREOXIDATION
- INERT HEAT TREATMENT NOT HARMFUL (AND APPARENTLY BENEFICIAL, SEE THIN SOLID FILMS 119, 195 (1984).

THE NEXT STEP

- QUANTITATIVELY RELATE TBC OXIDATION TO HIGH HEAT FLUX LIFE.

CS-85-1077

Figure 12.

EXPERIMENTAL

SPECIMEN CONFIGURATION

CERAMIC LAYER
ZrO_2 - 7% Y_2O_3
0.025 CM THICK
ATMOSPHERIC PRESSURE PLASMA SPRAYED

BOND COAT
Ni - 22% Co - 18% Cr - 12% Al - 0.4%Y
0.012 cm THICK
LOW PRESSURE PLASMA SPRAYED

SUBSTRATE
B1900 + Hf
1.3 cm CLYINDERS

HEAT TREATMENT
4 hr AT 1080 °C IN H_2

PREOXIDATION
0 to 20 hr AT 1200 °C IN AIR

TEST RIG
30 kW N_2 PLASMA TORCH
3000 °C FLAME
0.5 sec CYCLES
800 °C GRADIENT (CALCULATED) IN 0.5 SEC
1300 °C SURFACE TEMPERATURE (CALCULATED) IN 0.5 SEC

CS-85-1075

Figure 13.

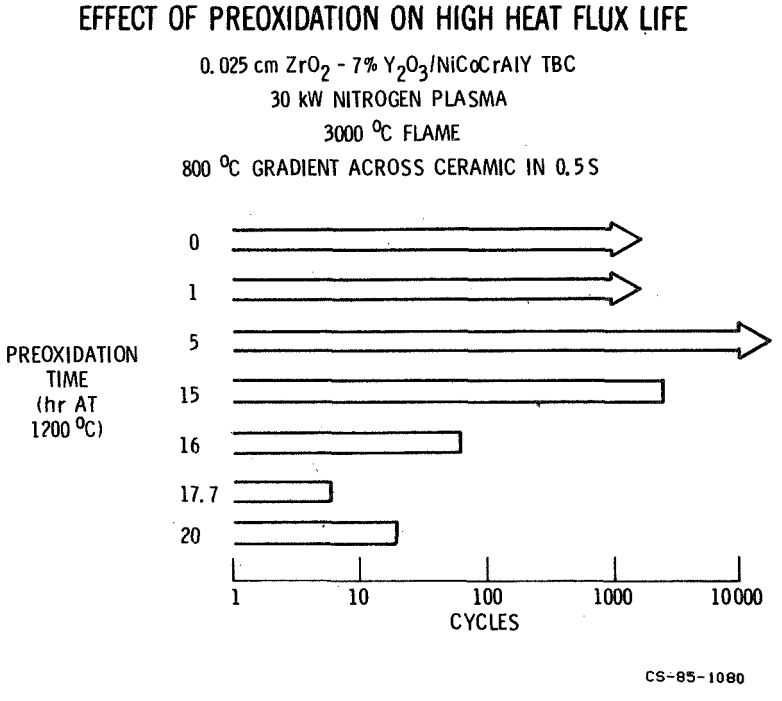

Figure 14.

EFFECT OF PREOXIDATION ON HIGH HEAT FLUX LIFE

0.025 cm ZrO_2 - 7% Y_2O_3/NiCoCrAlY
30 kW PLASMA
3000 °C FLAME
0.5 sec CYCLES

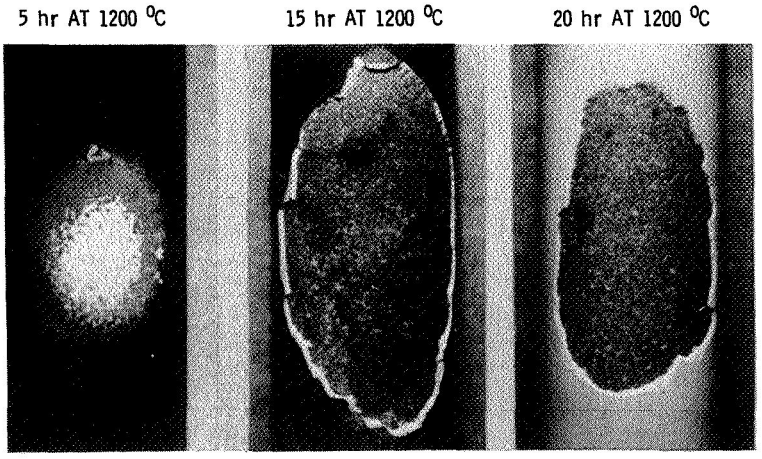

Figure 15.

TBC LIFE MODEL DEVELOPED FOR LOW HEAT FLUX
J. CERAM SOC. 67,517 (1984)

ASSUMPTIONS

- TIME DEPENDENCE - OXIDATION, W
- CYCLE DEPENDENCE - SLOW CRACK GROWTH DUE TO CYCLIC STRAIN
- OXIDIZED SPECIMEN BEHAVES AS IF CYCLIC STRAIN INCREASES

WORKING EXPRESSION

$$\sum_{N=1}^{N_f} \left[(1 - \varepsilon_r/\varepsilon_f)\ (w_N/w_c)^m + \varepsilon_r/\varepsilon_f \right]^b = 1$$

$\varepsilon_r/\varepsilon_f$ – RATIO OF THERMAL EXPANSION MISMATCH STRAIN TO FAILURE STRAIN

w_N/w_c – RATIO OF WEIGHT GAIN AFTER CYCLE N TO CRITICAL WEIGHT GAIN FOR ONE CYCLE FAILURE

m – EXPONENT EQUAL TO UNITY IF STRAIN INCREASES IN A LINEAR MANNER WITH WEIGHT GAIN

b – SUBCRITICAL CRACK GROWTH EXPONENT

N_f – CYCLES TO FAILURE

FORM OF EXPRESSION FOR PREOXIDATION

$$N_f \propto \left[(1 - \varepsilon_r/\varepsilon_f)\ (w_N/w_c)^m + \varepsilon_r/\varepsilon_f \right]^{-b}$$

CS-85-1076

Figure 16.

FIT OF HIGH HEAT FLUX DATA USING OXIDATION MODEL

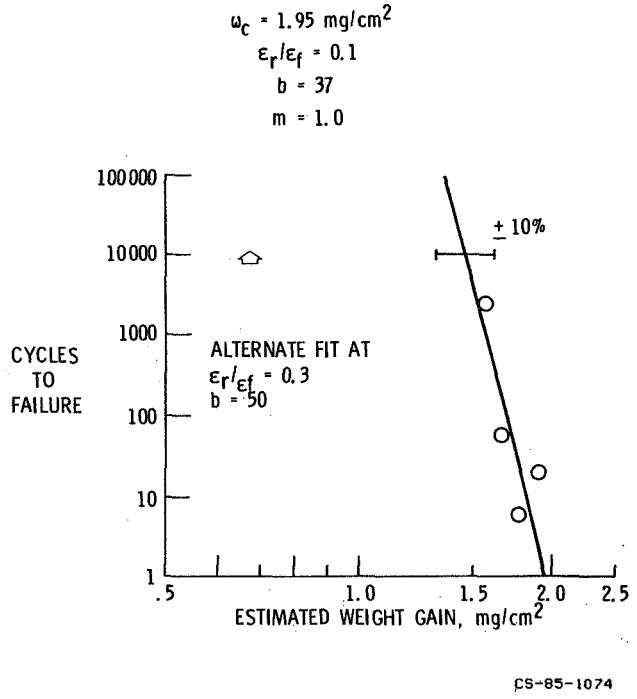

Figure 17.

CONCLUSIONS

- MODERATELY OXIDIZED 0.025 cm ZrO_2 - 7%Y_2O_3 TBC_s TOLERATE HIGH HEAT FLUX
- TBC LIFE A VERY STRONG FUNCTION OF AMOUNT OF PREOXIDATION
- MODEL DEVELOPED FOR LOW HEAT FLUX MAY BE ADEQUATE FOR HIGH HEAT FLUX

FUTURE NEEDS

- WEIGHT GAIN MEASUREMENTS
- ADDITIONAL POINTS BETWEEN 10 AND 15 HOUR PREOXIDATION
- COMPLEMENTARY PREOXIDATION/INERT FURNACE EXPERIMENTS

CS-85-1079

Figure 18.

EFFECT OF BOND COAT CREEP AND OXIDATION ON TBC INTEGRITY

E.C. Duderstadt and B.H. Pilsner
General Electric Company
Cincinnati, Ohio 45215

The potential of thermal barrier coatings (TBC's) on high-pressure turbine (HPT) nozzles and blades is limited at present by the inability to quantitatively predict TBC life for these components. The goal of the work described here was to isolate the major TBC failure mechanisms, which is part of a larger program aimed at developing TBC life prediction models. Based on the results of experiments to isolate TBC failure mechanisms, the effects of bond coat oxidation and bond coat creep on TBC integrity is discussed. In bond coat oxidation experiments, Rene' 80 specimens coated with a NiCrAlY/ZrO_2-8% Y_2O_3 TBC received isothermal pre-exposures at 2000 °F in static argon, static air, or received no pre-exposure. The effects of oxidation due to these pre-exposures were determined by thermal cycle tests in both static air and static argon at 2000 °F. To study the effect of bond coat creep on TBC behavior, four bond coats with different creep properties were evaluated by thermal cycle tests in air at 2000 °F. The test results, the relative importance of these two failure mechanisms, and how their effects may be quantified will also be discussed.

TABLE I.

MAIN THERMAL BARRIER COATING SYSTEM (weight percent)

Substrate(Rene' 80)	:	Ni-14Cr-9.5Co-5Ti-4Mo-3Al-0.17C-0.03Zr-0.015B
Bond Coating	:	Ni-22Cr-10Al-0.3Y (Low Pressure Plasma Spray)
Top Coating	:	ZnO_2 - $8Y_2O_3$ (Air Plasma Spray)

TABLE II.

BOND COAT CREEP SYSTEMS

Systems	Substrate/Bond Coating/Over Coating/Top Coating	Bond Coat Creep Strength
1	Rene' 80 / Ni-Cr-Al-Y / Aluminide / ZrO_2-Y_2O_3	Low
2	Rene' 80 / Superalloy 1/ Aluminide / ZrO_2-Y_2O_3	↓
3	Rene' 80 / Superalloy 2/ Aluminide / ZrO_2-Y_2O_3	↓
4	Rene' 80 / Superalloy 3/ Aluminide / ZrO_2-Y_2O_3	High

1. DETERMINE THERMAL BARRIER COATING FAILURE MECHANISMS

   -- Bond Coat Oxidation

   -- Bond Coat Creep

2. Thermal Barrier Coating Life Prediction Model

   -- Failure Mechanisms

   -- Key Mechanical Properties

   -- Thermomechanical Properties

Figure 1.

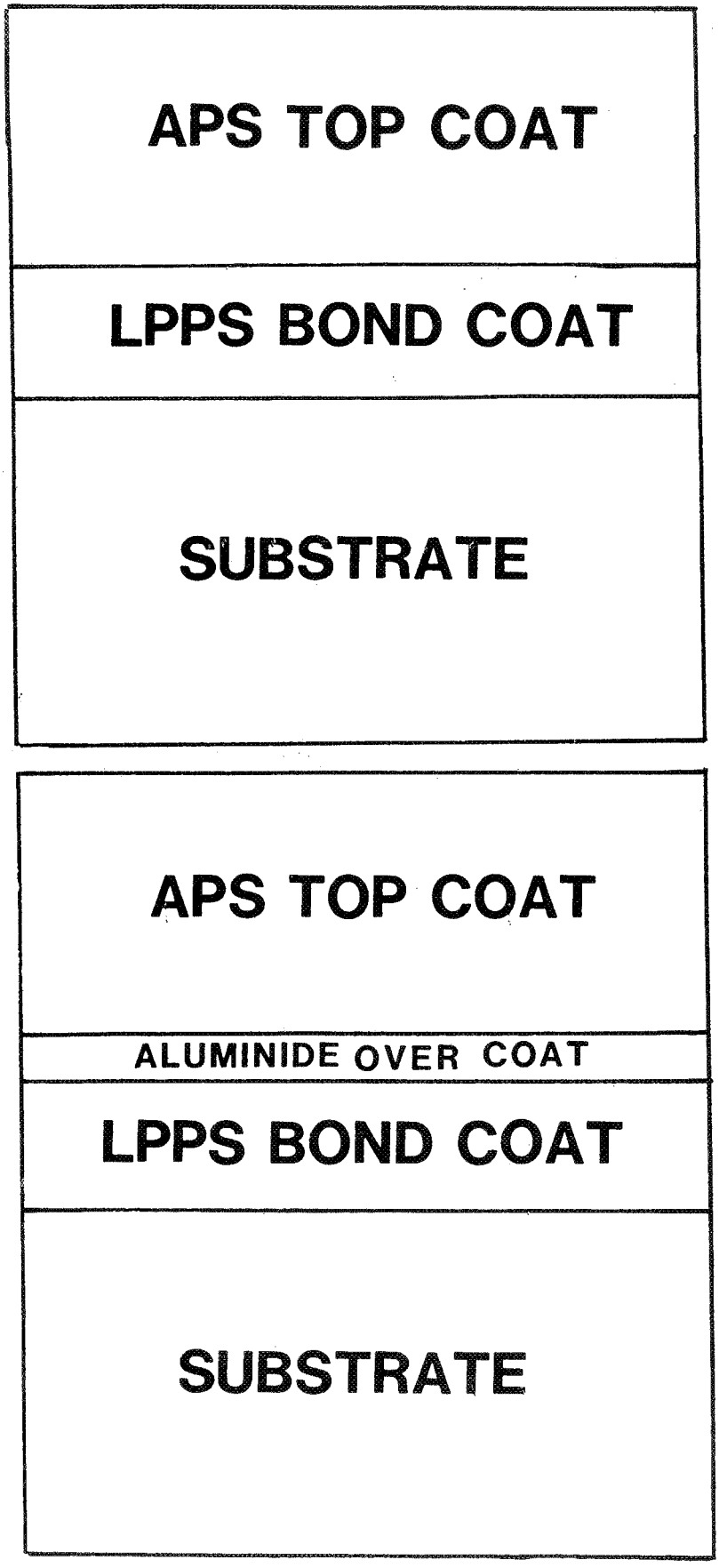
APS TOP COAT
LPPS BOND COAT
SUBSTRATE
APS TOP COAT
ALUMINIDE OVER COAT
LPPS BOND COAT
SUBSTRATE

Figure 2.

RAPID TEMPERATURE FURNACE

--- 10 minute heat up

--- 45 minute exposure at 2000 F

--- 15 minute forced cooling

Figure 3.

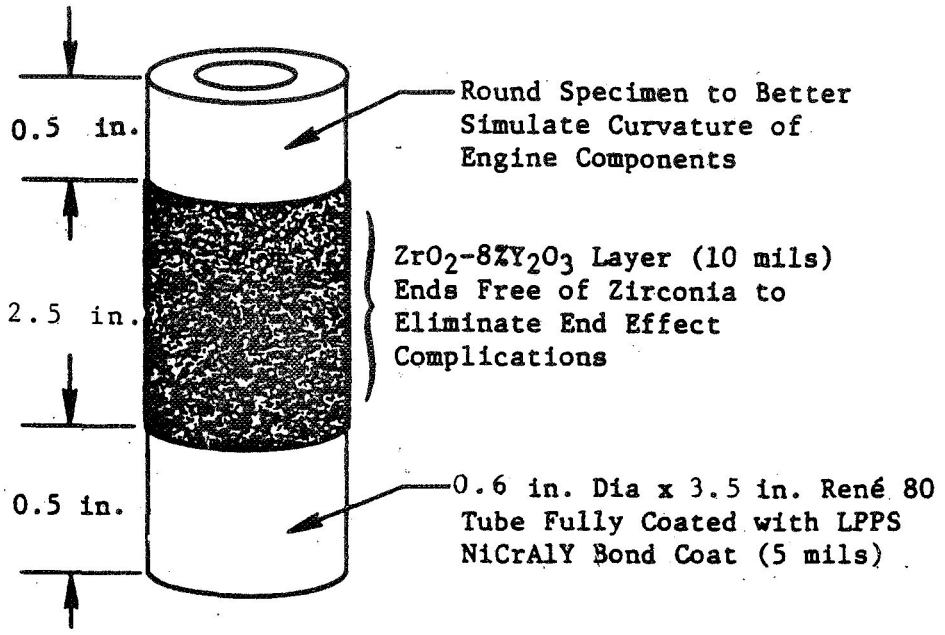

Figure 4.

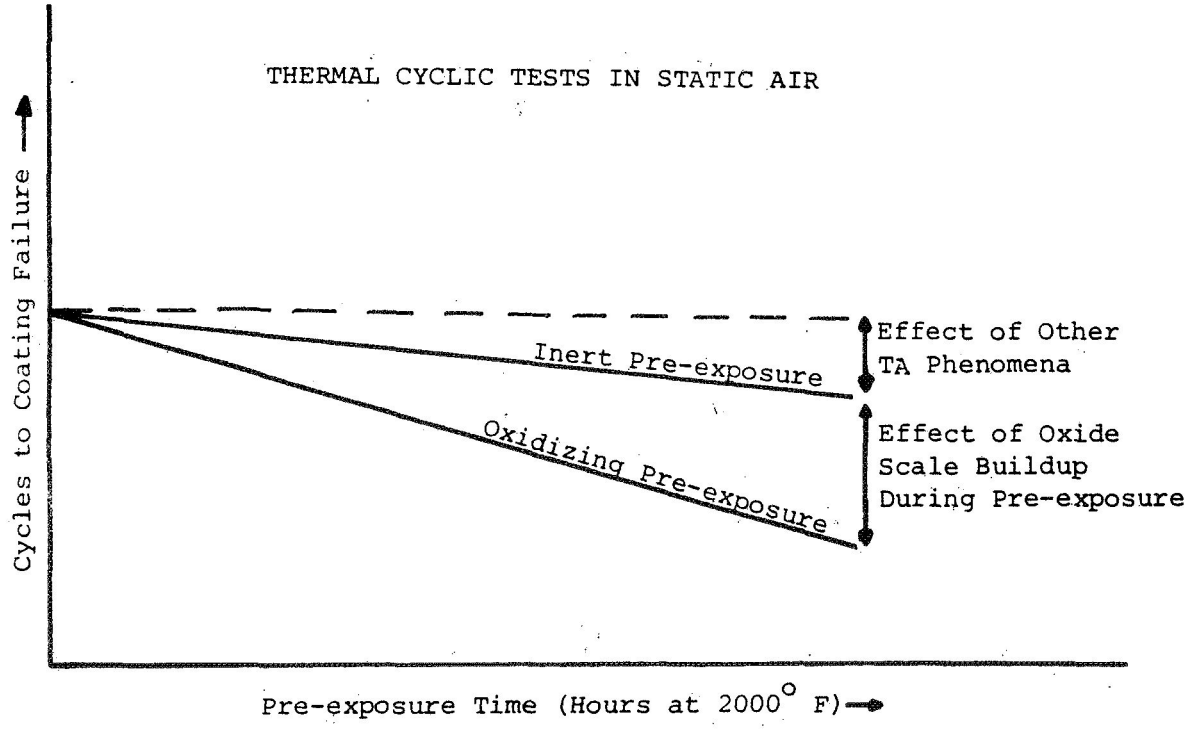

Figure 5.

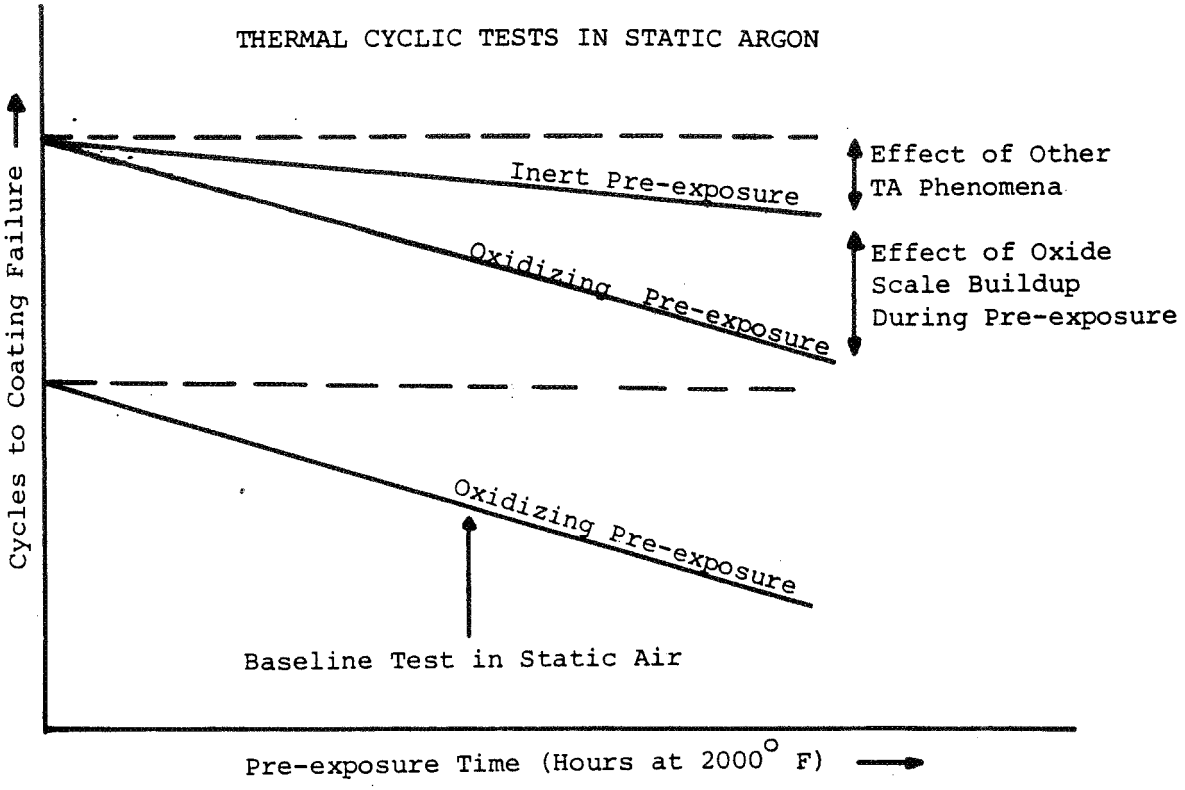

Figure 6.

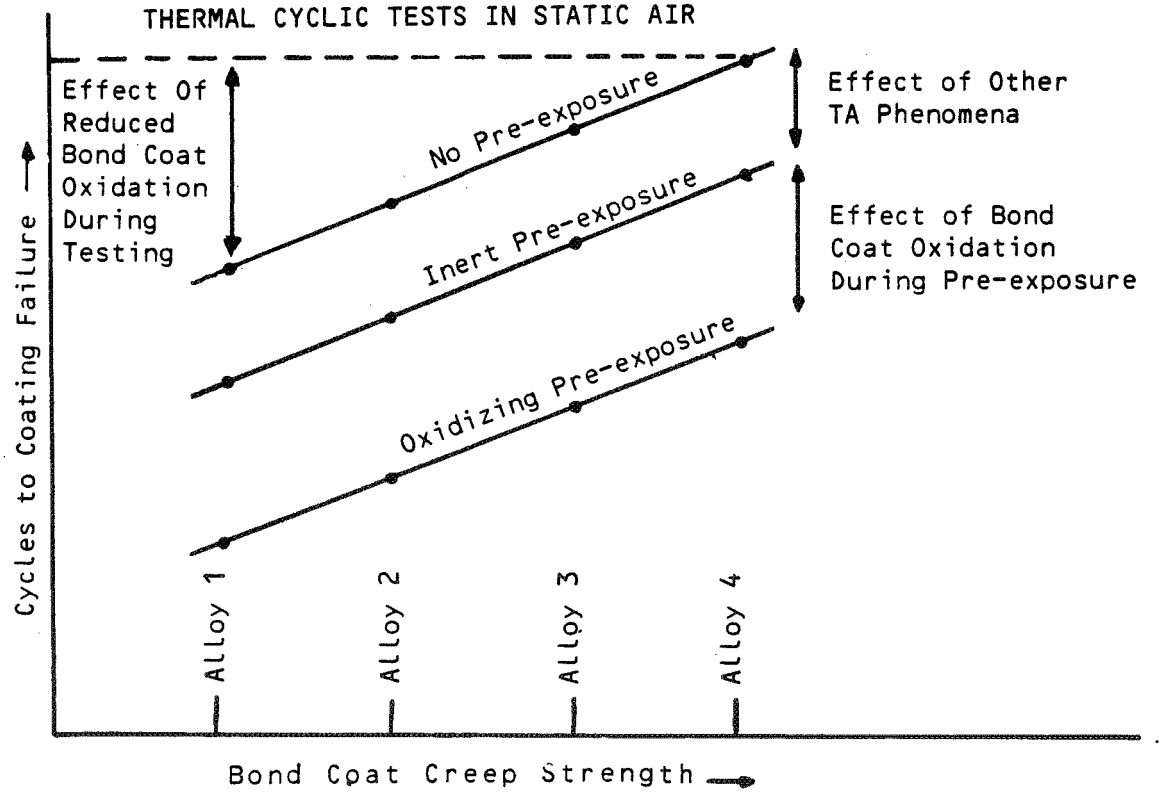

Figure 7.

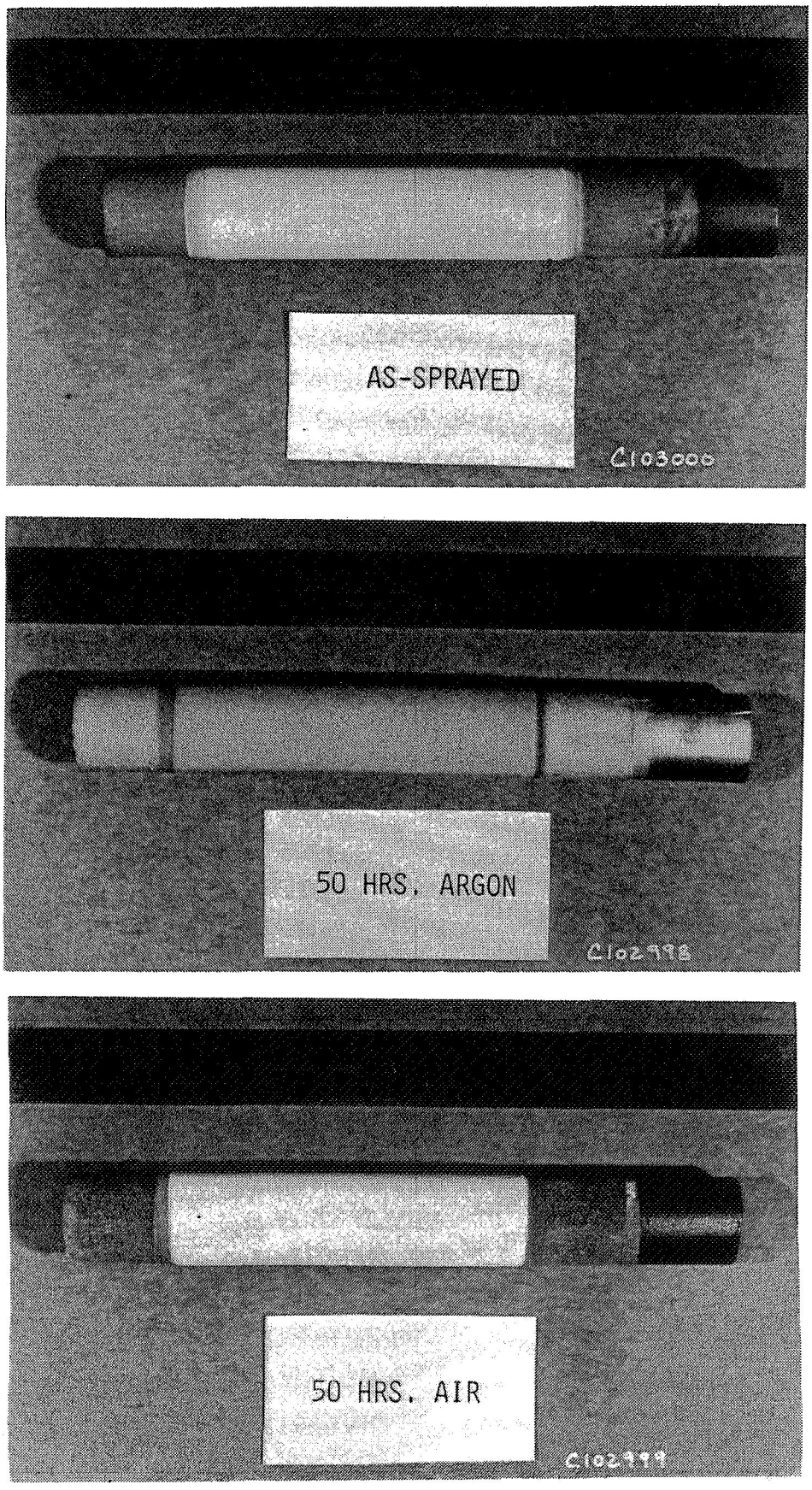

Figure 8.

Figure 9.

Figure 10.

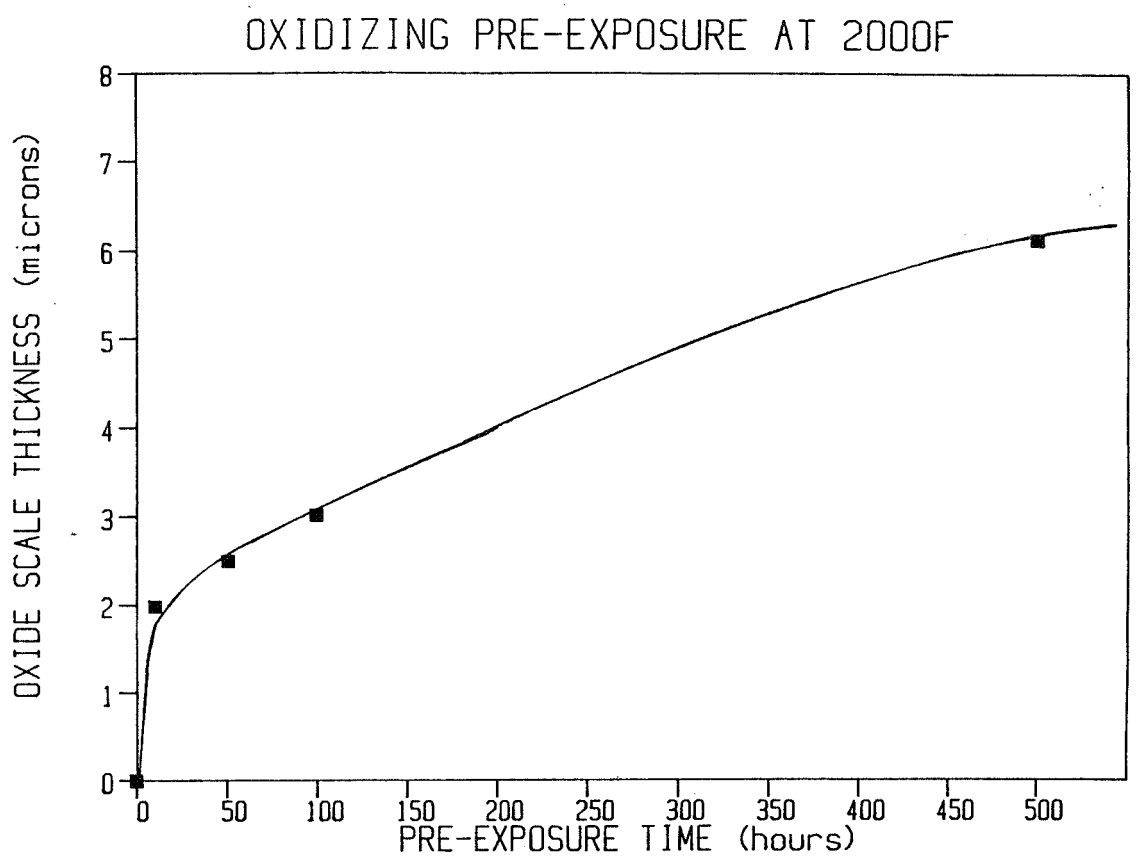

Figure 11.

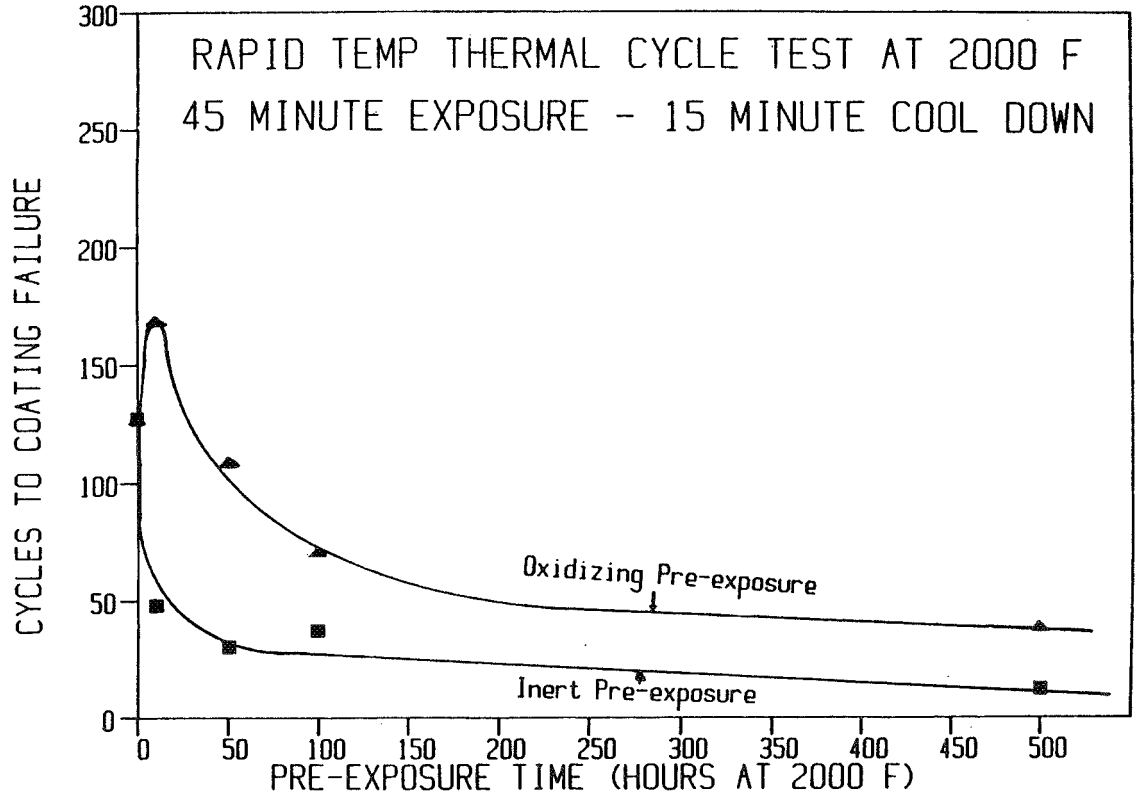

Figure 12.

AN INVESTIGATION OF ENVIRONMENTAL INFLUENCE ON THE CREEP BEHAVIOR OF A LOW PRESSURE PLASMA SPRAYED NiCoCrAlY ALLOY

M. G. Hebsur and R. V. Miner
NASA Lewis Research Center
Cleveland, Ohio

Low pressure sprayed MCrAlY overlay coatings are currently being used on advanced single crystal superalloy blades for gas turbine engines. Many studies have been made on the influence of coatings on the mechanical properties of superalloys in oxidizing or hot-corroding environments, but very few on the properties of the bulk coating alloy itself. In this study the creep behavior of a typical NiCoCrAlY alloy (PWA 276) has been studied in air and vacuum. The as-received low pressure plasma sprayed NiCoCrAlY plates were heat treated for 4 h at 1080 C followed by 32 h at 870 C, the heat treatment applied to coated superalloy parts. Standard creep specimens 12.7 mm long and 3.2 mm in diameter were then machined. Constant load creep -rupture tests were carried out in air and vacuum at 650, 850, and 1050 C and various initial stresses. In addition, some specimens were preoxidized at 1050 C for 100 h prior to testing.

At 650 and 870 C, rupture lives in vacuum were 2 to 3 times longer in air than in vacuum. The second stage creep rates were independent of test environment, however during tests in air tertiary creep began later, progressed at a lower rate, and continued to a greater strain at fracture than during tests in vacuum. In comparison, preoxidized specimens tested in air exhibited a lower second stage creep rate, a greater time to the onset of tertiary creep, but the same strain at fracture as virgin specimens tested in air. These effects appear consistent with a blunting of the initial surface pores in the material by testing in air or additionally by preoxidation. This would delay the onset of tertiary creep. Also, air appears to blunt the growing cracks during tertiary creep providing lower tertiary creep rates and greater strain to fracture. Further experiment is required to explain the effect of the preoxidation exposure in lowering the second stage creep rate.

At 1050 C, the dependence of rupture live on stress level was much higher than at the lower temperatures, the stress exponent being roughly -12, rather than about -3. Also, the scatter in life was greater than for the lower temperature tests. Within this scatter, rupture lives could not be said to be different for tests of the virgin specimens in air or vacuum, or for the preoxidized specimens tested in air. However, as at the lower temperatures, the strain to fracture was much greater for tests of either the virgin or preoxidized specimens tested in air than for tests in vacuum.

TYPICAL CREEP CURVES FOR NiCoCrAlY AT VARIOUS TEMPERATURES, STRESSLEVELS AND ENVIRONMENTS

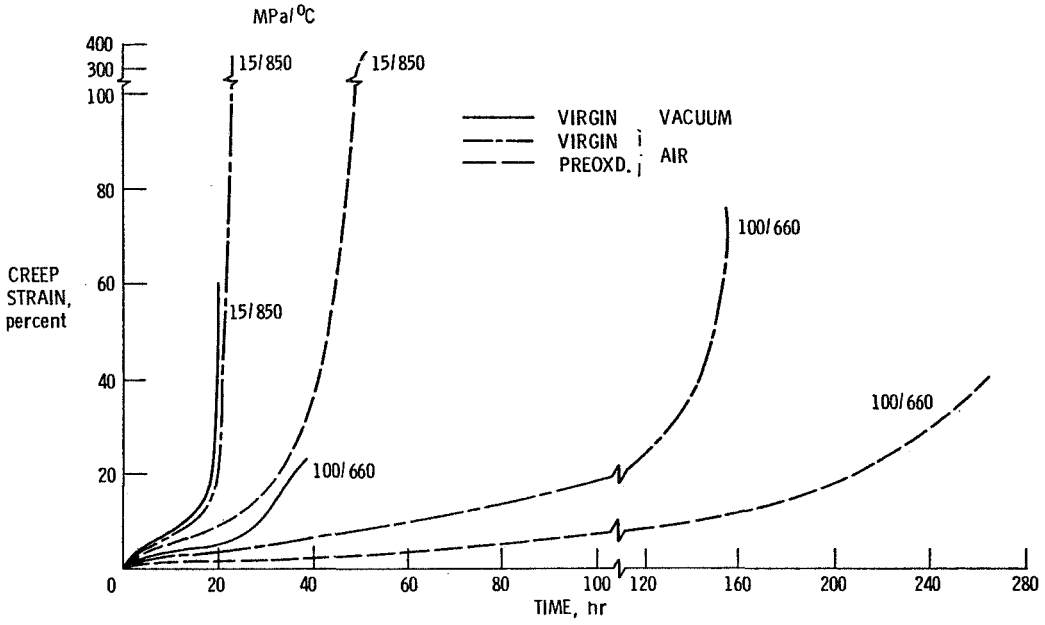

MCR VERSUS STRESS

OF NiCoCrAlY AT VARIOUS TEMPERATURE AND ENVIRONMENT

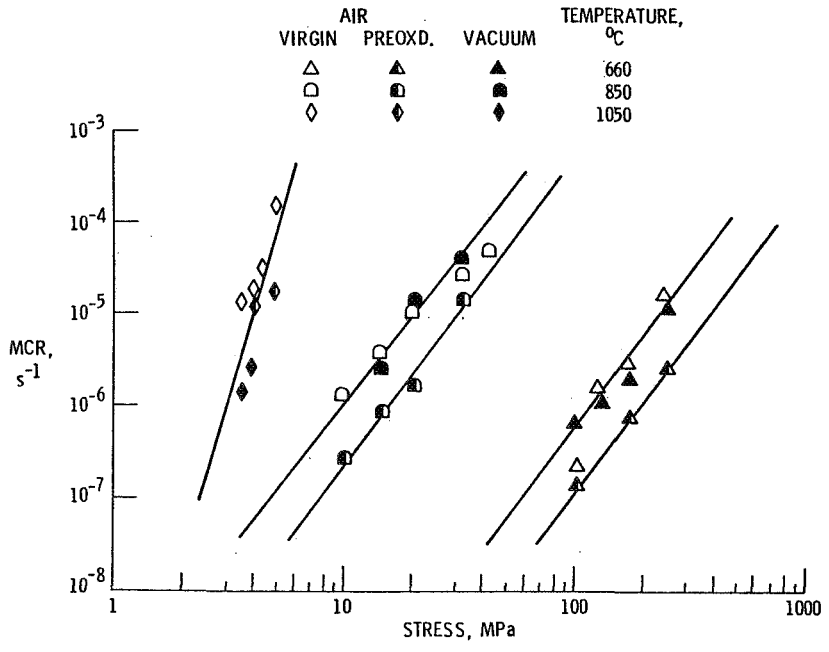

STRESS DEPENDENCE OF TIME TO FAILURE OF NiCoCrAlY AT VARIOUS TEMPERATURES AND ENVIRONMENTS

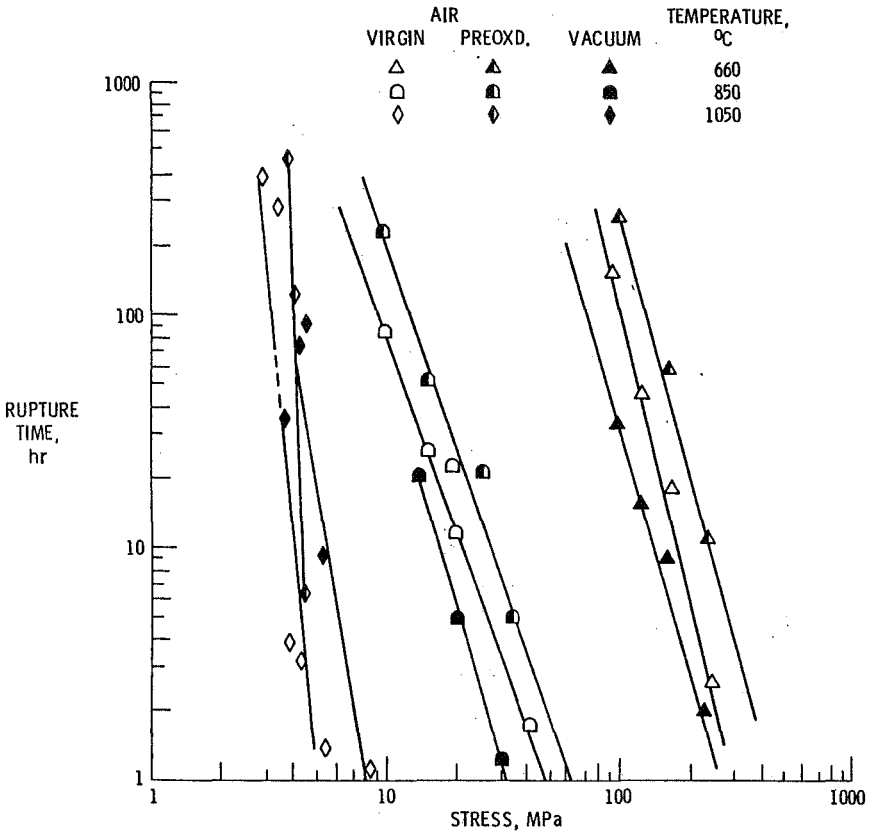

STRAIN TO FAILURE OF NiCoCrAlY AS A FUNCTION OF STRESS

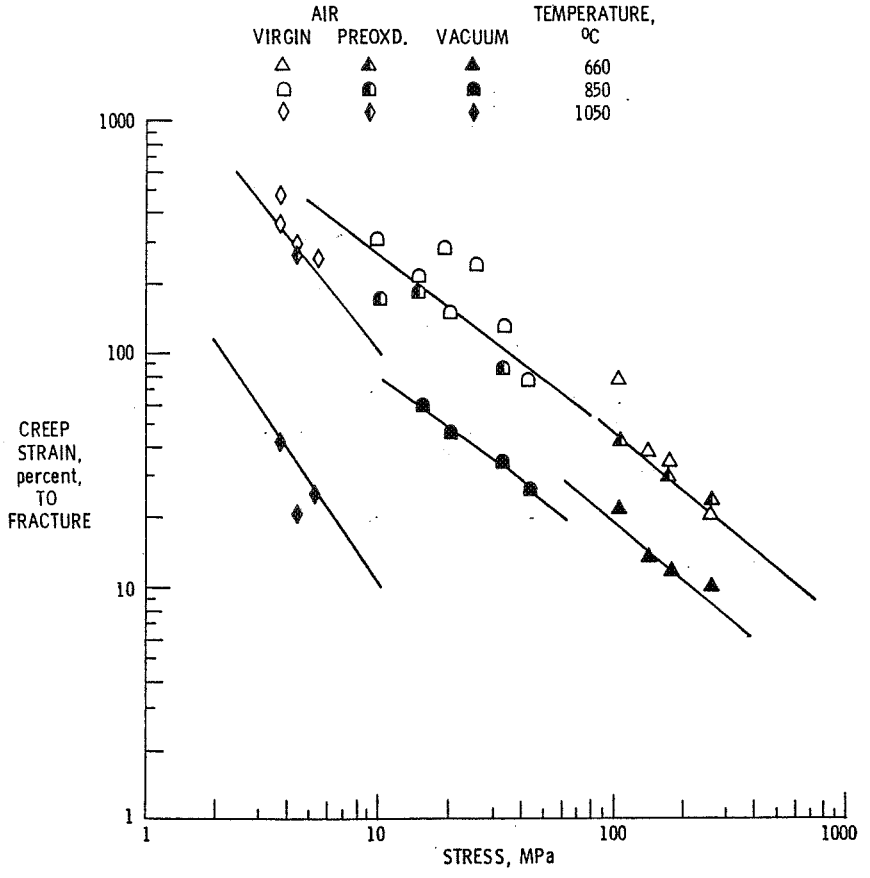

TIME TO THE ONSET OF TERTIARY CREEP

OF NiCoCrAlY VERSUS APPLIED STRESS AT VARIOUS TEMPERATURES AND ENVIRONMENT

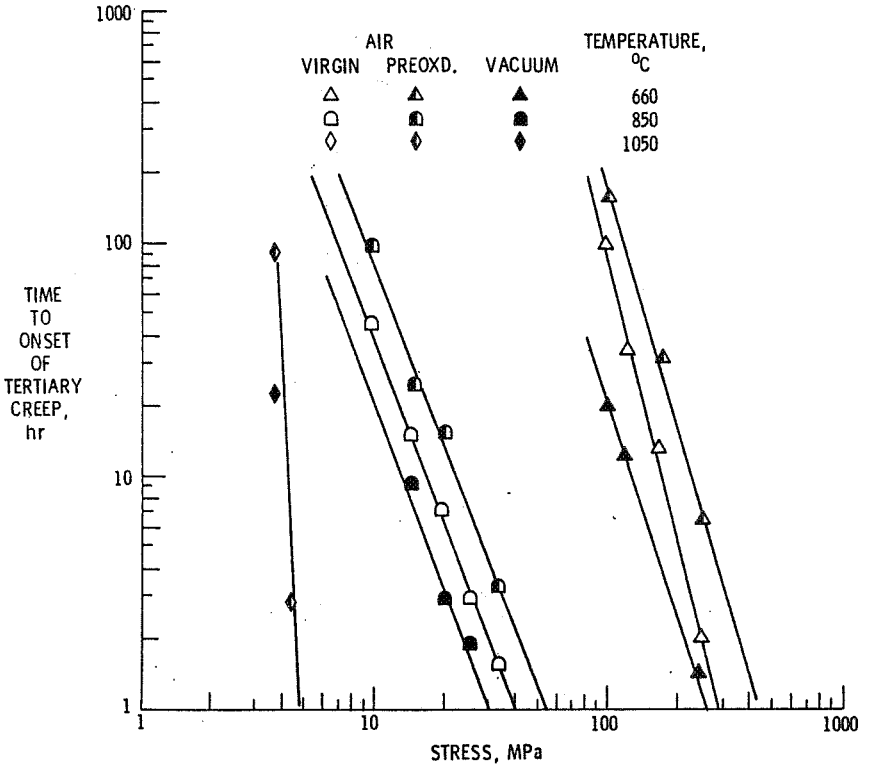

Figure 6.

TYPICAL SURFACES OF CREEP TESTED SPECIMENS
OF NiCoCrAlY

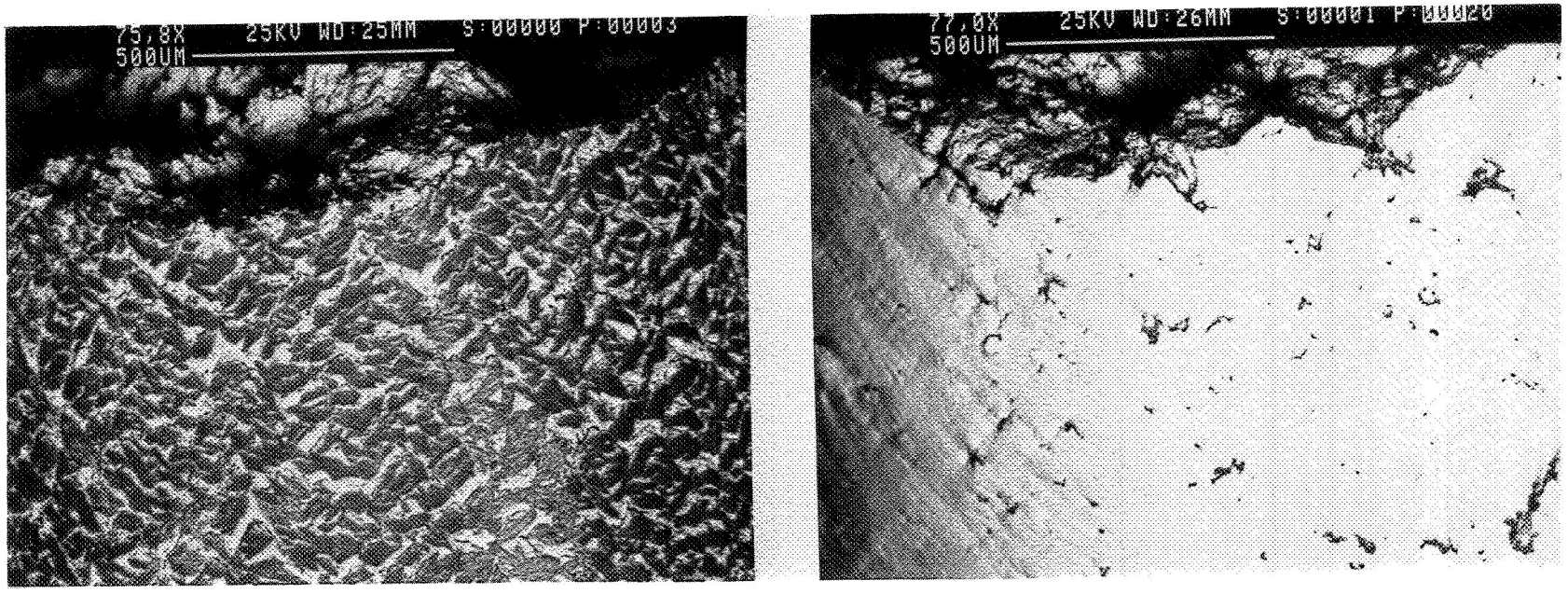

PREOXD/AIR

VIRGIN/VACUUM

Figure 7.

MICROSTRUCTURAL ASPECTS OF ZIRCONIA THERMAL BARRIER COATINGS

T.E. Mitchell, D.S. Suhr, R.J. Keller, V. Lanteri, and A.H. Heuer
Department of Metallurgy & Materials Science
Case Western Reserve University
Cleveland, Ohio 44106

Various combinations of plasma-sprayed bond coatings and zirconia ceramic coatings on a nickel-based superalloy substrate were tested by static thermal exposure at 1200°C and cyclic thermal exposure to 1000°C. The bond coats were based on Ni-Cr-Al alloys with additions of rare earth elements and Si. The ceramic coats were various ZrO_2-Y_2O_3 compositions, of which the optimum was found to be ZrO_2-8.9 wt.% Y_2O_3. Microstructural analysis showed that resistance to cracking during thermal exposure is strongly related to deleterious phase changes. Zones depleted of Al formed at the bond coat/ceramic coat interface due to oxidation and at the bond coat/substrate interface due to interdiffusion, leading eventually to breakdown of the bond coat. The 8.9% Y_2O_3 coating performed best because the as-sprayed metastable (high-Y_2O_3) tetragonal phase converted slowly into the low-Y_2O_3 tetragonal plus high-Y_2O_3 cubic-phase mixture, so that the deleterious monoclinic phase was inhibited from forming. Failure appeared to start with the formation of circumferential cracks in the zirconia, probably due to compressive stresses during cooling, followed by the formation of radial cracks due to tensile stresses during heating. Cracks appeared to initiate at the Al_2O_3 scale/bond coat interface and propagate through the zirconia coating. Comparisons have been made with the behavior of bulk ZrO_2-Y_2O_3 and the relationship between the microstructure of the tetragonal phase and the phase diagram. A separate investigation has also been made of the ZrO_2-Al_2O_3 interface.

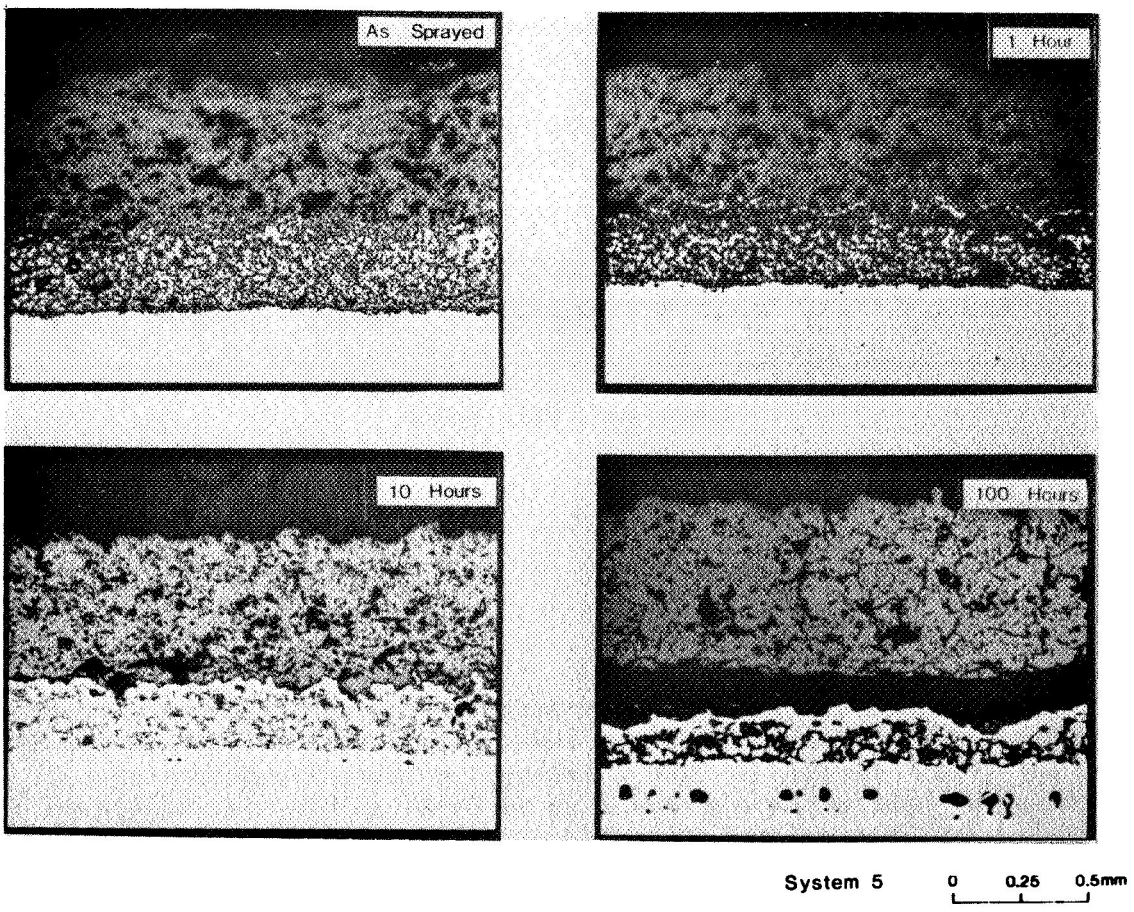

Fig. 1. Optical microstructures of an 8.9% Y_2O_3 system, as-sprayed and after static thermal exposure for 1, 10, and 100 h at 1200°C.

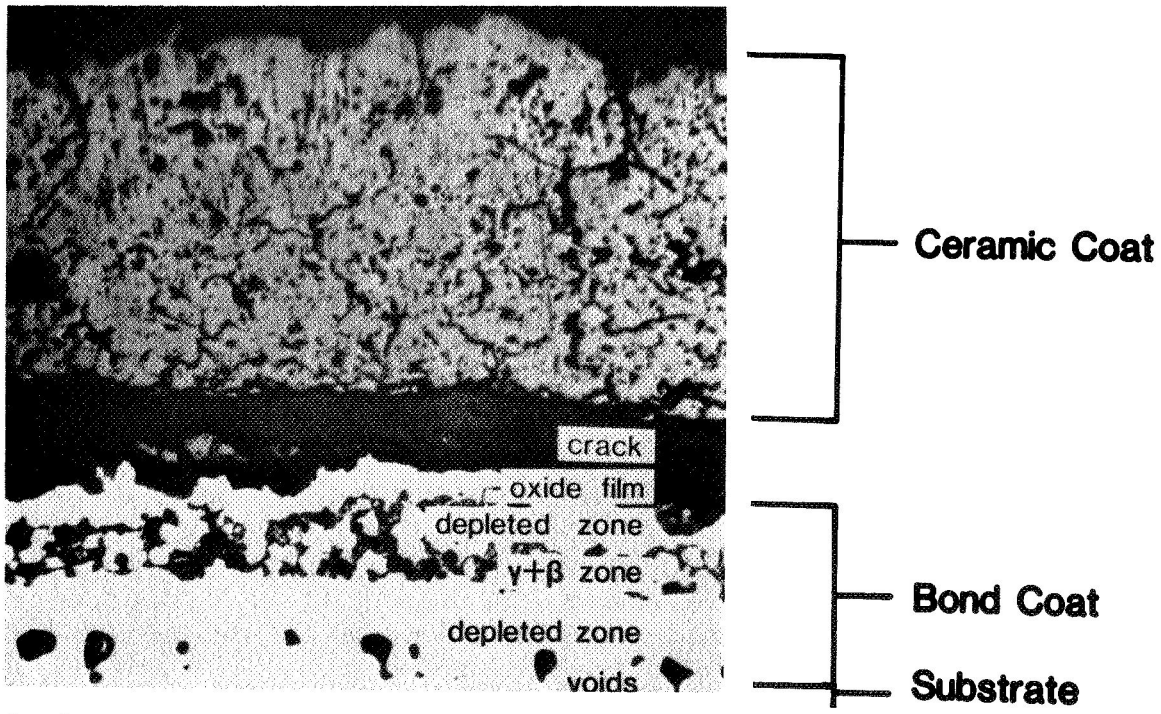

Fig. 2. General optical microstructure of an 8.9% Y_2O_3 system after 100 h static thermal exposure at 1200°C.

Table I. Effect of Y_2O_3 Content in the Ceramic Coat on the Number of 1000°C Cycles to Failure for Individual Specimens with a Given Bond Coat (Ni–Cr–Al with Y and Si Additions)

Y_2O_3 (wt%)	No. of cycles to failure
4.3	7
	15
6.1	233
	233
8.9	>500
	>500
	>500
19.6	321
	>500

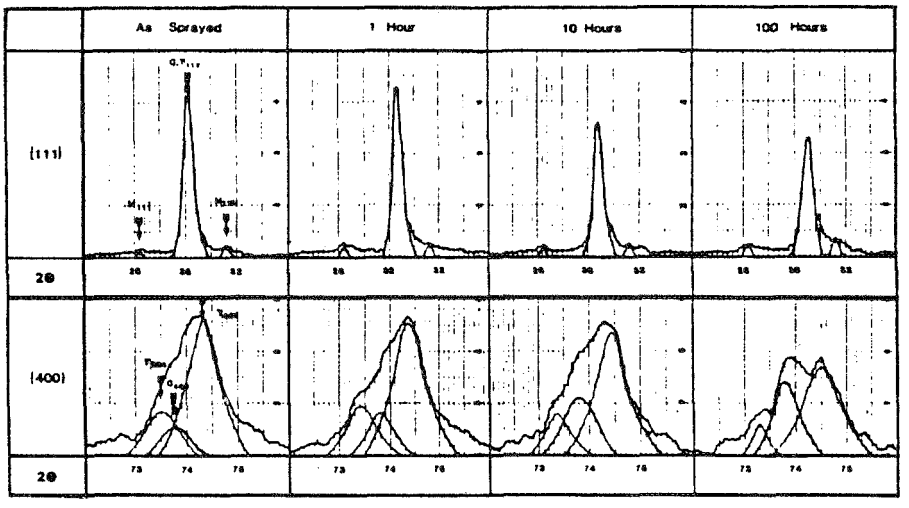

Fig. 3. Experimental X-ray diffraction patterns and deconvoluted peaks in the {111} and {400} regions for plasma-sprayed ZrO_2-8.9% Y_2O_3 after 1, 10, and 100 h static thermal exposure at 1200°C.

Table II. Phase Analyses (mol%) after Thermal Exposure at 1200°C

System (%Y_2O_3)	Phase	Time (h)			
		As-sprayed	1	10	100
4.3	Monoclinic	22	37	41	44
	Cubic	4	5	4	3
	Tetragonal	74	58	55	53
6.1	Monoclinic	16	17	18	20
	Cubic	6	9	10	11
	Tetragonal	78	74	72	69
8.9	Monoclinic	8	9	9	12
	Cubic	13	15	22	31
	Tetragonal	79	76	69	57
19.6	Monoclinic	3	3	2	2
	Cubic	70	76	84	88
	Tetragonal	27	21	14	10

Table III. Chemical Compositions (wt%) in the Bond Coat after Static Thermal Exposure at 1200°C

Time	Al	Si	Cr	Co	Ni	Ti	Phase	Remark
As-sprayed	4.5	2.8	26.9	2.2	63.6		γ/γ'	
	12.7	2.0	15.8	1.7	67.8		β	
1 h	2.5	1.1	19.7	2.8	73.9		γ/γ'	Depleted zone near ceramic coat
	6.1	1.0	11.6	1.9	79.4		β	Below depleted zone
	3.0	1.0	18.5	2.6	74.8		γ/γ'	Below depleted zone
	7.2	0.9	9.1	1.9	80.9		β	Near substrate
	9.9	1.6	17.6	2.7	67.8	0.4	γ/γ'	Near substrate
	2.1	1.4	19.2	3.5	73.3	0.5	γ	Depleted zone near substrate
10 h	2.4	1.2	17.6	4.6	74.2		γ/γ'	Depleted zone near ceramic coat
	3.6	1.8	17.4	4.2	73.0		γ/γ'	Middle of bond coat
	8.5	1.4	9.8	3.8	75.6	0.9	β	Middle of bond coat
	3.4	2.2	17.4	4.8	71.5	0.7	γ/γ'	Depleted zone near substrate
100 h	6.4	2.8	11.4	7.7	70.3	1.5	γ/γ'	Depleted zone near ceramic coat
	7.5	2.4	5.0	4.9	78.4	1.8	β	Middle of bond coat
	5.1	3.6	11.4	8.4	70.8	0.7	γ/γ'	Depleted zone near substrate

Table IV. Chemical Composition (wt%) of the Oxide Film Formed at the Ceramic Coat/Bond Coat Interface

Time at 1200°C (h)	Al_2O_3	Cr_2O_3	CoO	NiO
1	72.6	10.7	0.9	15.8
10	21.8	27.6	2.8	47.8
100	93.1	6.9		

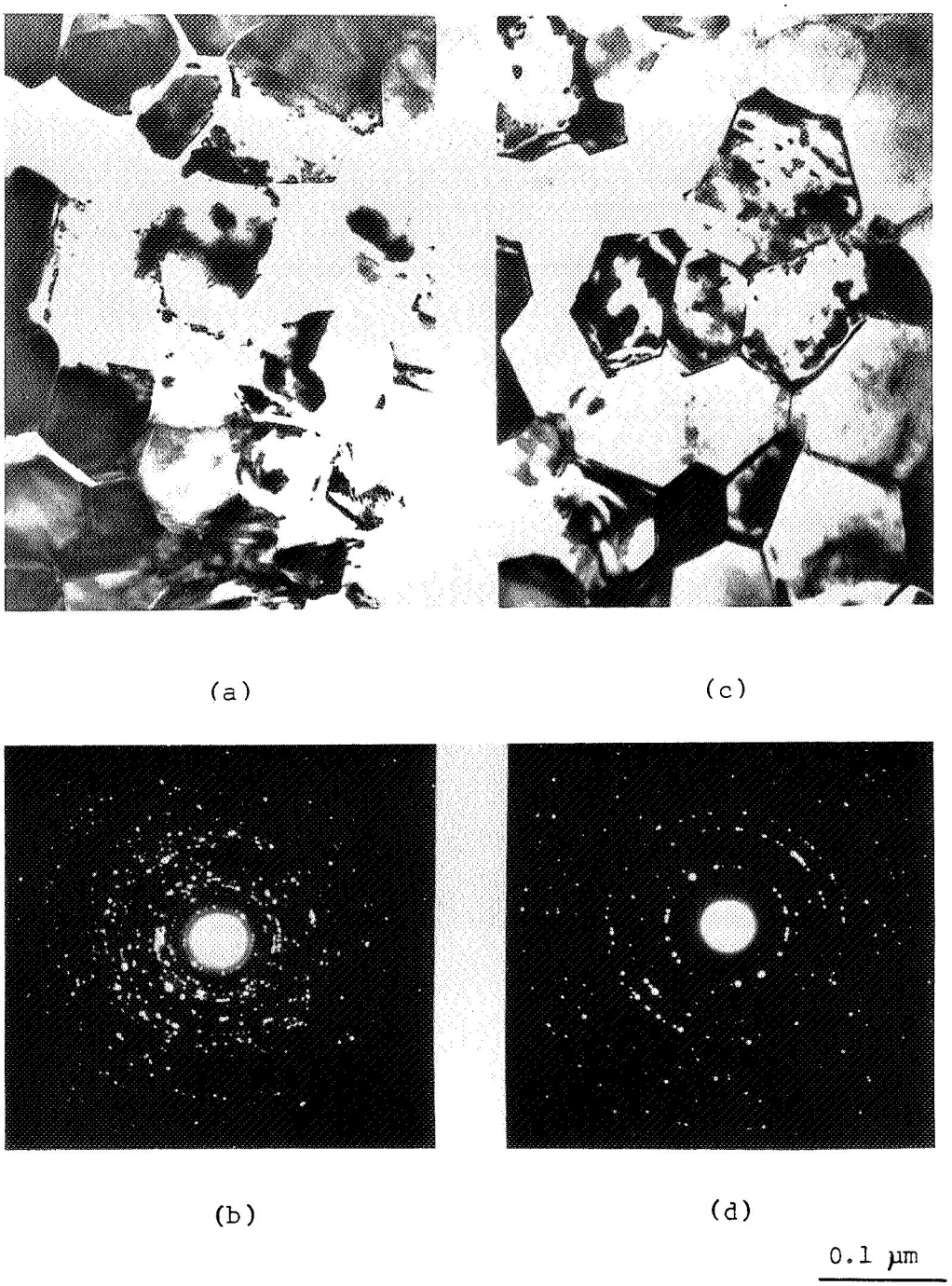

Fig. 4. (a)-(d) TEM micrographs of the as-sprayed 4.3% Y_2O_3 ceramic coating showing the separated regions of monoclinic and tetragonal (T') grains and their SAD ring pattern, (a)-(b) monoclinic ; (c)-(d) tetragonal (T')

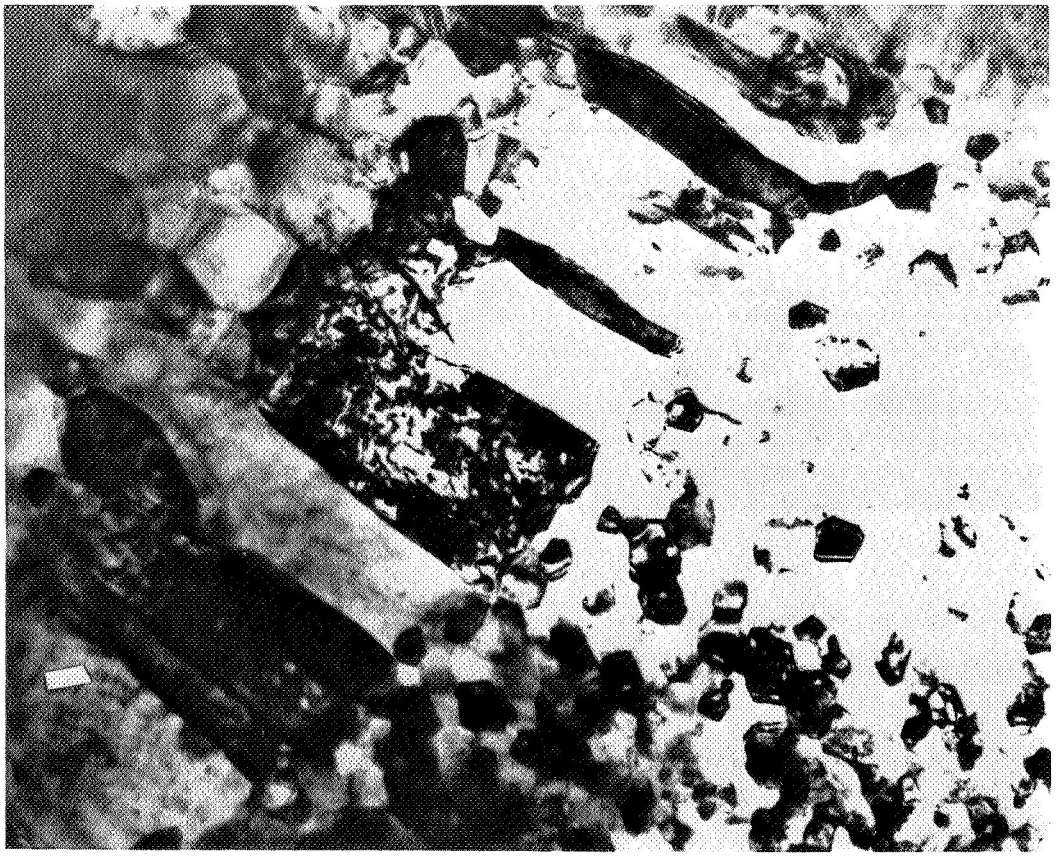

0.1 μm

Fig. 5. TEM micrograph of the as-sprayed 6.1% Y_2O_3 ceramic coating showing the non-equilibrium tetragonal $(T')_2$ columnar grains.

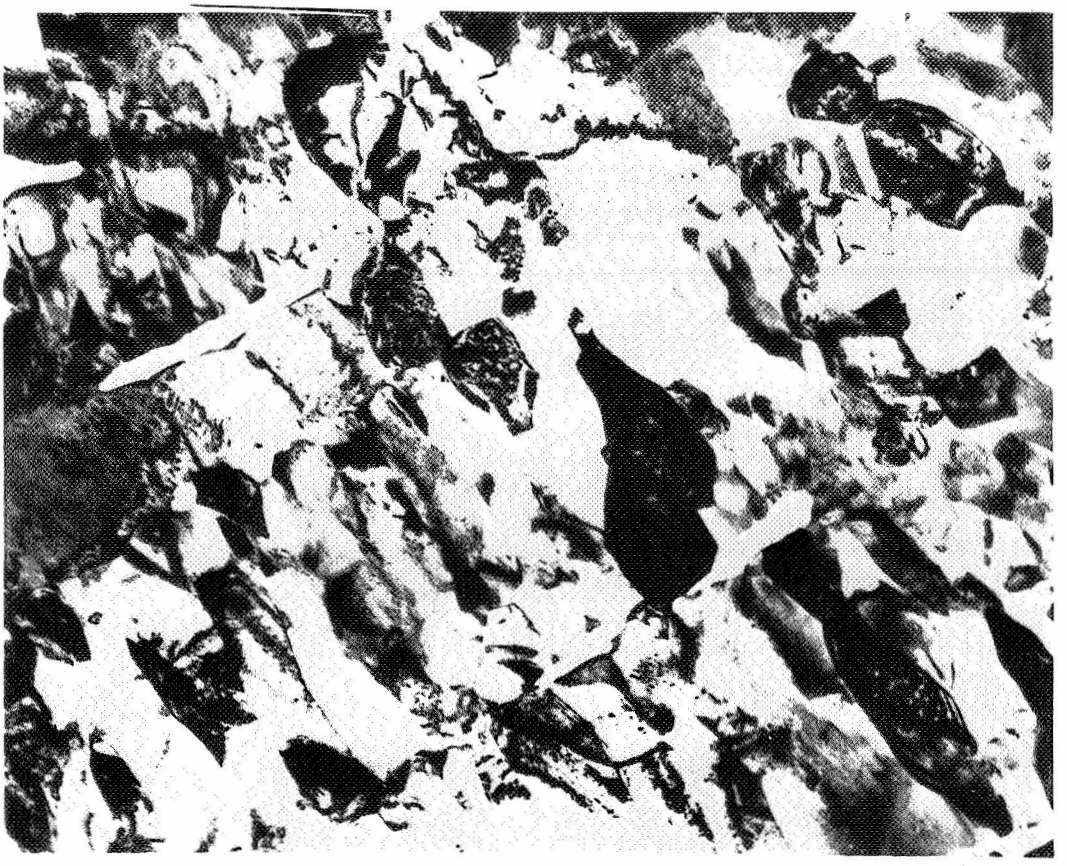

Fig. 6. TEM bright-field image showing the ZrO_2-Y_2O_3 splat morphology with columnar tetragonal grains which have grown perpendicular to the splat boundary (6.1% Y_2O_3) ceramic coat after 100 h at 1200°C.

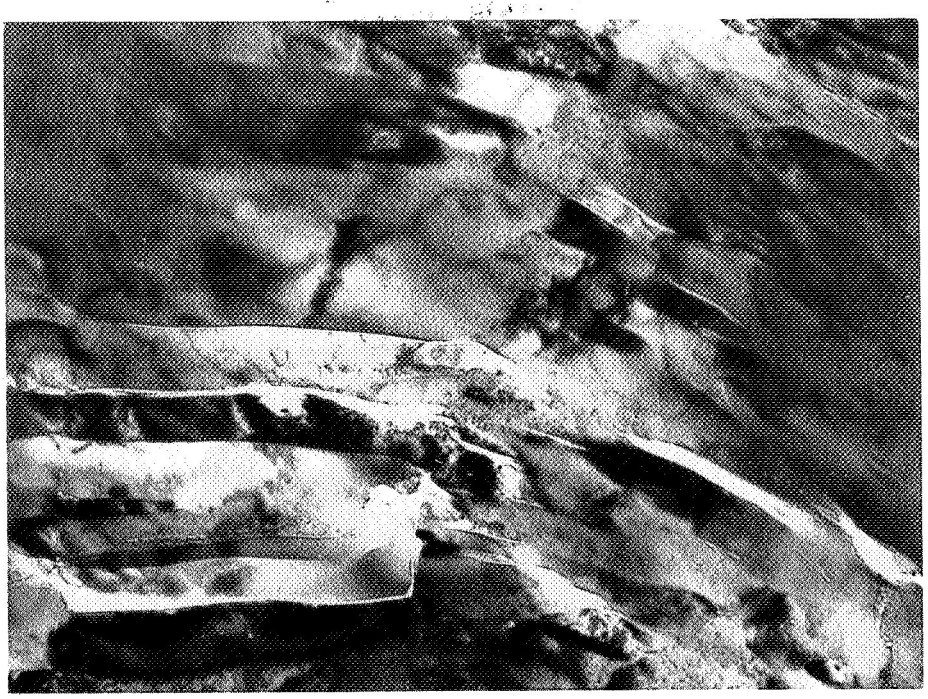

(a)

0.1 μm

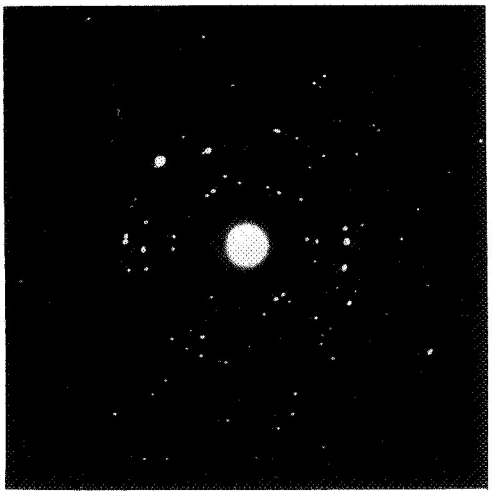

(b)

Fig. 7. (a)-(b) TEM micrograph of the columnar cubic grains within as-sprayed 19.6% Y_2O_3 ceramic coating showing intergranular microcracking (a) and the SAD ring pattern (b).

(a)
APB's

0.1 μm

(b)
Mottled
structure

0.1 μm

(c)
Colony
structure

0.1 μm

Fig. 8. (a)-(c) Three kinds of tetragonal phase TEM microstructure

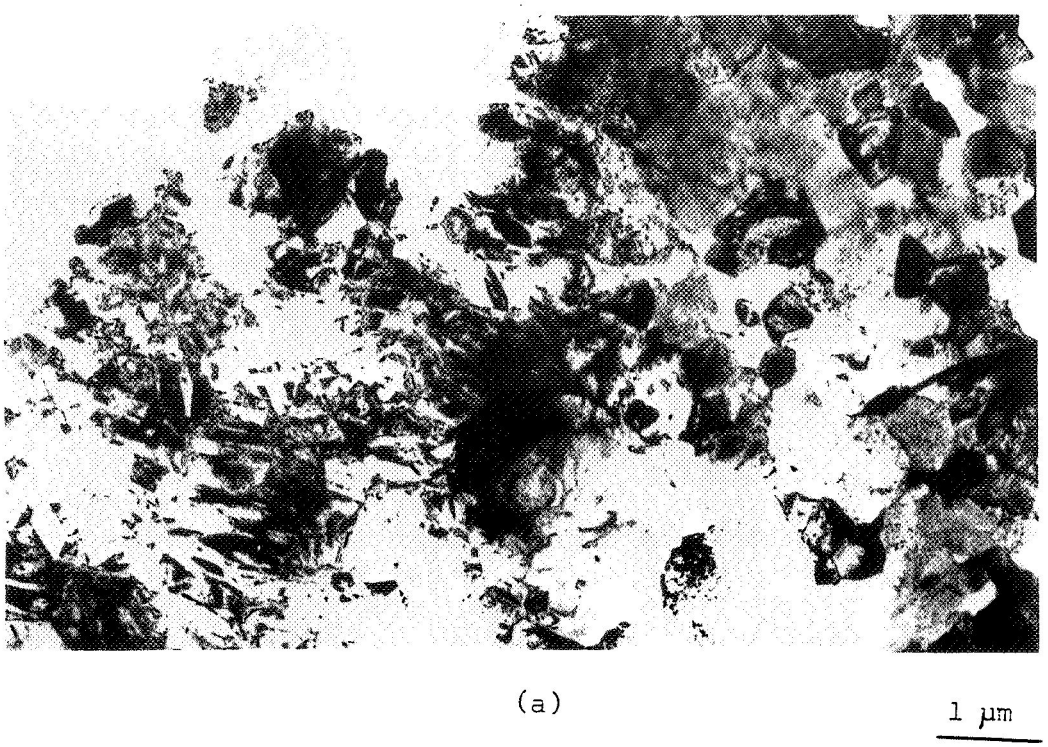

(a)

1 μm

(b)

(c)

0.1 μm

Fig. 9. (a)-(c) 4.3% Y_2O_3 ceramic coating after 100 hours exposure at 1200° C showing separate regions of monoclinic and tetragonal grains.

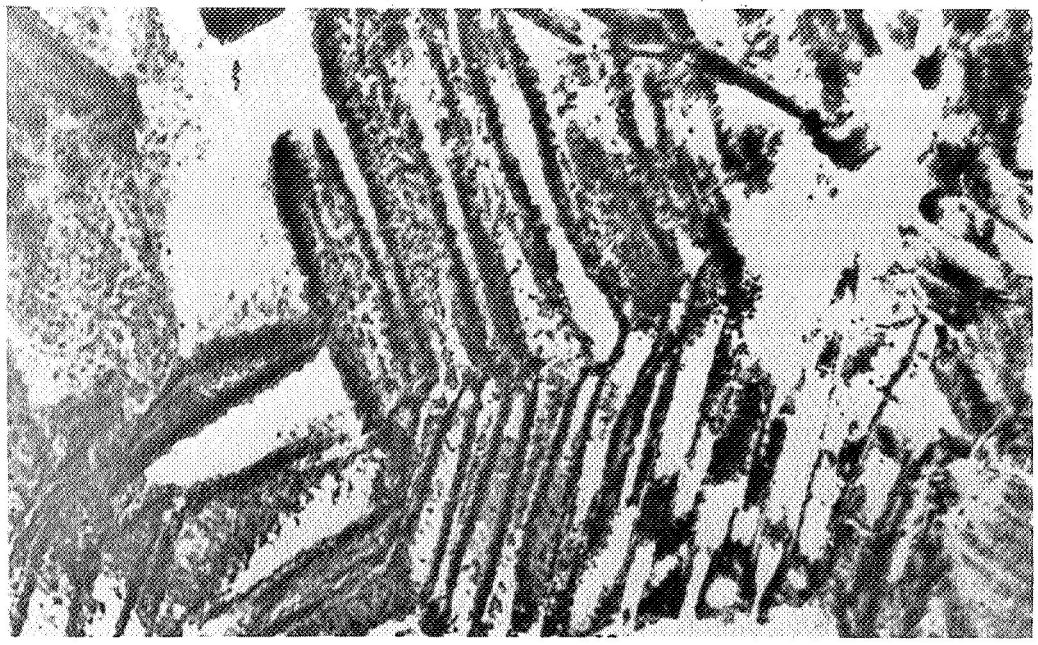

(a)

0.1 μm

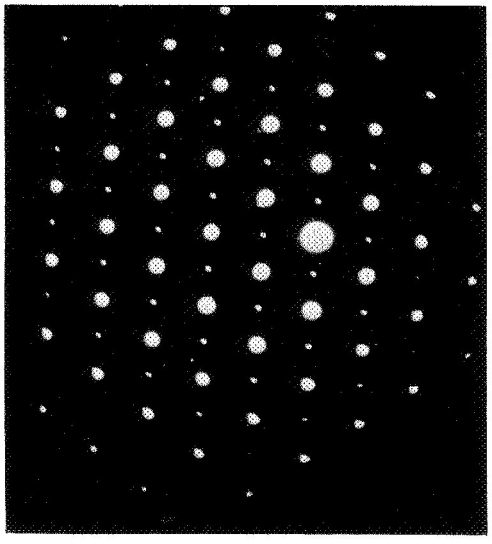

(b)

Fig. 10. 4.3% Y_2O_3 ceramic coating after 100 hours at 1200° C : (a) TEM micrograph of the tetragonal colony structure within large (~ 1.0 μm) grain and (b) corresponding [011] diffraction pattern.

0.2 μm

Fig. 11. 6.1% Y_2O_3 ceramic coating after 100 hours exposure at 1200° C showing splats formed by low Y_2O_3 concentration particle consisting of many twined monoclinic grain and splats formed by high Y_2O_3 concentration particle consisting of tetragonal grains.

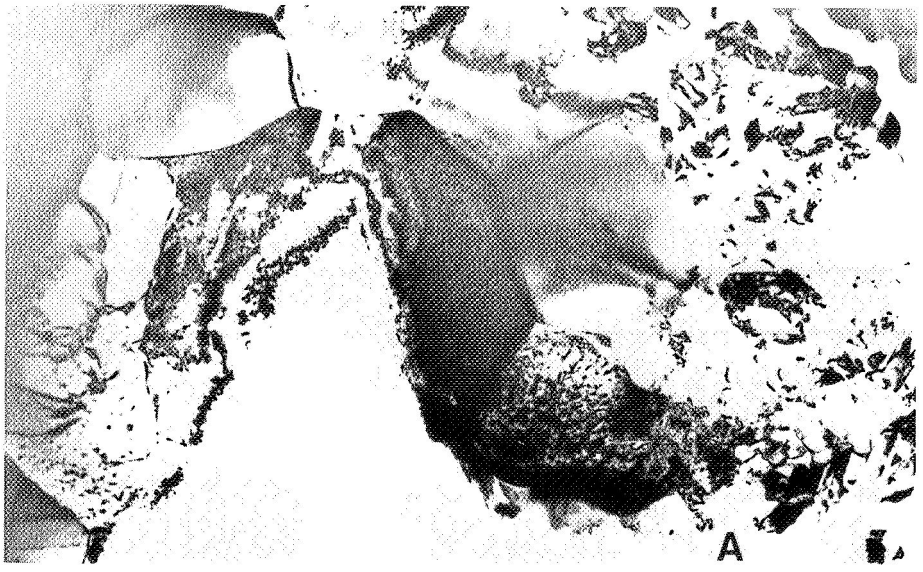

(a)

(b)

Fig. 12. (a)-(b) 19.6% Y_2O_3 ceramic coating after 100 hours exposure at 1200° C (a) monoclinic and cubic grains (b)higher magnification micrograph showing tetragonal grains(A) formed at the interface between monoclinic and cubic grains due to yttrium diffusion.

0.25 μm

Position	Al_2O_3	SiO_2	Cr_2O_3	CoO	NiO
1	2.2	43.1	9.3	4.3	41.1
2	5.7	55.2	6.9	2.8	29.3
3	25.0	3.3	65.2	0.6	5.8

Fig. 13. TEM micrograph of oxide scale after 1 hour thermal exposure at 1200° C and the result of point EDAX analyses (system 5). The oxide scale is adherent to the bond coating, however pores are present at the oxide scale/ceramic coating interface.

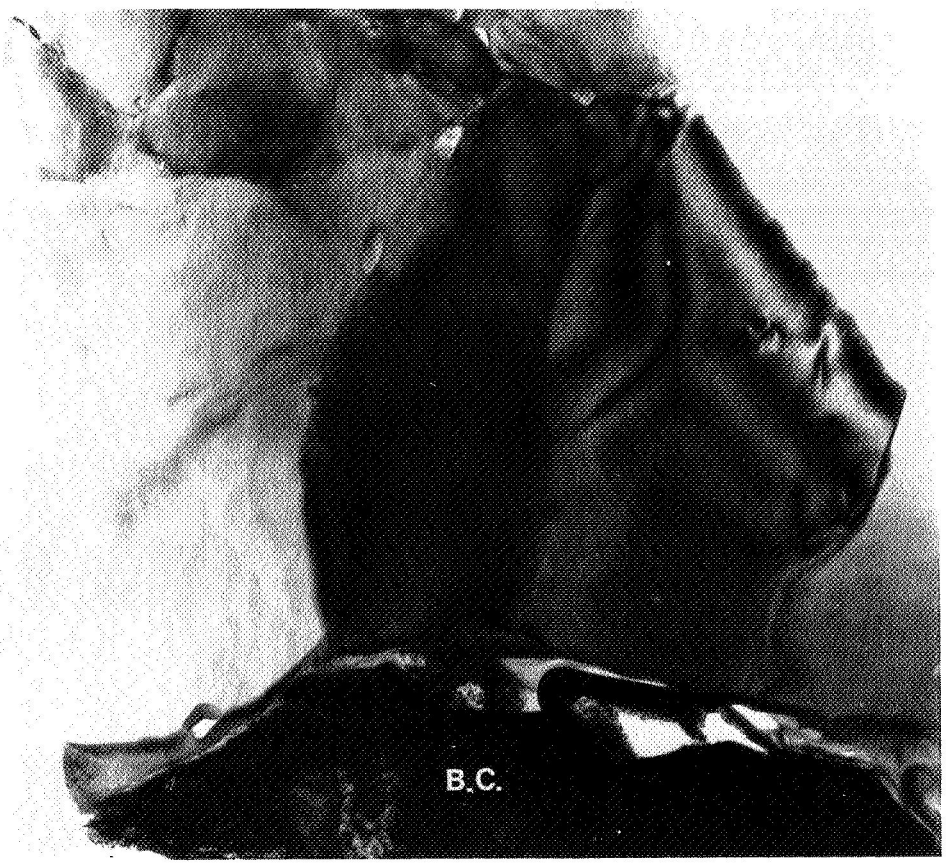

Fig.14. TEM micrograph of oxide film after 10 hours thermal exposure at 1200^{o} C showing the columnar grains of Al_2O_3 and the void formation at the oxide film/bond coating interface.

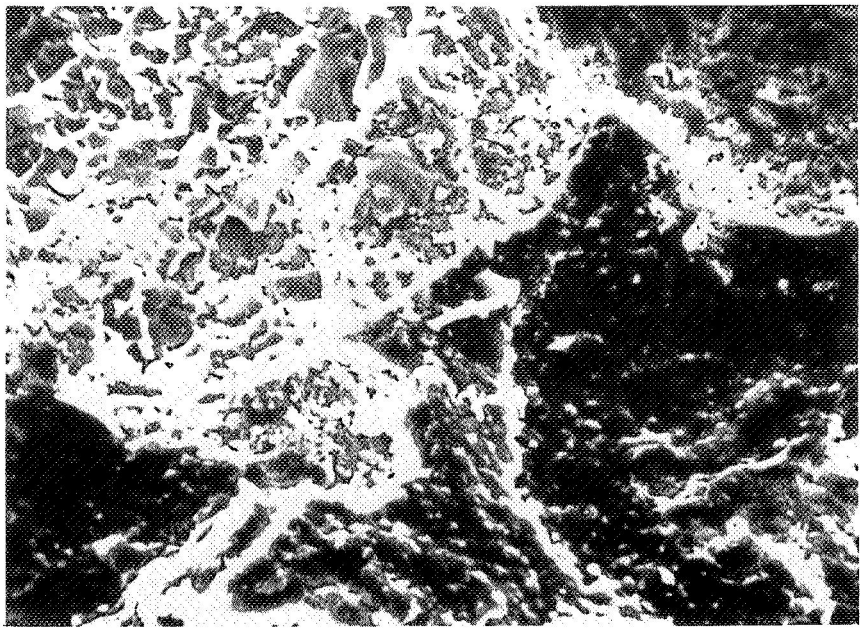

(a)

20 μm

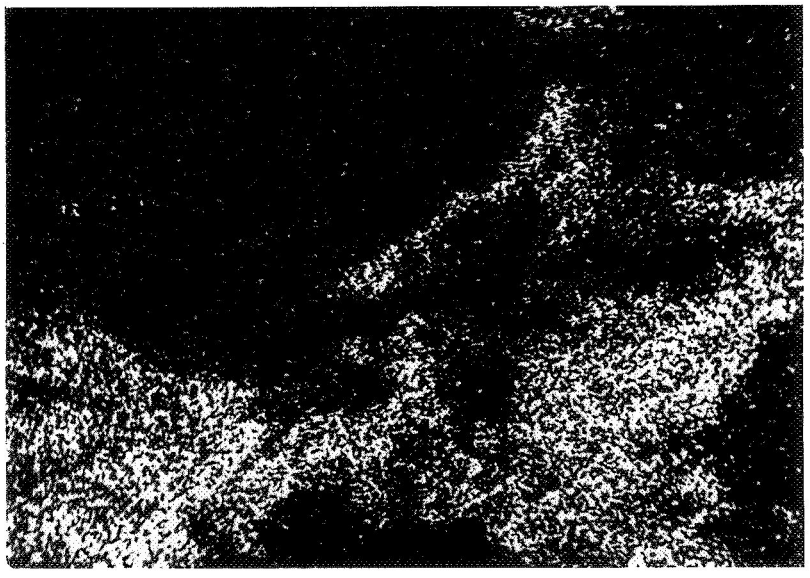

(b)

Fig.15. (a)-(b); (a) SEM micrograph of the bottom-side of ceramic coating (system 10) that had failed after 100 hours exposure and (b) microprobe X-ray map for Al.

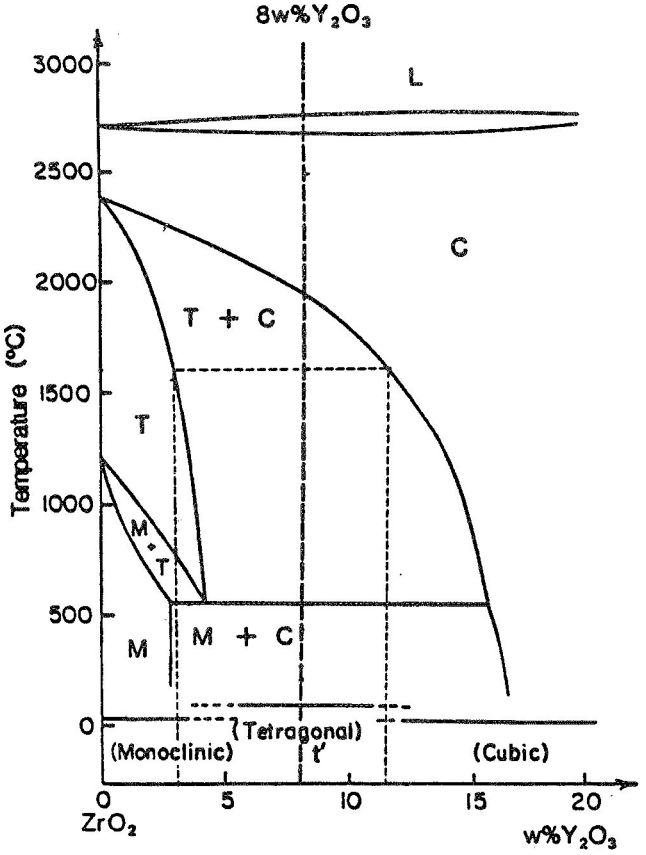

Fig. 16. Phase diagram of the ZrO_2-rich region of the system ZrO_2-Y_2O_3 (Ref. 4).

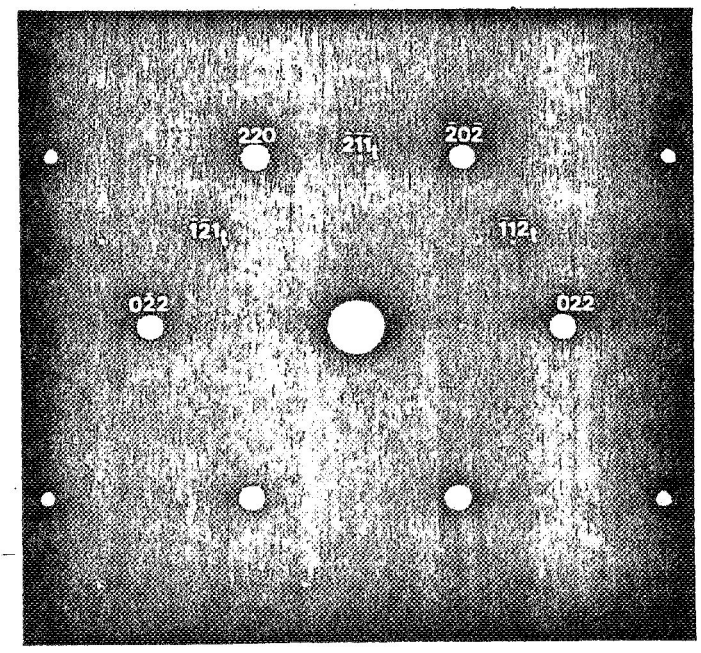

Fig. 17. Diffraction pattern, [$\bar{1}$11] zone axis.

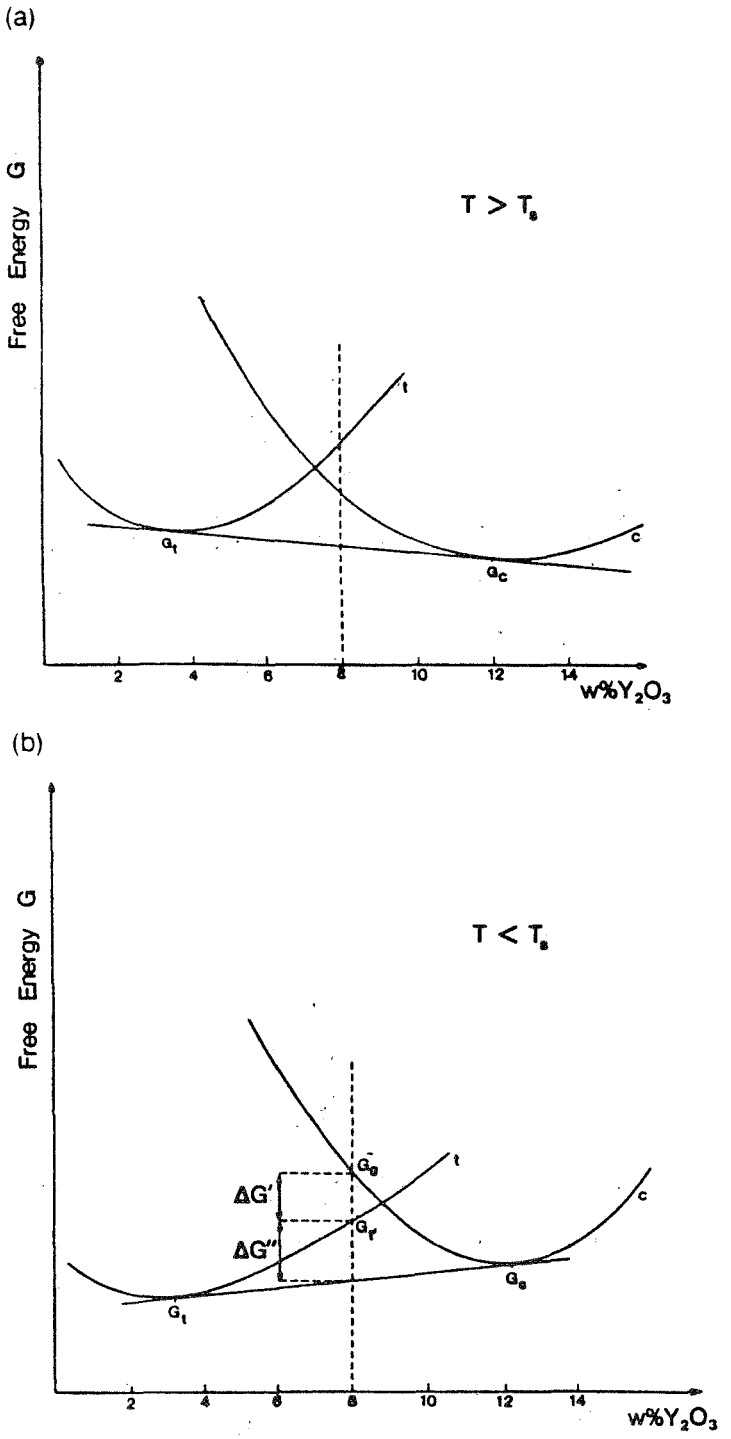

Fig.18. Free energy vs composition curves: (*a*) above the critical temperature T_0 and (*b*) below the critical temperature T_0.

THE ROLE OF MICROSTRUCTURE AND PHASE DISTRIBUTION IN THE FAILURE MECHANISMS AND LIFE PREDICTION MODEL FOR PSZ COATINGS

R.D. Sisson, Jr., Ichiro Sone, and R.R. Biederman
Worcester Polytechnic Institute
Worcester, Massachusetts 01609

Partially Stabilized Zirconia (PSZ) may become widely used for Thermal Barrier Coatings (TBC). Failure of these coatings can occur due to thermal fatigue in oxidizing atmospheres. The failure is due to the strains that develop due to thermal gradients, differences in thermal expansion coefficient and oxidation of the bond coating. The role of microstructure and the cubic, tetragonal and monoclinic phase distribution in the strain development and subsequent failure will be discussed. A new x-ray diffraction technique for accurate determination of the fraction of each phase in PSZ will be applied to understanding the phase transformations and strain development. These results will be discussed in terms of developing a model for life prediction in PSZ coatings during thermal cycling.

MICROSTRUCTURAL CHARACTERIZATION
OF PSZ COATING

- % POROSITY
- PORE SIZE
- CRACK MORPHOLOGY
- GRAIN SIZE
- PHASE FRACTION
- PHASE DISTRIBUTION
- PHASE COMPOSITIONS

Figure 1.

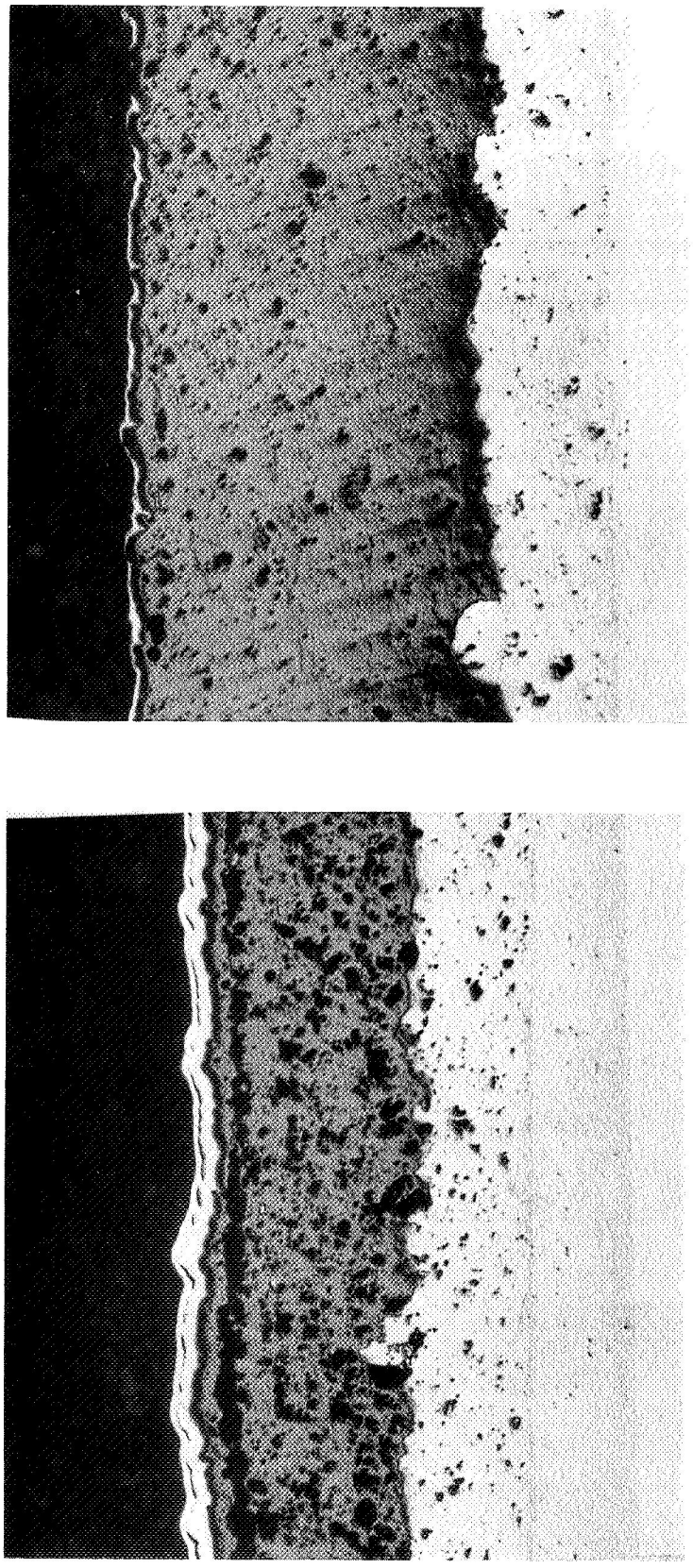

MICROSTRUCTURES OF PLASMA SPRAYED PSZ
FROM TWO DIFFERENT POWDER SOURCES

Figure 2.

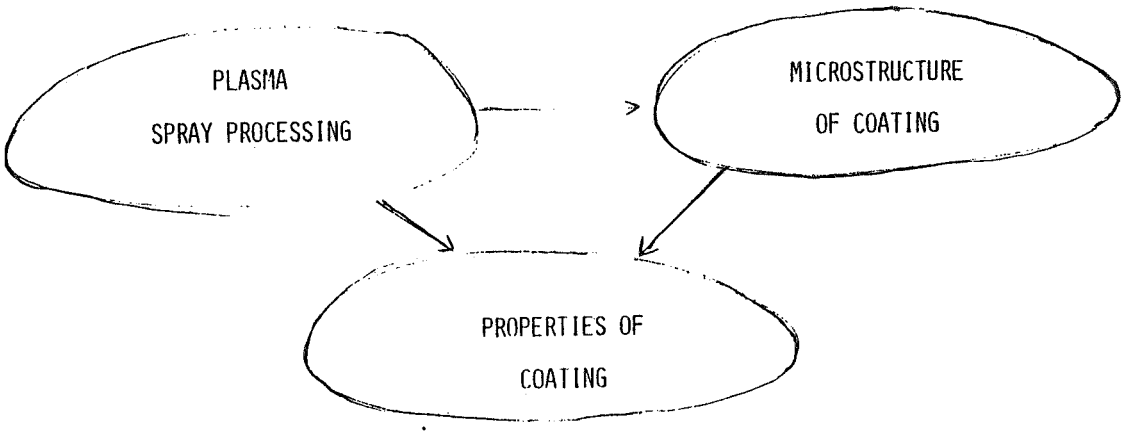

Figure 3.

FAILURE OF PSZ COATING DURING THERMAL CYCLING

- THERMAL GRADIENTS
- THERMAL EXPANSION MISMATCH
- BOND COAT OXIDATION

Figure 4.

PHASE TRANSFORMATIONS IN PSZ

$T \longrightarrow M + F$ EUTECTOID

$T' \longrightarrow T$? NONTRANSFORMABLE

TEMPERATURE EFFECTS

STRAIN/STRESS EFFECTS

Figure 5.

INCREASE TOUGHNESS OF PSZ COATING

- SEGMENTED COATINGS
- MICROCRACKS
- TRANSFORMATION TOUGHENING
- IMPROVE THERMAL EXPANSION MATCH
- OXIDATION RESISTANT BOND COATING

Figure 6.

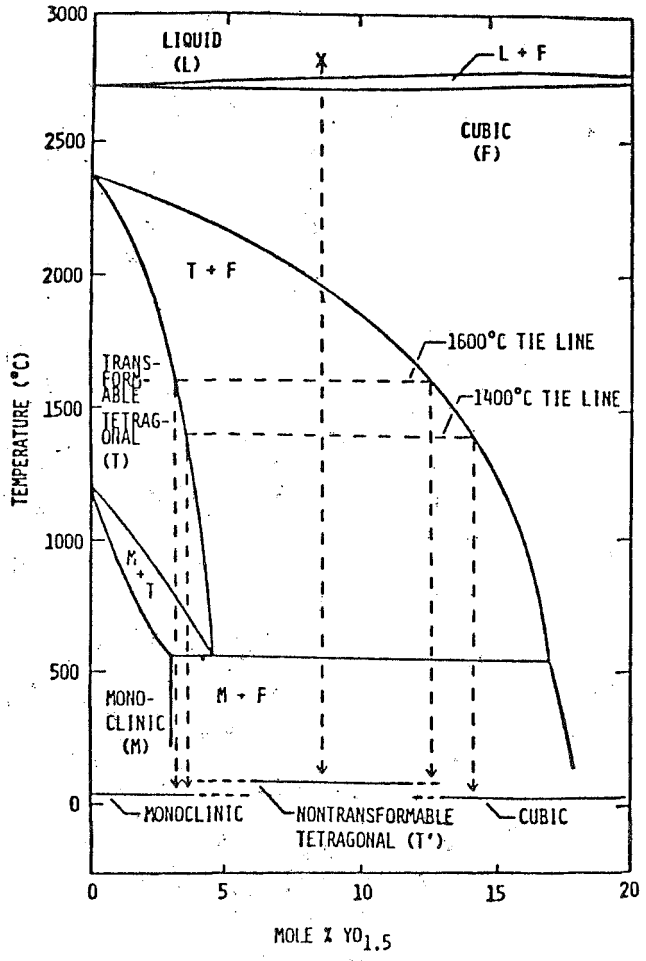

Low-yttria region of ZrO_2-$YO_{1.5}$ phase diagram

Figure 7.

QUANTITATIVE PHASE ANALYSIS BY X-RAY DIFFRACTION

- SEPARATION OF T FROM F IS DIFFICULT
- DECONVOLUTE THE (400) REGION
- MANY TECHNIQUES ARE QUALITATIVE
- NEW DECONVOLUTION TECHNIQUES

Figure 8.

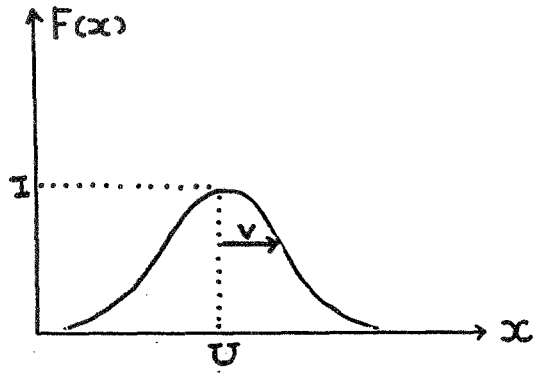

$$F(x) = I\ \mathrm{Exp}\left(-\tfrac{1}{2}[(x-U)/V]^2\right)$$

Three parameters

I, U, V

Figure 9.

$$\chi^2 = \sum_{i=1}^{n} \frac{(e_i - o_i)^2}{e_i}$$

where $e_i = I\ \mathrm{Exp}\left[-\tfrac{1}{2}[(x_i - U)/V]^2\right]$

o_i = Raw XRD data

Figure 10.

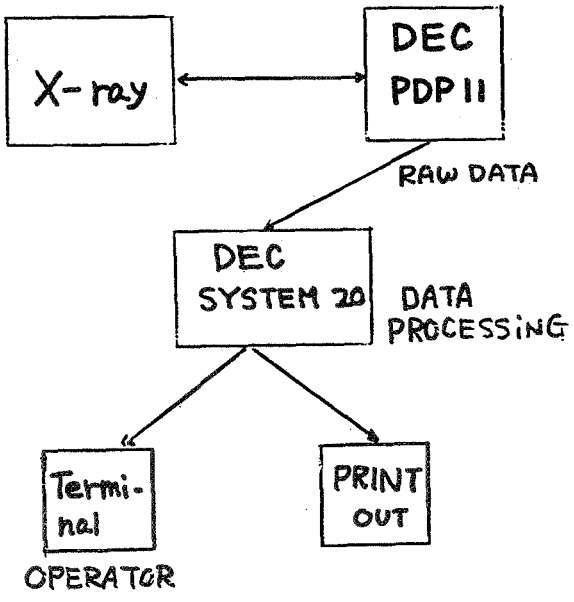

Figure 11.

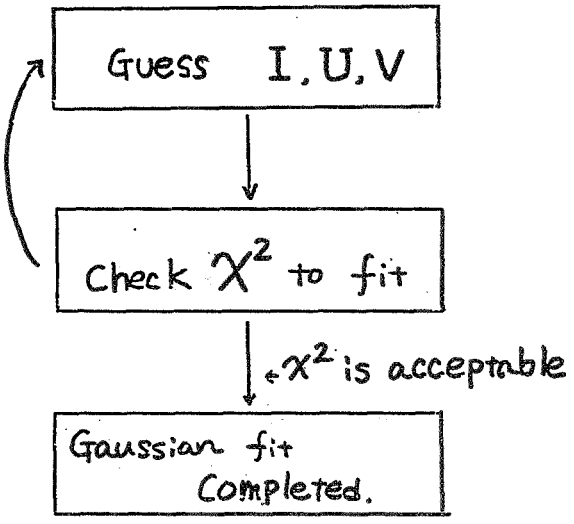

Figure 12.

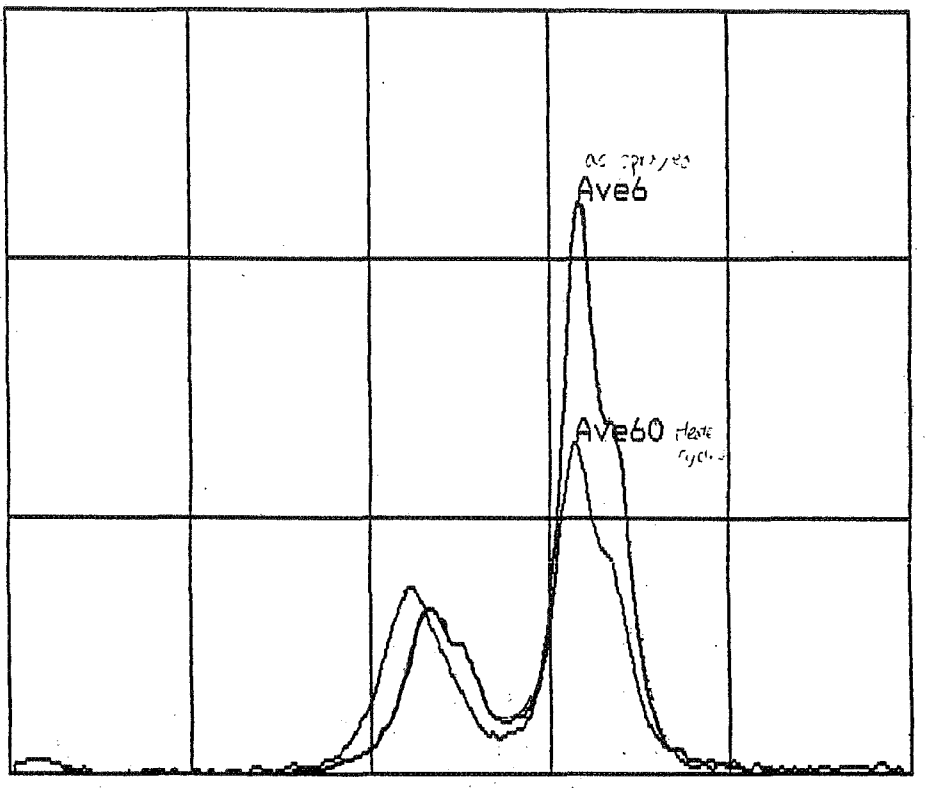

Figure 13.

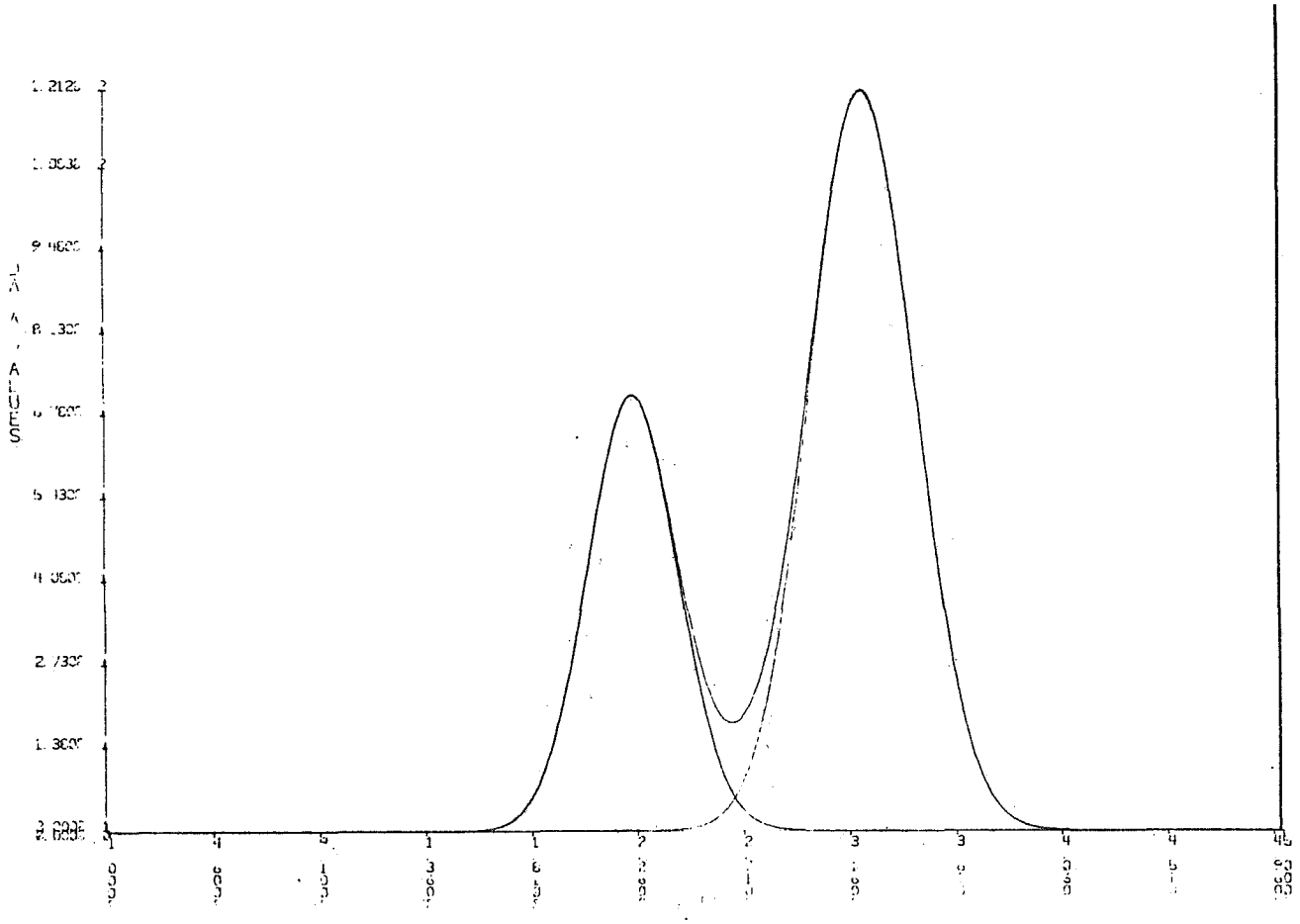

Figure 14.

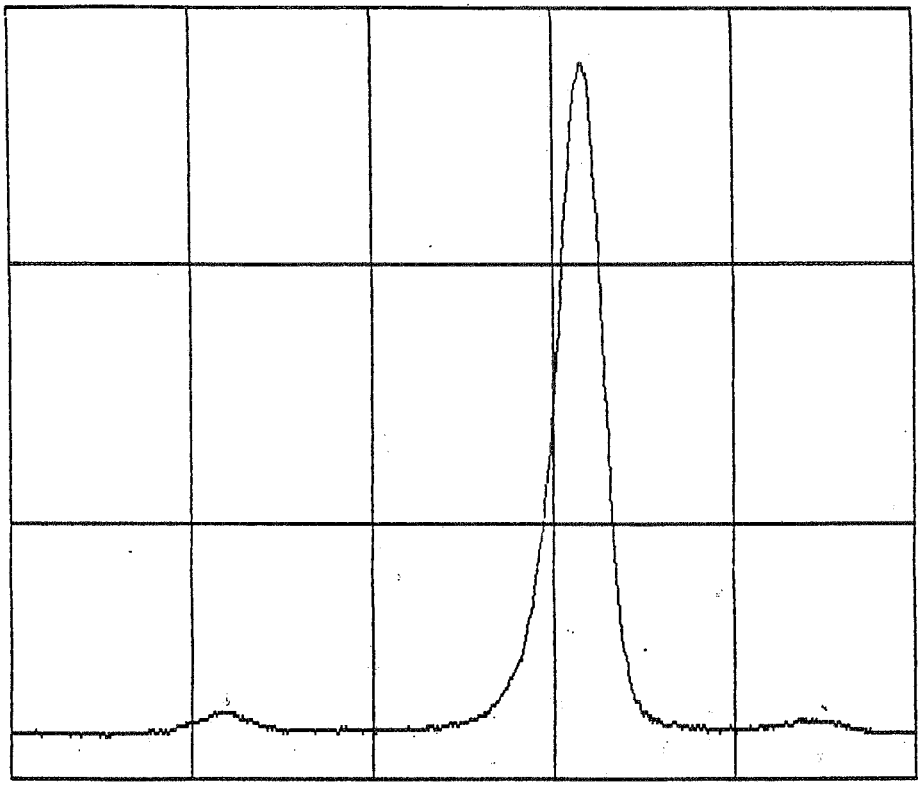

Figure 15.

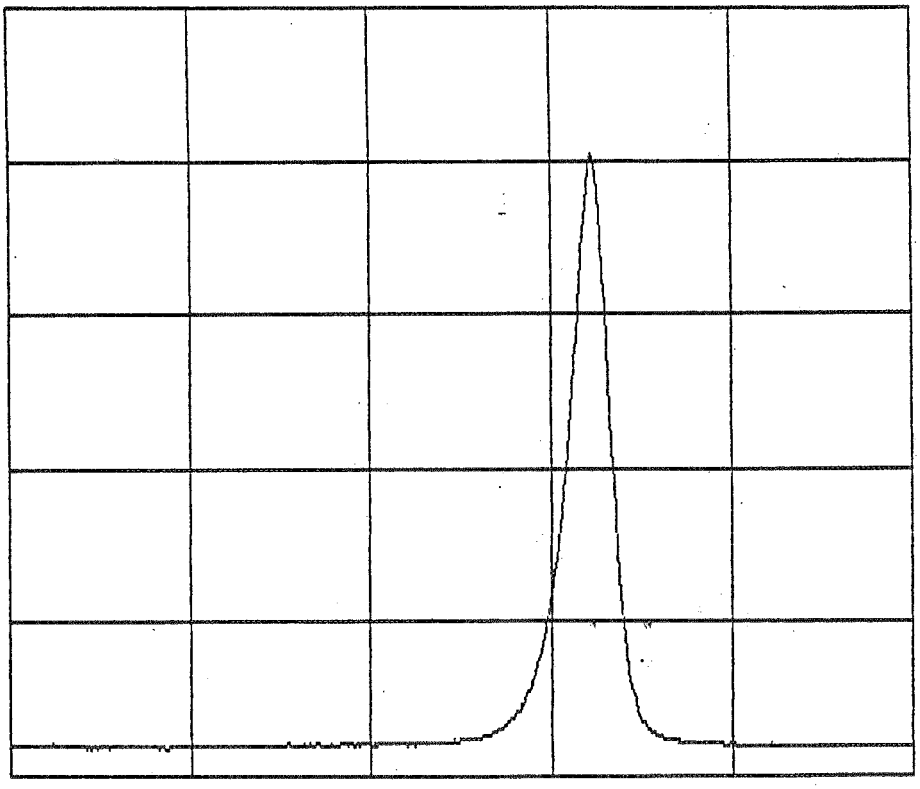

Figure 16.

Table I.

		COATING		POWDER	
		HEAT TREATED (CENTER)	AS SPRAYED (CORNER)	THERMALLY (CYCLED)	AS RECEIVED
PHASE (MOLE) FRACTION %	TET	91.9	98.3	78.9	80.0
	CUBIC	3.0	0.9	20.7	18.4
	MON	5.1	0.8	.5	1.6
PEAK INTENSITY (400) REGION (UNIT ARBITRARY)	400 TET	66.6	100.6	---	---
	004 TET	33.8	29.8	---	---
	400 FCC	3.7	1.4	---	---
PEAK INTENSITY (111) REGION UNIT ARBITRARY	111 (F+T)	882.9	1138.0	---	---
	111 M-N	37.3	7.7	---	---
	111 MON	20.1	4.2	---	---
INTENSITY RATIO $\frac{I\ (400)\ T}{I\ (004)\ T}$ THEORETICAL VALUE = 3.15		1.97 TEXTURE EFFECT	3.38		

CERAMIC OXIDE REACTIONS WITH V_2O_5 AND SO_3

R. L. Jones and C. E. Williams
Naval Research Laboratory
Washington, DC 20375-5000

Ceramic oxides are not inert in combustion environments, but can react with, inter alia, SO_3 and Na_2SO_4 to yield low melting mixed sulfate eutectics (mp 700-800°C), and with vanadium compounds to produce vanadates, e.g., YVO_4, or other species.

Assuming ceramic degradation to become severe only when molten phases are generated in the surface salt (as found for metallic hot corrosion), the reactivity of ceramic oxides can be quantified by determining the SO_3 partial pressure necessary for molten mixed sulfate formation with Na_2SO_4. The critical SO_3 pressures measured for Y_2O_3, CeO_2, and ZrO_2, for example, were of the order of < 10 Pa, 100 Pa, and 1000 Pa, respectively. Therefore, use of oxides such as CeO_2 rather than Y_2O_3 for stabilization of ZrO_2 may increase the resistance of ZrO_2-based ceramics to SO_3-Na_2SO_4 attack, as limited experience seems to confirm.

Vanadium pentoxide is an acidic oxide that reacts with Na_2O, SO_3, and the different ceramic oxides in a series of Lux-Flood type of acid-base displacement reactions. To elucidate the various possible vanadium compound-ceramic oxide interactions, a study was made of the reactions of a matrix involving, on the one axis, ceramic oxides of increasing acidity (Y_2O_3 < CeO_2 < ZrO_2 < GeO_2 < Ta_2O_5 (most acidic)), and on the other axis, vanadium compounds of increasing acidity (Na_3VO_4 < $NaVO_3$ < V_2O_5 (most acidic)). Resistance to vanadium compound reaction increased, up to ZrO_2, as the oxide acidity increased with, e.g., Y_2O_3 reacting with $NaVO_3$ and V_2O_5, although not Na_3VO_4, while CeO_2 reacted only with V_2O_5, and neither $NaVO_3$ or Na_3VO_4. Oxides more acidic than ZrO_2 displaced V_2O_5 (i.e., acted as a stronger acid than V_2O_5), giving such reactions as: $2\ Ta_2O_5 + 2\ NaVO_3 = Na_2Ta_4O_{11} + V_2O_5$. Sulfur trioxide interacts via the reaction, $2\ NaVO_3 + SO_3 = Na_2SO_4 + V_2O_5$, and can, for example, cause vanadation of CeO_2, which does not react with pure $NaVO_3$, by producing V_2O_5 in the melt.

Examination of Y_2O_3- and CeO_2-stabilized ZrO_2 sintered ceramics which were degraded in 700°C $NaVO_3$ has shown good agreement with the reactions predicted above, except that the CeO_2-ZrO_2 ceramic appears to be inexplicably degraded by $NaVO_3$.

POTENTIAL CERAMIC COATING BENEFITS TO NAVY

IMPROVED THERMAL EFFICIENCY

CORROSION RESISTANCE

USE OF LOW QUALITY FUEL

WITHSTAND 700°C OPERATION

Figure 1.

CERAMIC REACTION WITH FUEL CONTAMINANTS

$\underline{SO_3}$	$Y_2O_3 + SO_3 \rightleftharpoons Y_2O_2(SO_4)$
	$Y_2O_3 + SO_3 + Na_2SO_4 \rightleftharpoons Y_2(SO_4)_3\text{-}Na_2SO_4$
$\underline{V_2O_5}$	$Y_2O_3 + V_2O_5 \rightleftharpoons 2\ YVO_4$
$\underline{V_2O_5 + SO_3}$	$2\ NaVO_3 \rightleftharpoons Na_2O + V_2O_5$
	$2\ NaVO_3 + SO_3 \rightleftharpoons V_2O_5 + Na_2SO_4$
	$CeO_2 + V_2O_5 \rightleftharpoons 2\ CeVO_4$

Figure 2.

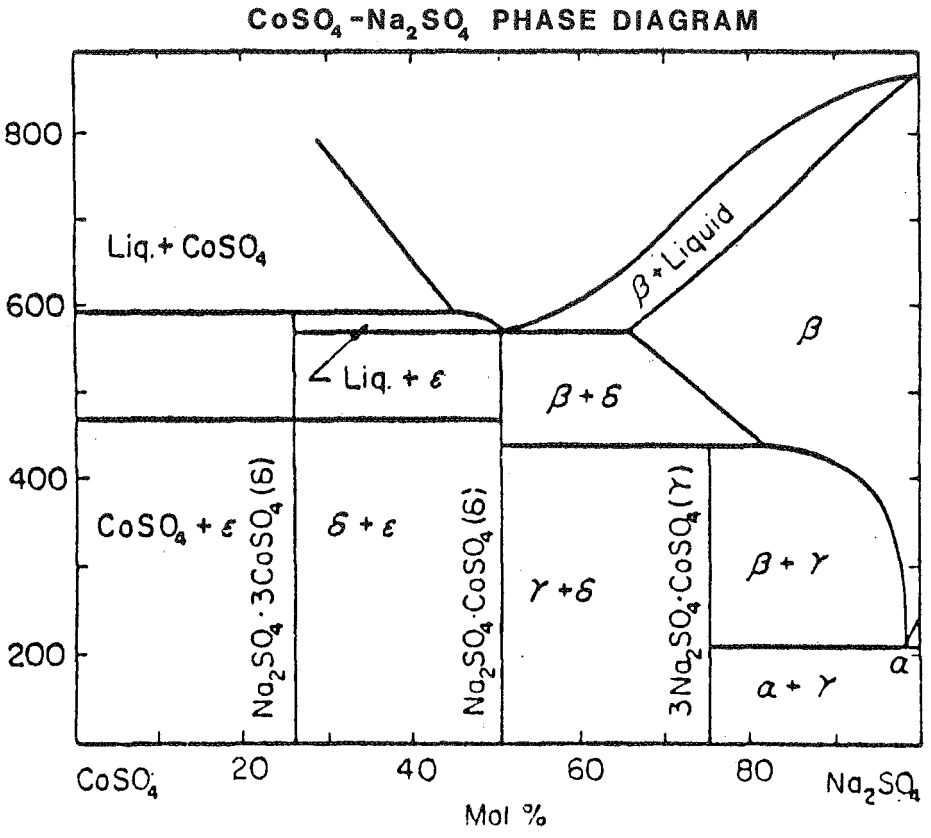

Figure 3.

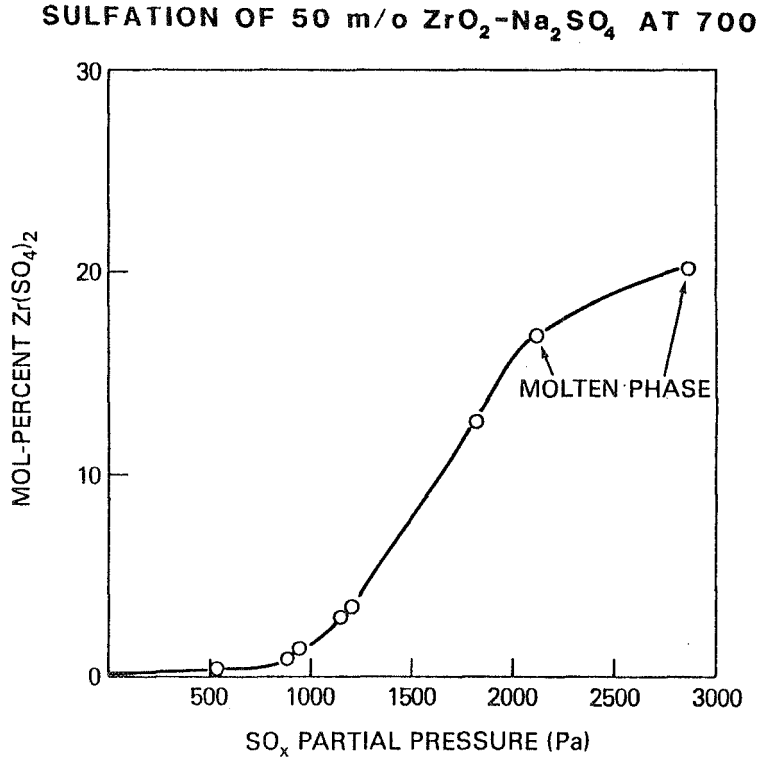

Figure 4.

SO_3 PARTIAL PRESSURE FOR MOLTEN MIXED SULFATE FORMATION AT 700°C

Y_2O_3	<10 Pa
CeO_2	100 Pa
ZrO_2	1000 Pa

Figure 5.

SODIUM VANADATE COMPOUNDS

—DECREASING ACIDITY→

$Na_2O + 6\ V_2O_5 \rightleftharpoons Na_2V_{12}O_{31}$	vanadium bronze I
$Na_2O + 3\ V_2O_5 \rightleftharpoons 2\ NaV_3O_8$	vanadium bronze II
$Na_2O + V_2O_5 \rightleftharpoons 2\ NaVO_3$	sodium metavanadate
$2\ Na_2O + V_2O_5 \rightleftharpoons Na_4V_2O_7$	sodium pyrovanadate
$3\ Na_2O + V_2O_5 \rightleftharpoons 2\ Na_3VO_4$	sodium orthovanadate

Figure 6.

C-2

VANADIUM-CERAMIC OXIDE REACTIONS

	Na_3VO_4	$NaVO_3$	V_2O_5
Y_2O_3	NR	YVO_4	YVO_4
CeO_2	NR	NR	$CeVO_4$
ZrO_2	NR	NR	ZrV_2O_7 (BUT SLOWLY)
GeO_2	$Na_4Ge_9O_{20}$	$Na_4Ge_9O_{20}$ (*)	NR
Ta_2O_5	$NaTaO_3$	$Na_2Ta_4O_{11}$	α-$TaVO_5$

NR = NO REACTION

(*) AS PPT FROM H_2O SOL'N

Figure 7.

INFLUENCE OF Na_2SO_4 AND SO_3 IN VANADIUM-CERAMIC REACTIONS

$$2\ NaVO_3 + SO_3 \rightleftharpoons V_2O_5 + Na_2SO_4$$

INCREASING SO_3 PROMOTES VANADATE FORMATION

$$CeO_2 + NaVO_3 + SO_3 \rightarrow CeVO_4$$

$$ZrO_2 + NaVO_3 + SO_3 \rightarrow NR$$

(AT LEAST UP TO 110 Pa OF SO_3 AT 700°C)

Figure 8.

DEGRADATION OF Y_2O_3-ZrO_2 BY $NaVO_3$ AT 700°C

Figure 9.

DEGRADATION OF CeO_2-ZrO_2 BY $NaVO_3$ AT 700°C

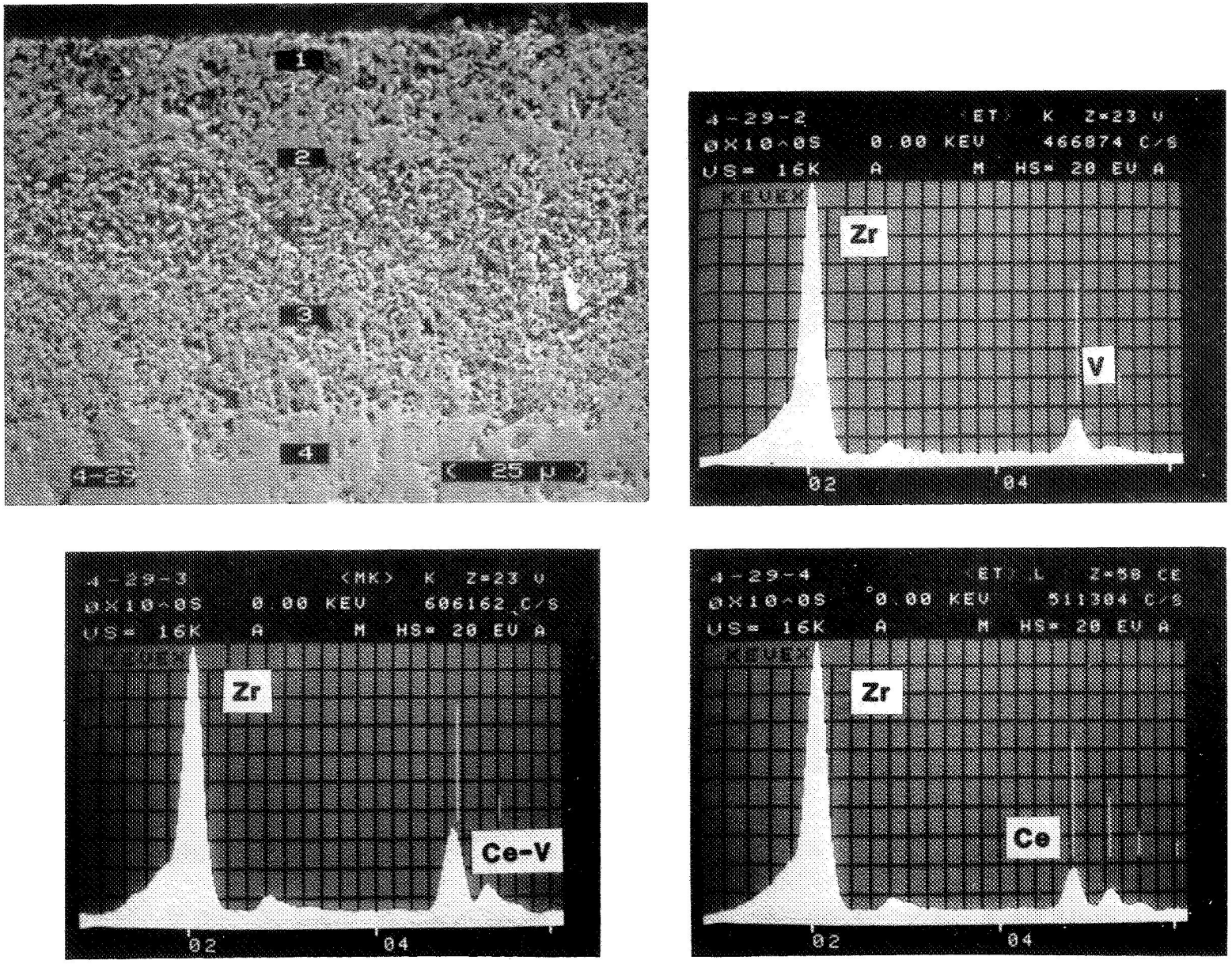

Figure 10.

ATTACK OF CeO_2-ZrO_2 BY $NaVO_3$ UNDER 40 Pa OF SO_3 AT 700°C

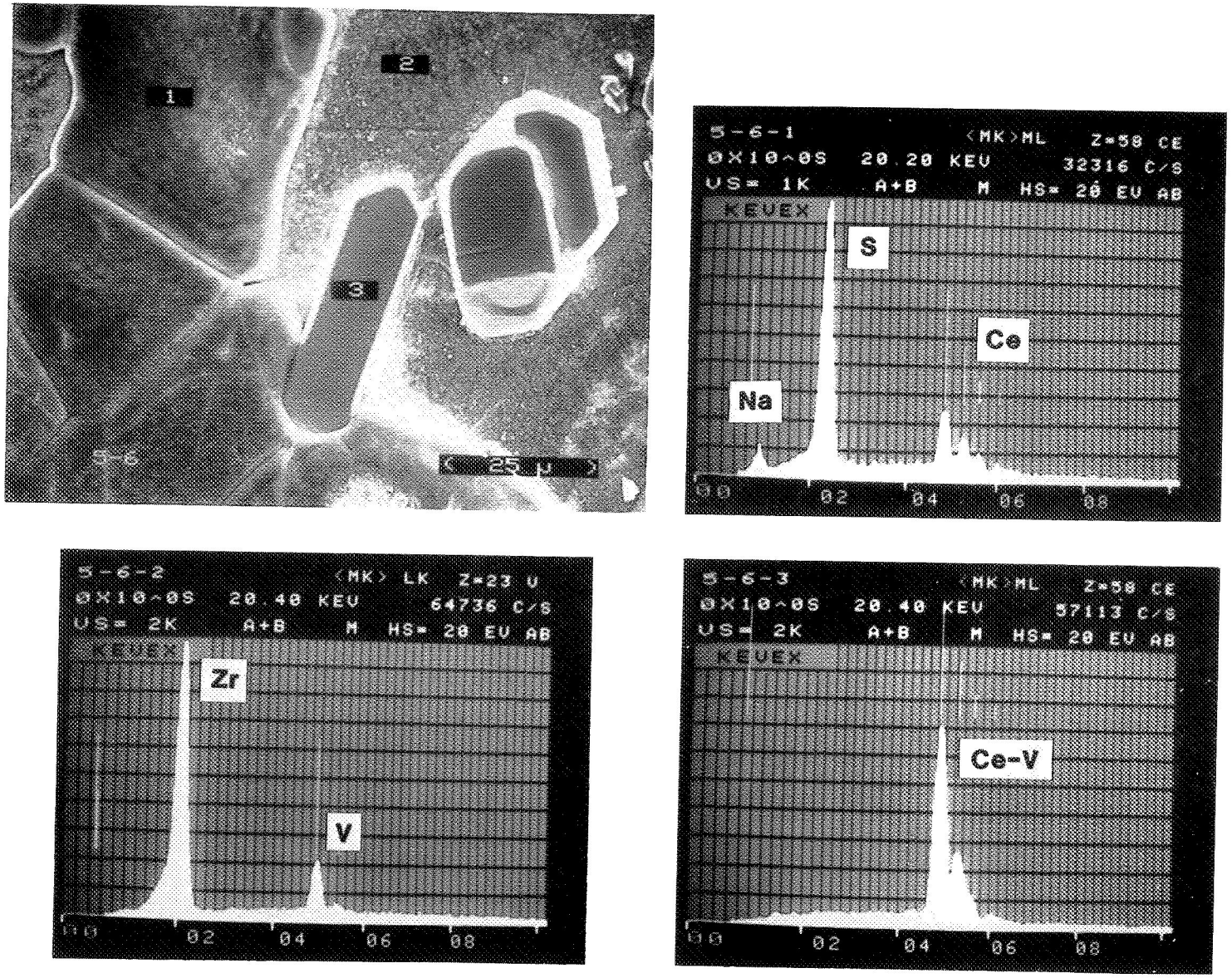

Figure 11.

CONCLUSIONS

CERAMIC CORROSION ELUCIDATED

GUIDELINES LAID FOR DEVELOPMENT OF CORROSION-RESISTANT CERAMICS

EFFECTS OF CERAMIC PROCESSING STILL TO BE IDENTIFIED

Figure 12.

DESTABILIZATION OF YTTRIA-STABILIZED ZIRCONIA INDUCED BY MOLTEN SODIUM VANADATE-SODIUM SULFATE MELTS*

A.S. Nagelberg and J.C. Hamilton
Combustion Research Facility
Sandia National Laboratories
Livermore, California 94550

The extent of surface destabilization of ZrO_2 - 8 wt % Y_2O_3 ceramic disks was determined after exposure to molten salt mixtures of sodium sulfate containing up to 15 mole% sodium metavanadate ($NaVO_3$) at 1173 K. The ceramic surface was observed to transform from the cubic/tetragonal to monoclinic phase, concurrent with chemical changes in the molten salt layer in contact with the ceramic. Significant attack rates were observed in both pure sulfate and metavanadate-sulfate melts. The rate of attack was found to be quite sensitive to the mole fraction of vanadate in the molten salt solution and the partial pressure of sulfur trioxide ($1x10^{6}$ to $1x10^{-3}$ atm) in equilibrium with the salt melt. The observed parabolic rate of attack is interpreted to be caused by a reaction controlled by diffusion in the salt that penetrates into the porous layer formed by the destabilization. The parabolic rate constant in mixed sodium metavanadate - sodium sulfate melts was found to be proportional to the SO_3 partial pressure and the square of the metavanadate concentration. In-situ Raman spectroscopic measurements allowed simultaneous observations of the ceramic phases and salt chemistry during the attack process.

[1] This work supported by the U.S. Dept. of Energy, Office of Basic Energy Sciences.

Table I

Exposure Environment Composition

(percent)

Initial Gas Composition		Equilibrium Composition at 1173 K		
O_2	SO_2	O_2	SO_2	SO_3
90	10	90	7.7	2.4
99	1	99	.76	.24
99.9	0.1	99.9	7.6×10^{-2}	2.5×10^{-2}
99.985	0.015	99.99	1.1×10^{-2}	3.7×10^{-3}
1	99	.25	97.	.15

Table II

Parabolic Rate Constants

($P_{SO_3} = 2.4 \times 10^{-3}$)

NaVO3 Concentration (mole percent)	Parabolic Rate Constant (cm2/sec)
0.0	1×10^{-11}
0.2%	1×10^{-11}
1.0%	1.7×10^{-10}
2.0%	5.4×10^{-10}
3.9%	1.5×10^{-9}

RAMAN EFFECT

$$\omega_I - \omega_S = \omega_{VIB}$$

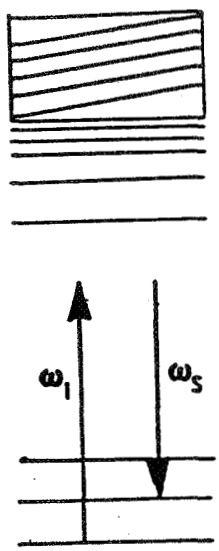

Figure 1.

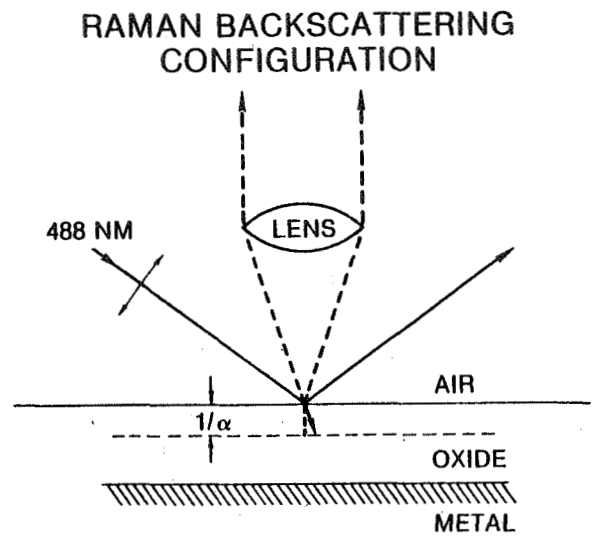

Figure 2.

RAMAN ADVANTAGES

1. NON-PERTURBING
2. IN SITU
3. QUANTITATIVE CHEMICAL COMPOUND IDENTIFICATION
4. SENSITIVE TO LATTICE SYMMETRY
5. LATERAL RESOLUTION - 1 μm
6. DEPTH RESOLUTION - (100 Å - 100 μm)
7. GAS ENVIRONMENT CHARACTERIZATION
8. SAMPLE/GAS TEMPERATURE
9. TEMPORAL RESOLUTION (*ms - hs*)

Figure 3.

$ZrO_2 - Y_2O_3$

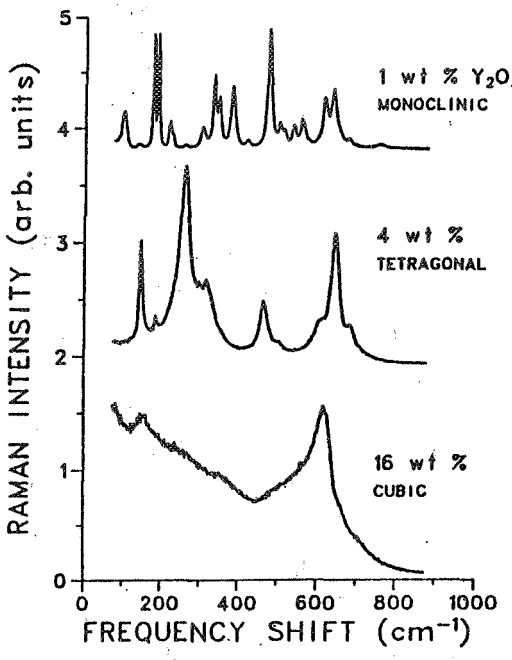

Figure 4.

Experimental Proceedure

- Stabilized zirconia ceramics immersed in sulfate-vanadate melts contained in platinum crucibles.
- Temperature, sulfur dioxide and sulfur trioxide content varied.
- Post-exposure analysis by electron microscopy, electron microprobe and Raman spectroscopy.

Figure 5.

ZrO_2 – 8 wt% Y_2O_3

Exposure: 900°C

Pure $Na_2V_2O_6$

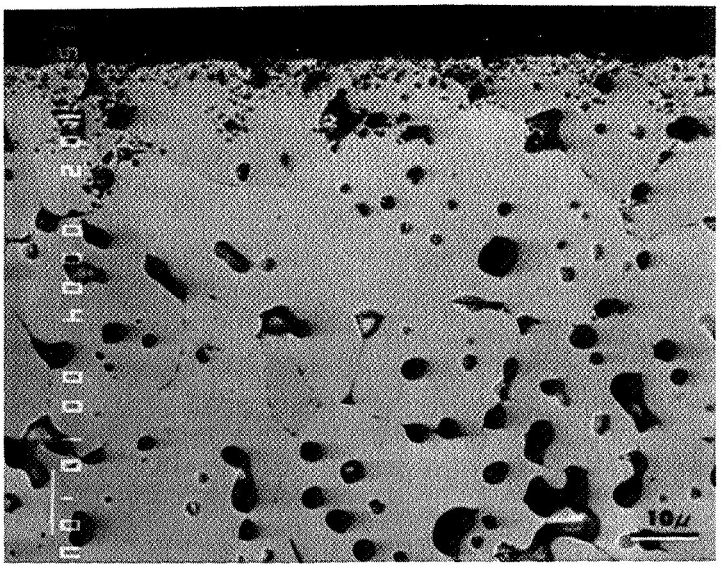

10 min.

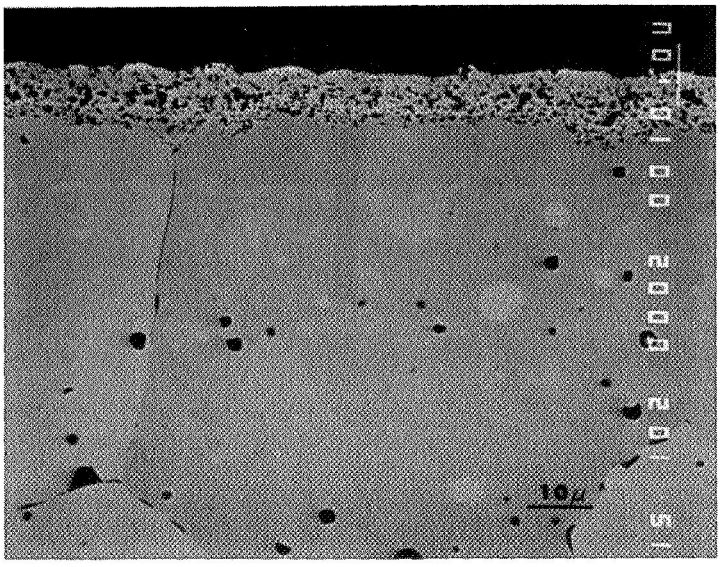

1 hr.

Figure 6.

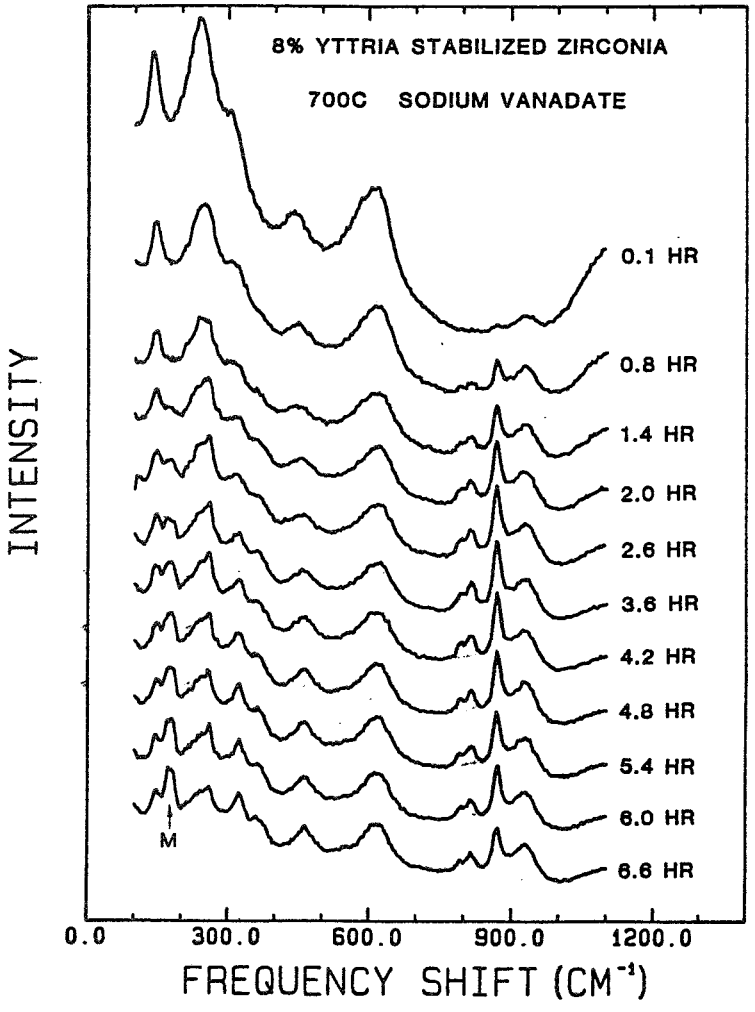

Figure 7.

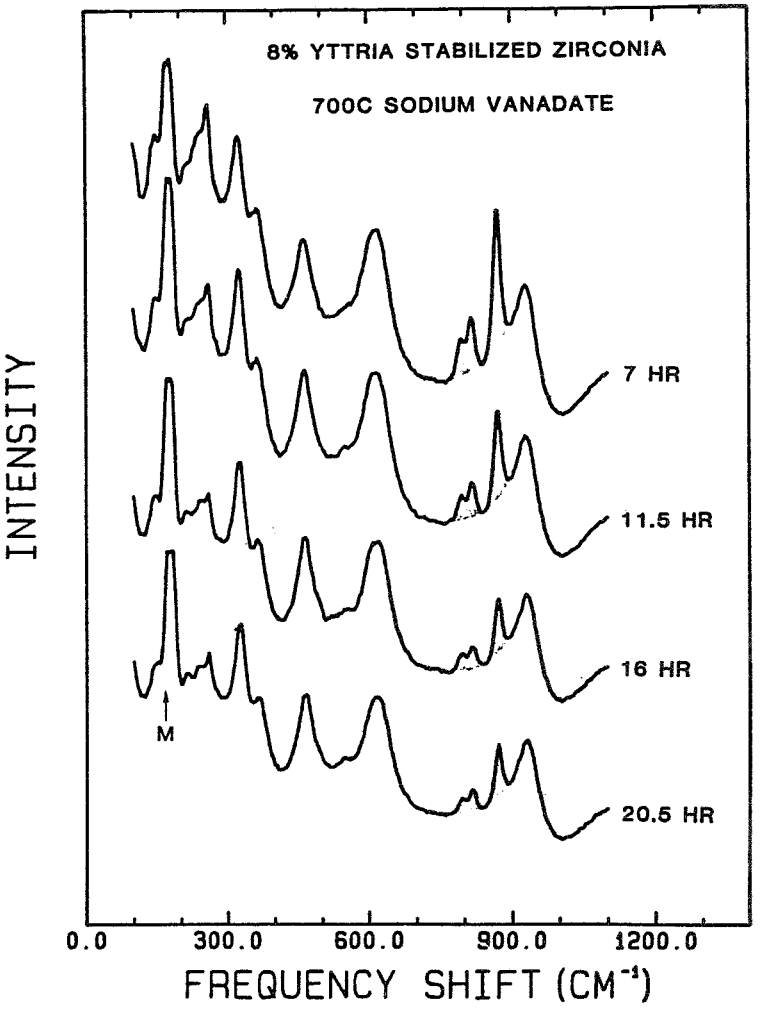

Figure 8.

ZrO_2 – 8wt% Y_2O_3
$NaVO_3$ 24hr 700°C

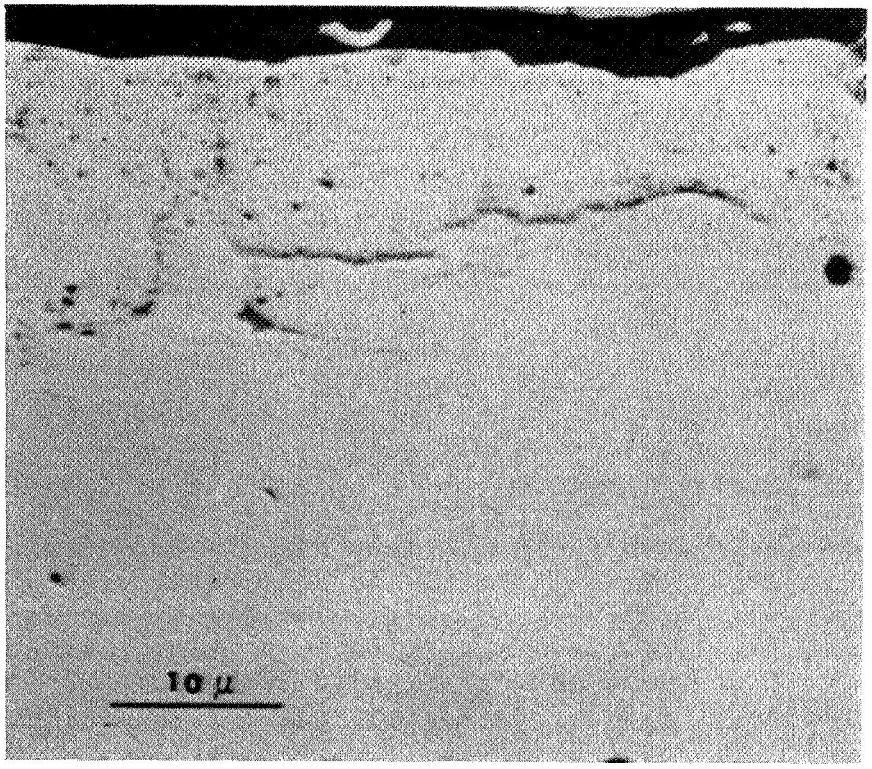

Figure 9.

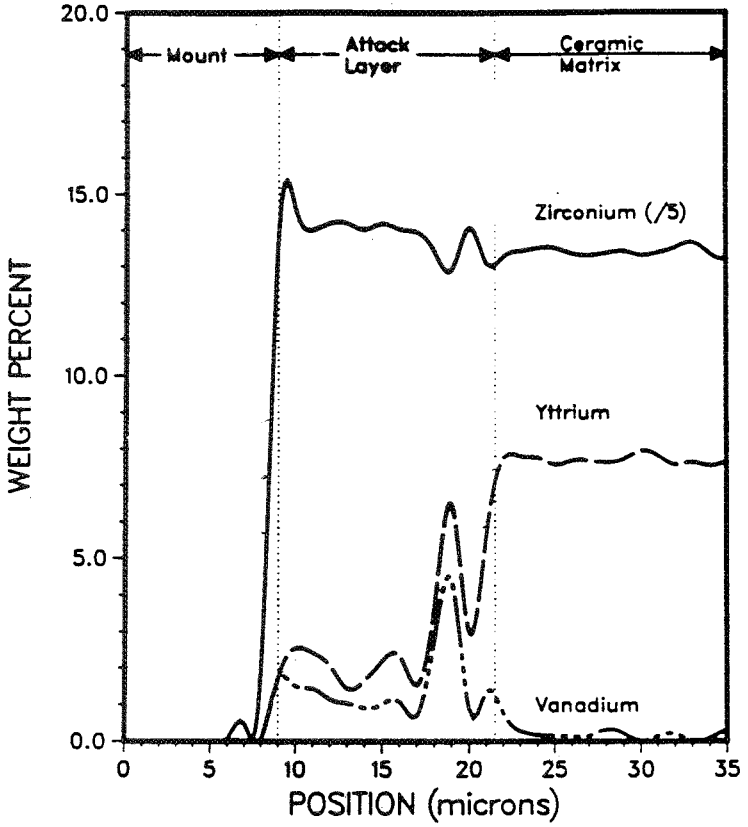

Figure 10.

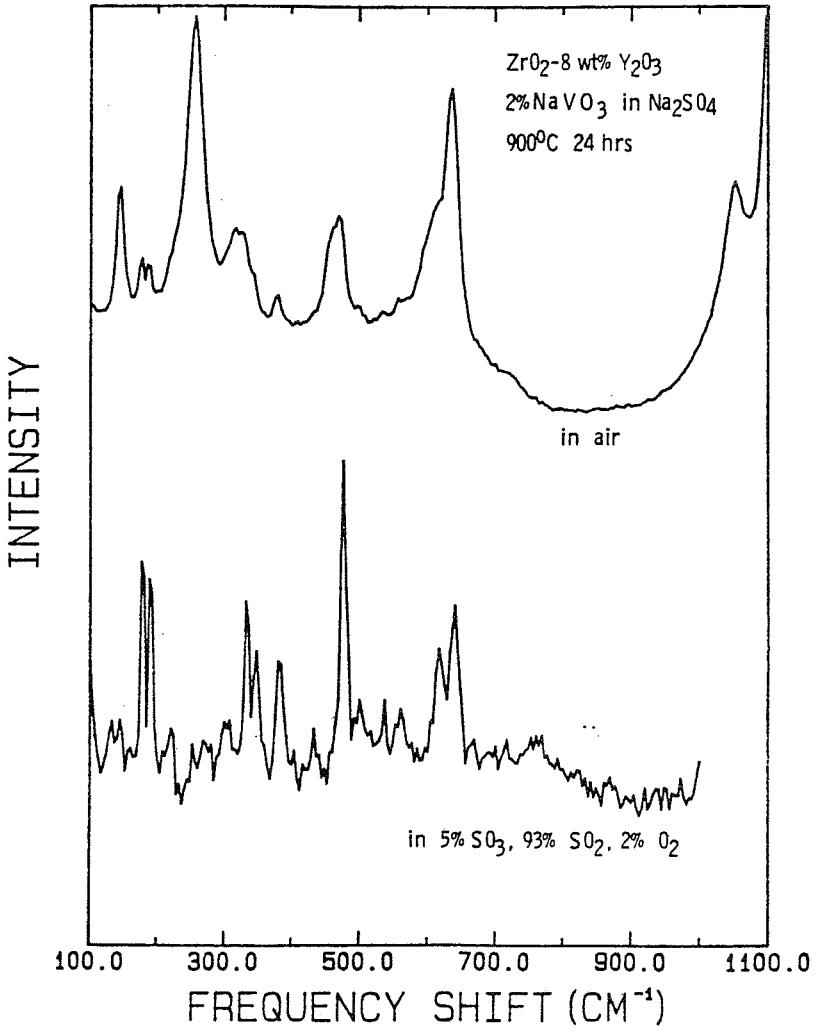

Figure 11.

ZrO_2 – 8 wt% Y_2O_3

Exposure: 900°C 24 hr.

2 mol% $Na_2V_2O_6$ in Na_2SO_4

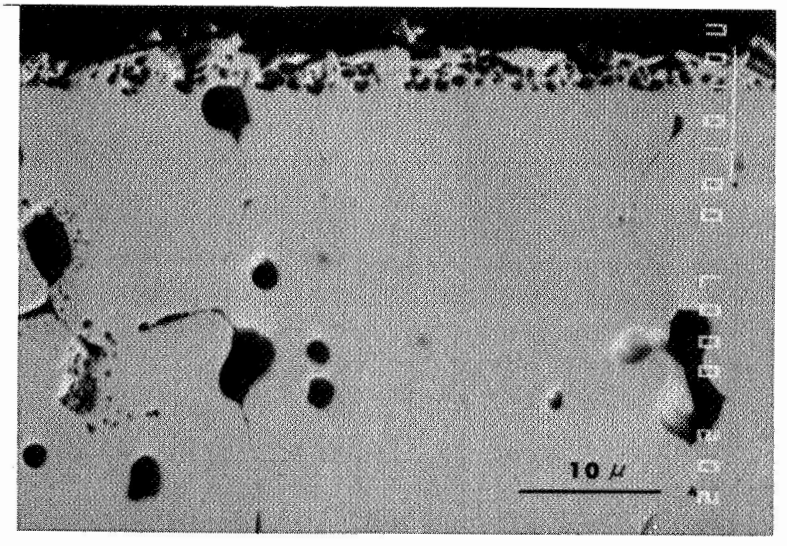

Exposed in air

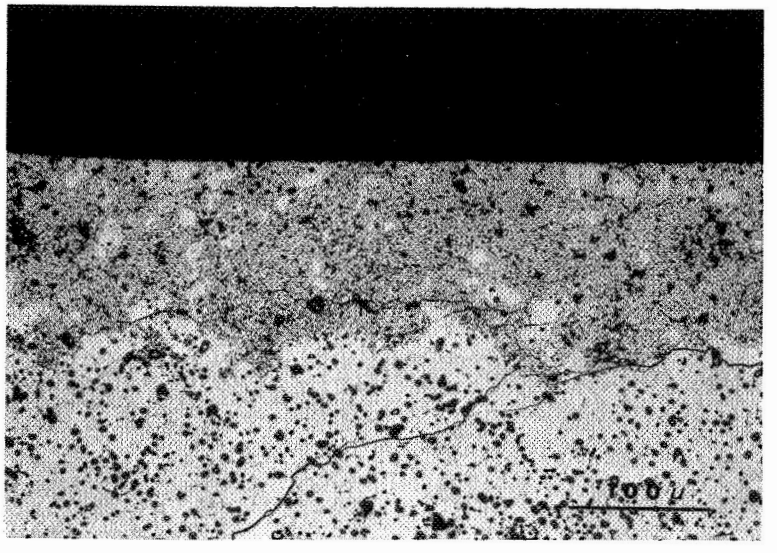

Exposed to 93% SO_2 5% SO_3 2% O_2

Figure 12.

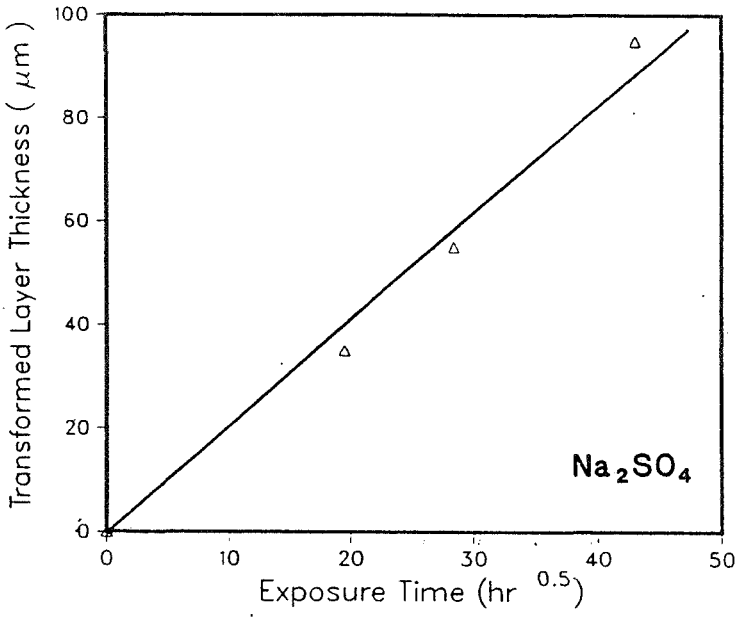

Figure 13.

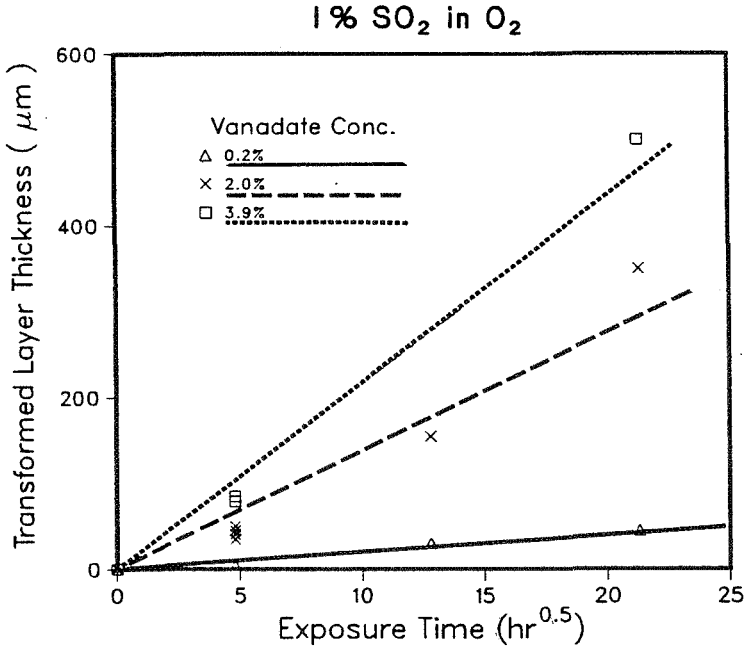

Figure 14.

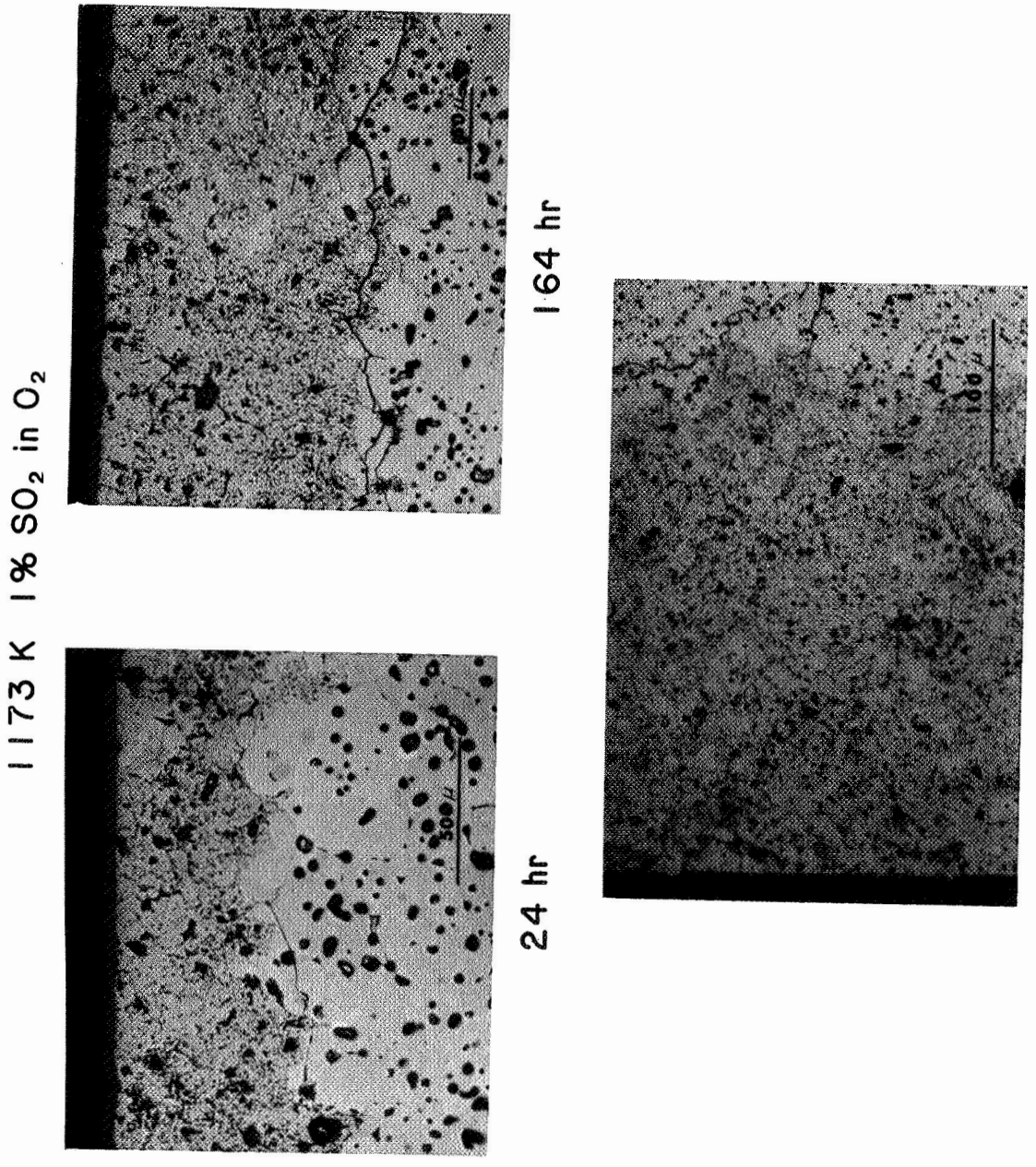

Figure 15.

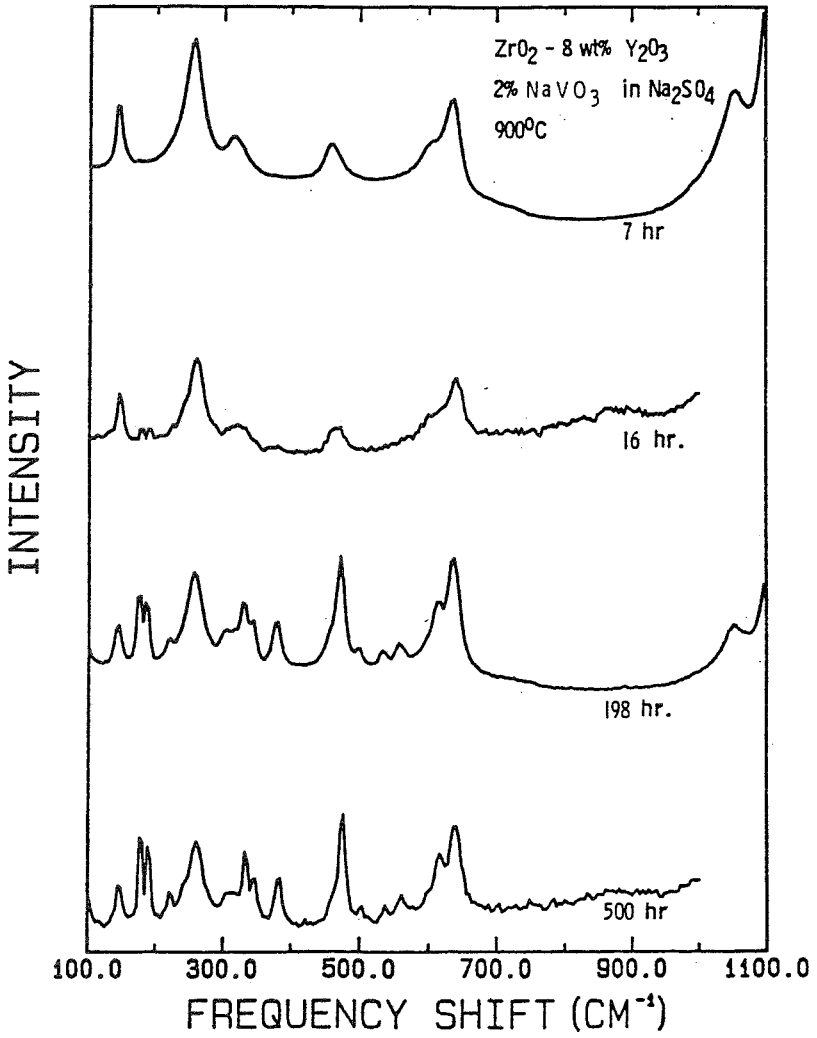

Figure 16.

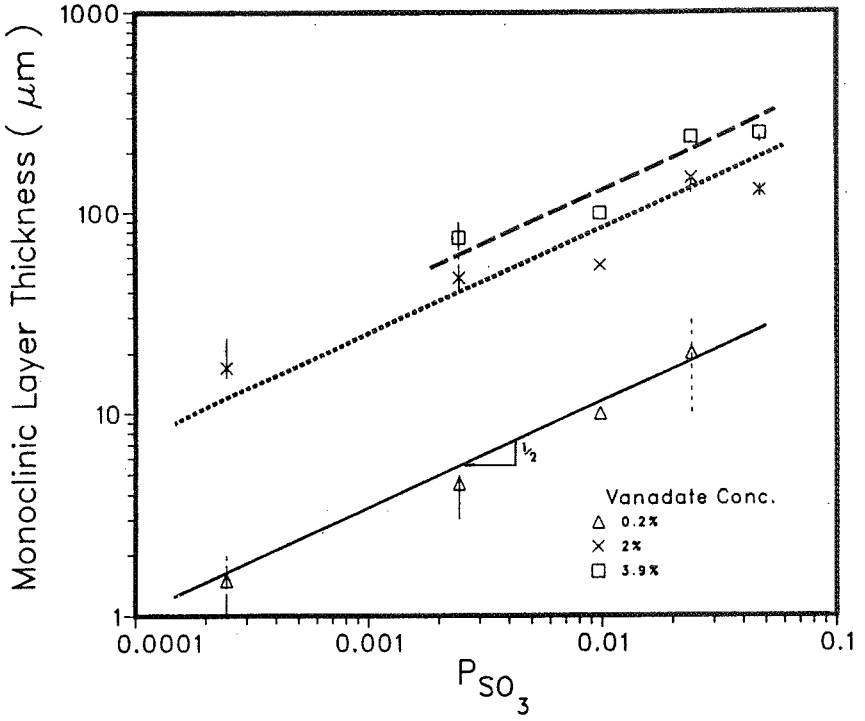

Figure 17.

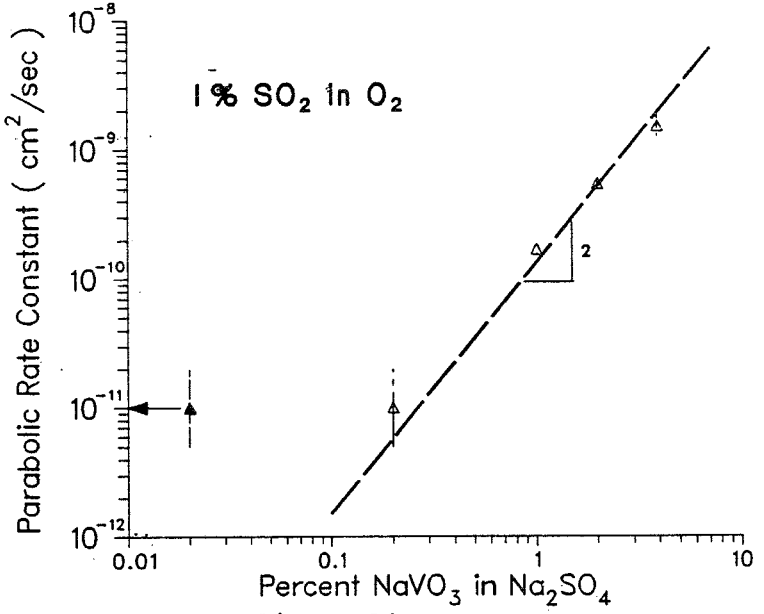

Figure 18.

YTTRIUM LEACHING REACTIONS

– in sulfate melts

$$Y_2O_3 + 3\ SO_3 \rightleftharpoons 2\ Y^{+3} + 3\ SO_4^{-2}$$

– in sulfate–vanadate melts

$$Y_2O_3 + V_2O_5 \rightleftharpoons 2\ Y^{+3} + 2\ VO_4^{-3}$$

Figure 19.

$$SO_2 + 1/2\ O_2 \rightleftharpoons SO_3$$

$$Na_2SO_4 \rightleftharpoons Na_2O + SO_3$$

$$a_{Na_2O} = \frac{K_2}{P_{SO_3}}\ a_{Na_2SO_4}$$

$$2\ NaVO_3 \rightleftharpoons Na_2O + V_2O_5$$

$$a_{V_2O_5} = \frac{K_3\ a_{NaVO_3}^2}{a_{Na_2O}}$$

$$= \frac{K_3\ P_{SO_3}\ a_{NaVO_3}^2}{K_2\ a_{Na_2SO_4}}$$

Figure 20.

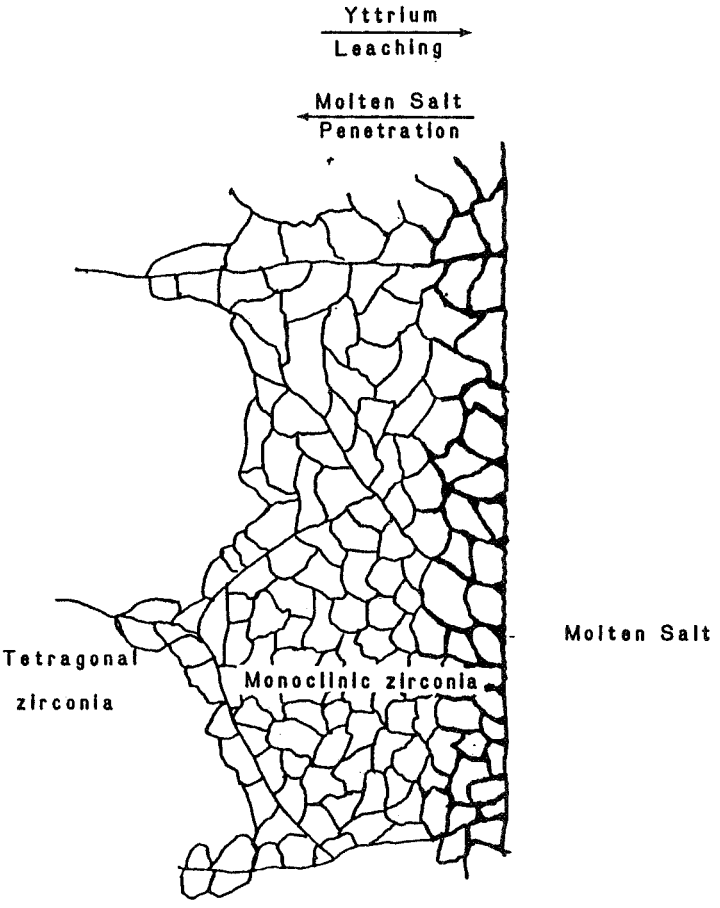

Figure 21.

1173 K 1% SO_2 in O_2

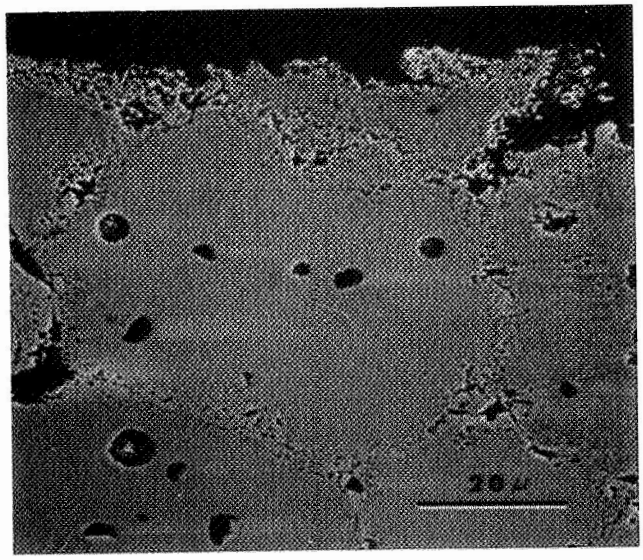

ZrO_2 – 1.5 wt% MgO

96 hr

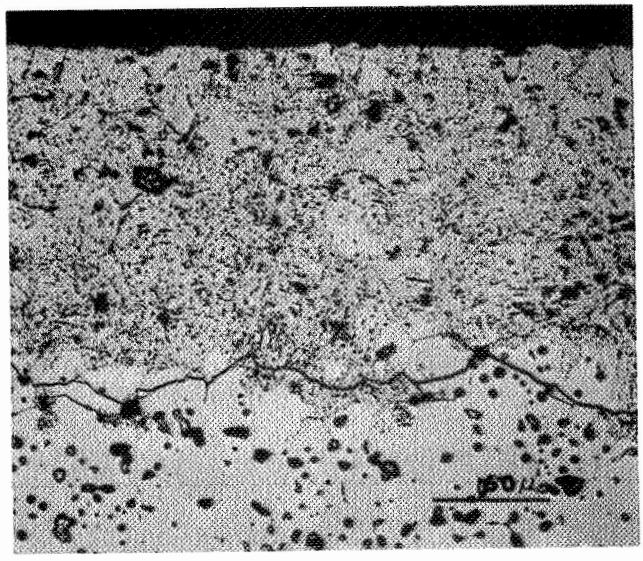

ZrO_2 – 8 wt% Y_2O_3

164 hr

Figure 22.

Summary

* Attack of zirconia ceramics is sensitive to sodium metavanadate concentration, and thus to vanadium impurity level in fuel.

* The attack is also sensitive to sulfur dioxide content of the environment.

* The attack follows parabolic kinetics and is proportional to the square root of the sulfur trioxide partial pressure.

Figure 23.

FINITE ELEMENT ANALYSIS OF THERMAL BARRIER COATINGS

G.C. Chang *
W. Phucharoen**
Cleveland State University
Cleveland, Ohio 44115

The near-term objective of this investigation is to develop an understanding of the states of stresses and strains in a Zirconia-yttria thermal barrier coating (TBC) experiencing a given temperature drop. Results so obtained are expected to facilitate experimental work. In order to gain realistic insights into the distribution of stresses and strains in a complex TBC, the finite element approach was selected to model a cylindrical TBC specimen. Experimental evidence reported in the literature indicated the presence of (near-sinusoidal) rough interface between the ceramic coat and the bond coat. Oxidation of the bond coat at ceramic-bond interface was observed, as was a small amount of cracking in the ceramics near the ceramic-bond interface. To account for these complex features, a plane-strain finite element computer program known as TBCOC has been developed, taking advantage of a generic computer code known as MARC. This generic code has been made available to this co-operative research effort through the use of a supercomputer (Cray I) at NASA Lewis Research Center. The TBCOC model contains 1316 nodal points and 2140 finite elements. It is capable of a uniform isothermal loading. Results of a sample computer run are presented. The loading for this run is a 180°F (100°C) drop from 1292°F (700°C). Material properties used are best estimates for 1292°F, based largely on experimental/commercial data as well as those used in the literature. These results have been favorably correlated with runs using a less sophisticated finite element model (the Basic TBC) in mid-1984. Stress build-ups (in shearing, radial, and to a lesser extent, hoop stresses) in the vicinity of the sinusoidal ceramic-bond interface have been observed. The greatest tensile stress concentration occurs in the ceramic layer in the immediate vicinity of the peaks of the sinusoidal interface. This tensile build-up nearly coincides with cracks observed in experimental work reported by other investigators in recent years.

* Professor
** Graduate Student

TABLE I. - MATERIAL PROPERTIES

	E (psi)	μ	ρ (pci)	α (in./in./°F)
Ceramic	4×10^6	0.25	0.204	5.56×10^{-6}
Bond Coat	20×10^6	0.27	0.252	8.42×10^{-6}
Substrate	25.5×10^6	0.25	0.280	7.73×10^{-6}

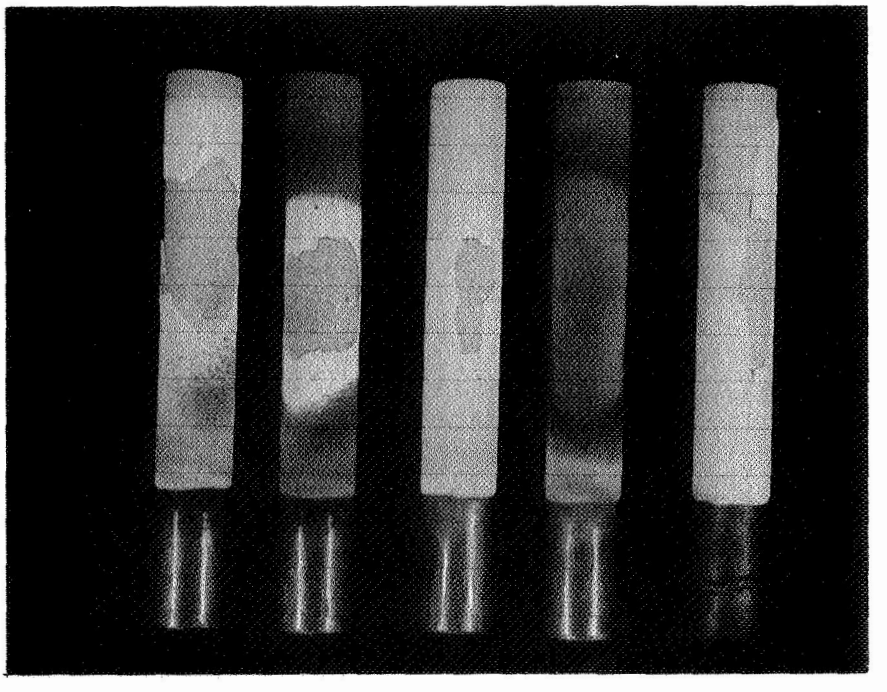

Figure 1. Cylindrical Specimens with Spalled Thermal Barrier Coatings

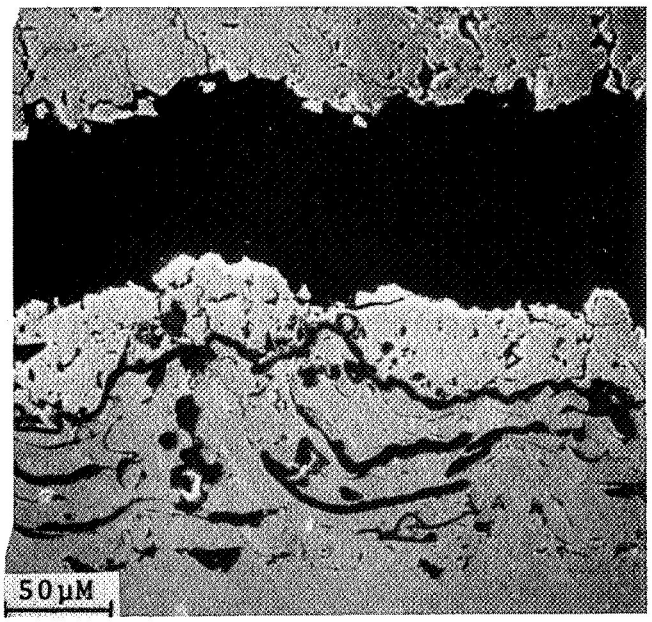

Figure 2. SEM Photomicrograph of the Cross Section of a Thermal Barrier Coating System. (Specimen has failed (delaminated) but not yet spalled.)

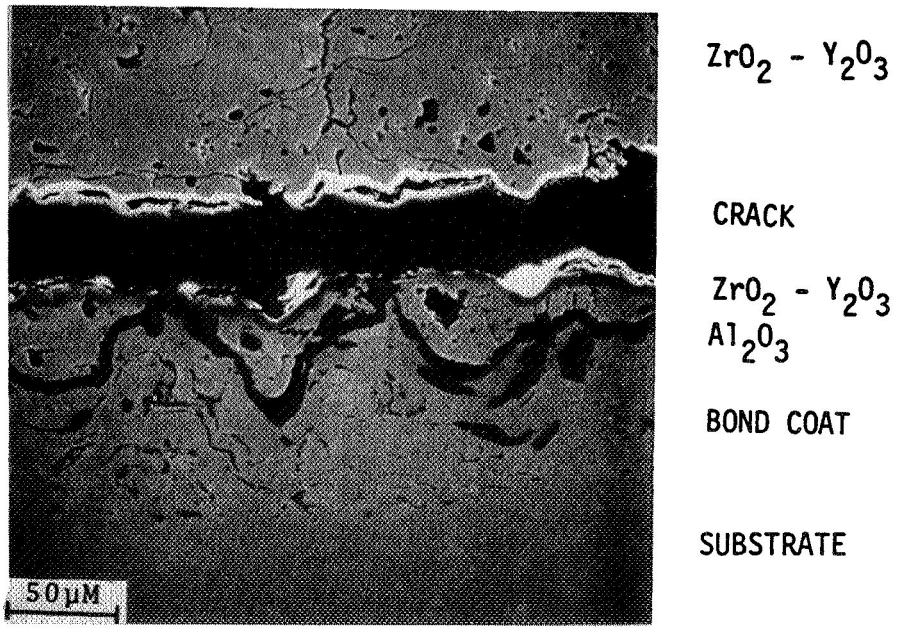

Figure 3. SEM Photomicrograph of the Cross Section of a Thermal Barrier Coating System. (Specimen has failed (delaminated) on cooling. Spalling would occur on subsequent heat up.)

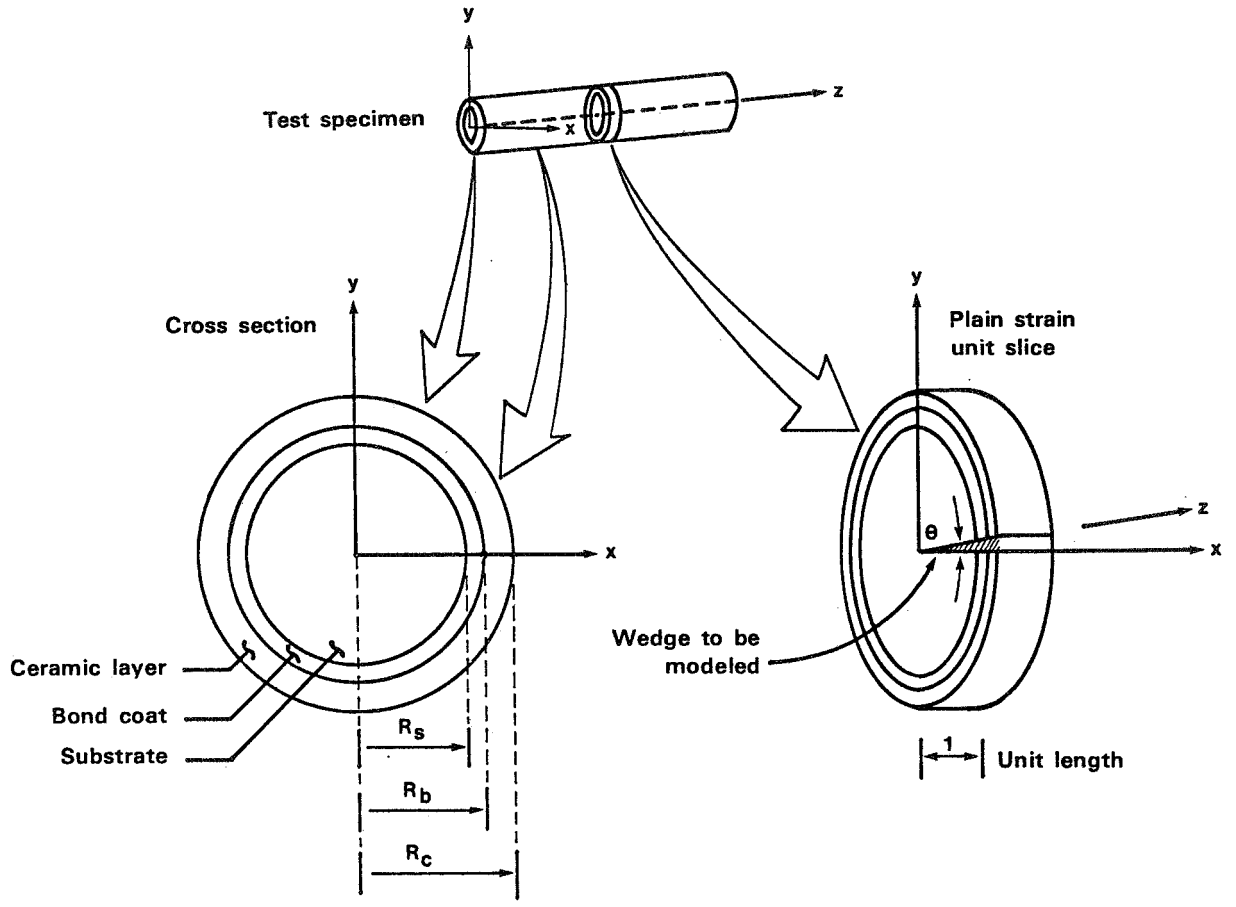

FIGURE 4. CYLINDRICAL TBC TEST SPECIMEN

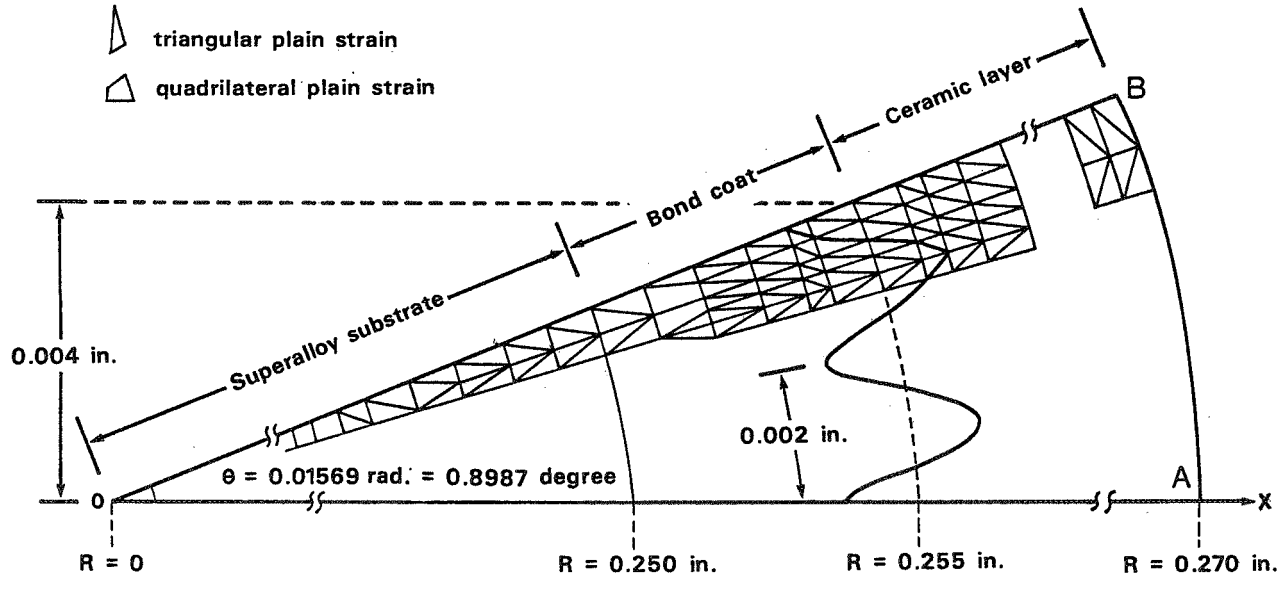

FIGURE 5. THE BASIC TBC FINITE ELEMENT MODEL

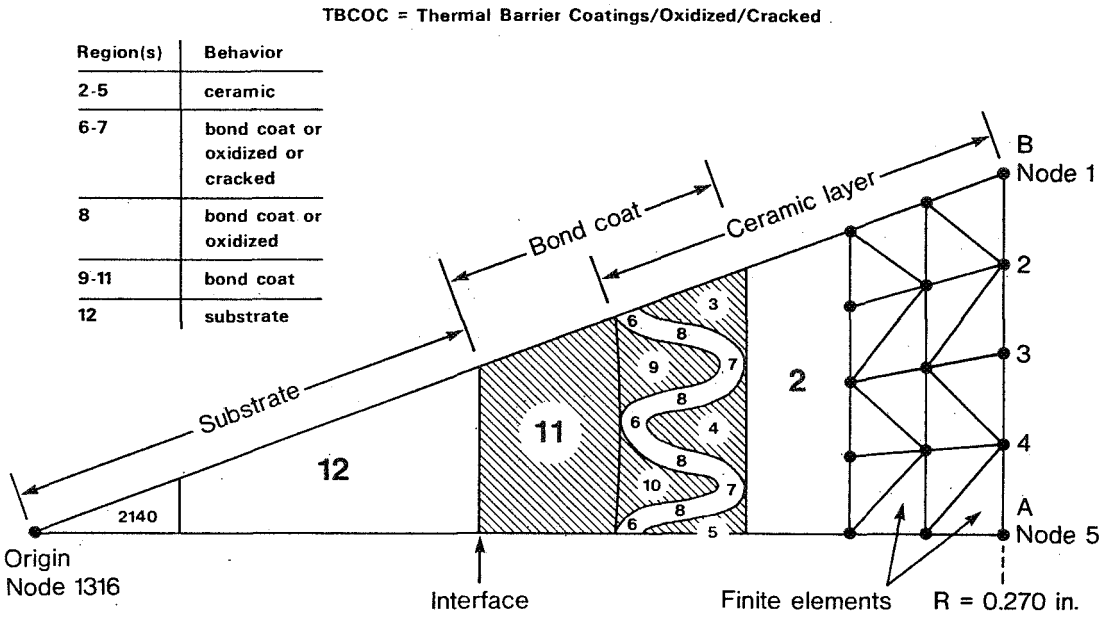

FIGURE 6. OVERVIEW OF THE ADVANCED TBCOC MODEL

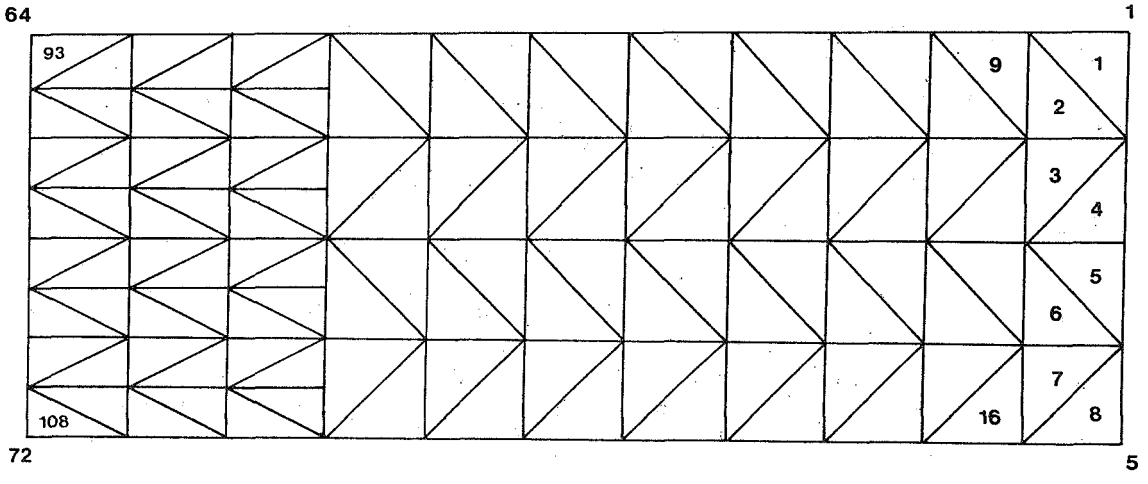

FIGURE 7. TBCOC MODEL (PART 1)

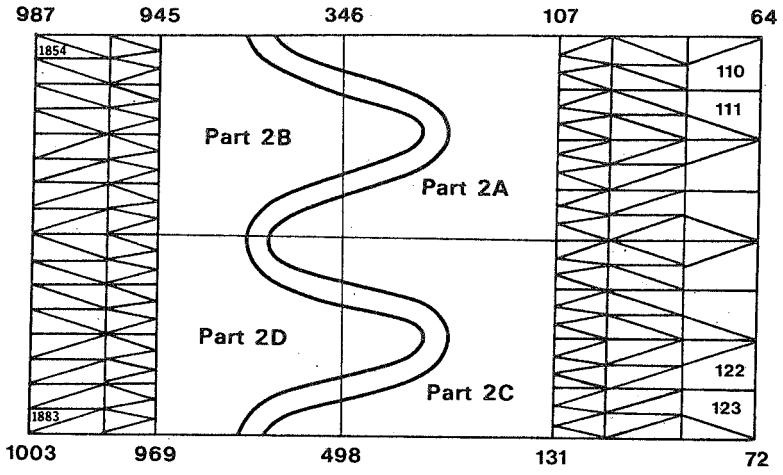

FIGURE 8. TBCOC MODEL (PART 2)

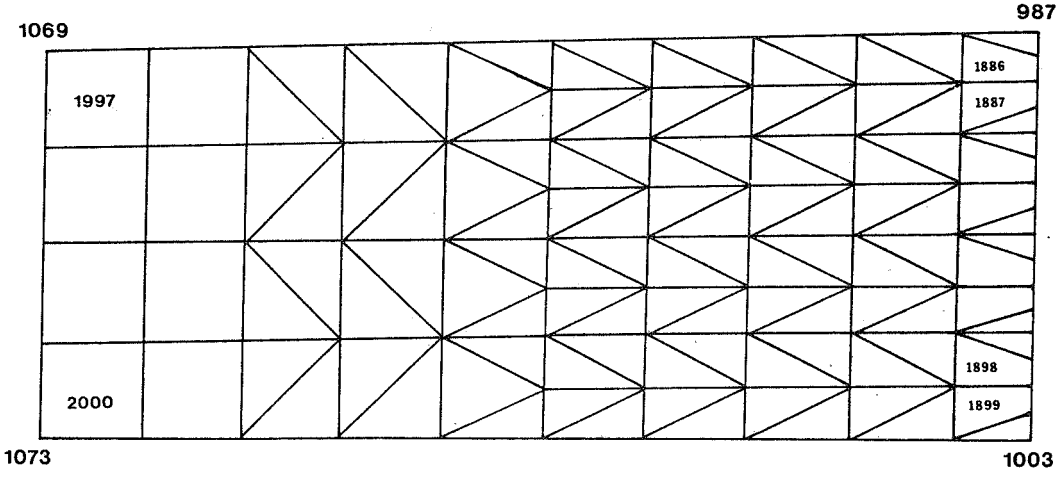

FIGURE 9. TBCOC MODEL (PART 3)

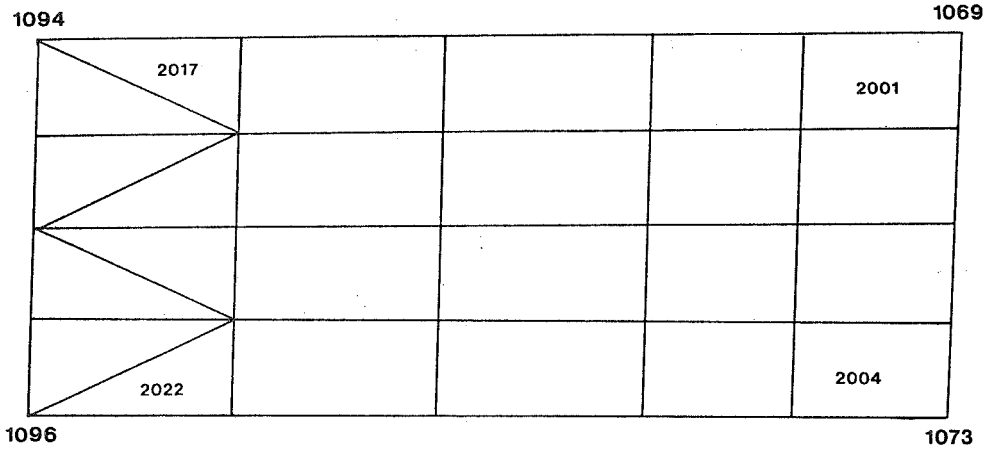

FIGURE 10. TBCOC MODEL (PART 4)

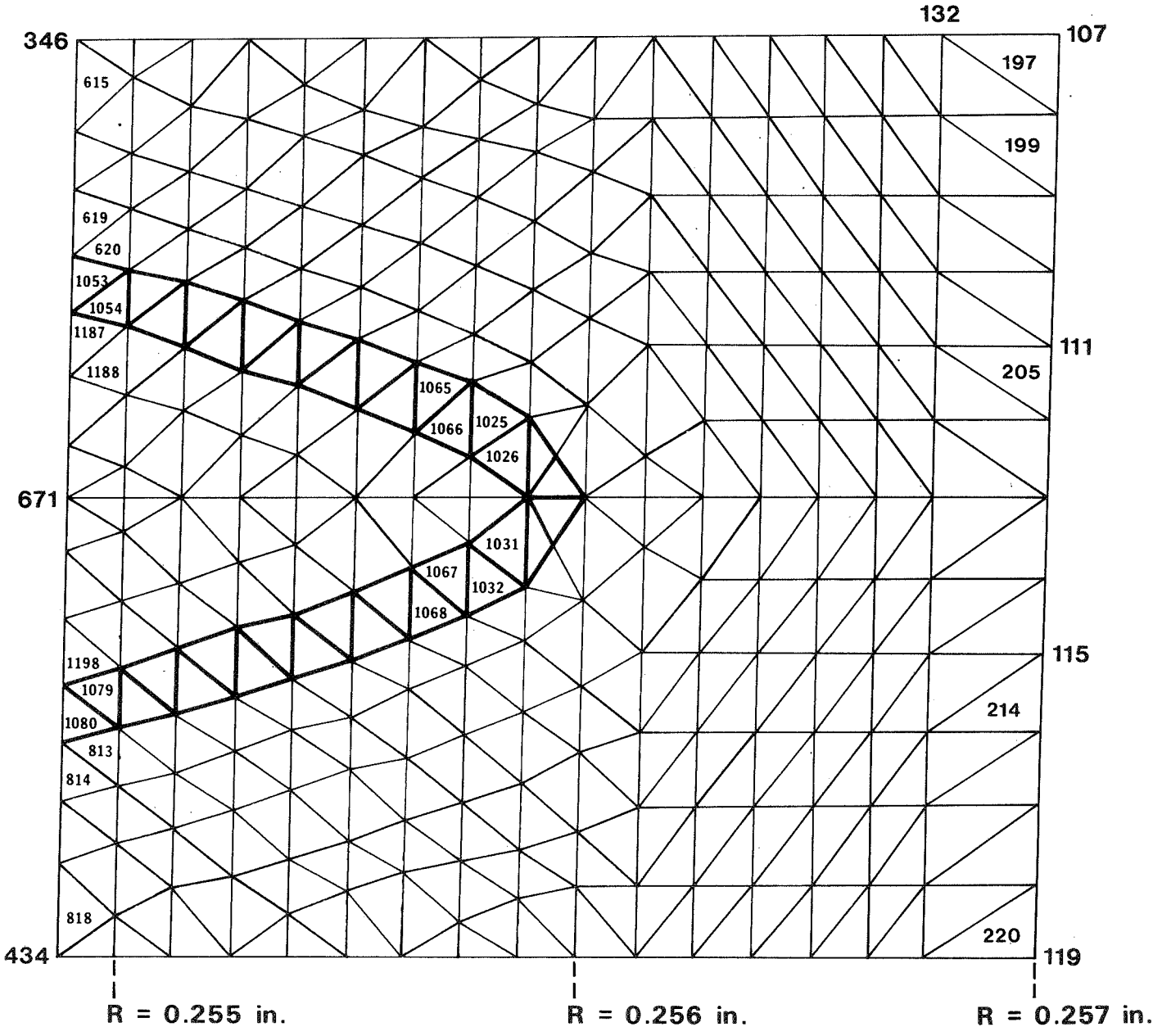

FIGURE 11. FINITE ELEMENT DETAILS (PART 2A)

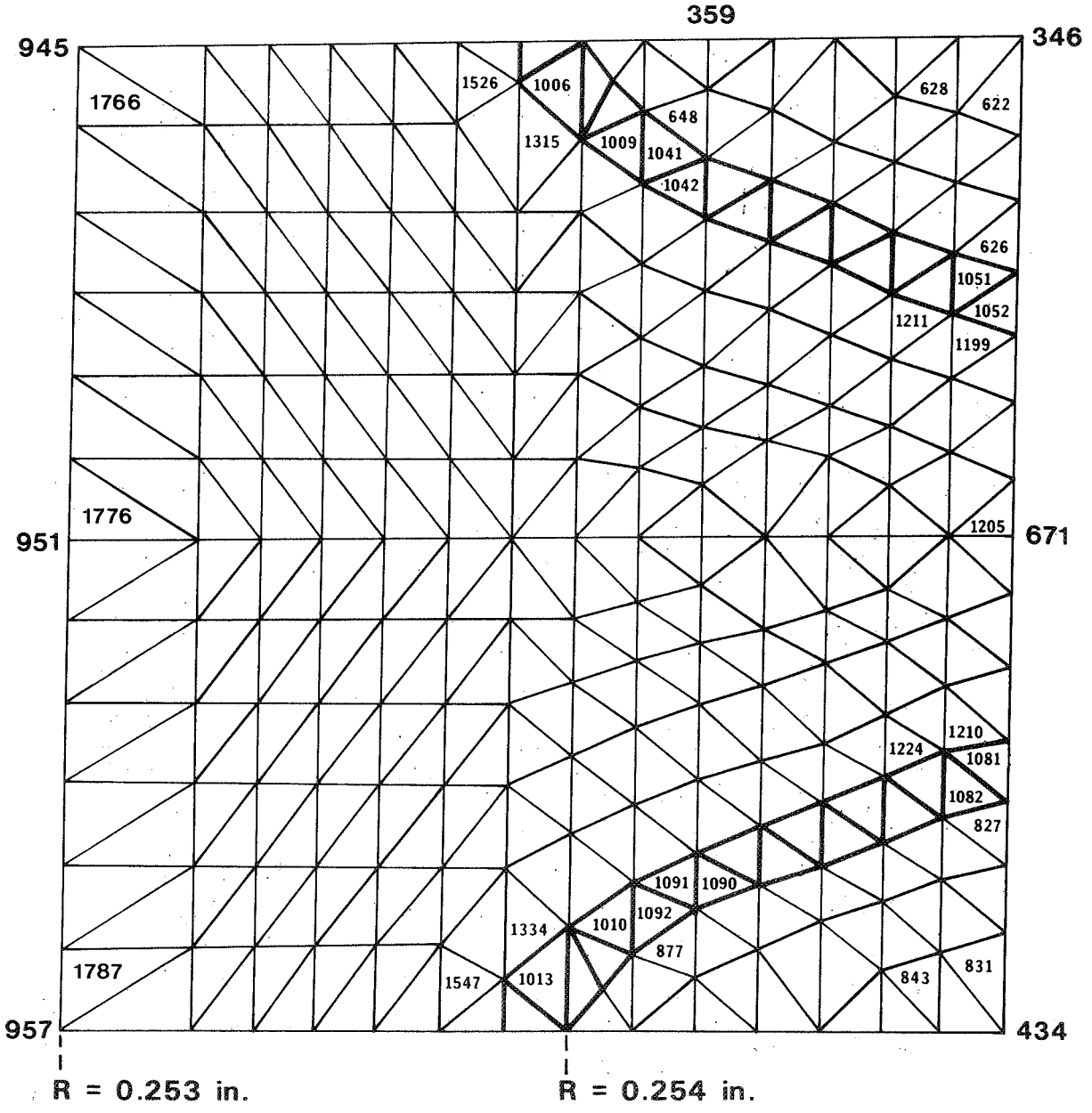

FIGURE 12. FINITE ELEMENT DETAILS (PART 2B)

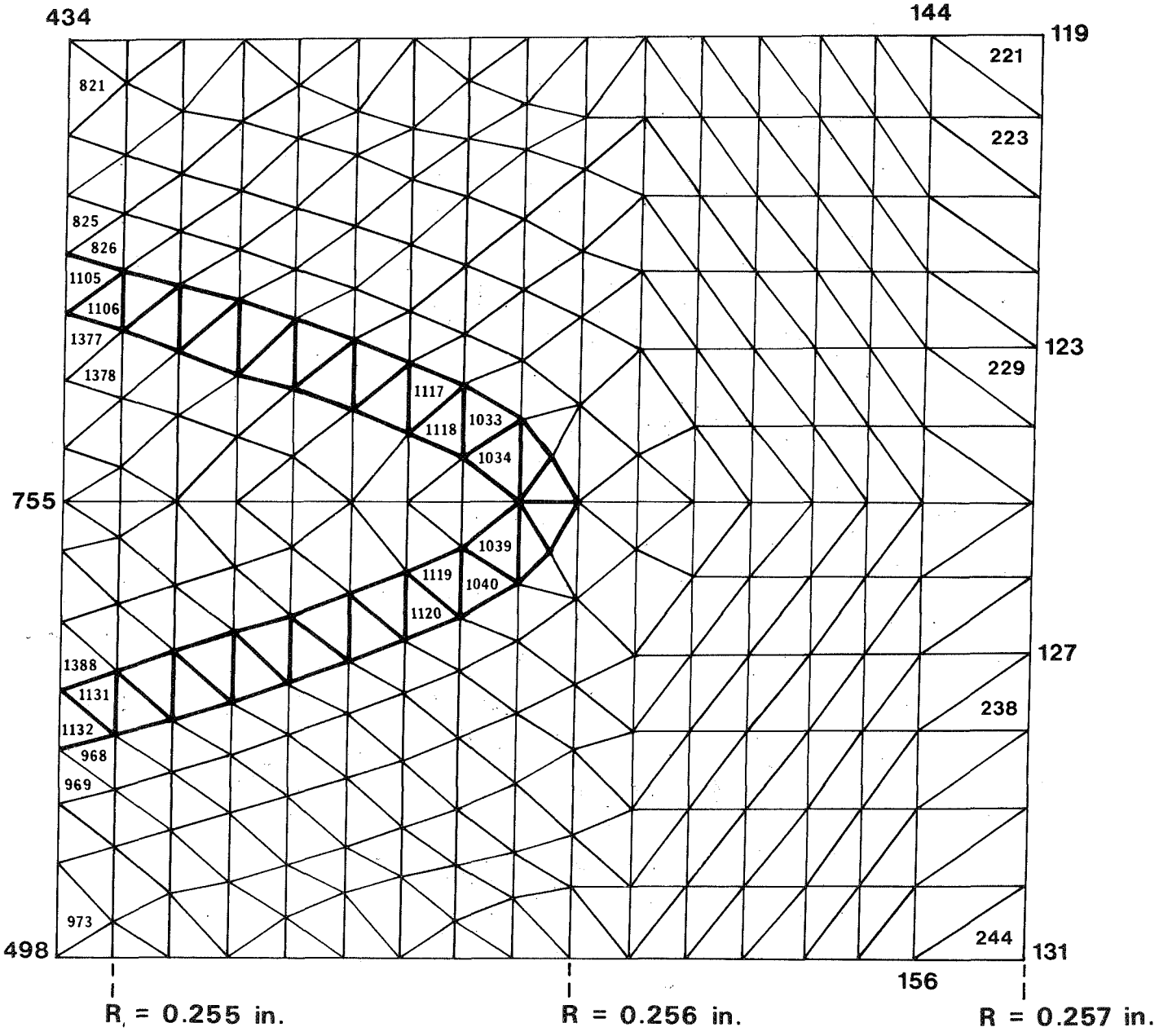

FIGURE 13. FINITE ELEMENT DETAILS (PART 2C)

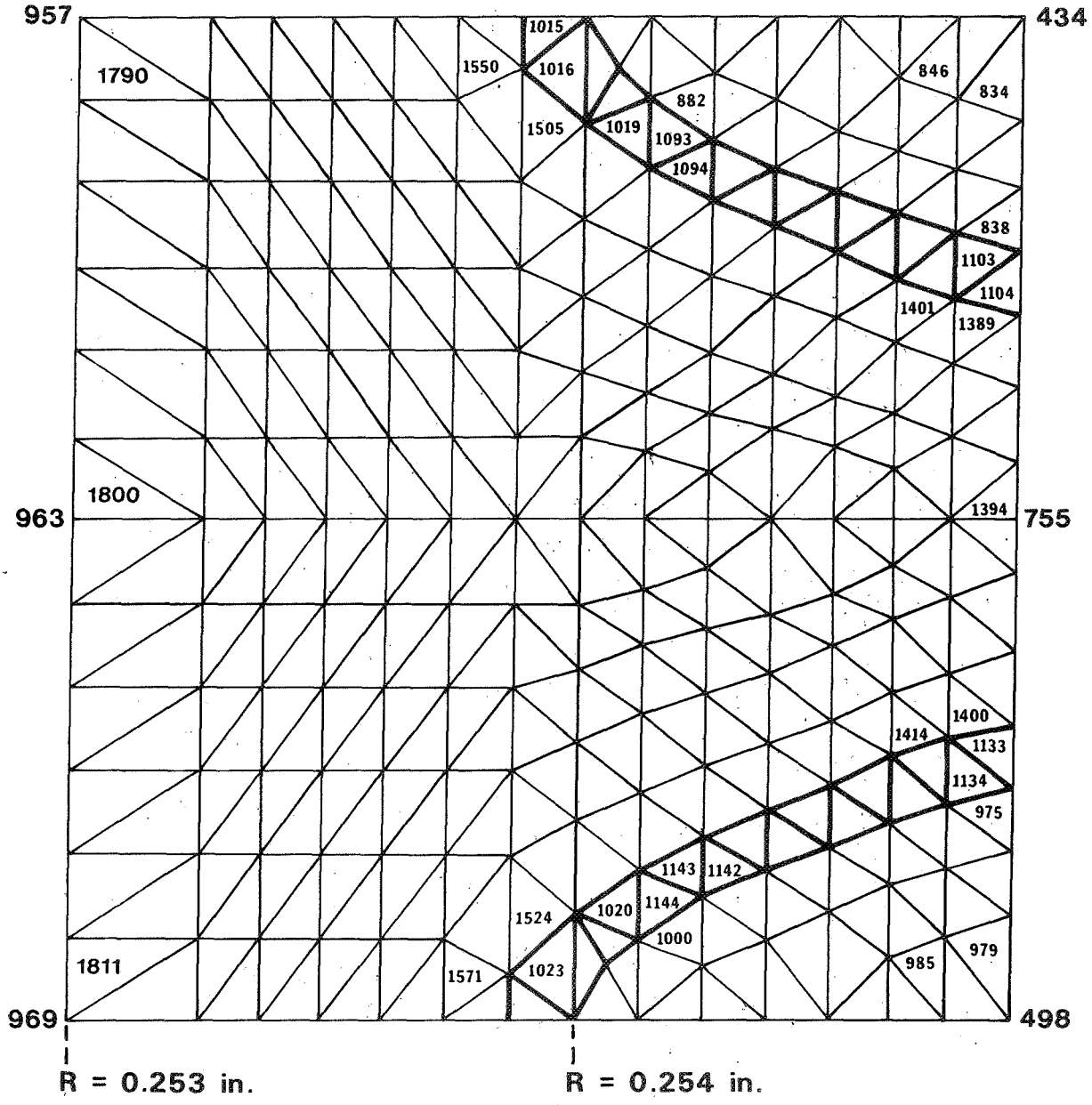

FIGURE 14. FINITE ELEMENT DETAILS (PART 2D)

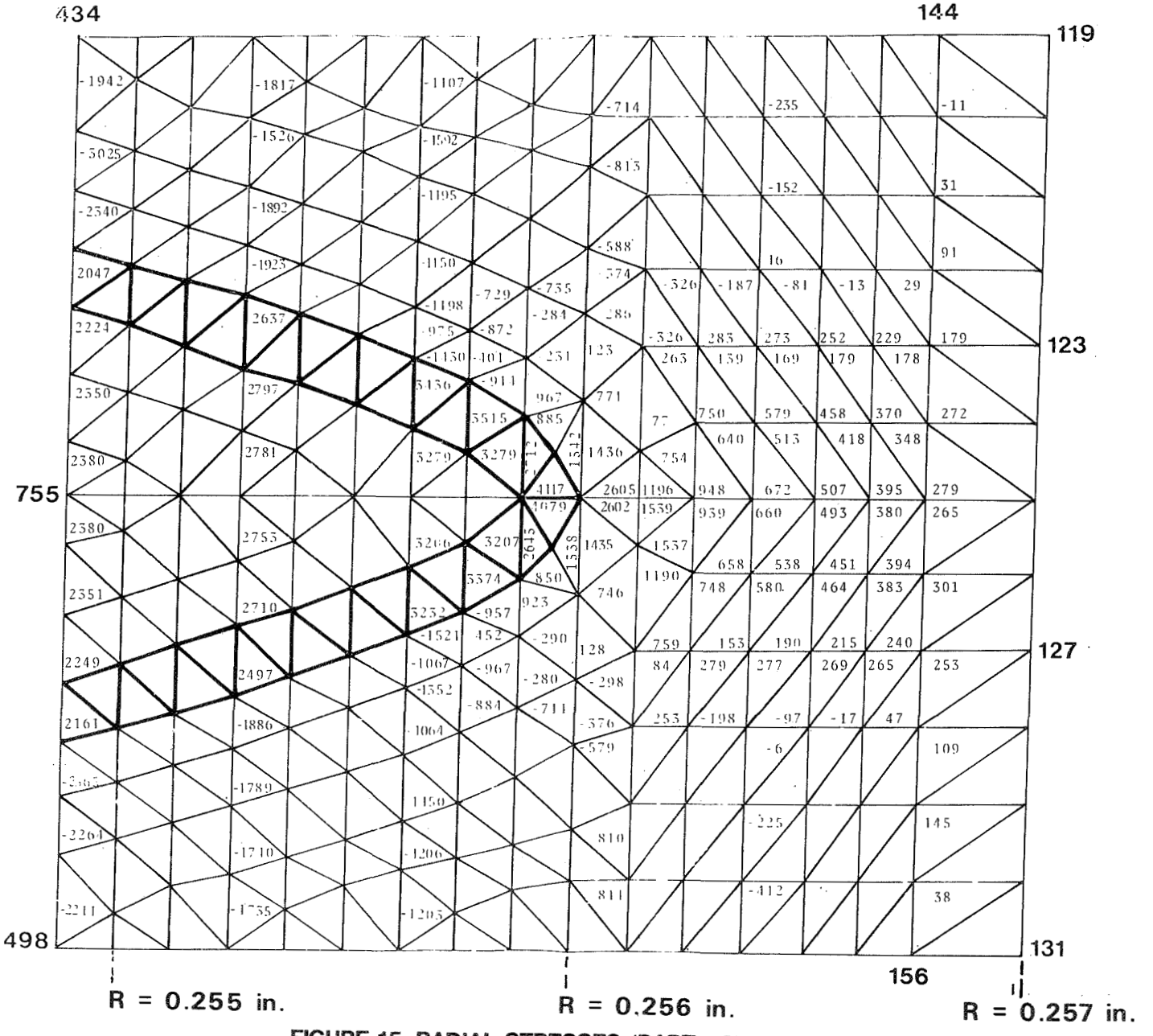

FIGURE 15. RADIAL STRESSES (PART 2C) IN PSI

ORIGINAL PAGE IS
OF POOR QUALITY

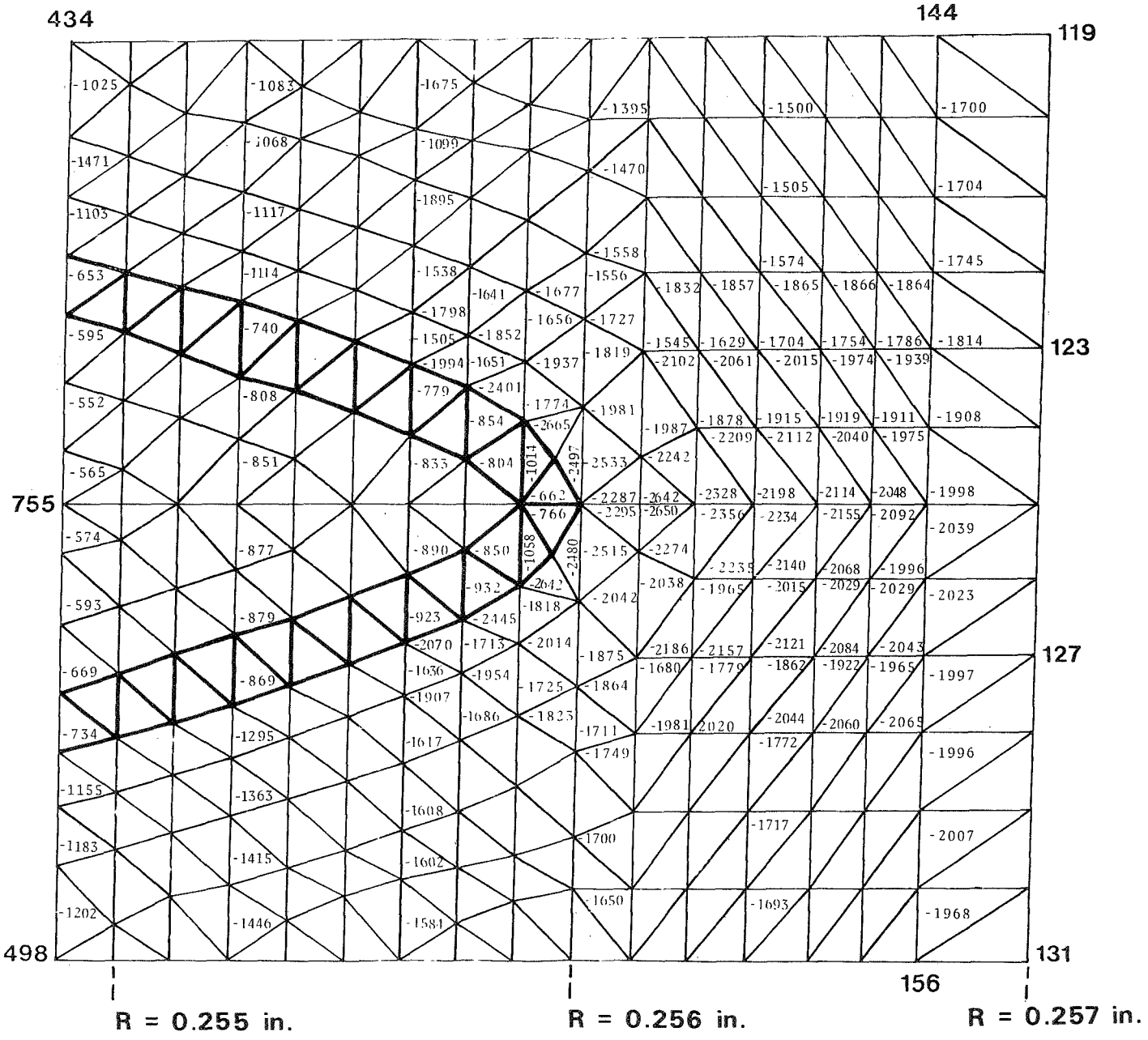

FIGURE 16. TANGENTIAL STRESSES (PART 2C) IN PSI

ORIGINAL PAGE IS
OF POOR QUALITY

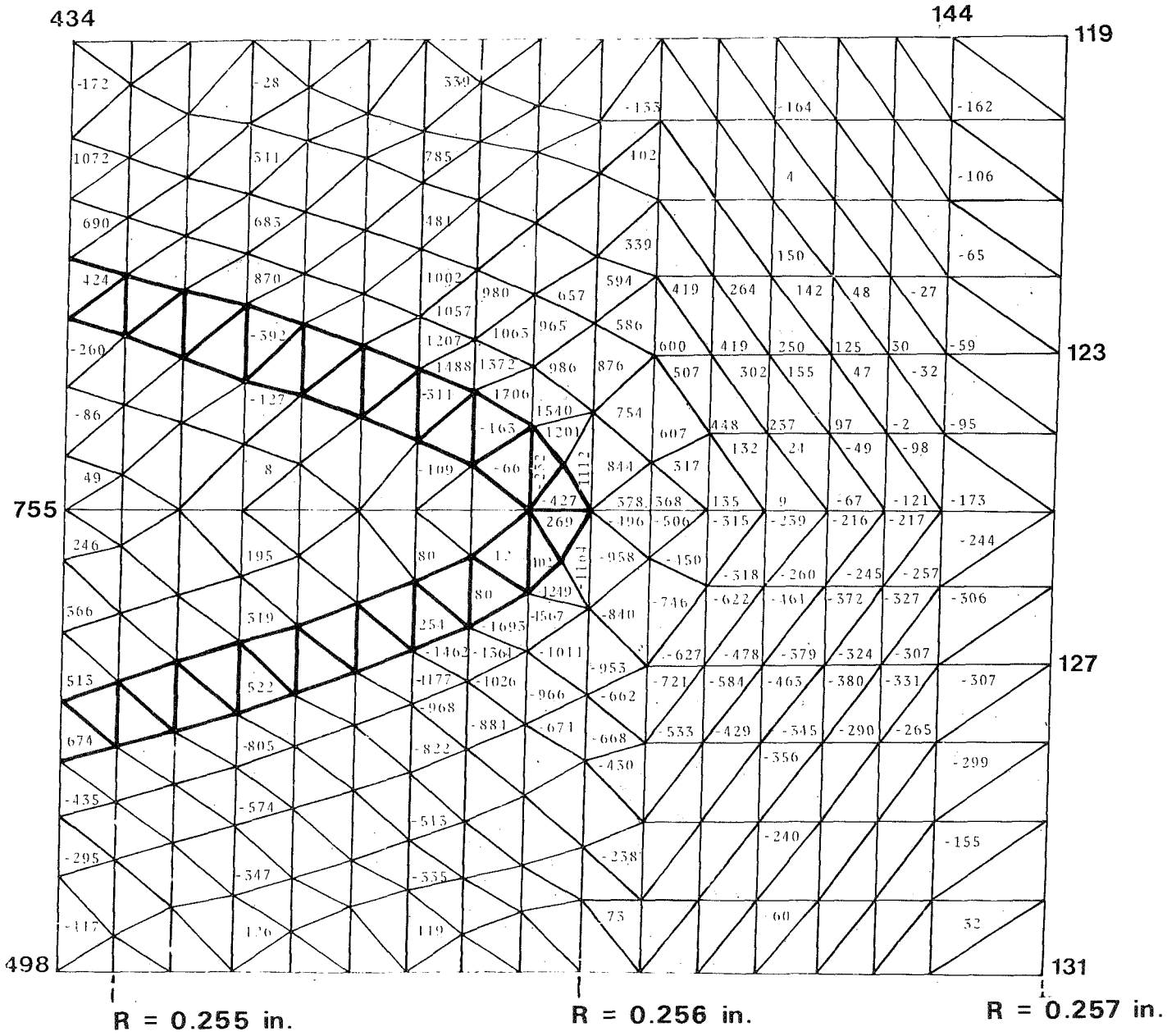

FIGURE 17. SHEARING STRESSES (PART 2C) IN PSI

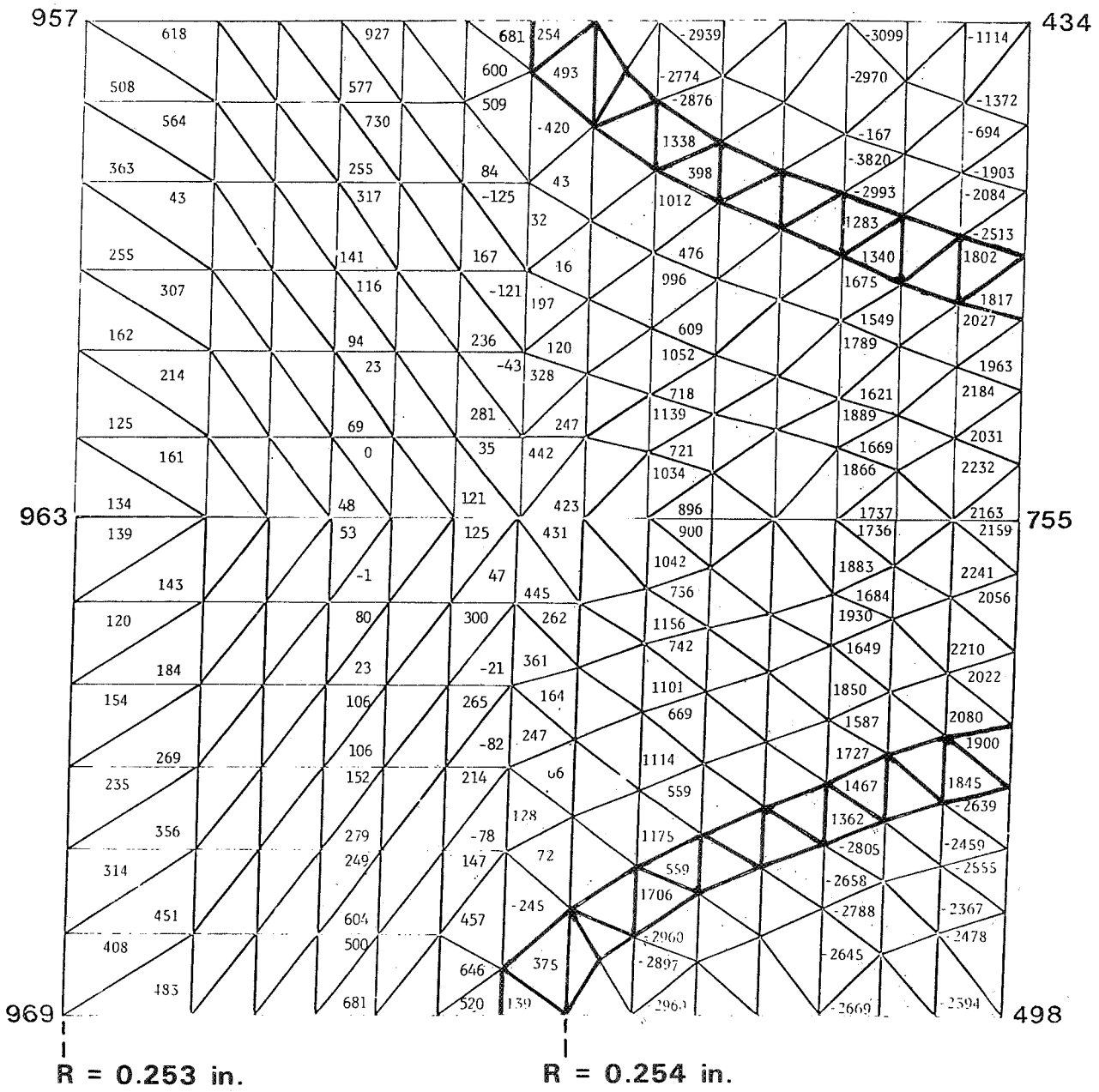

FIGURE 18. RADIAL STRESSES (PART 2D) IN PSI

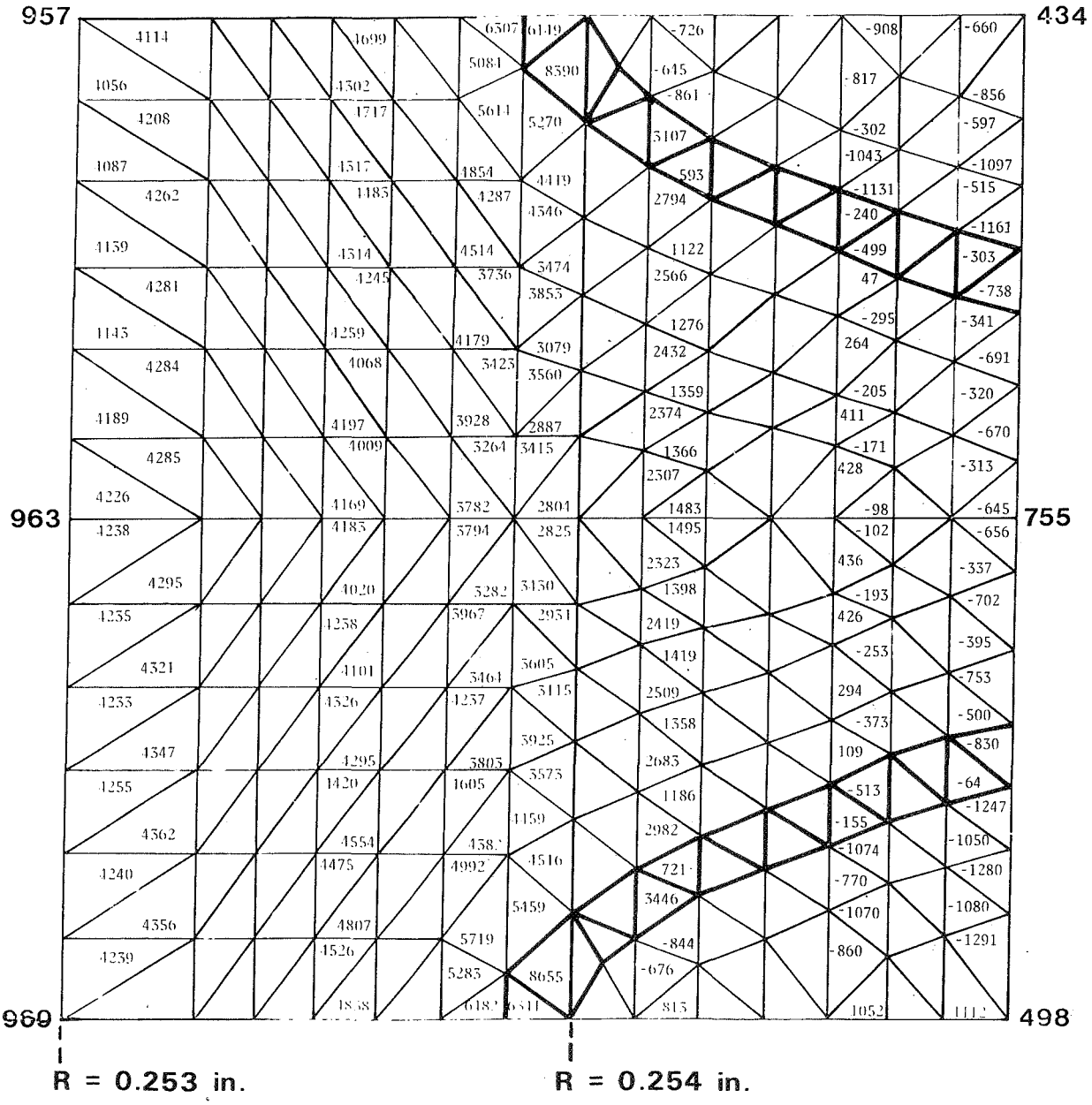

FIGURE 19. TANGENTIAL STRESSES (PART 2D) IN PSI

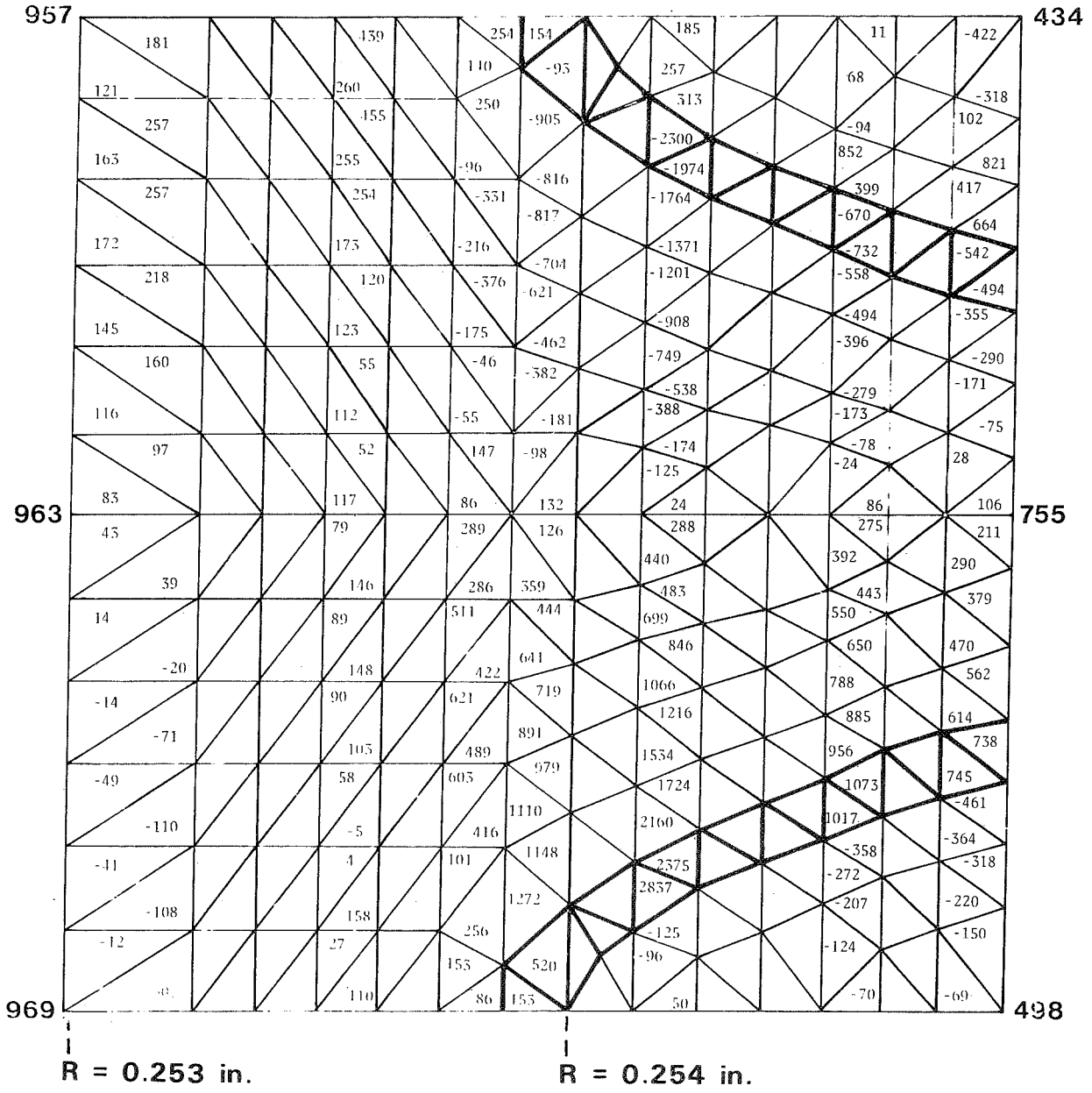

FIGURE 20. SHEARING STRESSES (PART 2D) IN PSI

EXAMINATION OF COATING FAILURE BY ACOUSTIC EMISSION*

Christopher C. Berndt
Cleveland State University
Cleveland, Ohio 44115

Coatings of NiCrAlY bond coat with a zirconia - 12 wt % yttria overlay were applied to disc-shaped specimens of U-700 alloy. A waveguide of 1-mm-diameter platinum was TIG welded to the specimen and allowed it to be suspended in a tubular furnace. The specimen was thermally cycled to 1150 °C, and the acoustic emission (AE) monitored. The weight gain per thermal cycle was also measured.

A computer system based on an IBM-XT microcomputer was used extensively to acquire the AE data with respect to temperature. This system also controlled the temperature by using a PD software loop. Several different types of AE analyses were carried out.

A major feature of these tests, not addressed by previous work in this area, was that the coatings covered 100 percent of the specimen and also that the AE was amplified at two different levels. It is believed that this later feature allows a qualitative appraisal of the relative number of cracks per AE event and also the relative size of cracks per AE event.

The difference in AE counts between the two channels is proportional to the number of cracks per AE event, and this parameter may be thought of as the "crack density." The ratio of the AE count differrence to the AE count magnitude of one channel is inversely proportional to the "crack growth." Both of these parameters allow the crack distribution and crack growth within each specimen to be qualitatively followed during the thermal cycling operation.

Recent results which used the above principles will be presented. It is shown that microcracking gave rise to a large amount of AE. However, the coating still survived more thermal cycles than a coating which exhibited macrocracking events. Data of this nature will be presented and the results discussed.

*Work done under NASA Cooperative Agreement NCC 3-27.

AIM

- TO STUDY THERMALLY INDUCED FAILURE PROCESSES EXPERIENCED BY THERMAL BARRIER COATINGS.

- TO ANALYSE THE FAILURE PROCESSES WITHIN COATINGS - i.e.,
  - WHAT IS THE SIZE OF ANY CRACKS?
  - HOW MANY CRACKS ARE THERE?

- TO FOCUS ON THE MICRO-MECHANICAL PROPERTIES OF COATINGS AND HOW THESE MAY VARY FROM COATING-TO-COATING.

Figure 1.

PREVIOUS WORK IN THIS RESEARCH AREA

1. D. ALMOND, M. MOGHISI AND H. REITER, " THE ACOUSTIC EMISSION TESTING OF PLASMA-SPRAYED COATINGS", THIN SOLID FILMS 108 (1983) 439-447.

2. N. RAVI SHANKAR et al., "ACOUSTIC EMISSION FROM THERMALLY CYCLED PLASMA-SPRAYED OXIDES", AM. CER. SOC. BULL. 62 NO. 5 (1983) 614-619.

3. C. C. BERNDT AND H. HERMAN, "FAILURE DURING THERMAL CYCLING OF PLASMA-SPRAYED THERMAL BARRIER COATINGS", THIN SOLID FILMS 108 (1983) 427-437.

4. C. C. BERNDT AND H. HERMAN, "FAILURE ANALYSIS OF PLASMA-SPRAYED THERMAL BARRIER COATINGS", THIN SOLID FILMS, 119 (1984) 173-184.

5. C. C. BERNDT, "ACOUSTIC EMISSION EVALUATION OF PLASMA-SPRAYED THERMAL BARRIER COATINGS", ASME J. ENG. FOR GAS TURBINES, 107 (1985) 142-146.

Figure 2.

SCHEMATIC OF EXPERIMENTAL DETAILS

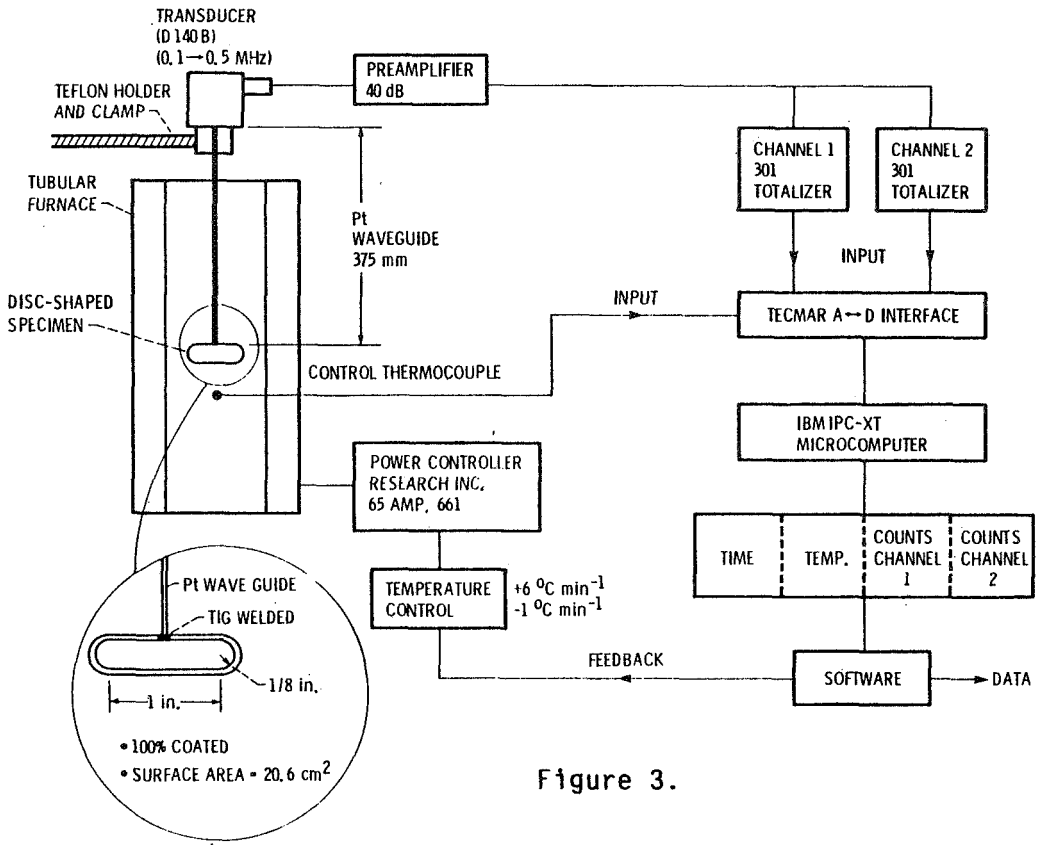

Figure 3.

SUMMARY OF EXPERIMENTAL DETAILS

1. A CLOSED LOOP DATA ACQUISITION AND CONTROL SYSTEM HAS BEEN BUILT.
2. SOFTWARE FOR DATA ACQUISITION AND ANALYSIS HAS BEEN DEVELOPED.
3. SPECIMENS PREPARED -

   BOND COAT OF Ni-16Cr-6Al-0.15Y (0.005 in.)

   CERAMIC COATING OF ZrO_2-12 wt.% Y_2O_3 (0.015 in.)

COATINGS EXAMINED

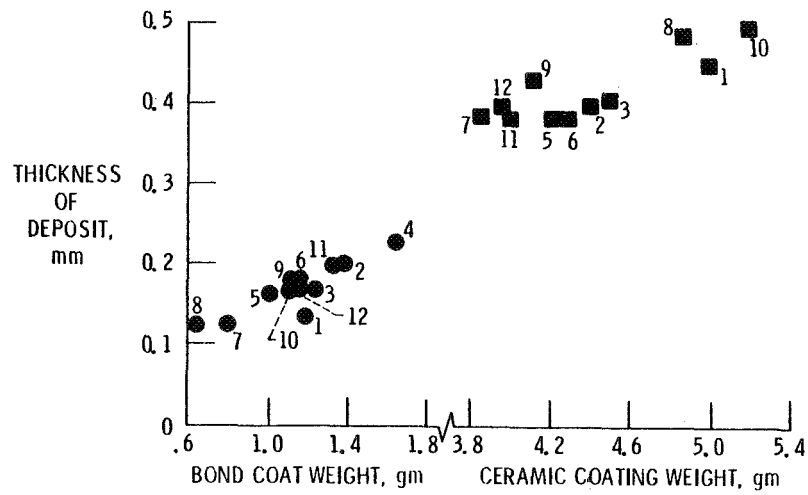

Figure 4.

THE NATURE OF THE AE DATA

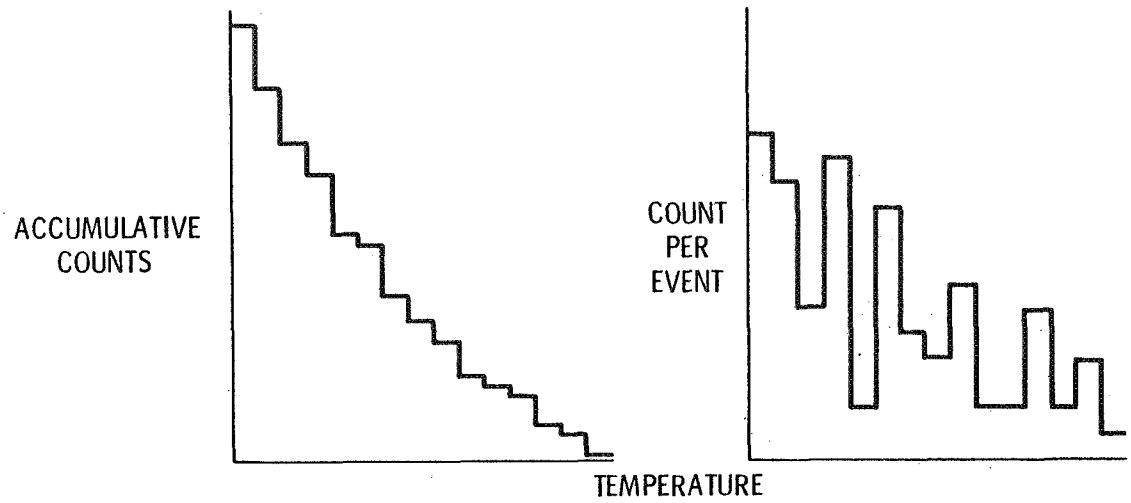

AT LEAST TWO TYPES OF DISTRIBUTIONS

1. SYSTEMATIC → FROM "CONTINUOUS" EMISSIONS.
2. STOCHASTIC → FROM "BURST" EMISSIONS.

Figure 5.

METHOD 1 OF ANALYSIS

DISCOUNT SIGNALS OF A CERTAIN MAGNITUDE AND THUS SET A LOWER BOUND FOR THE BURST EMISSION. CURVE FIT THE REMAINING DATA TO FIND THE SLOPE OF ACCUMULATIVE COUNTS VERSUS TEMPERATURE.

EXAMINE: -

1. HOW THE SLOPE CHANGES WITH RESPECT TO THE BOUND LEVEL AND THERMAL CYCLE.

i.e.; $\left[\frac{\partial\,(\Sigma\ \text{COUNTS})}{\partial T}\right]_{\text{BOUND LEVEL}}$ VERSUS THERMAL CYCLE NUMBER

$\left[\frac{\partial\,(\Sigma\ \text{COUNTS})}{\partial T}\right]_{\text{THERMAL CYCLE NUMBER}}$ VERSUS BOUND LEVEL

Figure 6.

ACCUMULATIVE COUNTS VERSUS TEMPERATURE ANALYSIS

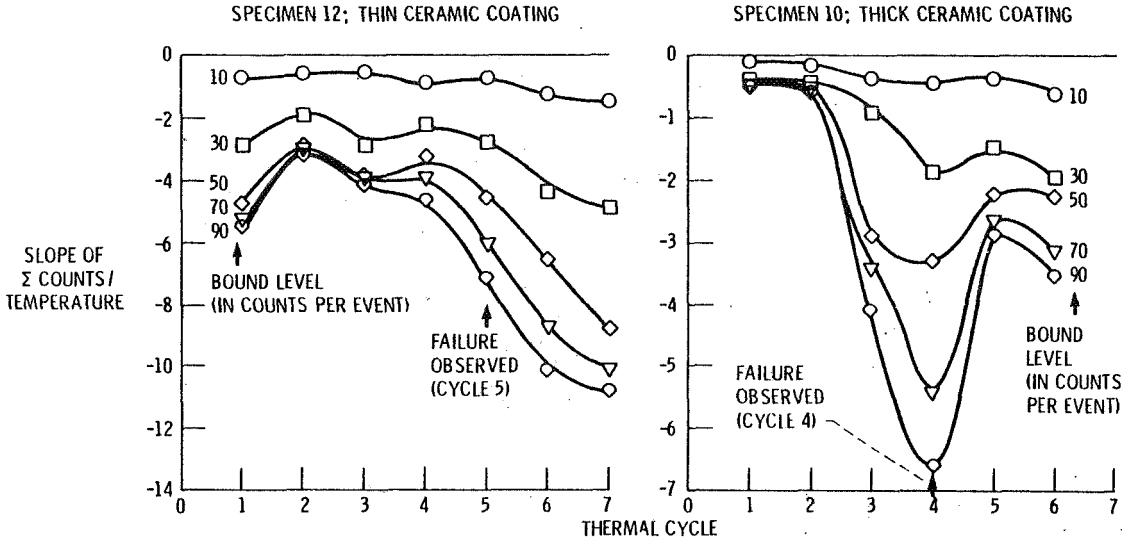

Figure 7.

THEORY OF AE

- CRACKING PROCESSES GENERATE ELASTIC WAVES i.e., MOVEMENT OF ATOMS.
- THIS ELASTIC WAVE DISTORTS A PIEZOELECTRIC MATERIAL AND GIVES RISE TO AN ELECTRICAL SIGNAL.

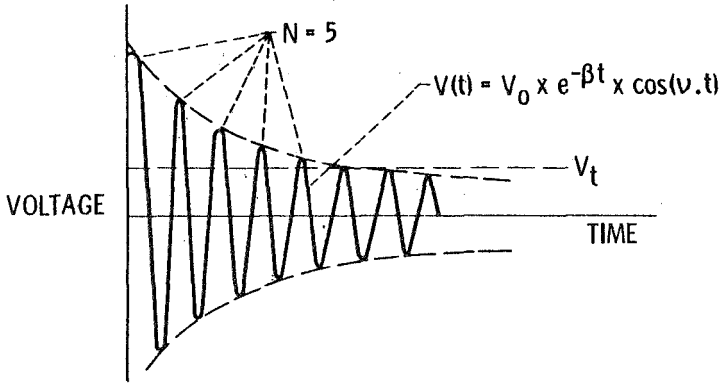

- V(t) - VOLTAGE AS A FUNCTION OF TIME
- V_0 - INITIAL VOLTAGE
- β - DAMPING CONSTANT
- t - TIME
- ν - RESONANT FREQUENCY OF THE TRANSDUCER (= 140 KHz)
- V_t - THRESHOLD VOLTAGE (= 1 V)
- N - NUMBER OF COUNTS ABOVE V_t

Figure 8.

AE DEFINITIONS AND EQUATIONS

$$\beta = \frac{\text{LOGARITHMIC DECREMENT}}{\text{PERIOD OF OSCILLATION}} = \frac{\gamma}{T}$$

$$\gamma = \ln\left(\frac{V_{n+1}}{V_n}\right)$$

RESULT IS: -

$$V_{(t)} = V_0 + e^{(-\gamma.\nu.t)} \times \cos(\nu t)$$

ALSO: -

$$N = \frac{1}{\gamma} \times \ln\left(\frac{V_0}{V_t}\right)$$

REMEMBER THAT AE IS THE SUPERPOSITION OF CONTINUOUS WAVES THEREFORE BEWARE OF CONFOUNDING AE SIGNALS. DEADTIME OF THE TRANSDUCER IS ABOUT 100us. DIGITAL UPDATING OF THE APPARATUS IS 0.3us THEREFORE NO ALIASING OF THE COUNTS PER EVENT OCCURS.

Figure 9.

METHOD 2 OF ANALYSIS

EXAMINE THE ACCUMULATIVE COUNTS OF BOTH AE CHANNELS WITH RESPECT TO THERMAL CYCLING.

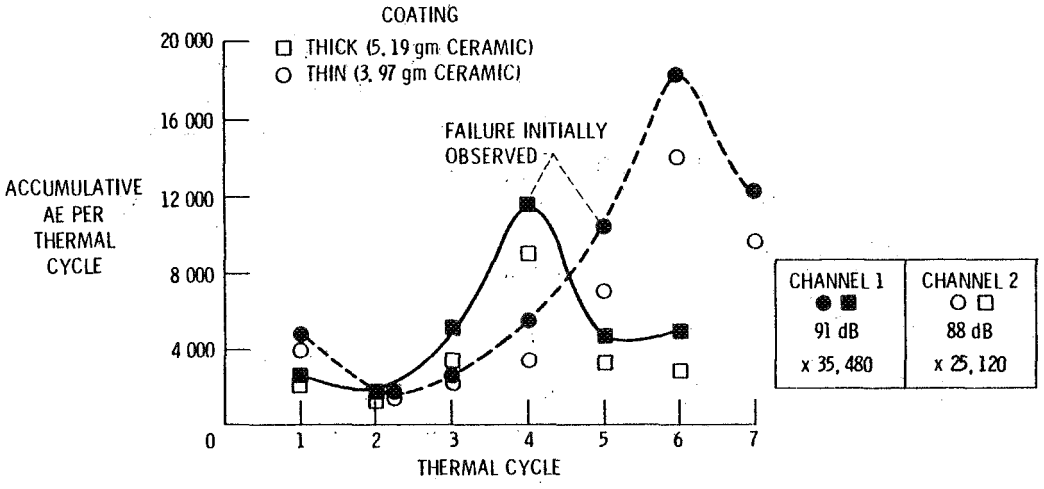

1. THE ACCUMULATIVE AE RESPONSE AFTER FAILURE IS DIFFERENT FOR BOTH SAMPLES. THE NUMBER OF COUNTS MAY EITHER INCREASE OR DECREASE AFTER VISUAL FAILURE.
2. THE DIFFERENCES BETWEEN THE CHANNELS CHANGE FOR EACH COATING.

Figure 10.

INFORMATION DERIVED FROM EXAMINING DIFFERENT AMPLIFICATIONS OF THE SAME SIGNAL

EXAMINE THE NUMBER OF PEAKS PER EVENT.

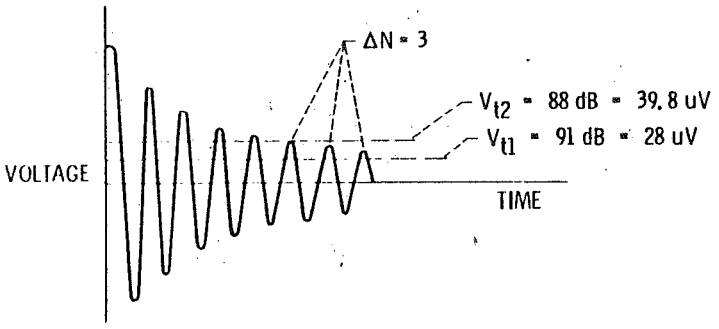

- MORE PEAKS WILL BE COUNTED AT THE LOWER THRESHOLD (i.e., HIGHER AMPLIFICATION).
- THE COUNT DIFFERENCE BETWEEN CHANNELS IS AN INDICATION OF THE RELATIVE NUMBER OF EVENTS.

Figure 11.

EXAMINATION OF COUNT DIFFERENCE DATA

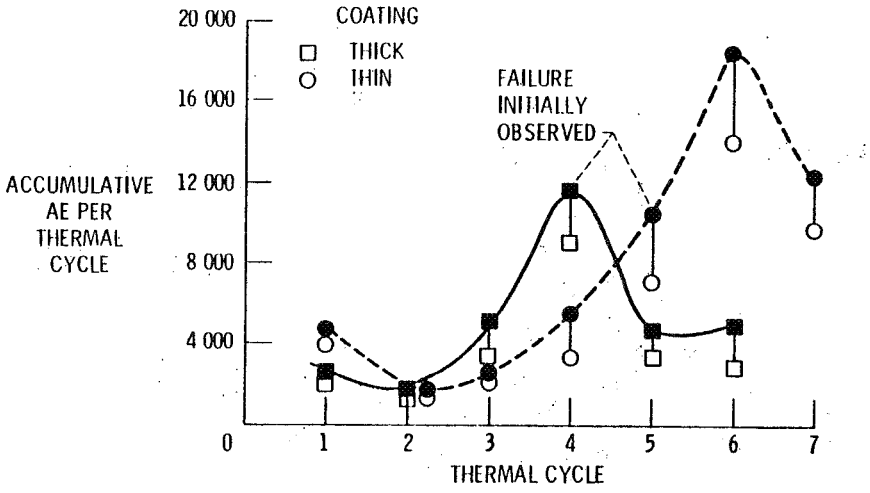

IMPLICATION

1. ΔN α NUMBER OF CRACKS
2. $\frac{\text{NORMALIZED}}{\Delta N} \alpha \frac{1}{\text{SIZE OF CRACK}}$

Figure 12.

A SIMPLE EXAMPLE

CONSIDER THAT ΔN FOR AN EVENT IS 3 COUNTS

CRACK TYPE	COUNTS CHANNEL 1	COUNTS CHANNEL 2	ΔN	$\frac{\Delta N}{N_1}$
SMALL	10	7	3	0.30
LARGE	50	47	3	.06
5 SMALL	50	35	15	.30
5 LARGE	250	235	15	.06

ASSESSMENT OF NUMBER OF EVENTS

ASSESSMENT OF CRACK SIZE

Figure 13.

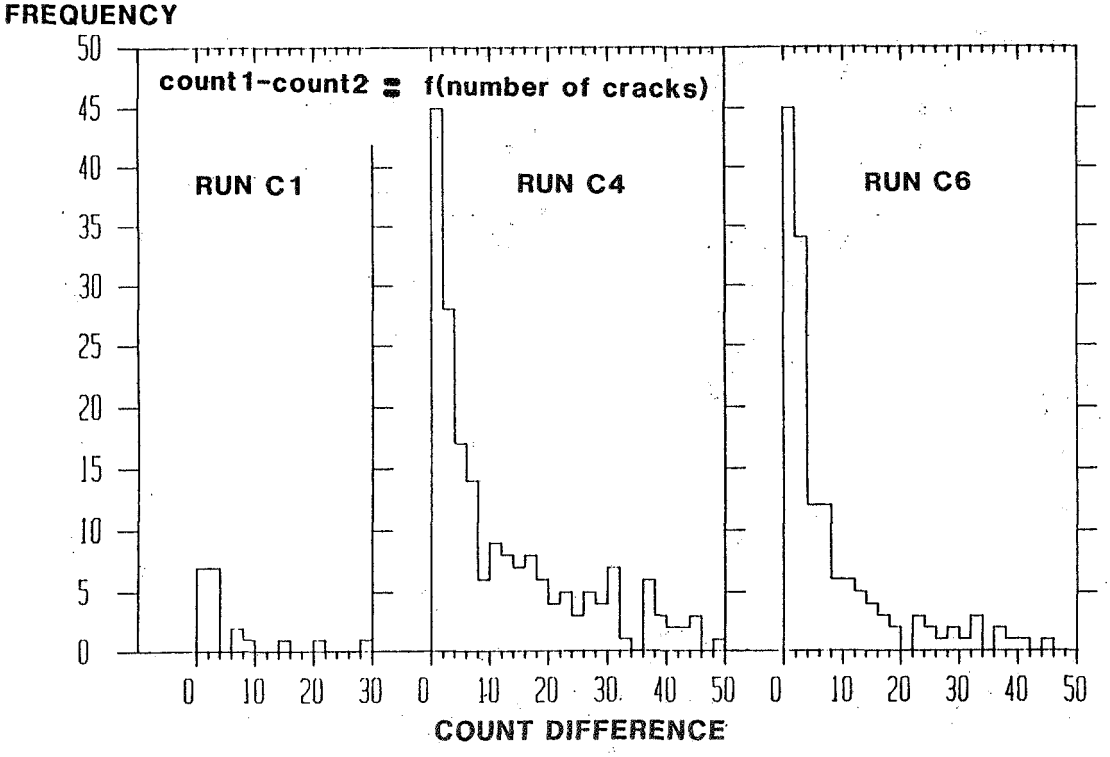

Figure 14.

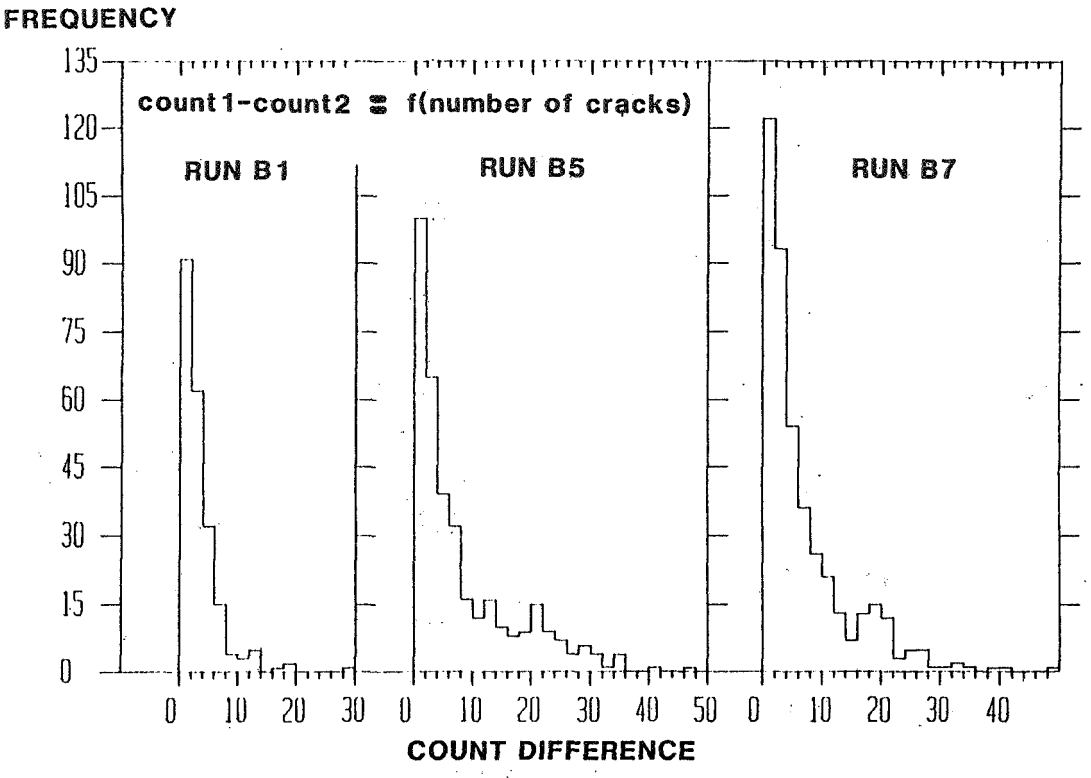

Figure 15.

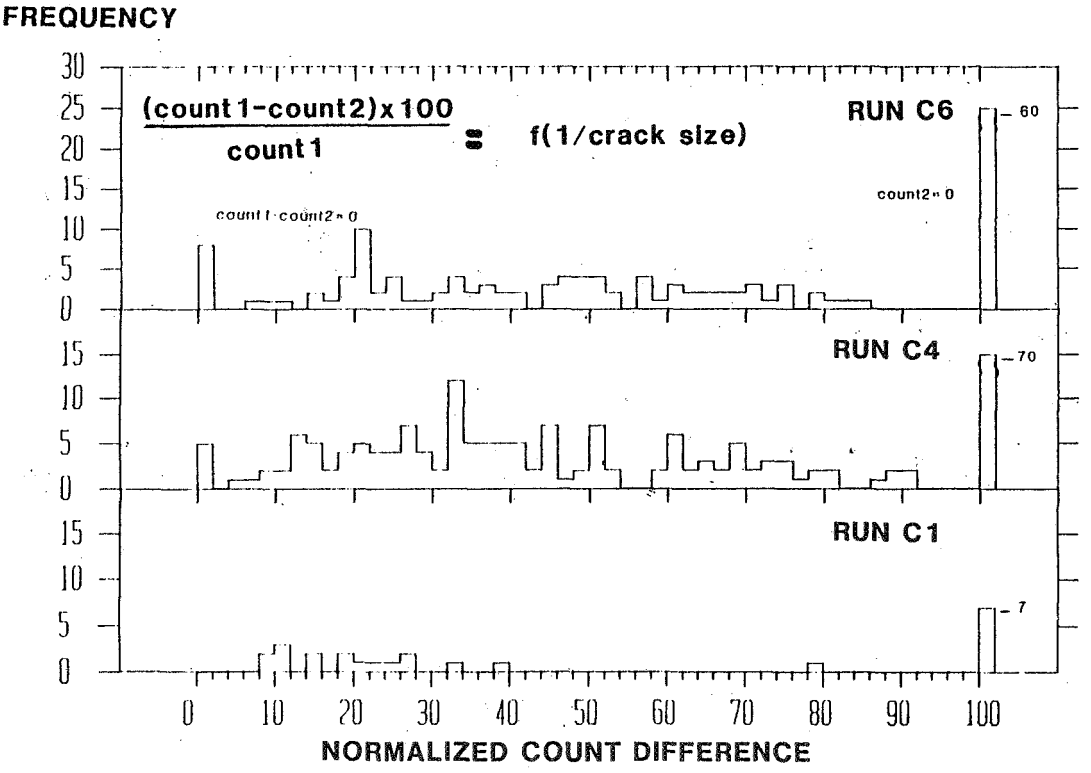

Figure 16.

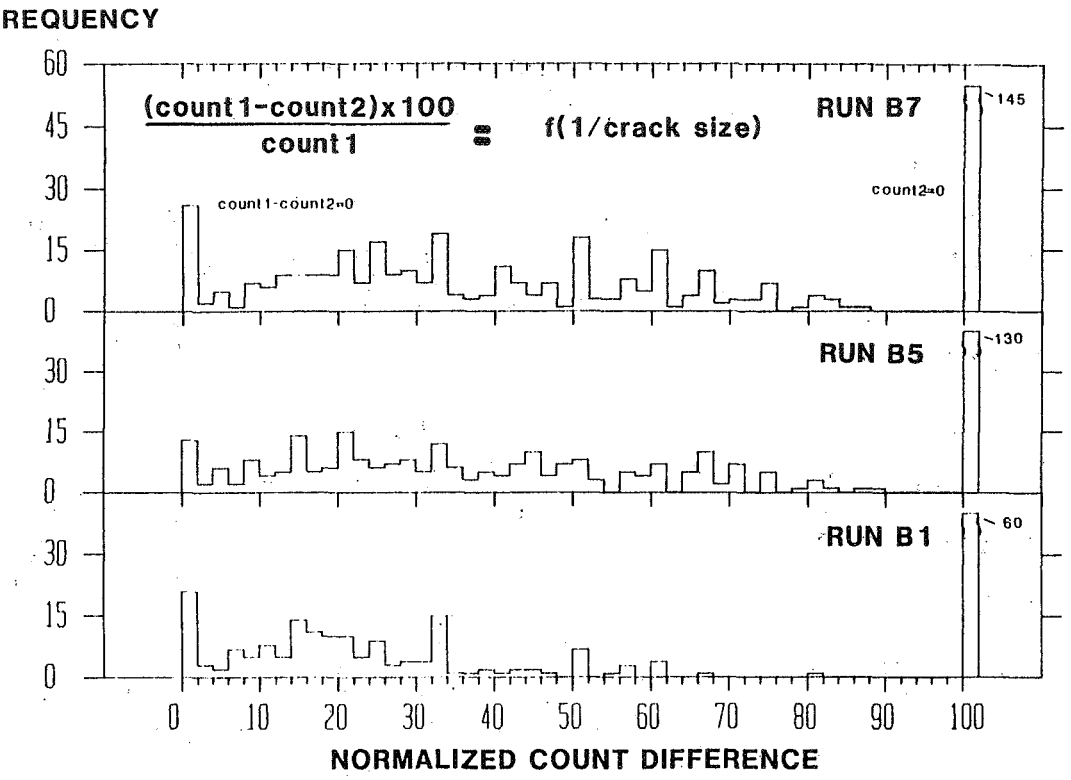

Figure 17.

SUMMARY OF "BURST EMISSION ANALYSIS"

1. The slope of Σ counts/temperature becomes more negative with respect to thermal cycle number up to the cycle where failure was first observed.

2. The sample which exhibited the least total number of AE counts also showed the greatest influence of "bound level" on " Σ counts/temperature".

3. AE burst events greater than 30 to 50 counts per event gave rise to a rapid increase in the observed accumulative AE.

4. The effect of bound level on Σ counts/temperature can be observed prior to visible failure.

Figure 18.

SUMMARY OF COUNT DIFFERENCE DATA

1. There is a wide distribution (from 1 to about 50) for the "number of cracks" which most commonly occur per AE event.

2. The crack distributions vary from cycle-to-cycle and from specimen-to-specimen.

3. The distribution for the number of cracks is greater for run C than for run B.

Figure 19.

SUMMARY OF NORMALIZED COUNT DIFFERENCE DATA

1. The distribution of the (1/crack size) function spreads on increased thermal cycling. This represents the growth (and nucleation) of cracks.

2. Generally, on thermal cycling, either;
   (i) the number of small cracks increases, or,
   (ii) the minimum growth increment of cracking decreases.

3. There is an increase in the AE activity of large cracks.

Figure 20.

EVALUATION OF THE CRACK DENSITY FUNCTION WITH RESPECT TO THE ACCUMULATIVE AE COUNTS

1. The crack density function (CDF) is not dependent on the accumulative AE counts. i.e.; different crack distributions may give rise to the same AE count for different samples.

2. An increase in the AE count will also show an increase in the CDF (for any one sample).

3. Major crack density peaks are observed between different samples and during the thermal cycling of specific samples.

Figure 21.

FINAL SUMMARY

1. AE methods have been found useful in examining the failure processes within plasma-sprayed coatings which are subjected to thermal cycling experiments.

2. A "crack density function" has been derived from the AE of the sample.

3. The CDF is qualitatively related to the crack size and number of cracks within a coating system.

Figure 22.

DETERMINING BONDING, THICKNESS, AND DENSITY VIA THERMAL WAVE IMPEDANCE NDE

D. R. Green
Westinghouse Hanford Company
Richland, Washington 99352

Bonding, density, and thickness of coatings have a vital effect on their performance in many applications. Pioneering development work by the author on thermal wave nondestructive evaluation (NDE) methods during the past 25 years has resulted in an array of useful techniques for performing bonding, density, and thickness measurements in a practical shop environment. The most useful thermal wave methods for this purpose are based on thermal wave surface impedance measurement or scanning. A pulse of heat from either a thermal transducer or a hot gas pulse is projected onto the surface, and the resulting temperature response is analyzed to unfold the bonding, density, and thickness of the coating. An advanced emissivity independent infrared method has been applied to detect the temperature response. These methods have recently been completely computerized and can automatically provide information on coating quality in near real-time using the proper equipment. Complex shapes such as turbine blades can be scanned. Microscopic inhomogeneities such as microstructural differences and small, normal, isolated voids do not cause problems but are seen as slight differences in the bulk thermal properties. Test objects with rough surfaces can be effectively nondestructively evaluated using proper thermal surface impedance methods. No contact with the test object is required, and no couplants or other contaminants are used. Thermal wave NDE might be called a "Wave of the Future", as well as a "Wave at the Past". Recent work done on thermal wave NDE by independent groups in the U.S., as well as abroad, has confirmed the potential of some of these methods for practical coating NDE applications. Some of the basic principles involved, as well as metallographic results illustrating the ability of the thermal wave surface impedance method to detect natural nonbonds under a two-layer thermally sprayed coating, will be presented in this paper.

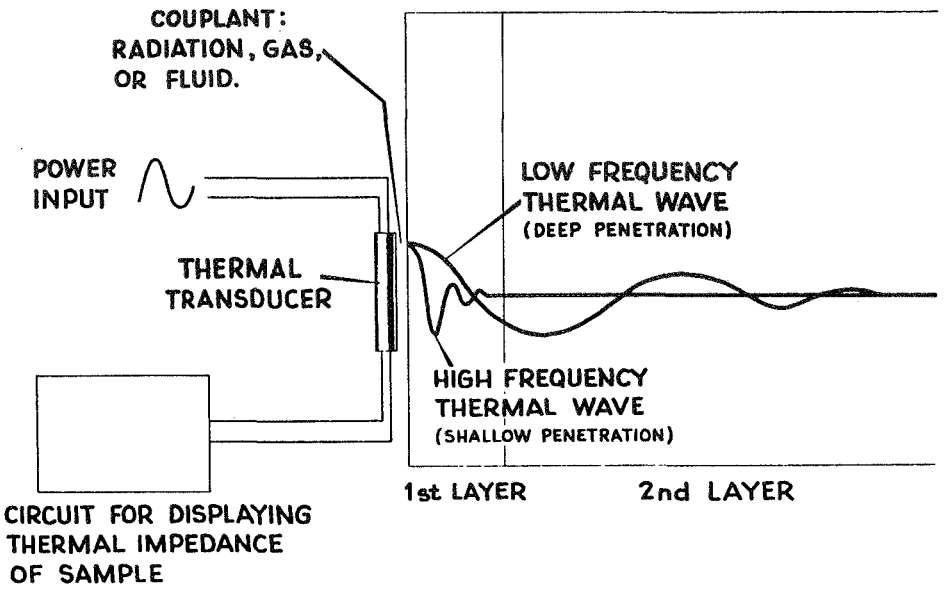

Figure 1.

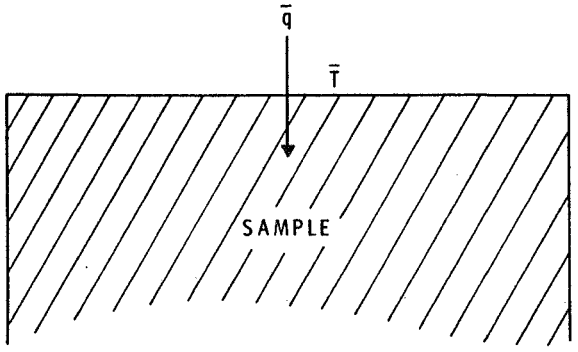

FOR SINUSOIDAL $\bar{q}$ AND $\bar{T}$, THE THERMAL SURFACE IMPEDANCE IS DEFINED AS

$$Z = \left[\frac{\bar{T}}{\bar{q}}\right]_{x=0}$$

Figure 2.

$$\text{Heat Flow, } g = C\, e^{-(1-j)x/\delta} \qquad (1)$$

$$\text{Penetration Depth, } \delta = \sqrt{\frac{K}{\pi f S \rho}} \qquad (2)$$

$$\text{Surface Thermal Impedance, } Z = \left[T/q\right]_{x=0} \qquad (3)$$

Figure 3.

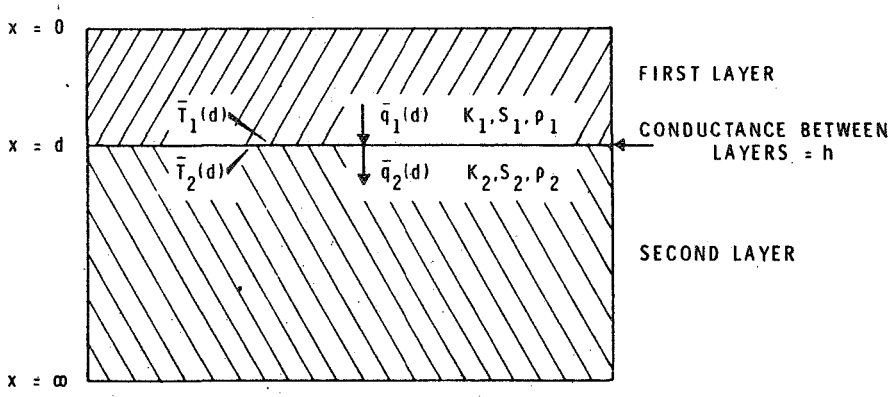

BOUNDARY CONDITIONS

$$\lim_{x \to \infty} \bar{q} = 0$$

$$\bar{q}_1(d) = \bar{q}_2(d)$$

$$\bar{T}_1(d) = \bar{T}_2(d) + \frac{\bar{q}_2(d)}{h}$$

Figure 4.

THERMAL SURFACE IMPEDANCE FOR A LAYER IN GOOD CONTACT WITH A SEMI-INFINITE SECOND LAYER

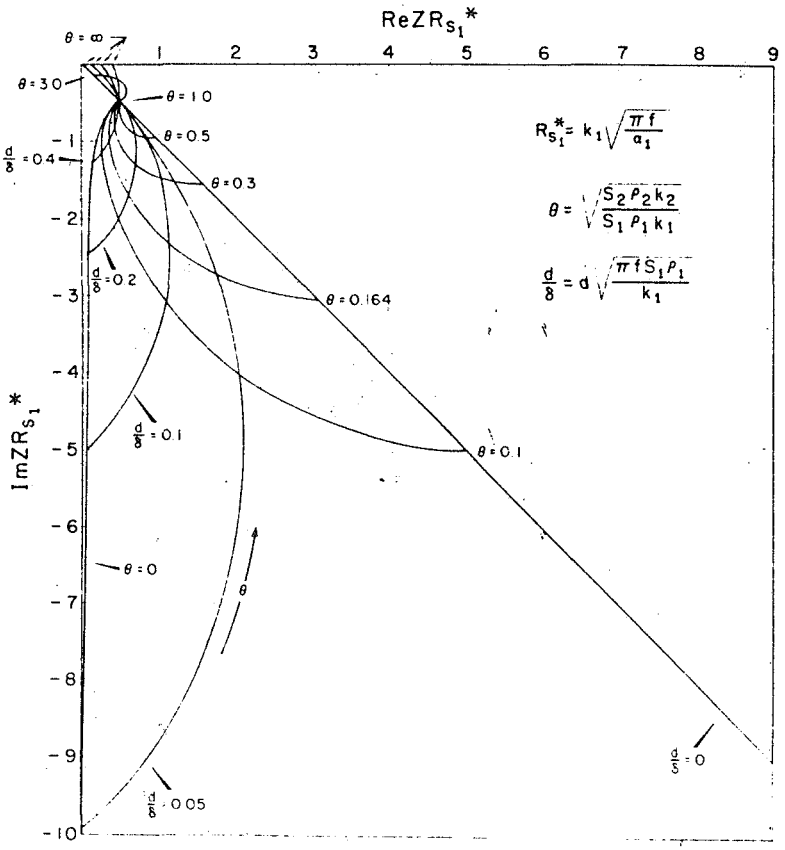

Figure 5.

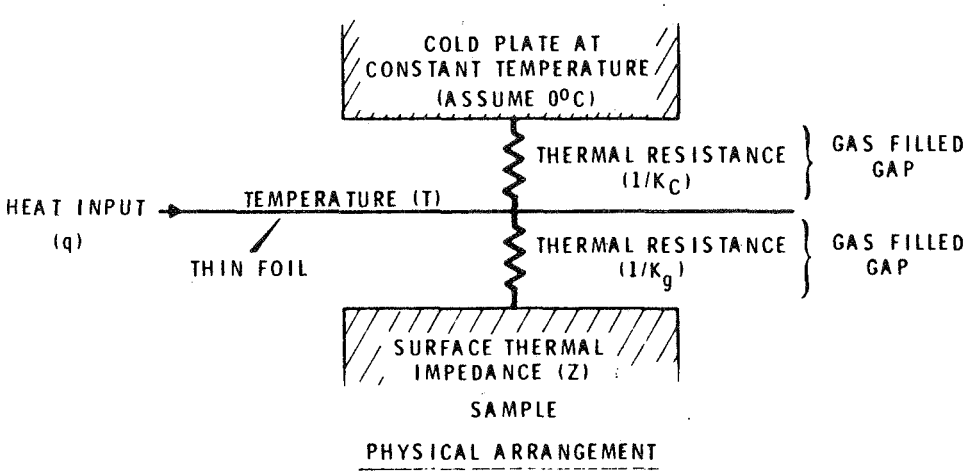

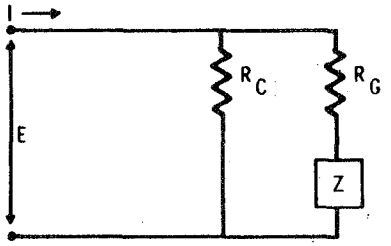

ELECTRICAL QUANTITY	THERMAL EQUIVALENT
E	T
I	q
R	1/K
Z = E/I	Z = T/q

Figure 6.

RELATIONSHIP BETWEEN THERMAL INPUT IMPEDANCE OF TRANSDUCER, AND THERMAL SURFACE IMPEDANCE OF SAMPLE

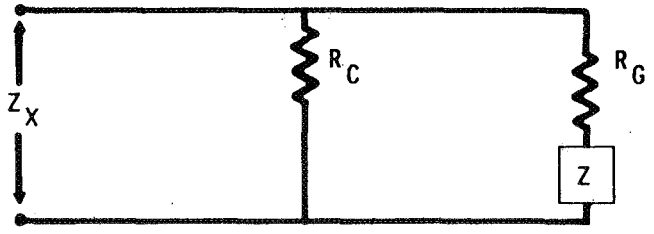

$$\frac{1}{Z_X} = \frac{1}{R_C} + \frac{1}{R_G + Z}$$

HENCE

$$Z = \frac{R_C Z_X}{R_C - Z_X} - R_G$$

AND

$$Z_X = \frac{R_C(R_G + Z)}{R_C + R_G + Z}$$

Figure 7.

BLOCK DIAGRAM OF THE SINUSOIDAL THERMAL WAVE TESTER

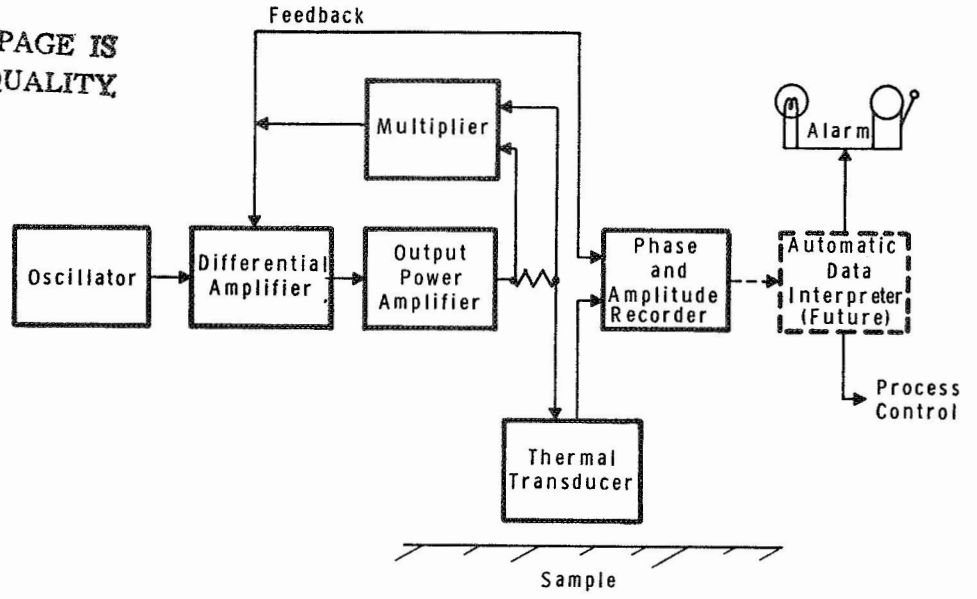

Figure 8.

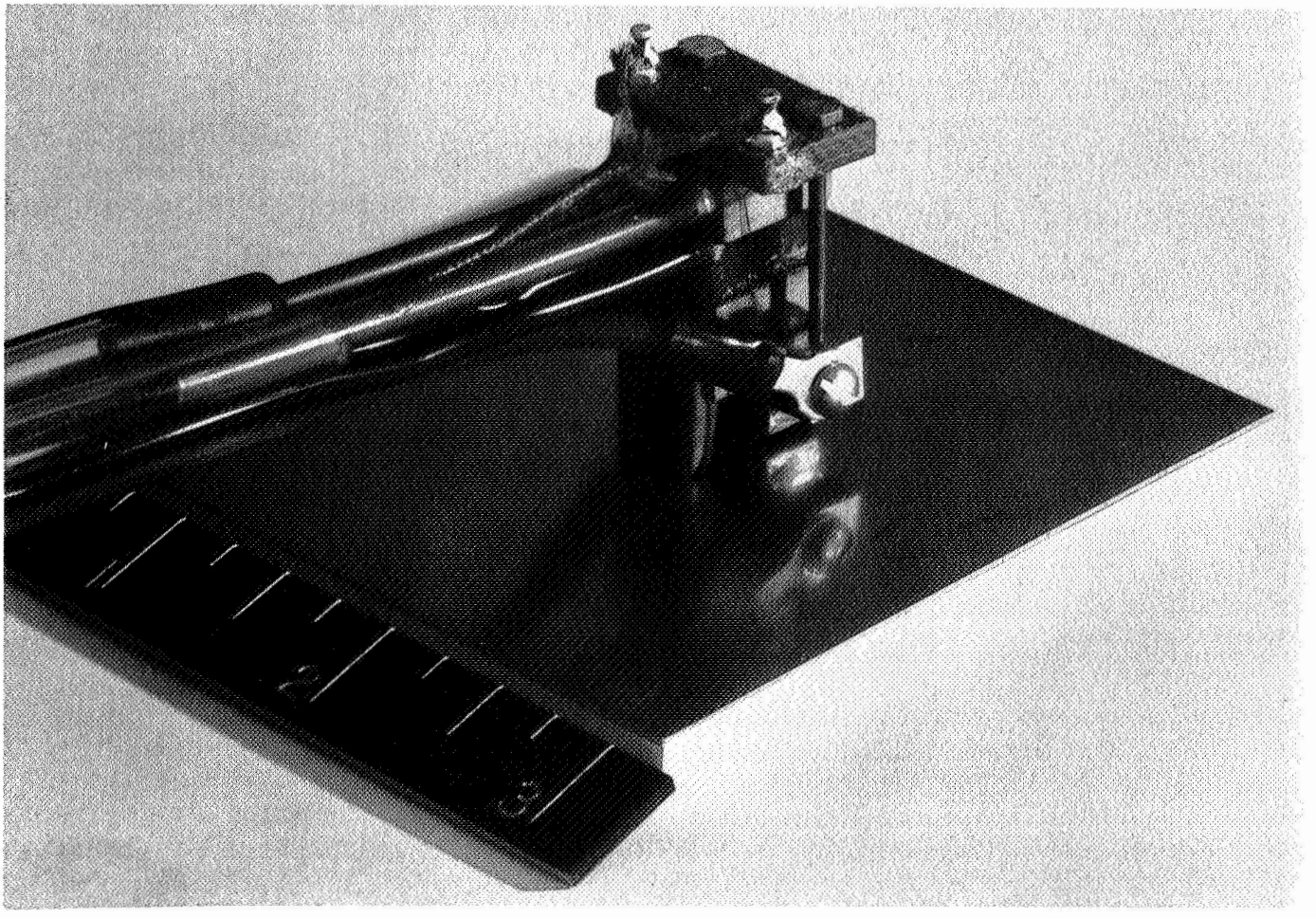

Figure 9.

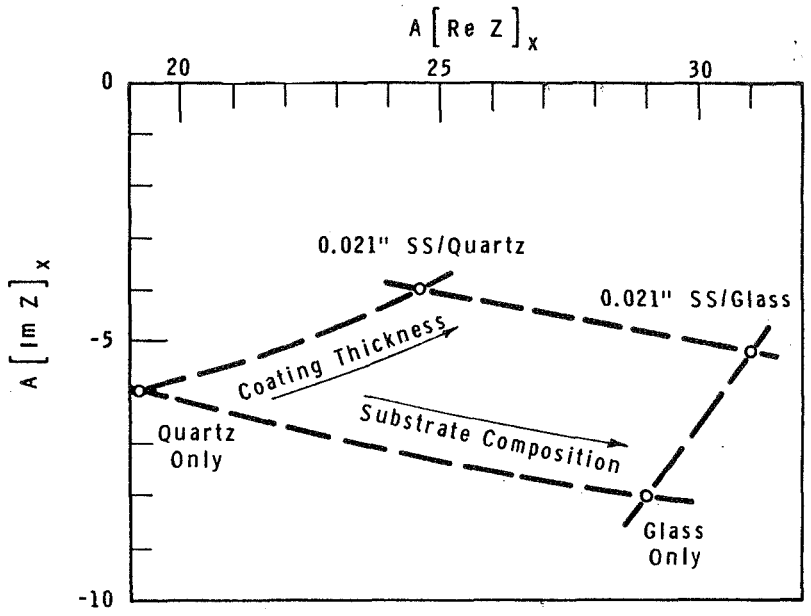

Figure 10.

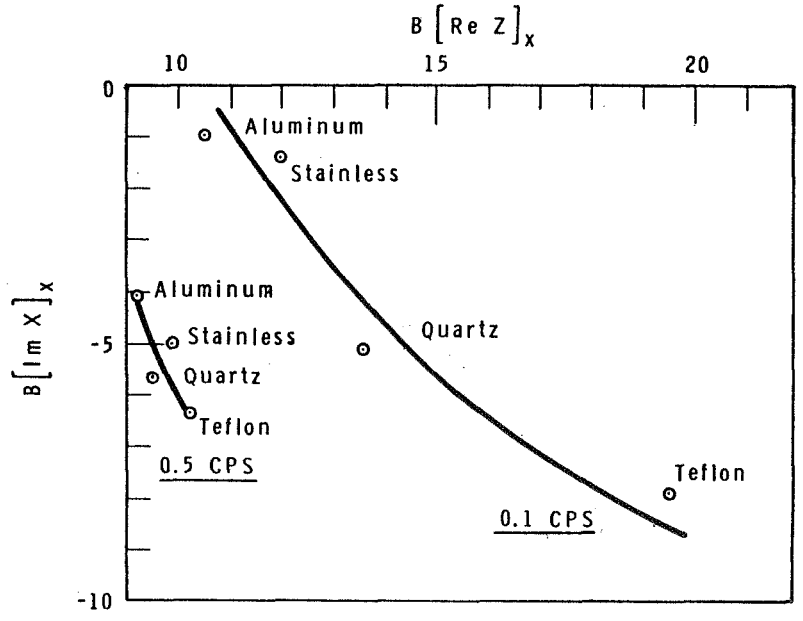

Figure 11.

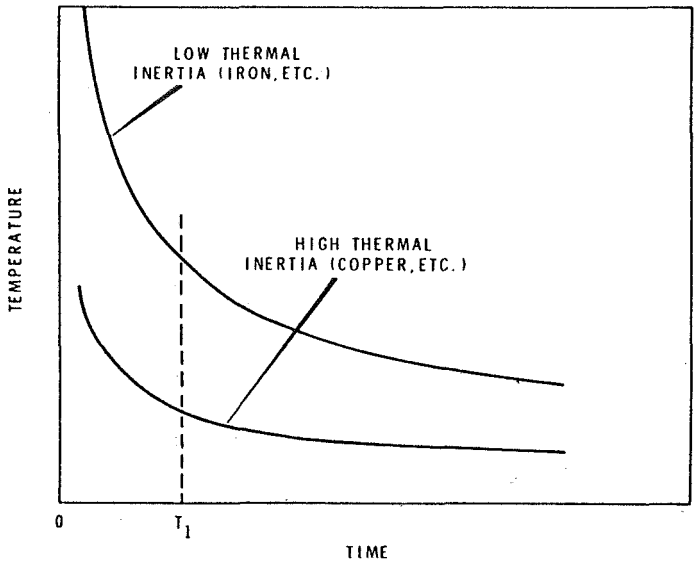

Figure 12.

$$\frac{\mathcal{L}\{f(t)\}}{\mathcal{L}\{y(t)\}} = Z(\bar{p})$$

THEN, FROM THE DEFINITION OF THE LAPLACE TRANSFORM,

$$\mathcal{L}\{f(t)\} = \int_0^\infty e^{-\bar{p}t} f(t)dt$$

$$\mathcal{L}\{y(t)\} = \int_0^\infty e^{-\bar{p}t} y(t)dt$$

WHEN f(t) AND y(t) CONVERGE SO THAT THESE TWO INGEGRALS ARE BOUNDED AFTER REPLACING $\bar{p}$ BY $j\bar{\omega}$, WE CAN WRITE:

$$\mathcal{L}\{f(t)\} = \int_{0,}^\infty e^{-\bar{j}\omega t} f(t)dt$$

$$= \int_0^\infty f(t) \cos \omega t \, dt - \bar{j} \int_0^\infty f(t) \sin \omega t \, dt$$

AND

$$\mathcal{L}\{y(t)\} = \int_0^\infty e^{-\bar{j}\omega t} y(t)dt$$

$$= \int_0^\infty y(t) \cos \omega t \, dt - \bar{j} \int_0^\infty y(t) \sin \omega t \, dt$$

AND HENCE,

$$Z(\bar{j}\omega) = \frac{\int_0^\infty f(t) \cos \omega t \, dt - \bar{j} \int_0^\infty y(t) \sin \omega t \, dt}{\int_0^\infty y(t) \cos \omega t \, dt - \bar{j} \int_0^\infty y(t) \sin \omega t \, dt}$$

Figure 13.

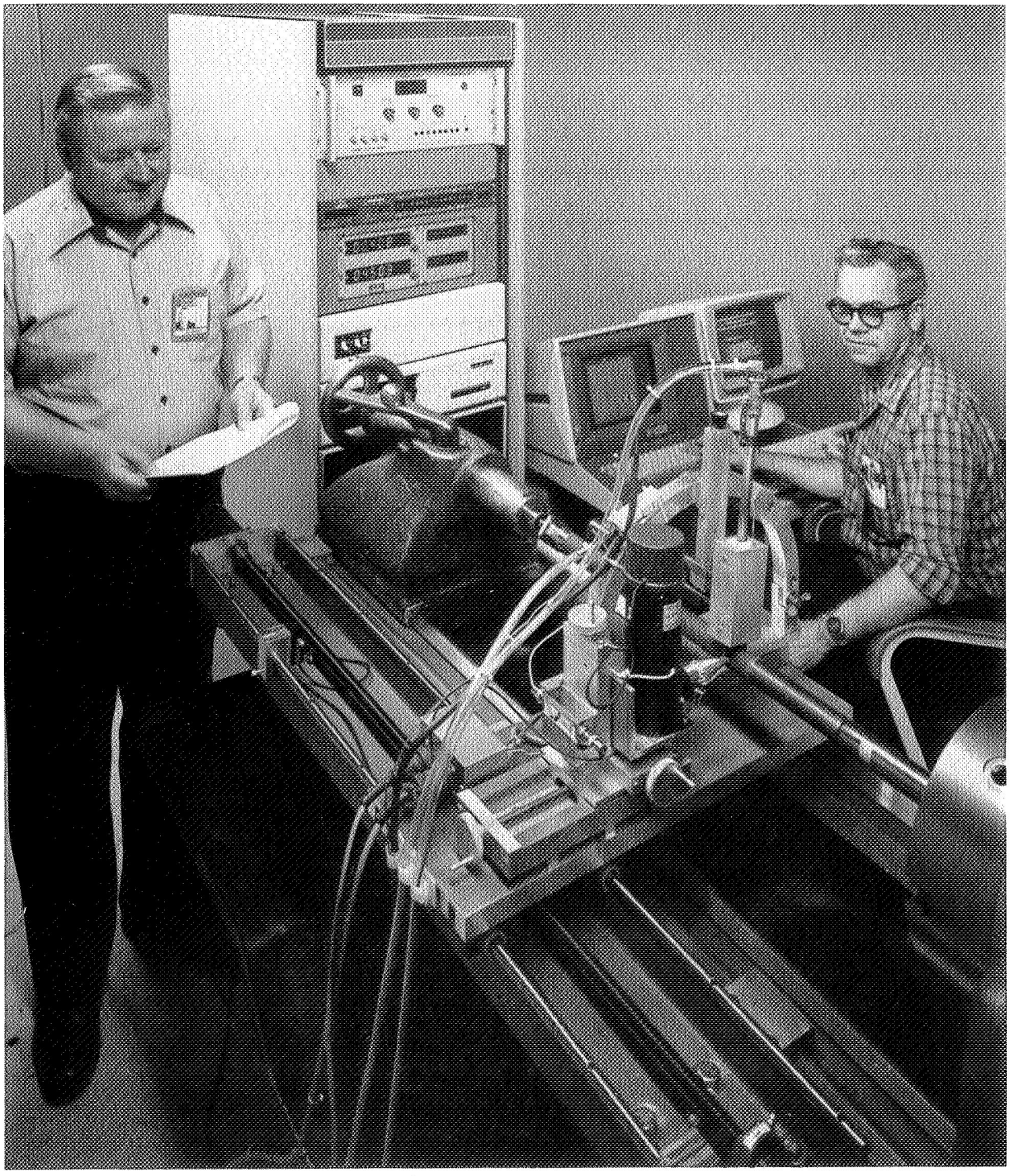

Figure 14.

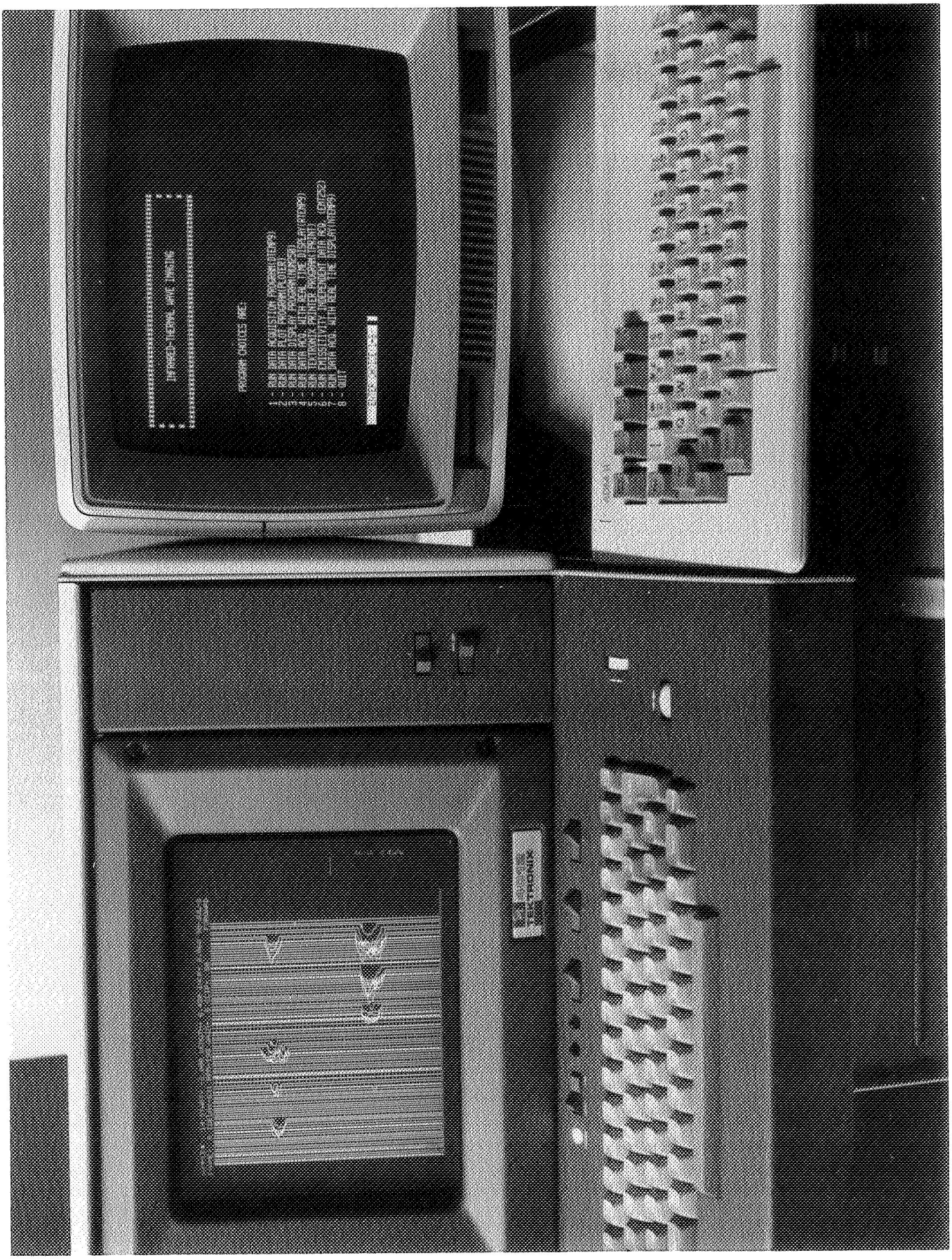

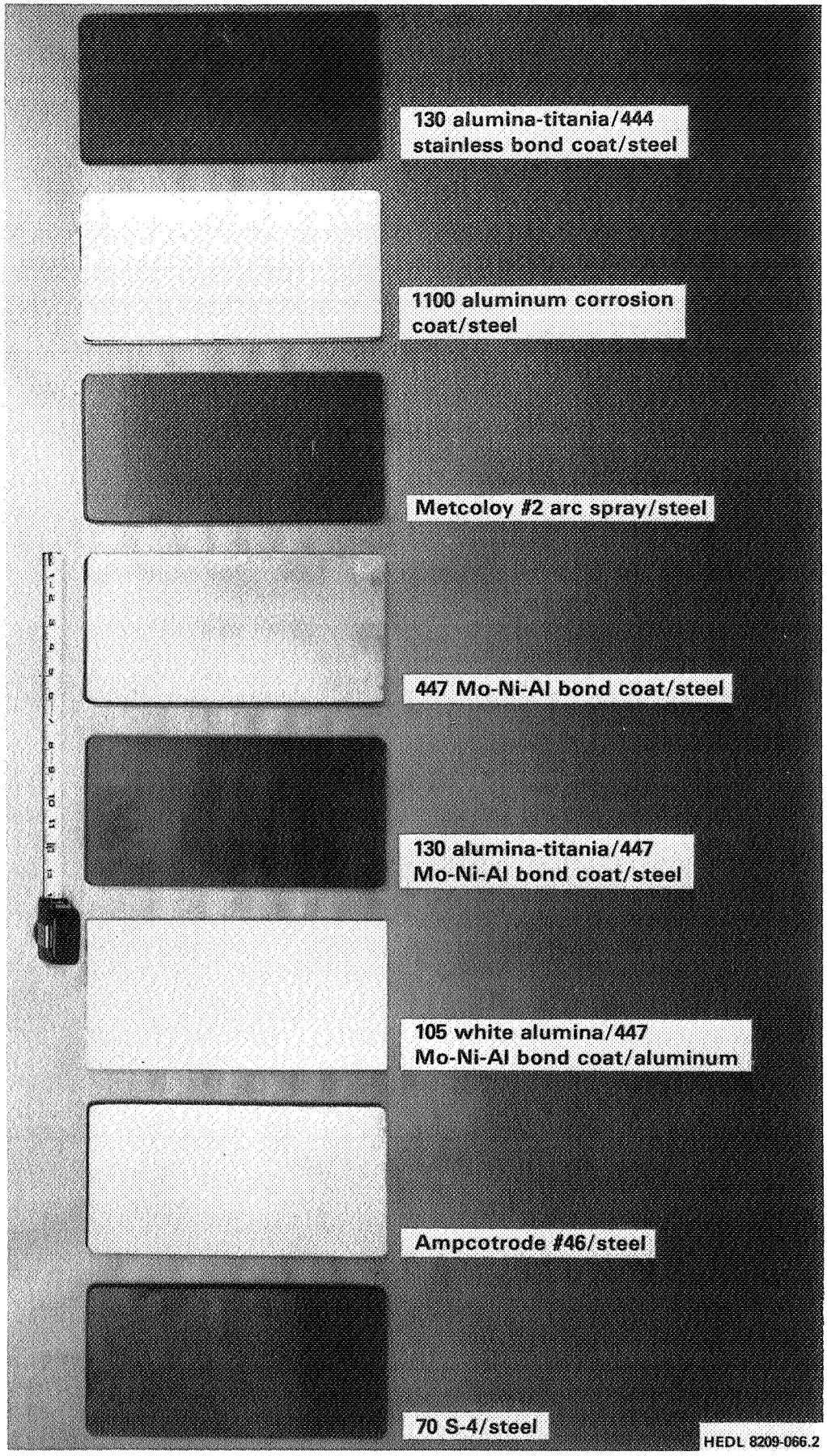

Figure 16.

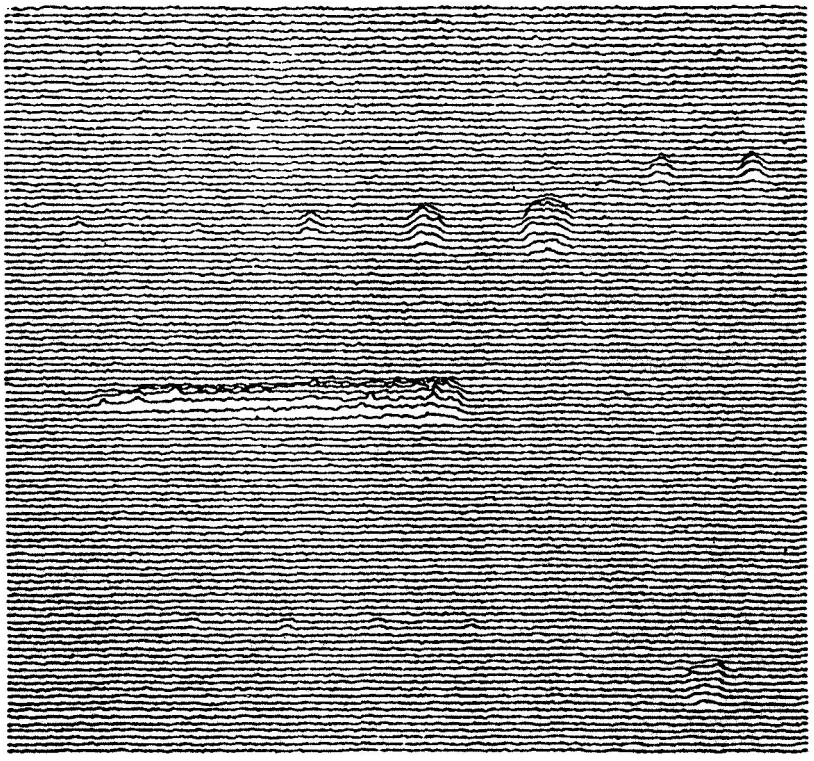

EMISSIVITY INDEPENDENT INFRARED-THERMAL SCAN RESULT SHOWING ALL NONBONDS IN SIDE #1 OF PSNS CYLINDRICAL THERMAL SPRAYED TEST SPECIMEN #11.

Figure 17.

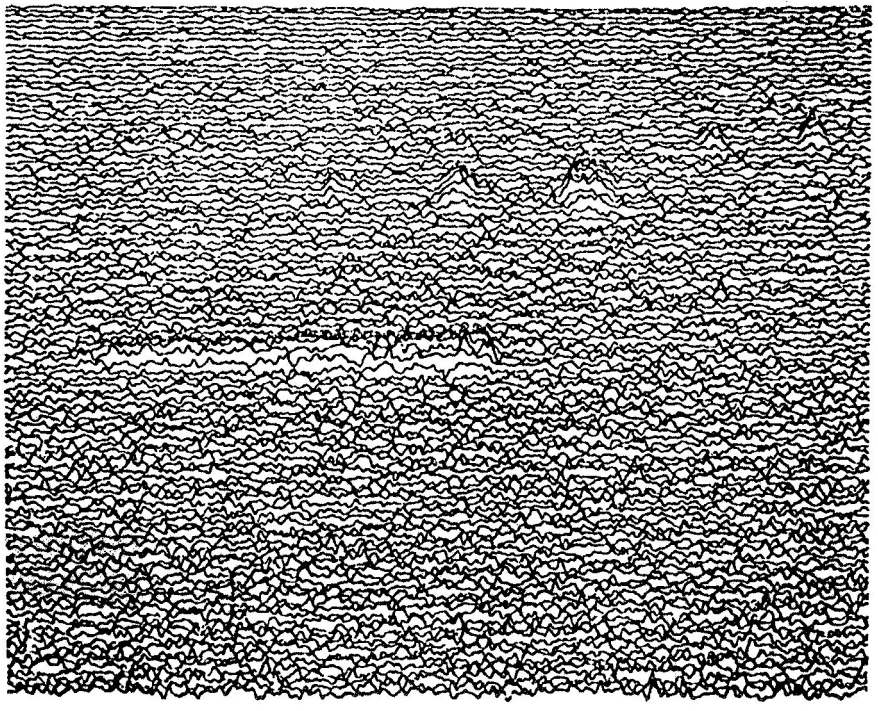

ORDINARY EMISSIVITY DEPENDENT INFRARED-THERMAL SCAN RESULTS ON SIDE #1 OF PSNS CYLINDRICAL THERMAL SPRAYED TEST SPECIMEN #11. NOTE THAT MOST 1/8 INCH DIAMETER NON-BOND INDICATIONS ARE HIDDEN IN THE BACKGROUND EMMISSIVITY VARIATIONS.

Figure 18.

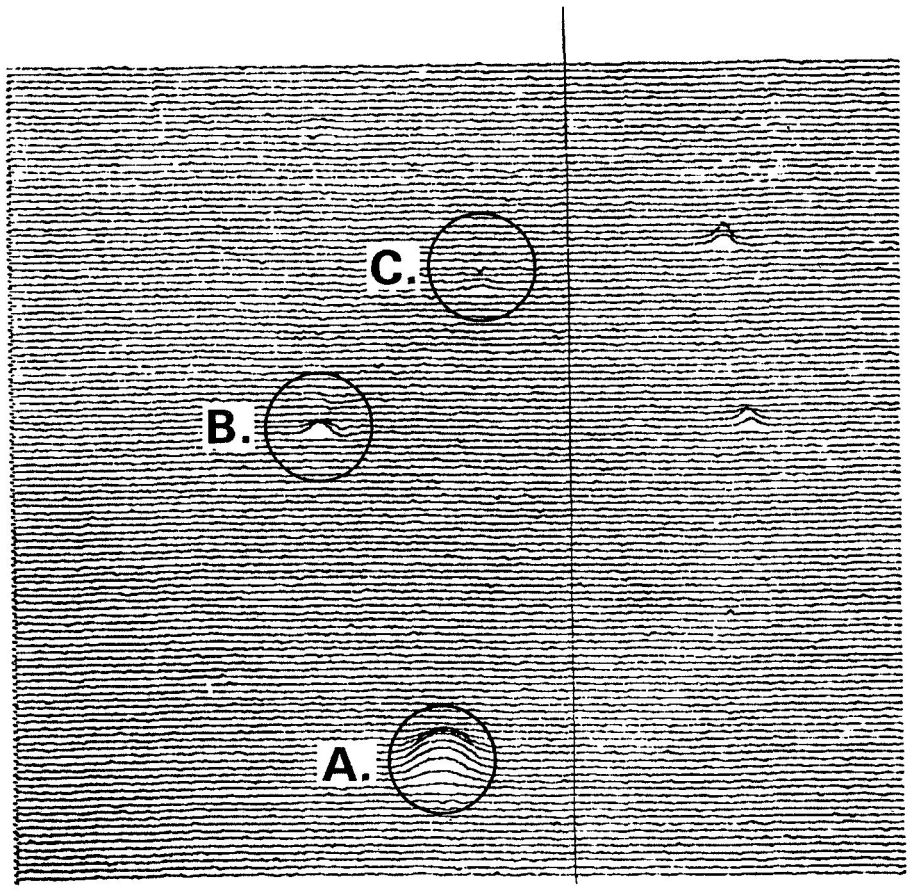

Figure 19.

Figure 20.

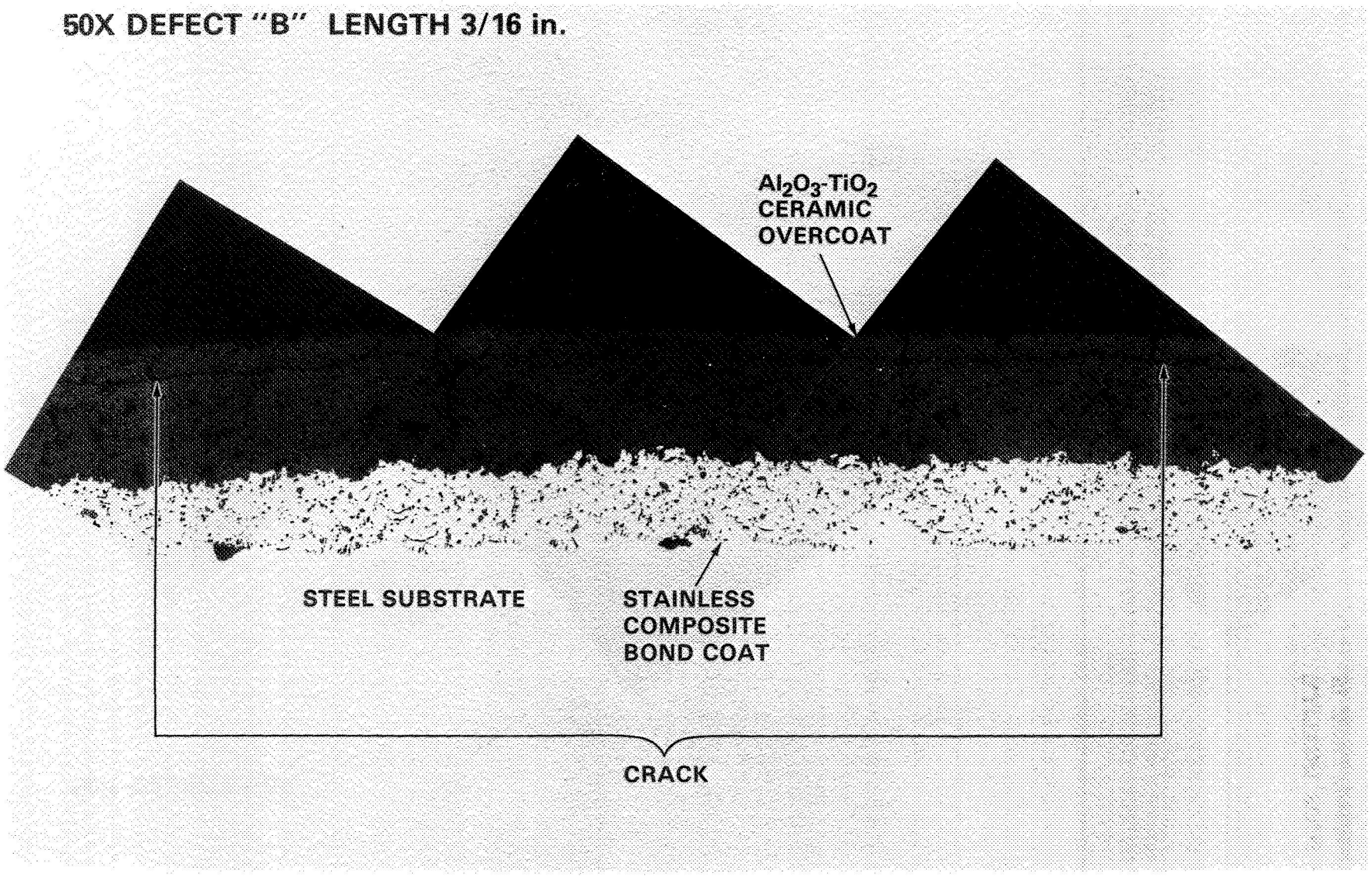

Figure 21.

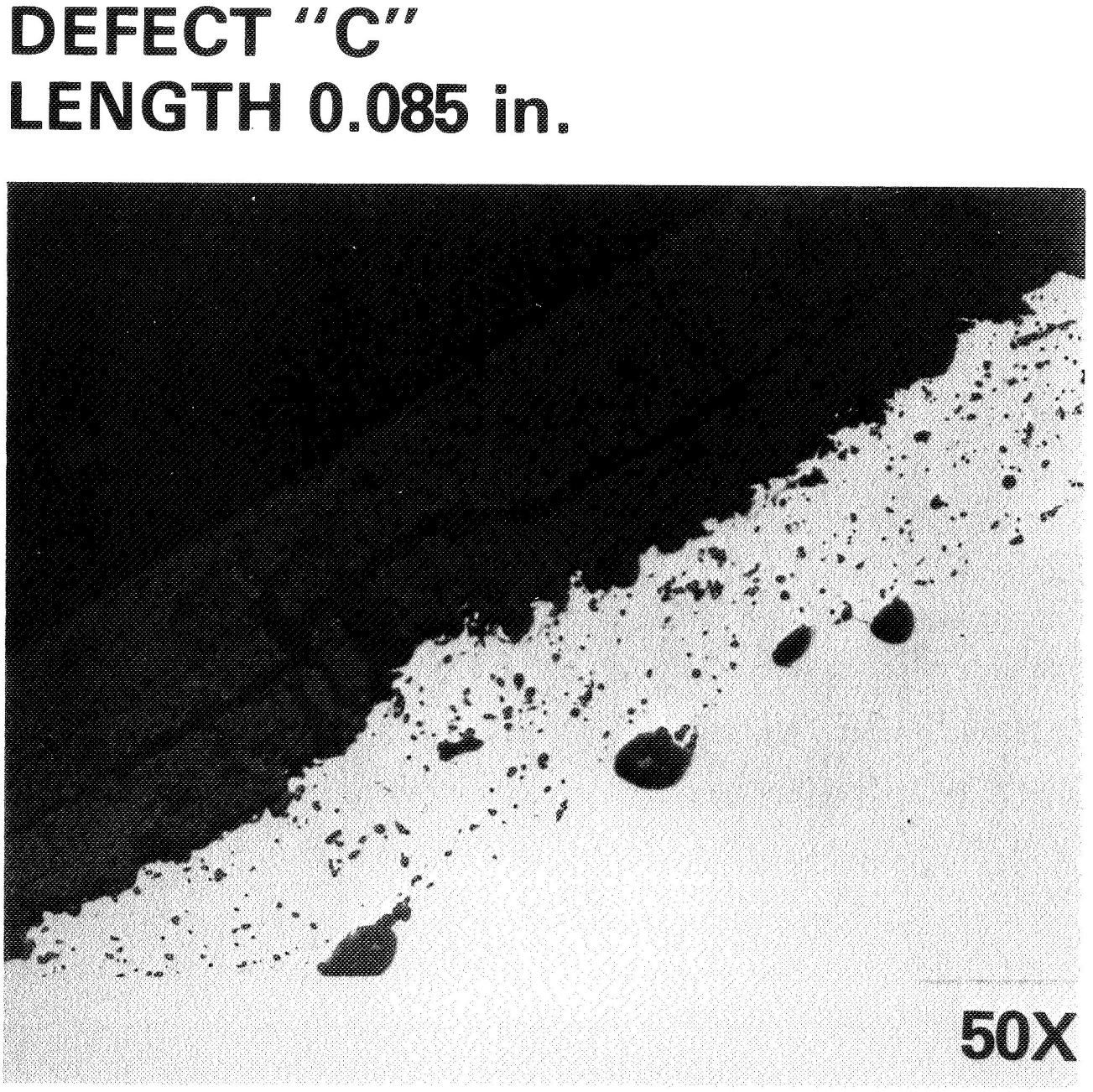

Figure 22.

CHARACTERIZATION OF ZrO_2-Y_2O_3 THERMAL SPRAY POWDER SYSTEMS

Thomas E. Mantkowski and David V. Rigney
Aircraft Engine Business Group
General Electric Company, Evendale, Ohio 45215-6301

and

Marc J. Froning and N. Jayaraman
Department of Materials Science and Metallurgical Engineering
University of Cincinnati, Cincinnati, Ohio 45221-0012

The overall objective of this program is to establish the interrelation between the raw material in the coating process and the performance of the coating deposit. It is anticipated that these interrelations will help establish more precise specifications for the procurement of raw materials. This paper presents some of the preliminary results of this program.

Powder samples of ZrO_2-8% Y_2O_3 manufactured by different processes such as (i) spray drying, (ii) spray drying and sintering, (iii) sintering and crushing, (iv) casting and crushing, and (v) casting, crushing and fusing were initially characterized for particle size and shape, microstructure and morphology, surface area, density, flow characteristics, and qualitative and quantitative phase distribution. The powder manufacturing process did appear to have significant effects on all the above characteristics. For example, the two extreme cases were: (i) the spray dried powders were spherical and inhomogeneous with a large surface area, low density and low mass flow rate, and contained primarily the monoclinic ZrO_2 phase with additional small amounts of free Y_2O_3; (ii) the fused, cast and crushed powders were dense irregular particles with a low surface area and high mass flow rate and contained primarily cubic phase with small amounts of monoclinic and additional unidentified phase. Both narrow and wide size distributions of particle sizes were found in the as received powder samples.

The powders were air-plasma-sprayed using identical spray parameters on Hastalloy-x substrate with a VPS NiCrAlY bond coating. The coated samples were characterized for microstructure, erosion resistance and qualitative and quantitative phase distribution. The coatings ranged from highly dense to highly porous and this appeared to primarily depend upon the initial particle size. The coated samples were subjected to thermal cycling, and similar characterization was carried out on the exposed samples. In general, as observed by other investigators, the highly porous coatings appeared to withstand a greater number of thermal cycles. Further work is in progress to confirm the preliminary thermal cycling test results, and in characterizing the coated and thermal cycled samples.

TABLE 1

CHEMICAL COMPOSITION OF EXPERIMENTAL POWDERS

Vendor Codes	Powder Types	Composition [by KEVEX]	Composition [wet chemistry]
W	Spray Dried	2.60% Hf [0.0-3.0] 3.40% Y [2.1-4.6]	0.6% Si 0.9% Hf 6.8% Y
J	Spray Dried	0.24% Ca [0.0-0.6] 0.00% Ti [0.0-0.5] 2.60% Hf [0.0-1.2] 8.60% Y [8.4-35.6]	0.3% Ti 0.4% Si 1.3% Hf 7.3% Y
A	Spray Dried	0.00% Ti [0.0-0.3] 0.00% Ca [0.0-0.3] 0.31% Fe [0.0-0.3] 2.19% Hf [0.0-2.3] 12.20% Y [5.1-15.3]	0.2% Ti 0.7% Si 8.4% Y
C	Spray Dried & Sintered	2.41% Hf [1.5-3.1] 9.10% Y [8.7-11.8]	0.2% Ti 0.7% Si 7.6% Y
B	Sintered & Crushed	0.00% K [0.0-0.2] 0.25% Ni [0.0-0.0] 1.49% Hf [0.9-3.3] 11.10% Y [7.0-13.0]	0.2% Ti 0.3% Si 8.2% Y
Y	Sintered & Crushed	0.00% Ca [0.0-0.3] 0.00% Ti [0.0-0.3] 0.00% Fe [0.0-1.1] 1.35% Hf [0.0-2.5] 7.81% Y [4.7-7.0]	0.1% Ti 0.2% Si 1.5% Hf 7.4% Y
J	Cast, Crushed, & Fused	0.00% Ti [0.0-0.3] 2.11% Hf [0.6-1.4] 8.16% Y [4.3-12.4]	0.1% Si 0.2% Ti 7.0% Y
H	Fused, Cast, & Crushed	0.00% Ti [0.0-0.1] 0.00% Mg [0.0-0.2] 1.21% Hf [0.0-1.5] 10.20% Y [6.4-8.0]	0.2% Mg 0.1% Ti 0.3% Si 8.6% Y
J	Fused, Cast, & Crushed	0.00% Mn [0.0-0.2] 0.14% Ti [0.0-0.0] 1.95% Hf [0.0-1.3] 9.24% Y [4.9-8.5]	0.1% Si 0.2% T 6.4% Y

TABLE 2

PLASMA SPRAY PARAMETERS

	Air	Vacuum
Plasma Gun	Metco 7M	Metco 7MB
Primary/Secondary Gas	N_2/H_2	Ar/H_2
Gun Power	36 KW	50 KW
Traverse Rate	100 sfpm	100 sfpm
Powder Feed Rate	6 Lbs./Hr.	10 Lbs./Hr.
Preheat	None	$1800^{\circ}F$
Spray Distance	5 In.	12 In.
Other	90° air impingement cooling	40 torr Abs. Pressure, RTA cleaned

TABLE 3

PHYSICAL PROPERTIES OF THE AS-RECEIVED EXPERIMENTAL POWDERS

Vendor Codes	Powder Types	Shape [by SEM]	Color	Density [g/mil]	Flowability [hall, g/s]	Size [Microtrac]	Surface Area [sq. m/g]
W	Spray Dried	Porous Spheres	White	5.54	5.2	*	3.60
J	Spray Dried	Spheres	White	5.55	6.4	MD=46.7 SD=23.0	1.60
A	Spray Dried	Spheres	Pale Yellow	5.60	7.2	*	1.39
C	Sintered	Rough Spheres	Pale Yellow	5.82	7.6	MV=67.7 SD=30.0	0.187
B	Sintered & Crushed	Rough Spheres	Light Yellow	5.96	7.0	MV=74.4 SD=25.4	0.256
Y	Sintered & Crushed	Irregular	Light Yellow	5.96	7.0	MV=53.2 SD=31.5	0.39
J	Cast, Crushed and Fused	Spheres/ Angular/ Acicular	Dark Yellow	5.67	9.6	MV=50.0 SD=23.4	0.073
H	Fused, Cast, and Crushed	Irregular	Dark Yellow	6.03	8.7	MV=65.4 SD=35.6	0.00656
J	Fused, Cast, and Crushed	Angular	Dark Yellow	6.05	8.3	MV=51.1 SD=22.0	0.081

* Powders Dissolve in Water

TABLE 4

TBC LIFE AND EROSION RESISTANCE

Vendor Codes	Powder Types	Erosion Resistance [sec/mil]	Thermal Cycles to Failure
W	Spray Dried	9.5	40
J	Spray Dried	7.4	285
A	Spray Dried	4.1	700
C	Sintered & Crushed	6.1	660
B	Sintered & Crushed	7.1	1000
Y	Sintered & Crushed	6.6	410
J	Cast, Crushed & Fused	10.5	380
H	Fused, Cast & Crushed	9.6	310
J	Fused, Cast & Crushed	11.6	390

Vendor J-Spray Dried

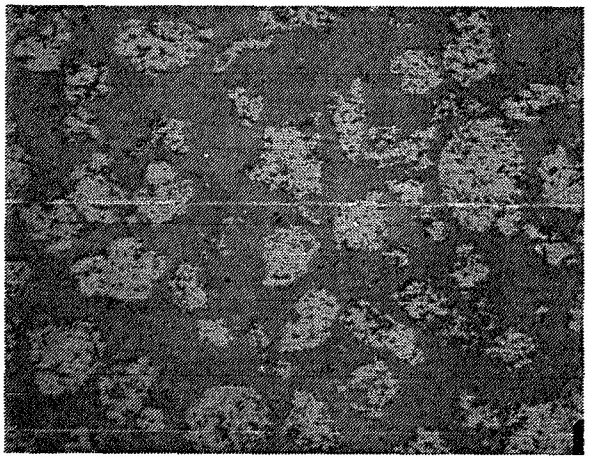

Vendor B-Sintered

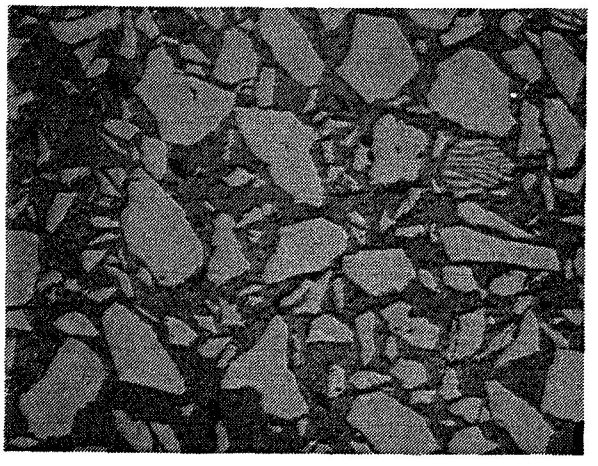

Vendor H-Cast & Crushed

Figure 1. - Metallographic evaluation of ZrO_2 - $8Y_2O_3$ powders.

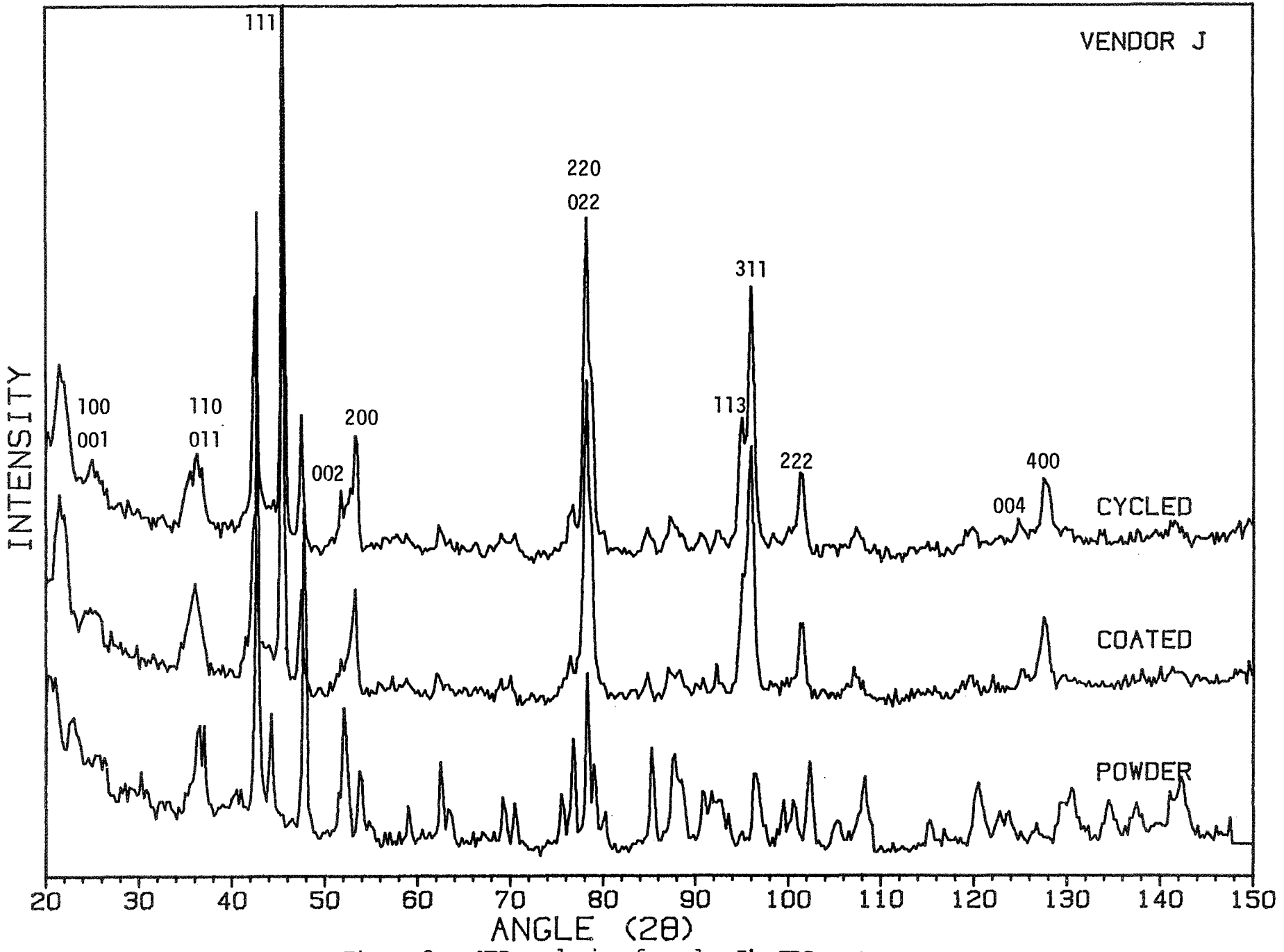

Figure 2. - XRD analysis of vendor J's TBC system.

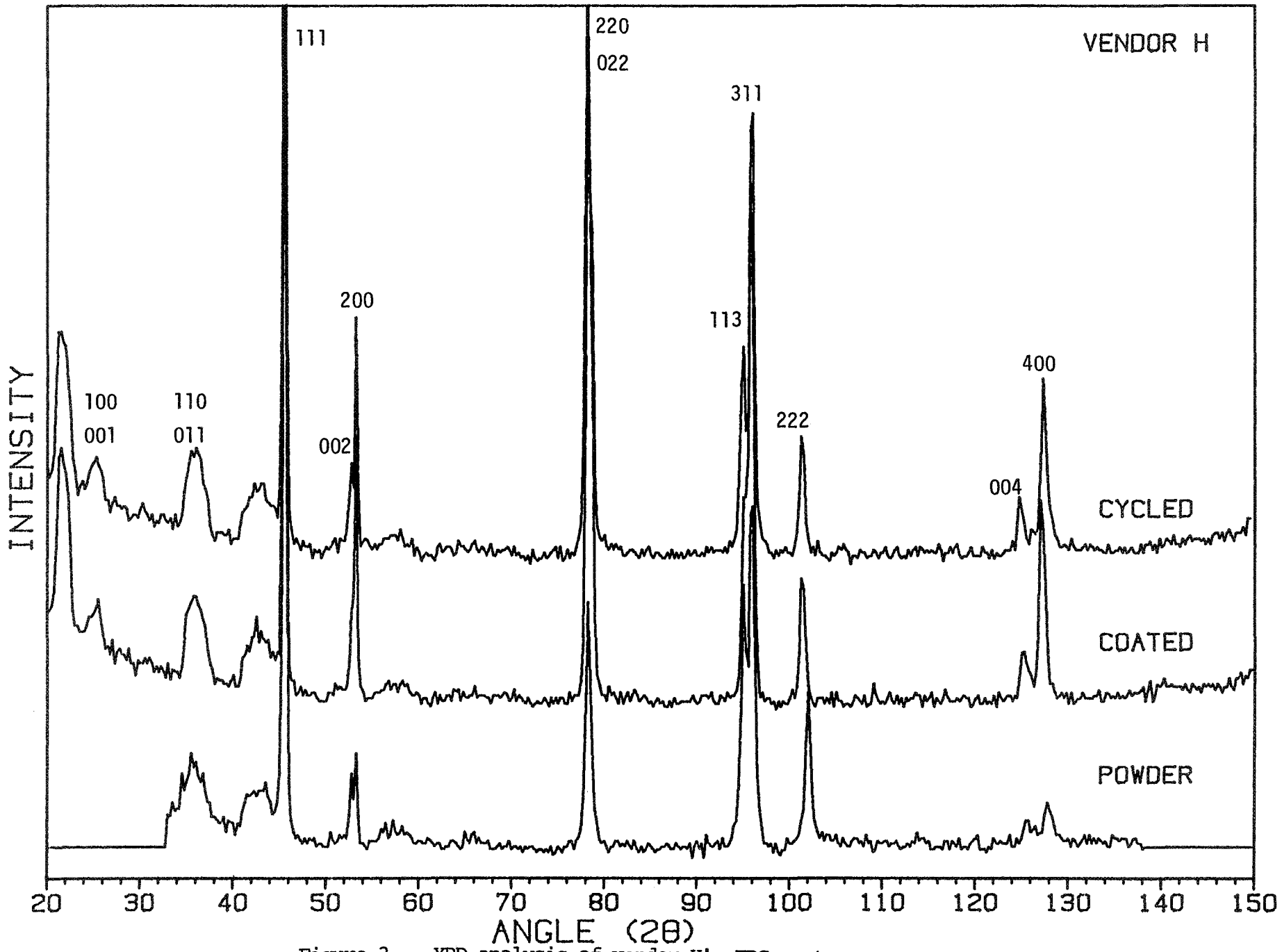

Figure 3. - XRD analysis of vendor H's TBC system.

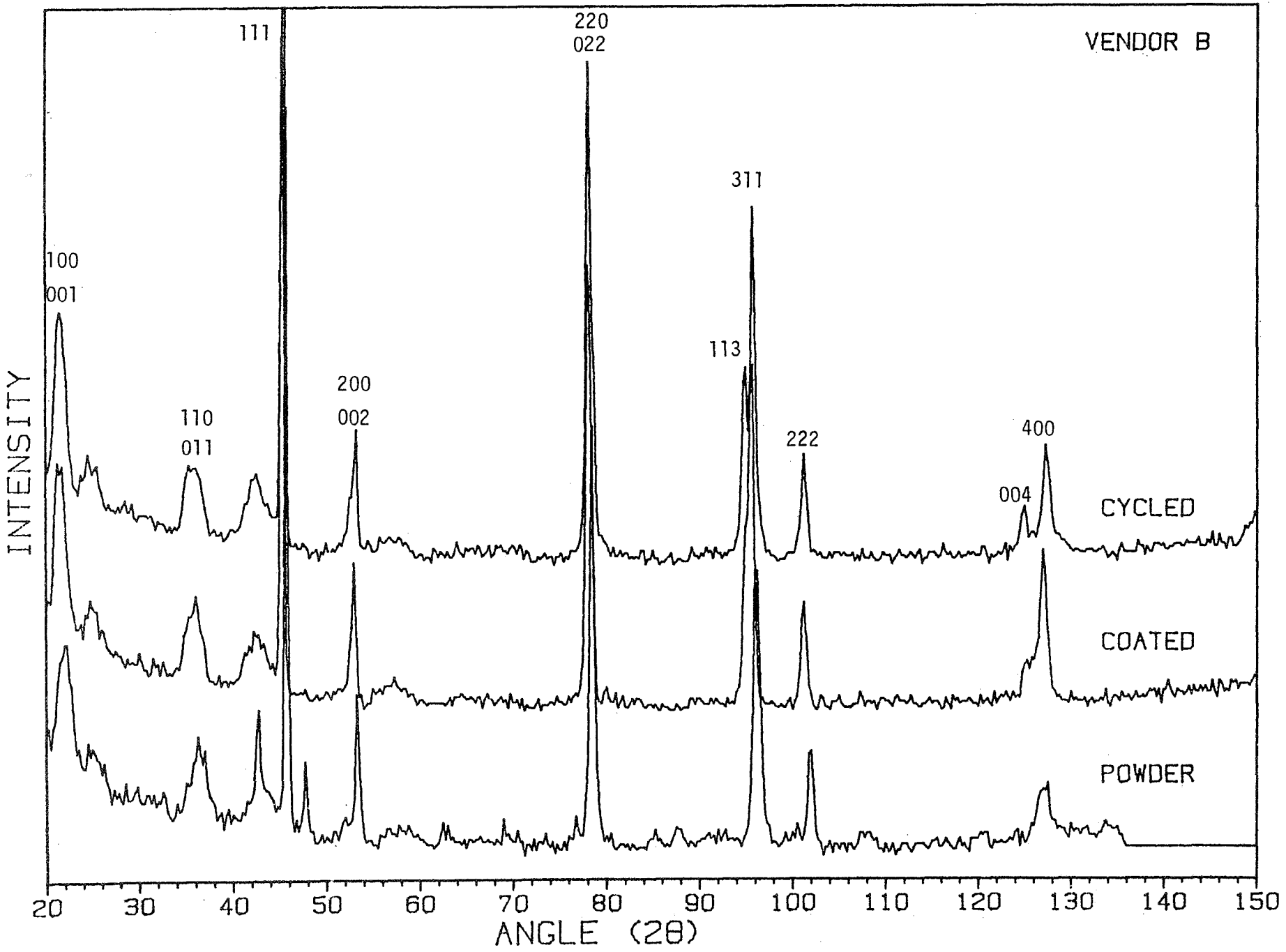

Figure 4. - XRD analysis of vendor B's TBC system.

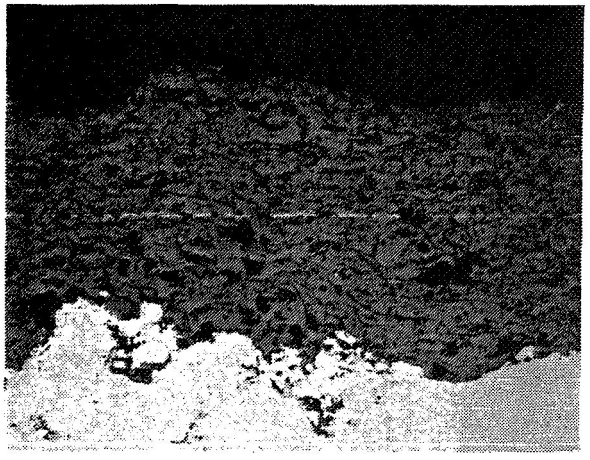

Vendor J

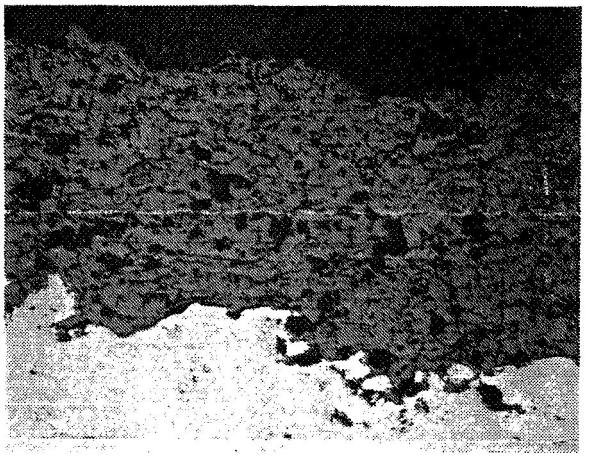

Vendor B

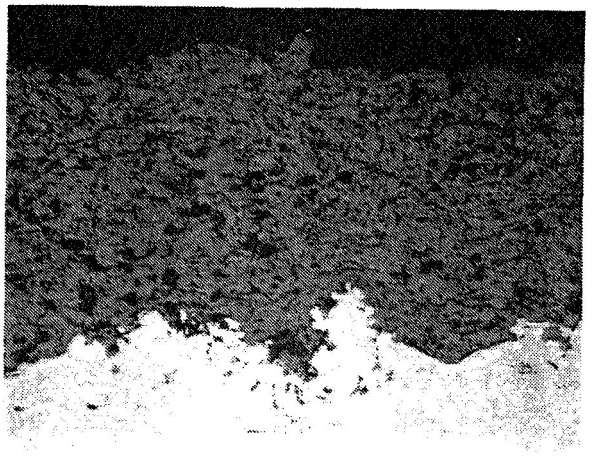

Vendor H

Figure 5. - Metallographic evaluation of as-sprayed TBC's.

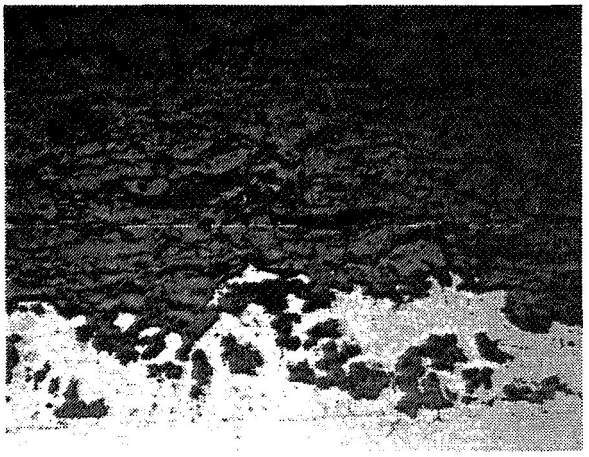

Vendor J-285 Cycles

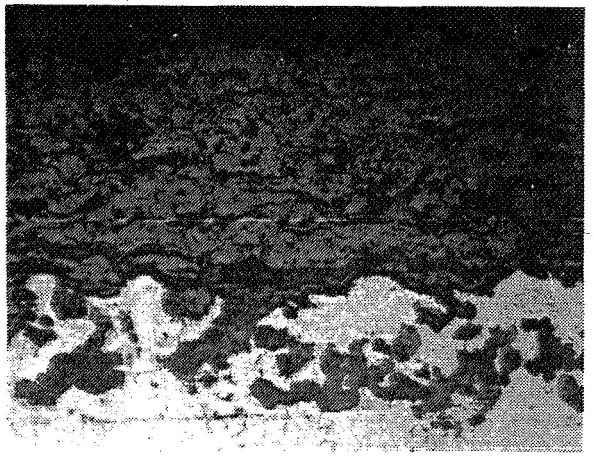

Vendor B-1000 Cycles

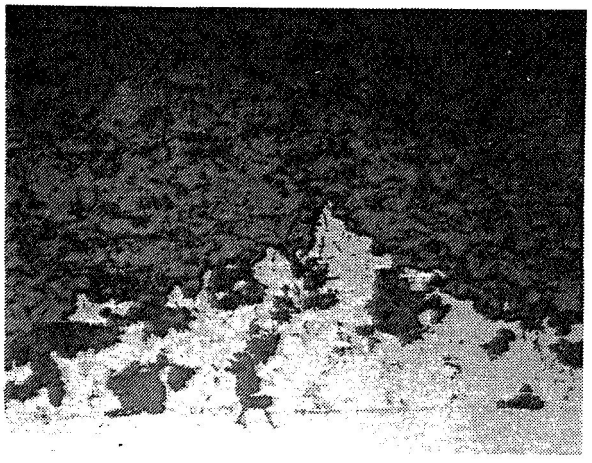

Vendor H-310 Cycles

Figure 6. - Metallographic evaluation of exposed TBC's.

ALUMINUM OXIDE BARRIERS IN MCrAlY SUPERALLOY SYSTEMS

Kenneth G. Kreider
National Bureau of Standards
Gaithersburg, Maryland 20899

An investigation was made of sputtered aluminum oxide diffusion barriers to protect gas turbine engine blade and vane alloys from their coatings. MAR M200 + Hf coated with sputtered NiCoCrAlY and MAR M509 coated with sputtered FeCrAlY were obtained both with and without 1 μm and 2 μm sputtered Al_2O_3 barrier layers. Electron dispersive X-ray analysis was used to determine the concentration profiles of as-received and heat treated samples.

The Al map of a MAR M200 + Hf sample with a NiCoCrAlY coating and a 1 μm barrier after a 1080°C, 50 hour heat treatment in air is presented in Fig. 1. The diffusion profiles of a sample heat treated under the same conditions without the barrier is given in Fig. 2. A gradual transition from the coating (46% Ni, 23% Co, 18% Cr, 12% Al, 0.5% Y) to the base alloy (70% Ni, 10% Co, 9% Cr, 5% Al plus Ti, Hf, Cb, B, C) is observed across the interface which is 80 μm from the surface. Aluminum depletion due to oxidation is observed at the surface. Figure 3 shows the profiles with a 1 μm barrier. The interdiffusion of Ni, Co, Cr, and Al appear similar.

A clearer indication of the penetration through the barrier layer is presented in Figs. 4 and 5 which show the diffusion profiles for samples with MAR M509 (54% Co, 24% Cr, 10% Ni plus W, Ta, Ti, Zr, and C) and coating (70% Fe, 18% Cr, 11% Al, 0.7% Y). The iron and aluminum are penetrating up to 60 μm into the base alloy. The coating problem is illustrated in Fig. 6 where metallic bridges seem to cross the Al_2O_3 barrier. Apparently, the sputtered alumina is cracking in tension during heating which leads to interdiffusion of Fe, Al, and Co.

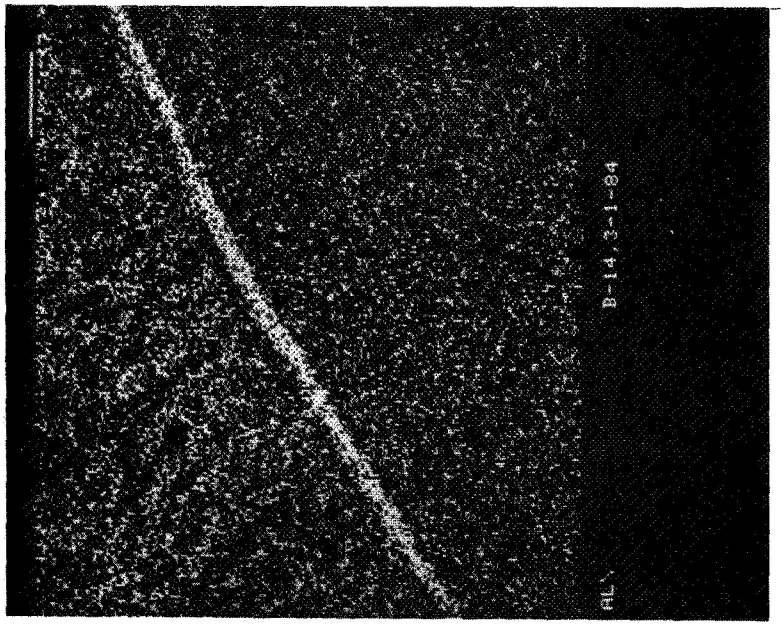

Figure 1. - Al map of D14 (580x). Heat treated at 1080 °C for 50 hr.

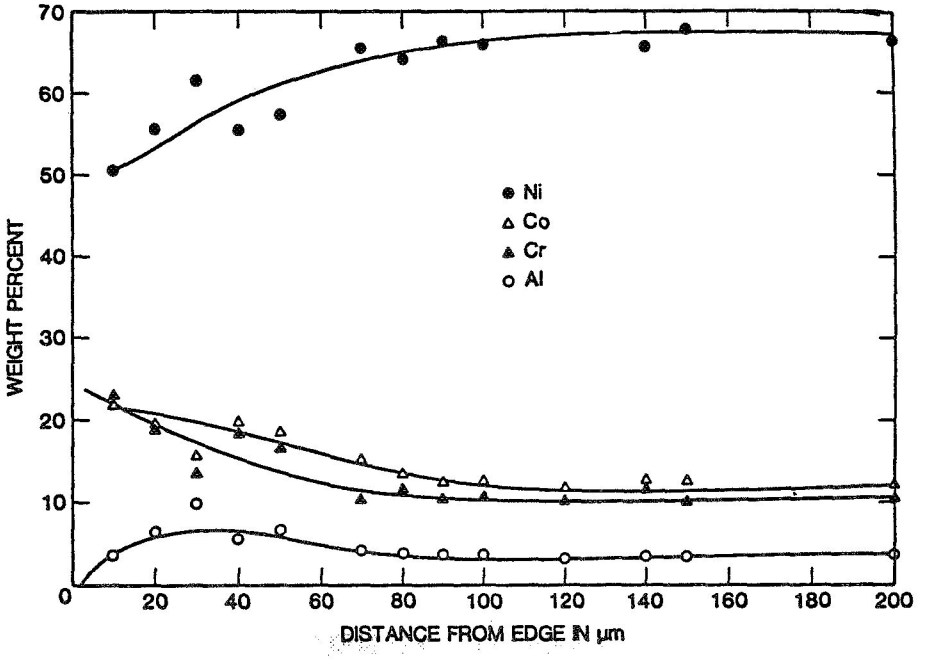

Figure 2. - Diffusion profiles of D4. Heat treated at 1090 °C for 50 hr without barrier.

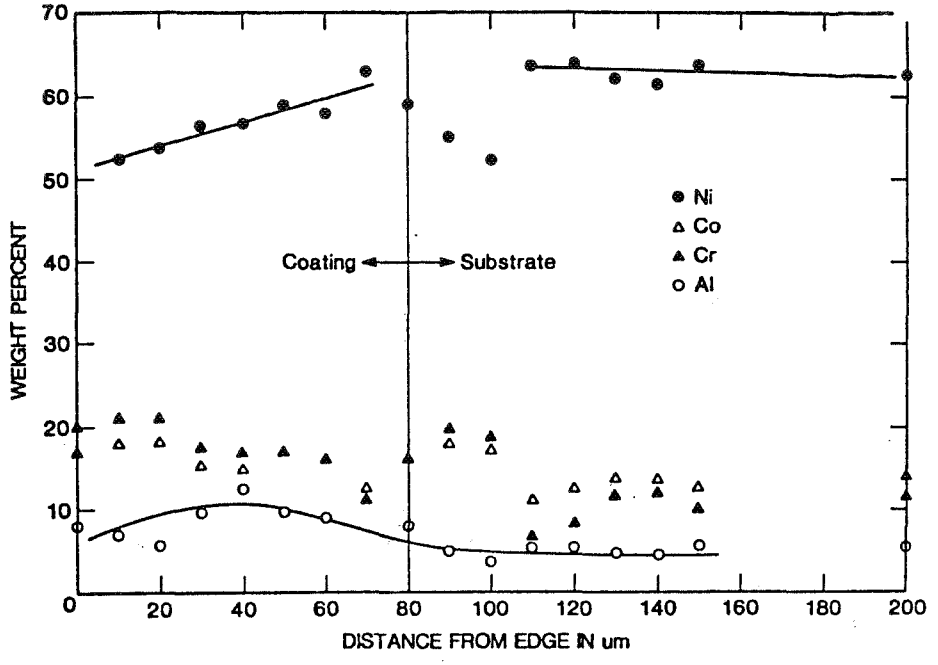

Figure 3. - Diffusion profiles of D14. 1-μm barrier layer, 1080 °C, 50 hr.

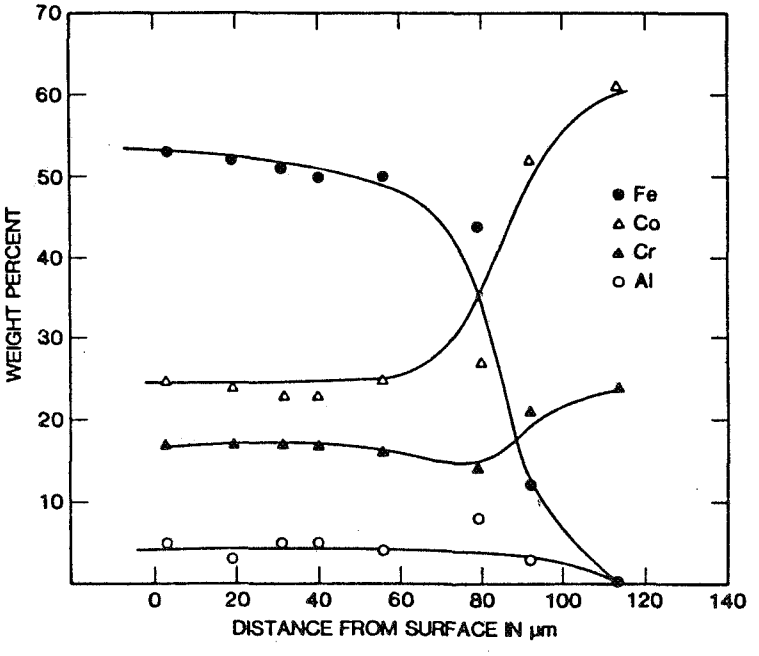

Figure 4. - Diffusion profiles of A40. No barrier layer, 1075 °C, 50 hr.

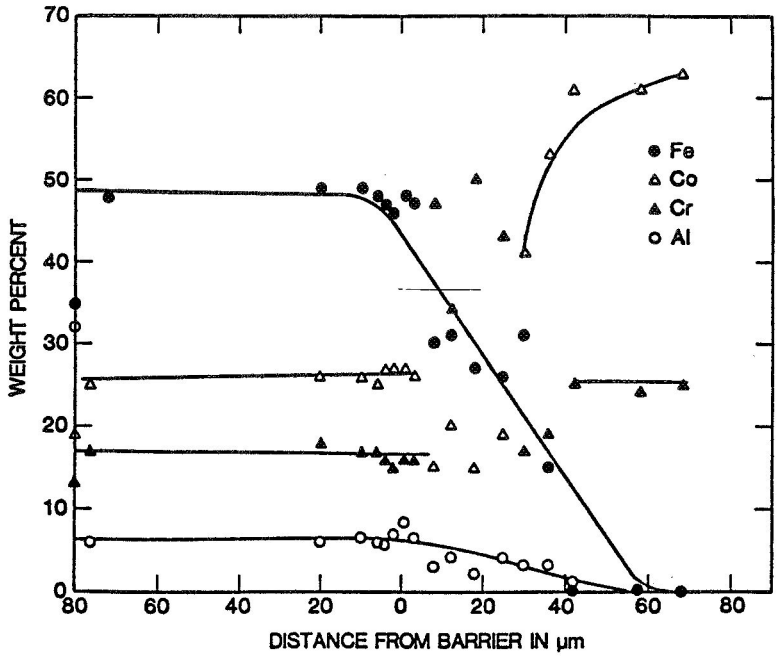

Figure 5. - Diffusion profiles of A19. 2-μm barrier, 1075 °C, 86 hr.

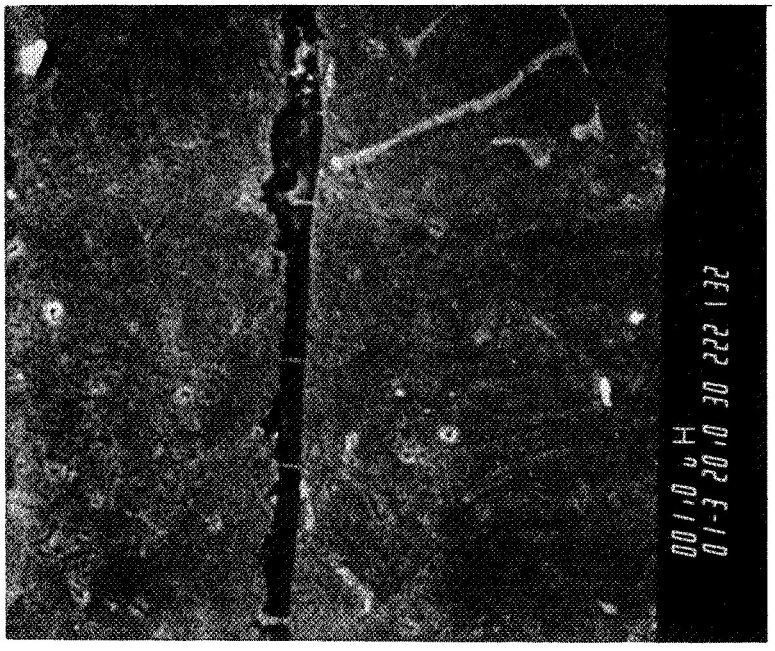

Figure 6. - Scanning electron micrograph of A19. Note bridging of Al_2O_3 barrier layer with metal.

ADVANCED THERMAL BARRIER COATING SYSTEMS

M.R. Dorfman and J.D. Reardon
Materials Engineering and R&D Development
METCO Inc.
Westbury, New York 11590

Current state-of-the-art thermal barrier coating (TBC) systems consist of partially stabilized zirconia coatings plasma sprayed over a MCrAlY bond coat. Although these systems have excellent thermal shock properties, they have shown themselves to be deficient for a number of several diesel and aircraft applications.

Two new ternary ceramic plasma coatings are discussed with respect to their possible use in TBC systems. Zirconia-ceria-yttria (ZCY) coatings have been developed with low thermal conductivities, good thermal shock resistance and improved resistance to vanadium containing environments, when compared to the baseline yttria stabilized zirconia (YSZ) coatings. In addition, dense zirconia-titania-yttria (ZTY) coatings have been developed with particle erosion resistance exceeding conventional stabilized zirconia coatings.

Both coatings have been evaluated in conjunction with a NiCr-Al-Co-Y_2O_3 bond coat. Also, multilayer or hybrid coatings consisting of the bond coat with subsequent coatings of zirconia-ceria-yttria and zirconia-titania-yttria have been evaluated. These coatings combine the enhanced performance characteristics of ZCY with the improved erosion resistance of ZTY coatings.

Improvement in the erosion resistance of the TBC system should result in a more consistent ΔT gradient during service. Economically, this may also translate into increased component life simply because the coating lasts longer.

TABLE I. - HOT PARTICLE EROSION

VOLUME OF COATING LOSS ($CM^3 \times 10^4$) PER GRAM OF ABRASIVE

IMPINGEMENT ANGLE	YTTRIA STABILIZED ZIRCONIA #1	YTTRIA STABILIZED ZIRCONIA #2	CERIA STABILIZED ZIRCONIA #3	CERIA STABILIZED ZIRCONIA #4	ZIRCONIA TITANIA YTTRIA #5
30^0	1.45	1.35	1.43	2.06	0.29
60^0	1.55	2.12	2.05	4.64	0.83

TYPICAL SPRAY DRIED
COMPOSITE POWDER

TYPICAL PRE-STABILIZED
SPHERICAL POWDER

Figure 1. - SEM photomicrographs (x700).

TABLE II. - SPRAY PARAMETERS

	YTTRIA STABILIZED ZIRCONIA		CERIA STABILIZED ZIRCONIA		ZIRCONIA TITANIA YTTRIA COMPOSITE
PLASMA GUN	9MB		9MB		9MB
NOZZLE	732		732	730	731
POWDER PORT	#2		#2	#2	#2
GAS TYPE	ARGON/HYDROGEN		AR/H_2	$N2/H_2$	ARGON/HYDROGEN
SPRAY DISTANCE (MM)	65	100	100	100	76
SPRAY RATE (GMS/MIN)	45.4	45.4	45.4	45.4	37.8
PRESSURE:					
PRIMARY	100	75	75	50	100
SECONDARY	50	50	50	50	50
FLOW:					
PRIMARY	80	80	80	75	75
SECONDARY	15	15	15	15	15
CURRENT	600	600	600	500	600
VOLTAGE	70	70	70	80	70
COATING	1	2	3	4	5

Figure 2. - Yttria stabilized zirconia coating microstructures (x100).

Figure 3. - Ceria stabilized zirconia coating microstructures (x100).

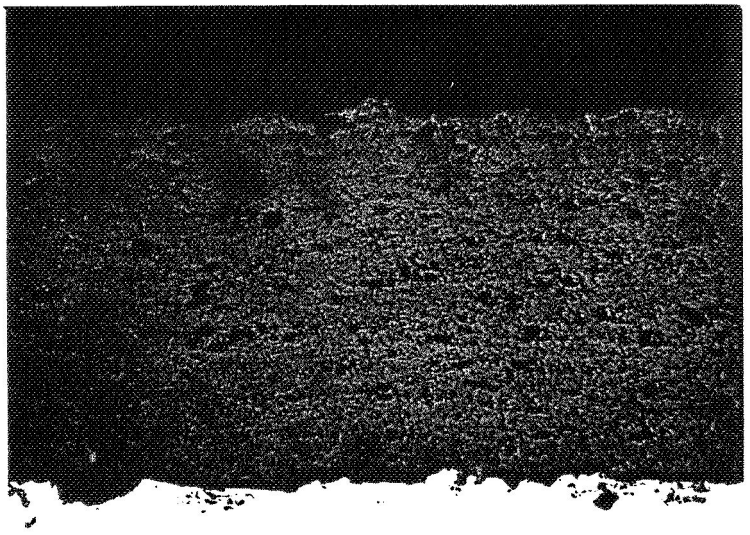

COATING #5

Figure 4. - Zirconia, titania, yttria coating microstructure (x100).

*HIGH TEMPERATURE PARTICLE EROSION

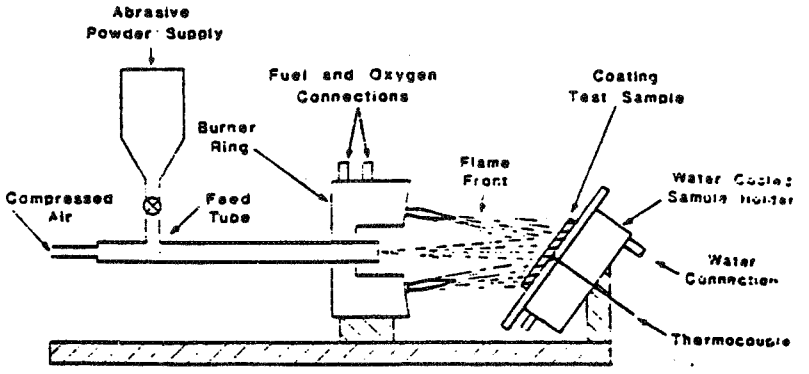

*COHESIVE STRENGTH

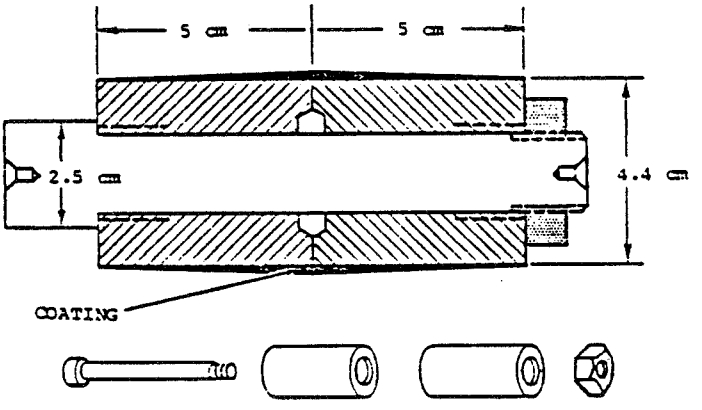

*CYCLIC THERMAL SHOCK

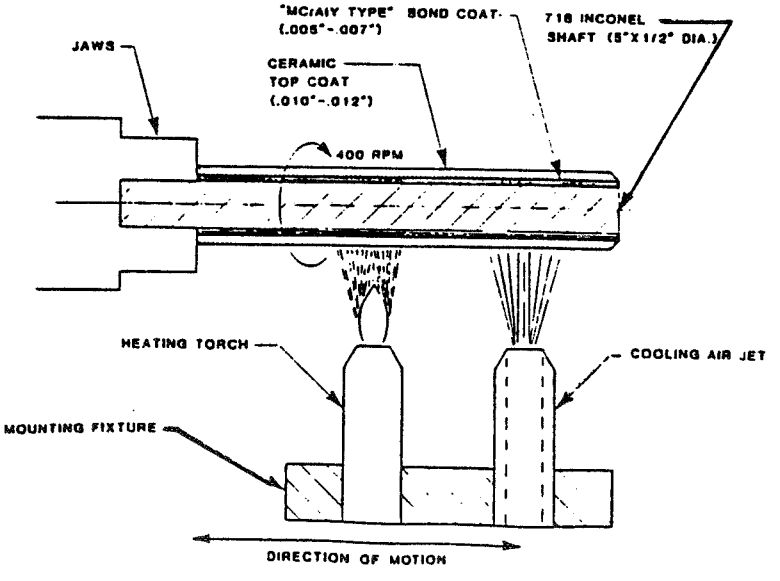

Figure 5. - Experimental test procedure.

TABLE III. - POWDER CHARACTERISTICS

	YTTRIA STABILIZED ZIRCONIA	CERIA STABILIZED ZIRCONIA WITH YTTRIA	ZIRCONIA-TITANIA-YTTRIA COMP. POWDER
NOMINAL CHEMISTRY (WT%)	ZIRCONIA BASE YTTRIA - 8%	ZIRCONIA BASE CERIA - 26% YTTRIA - 2.5%	ZIRCONIA BASE TITANIA - 18% YTTRIA - 10%
POWDER SIZE	-120 MESH +10 MICRONS	-170 MESH +10 MICRONS	-200 MESH +10 MICRONS
POWDER MORPHOLOGY	PRE-STABILIZED SPHERICAL POWDER	PRE-STABILIZED SPHERICAL POWDER	SPHERICAL SPRAY DRIED COMPOSITE

MICROLAMINATE COMPOSITES - AN ALTERNATE APPROACH TO THERMAL BARRIER COATINGS

R.F. Bunshah, C.V. Deshpandey, and B.P. O'Brien
University of California
Department of Materials Science and Engineering
Los Angeles, California 90024

Ceramic thermal barrier coatings suffer from a major drawback - i.e., brittle behavior. An alternate approach is microlaminate composite coatings consisting of alternate layers of metal and oxide. As the thickness of the individual laminae decreases while keeping the total thickness of the coating constant, the thermal conductivity drops markedly. Data on the Fe-Cu system will be presented. A model is proposed for an MCrAlY-Al_2O_3 microlaminate coating for thermal barriers. The methods of fabrication will also be discussed.

OBJECTIVE

To demonstrate the potential for low thermal conductivity microlaminate composites as an alternate to bulk ceramics.

Advantage: Improved fracture toughness at equivalent thermal conductivity.

MICROLAMINATE COMPOSITES

Bulk mateiral or coatings upto 0.040" thickness consisting of alternate layers of different materials.

MATERIAL COMBINATIONS STUDIED

Metal-Metal: Fe-Cu, Ni-Cu, Ti-Ni, Ca-Cu
Metal Ceramic: Ni-TiC, MCrAlY-Al_2O_3
Ceramic-Ceramic: TiC/TiB_2

METHOD OF PREPARATION

Electron beam evaporation from metal or ceramic sources.

DEPOSITION RATE

Upto 10 μm per minute

LAMINATE THICKNESS

1 m to 40μm

PROPERTIES STUDIES

Strength, ductility and thermal conductivity

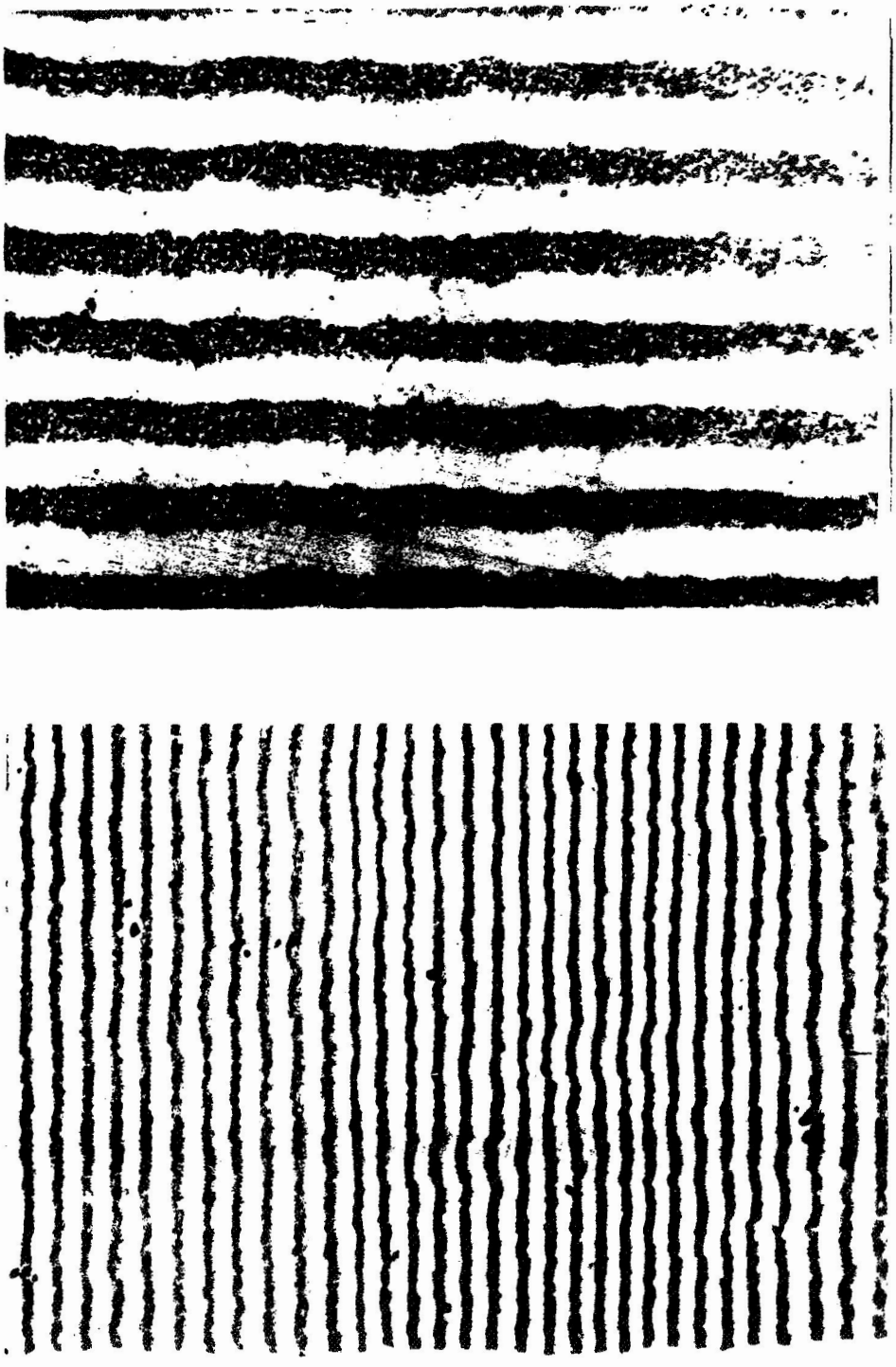

Electron micrographs of "MCrAlY" microlaminate prepared using electron beam evaporation thickness 2 m(by Movchan et. al. at Paton Institute, USSR.

Shown in the figure below is the thermal conductivity (perpendicular to laminae plane) of Fe/Cu condensates as a function of laminae thickness. The total thickness = 40 mils (1000μm)

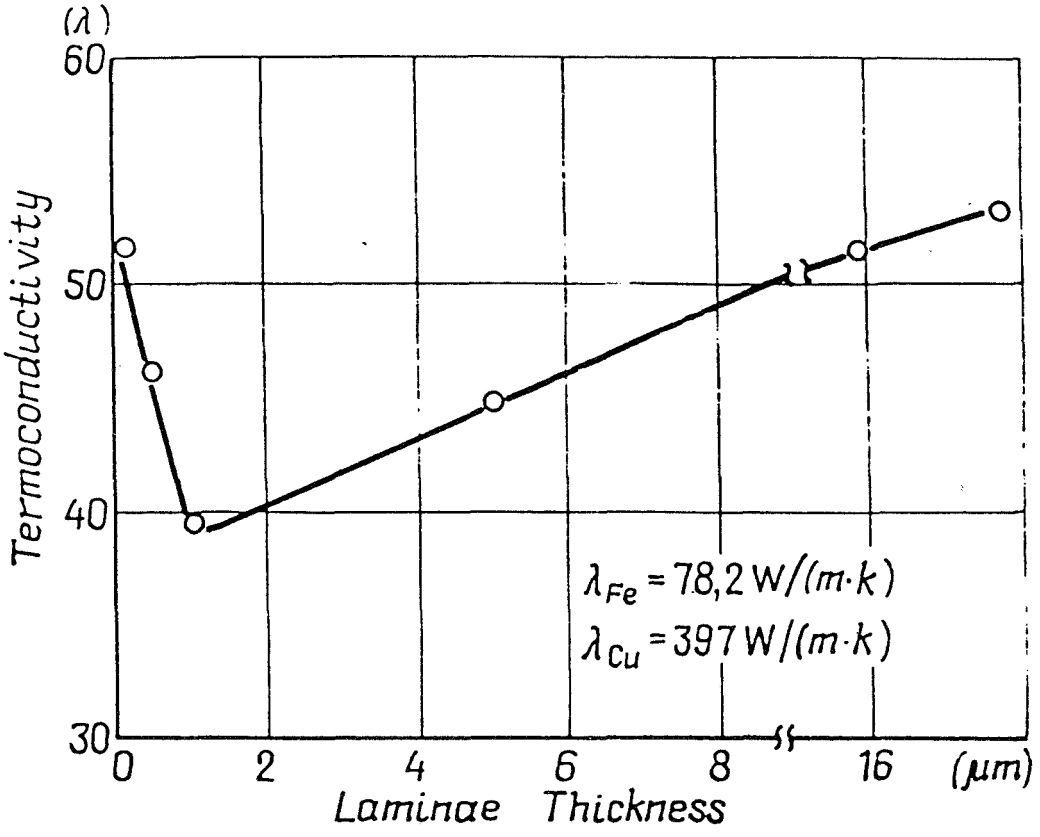

C-3

It should be noted that thermal conductivity of the condensate is much lower than could be expected from simple rule of mixtures. For this particular case the value would be 238 w/km, if calculated using the rule of mixtures.

This drop in thermal conductivity is believed to be associated with interfaces which in some way block the transfer of heat across it. Considering this assumption the expression for thermal conductivity of the microlaminate can be written as

$$K = V_{f_{Cu}} \cdot K_{Cu} + V_{Fe} \cdot K_{Fe} + n_I \cdot K_I \qquad (1)$$

where V_f is the volume fraction, K the thermal conductivity and n_I is the number of interfaces given by the expression

$$n_I = t/\Delta x - 1 \qquad (2)$$

where t is the laminate thickness and Δx is the laminae thickness.

Using Equations 1 and 2, and the data shown in Figure 1, contribution of interfaces to the thermalconductivity is calculated. Shonw in the figure below is the thermal conductivity contribution due to interfaces as a function of the number of interfaces.

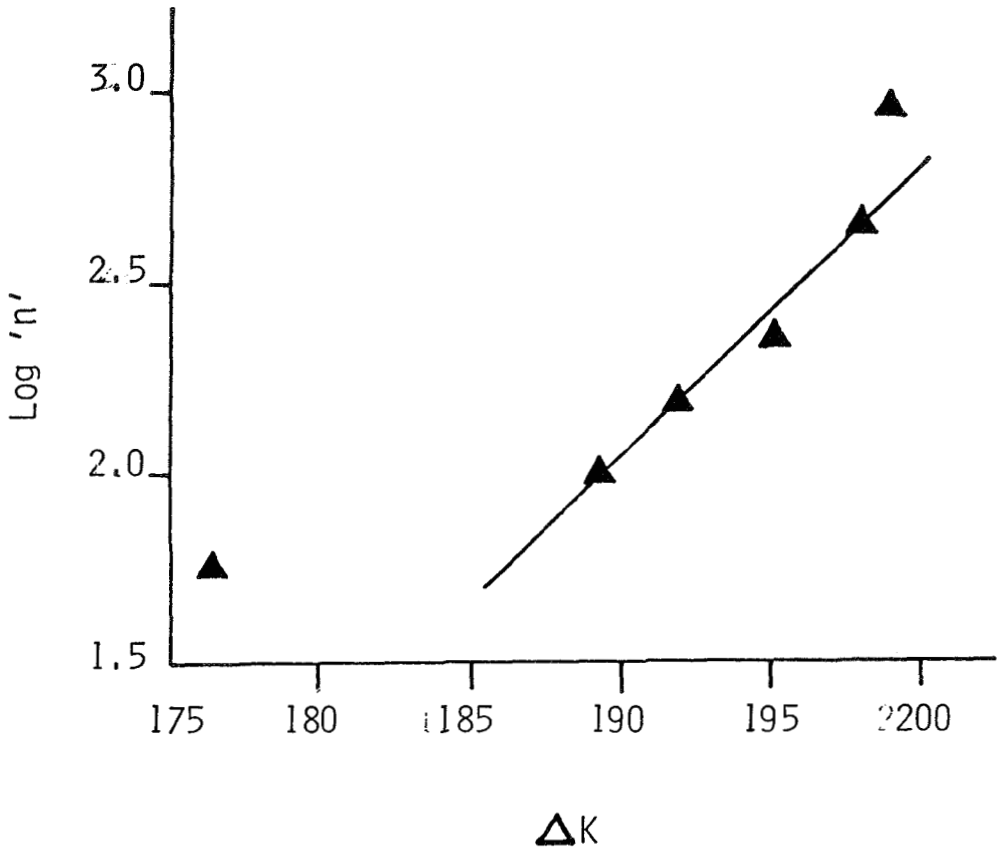

It can be seen that the data can be fitted into an expression of the form

$$n_I = A \exp^{-\Delta K_c}$$

Where c is the slope of the plot Log $n_I V_S \Delta K$ and A is a constant

The constant 'A' should account for the materials characteristics and types of phonon scattering mechanisms involved at the interfaces. Detailed investigations are required to establish a qualitative expression for 'A' in terms of materials properties and phonon scattering modes.

However assuming that the interfaces would behave in the same manner as in case of Fe-Cu microlaminate we have calculated assuming the same percentage contribution by the interfaces, the thermal conductivity of MCrAlY/αAl_2O_3 microlaminate. The data is plotted in the figure below.

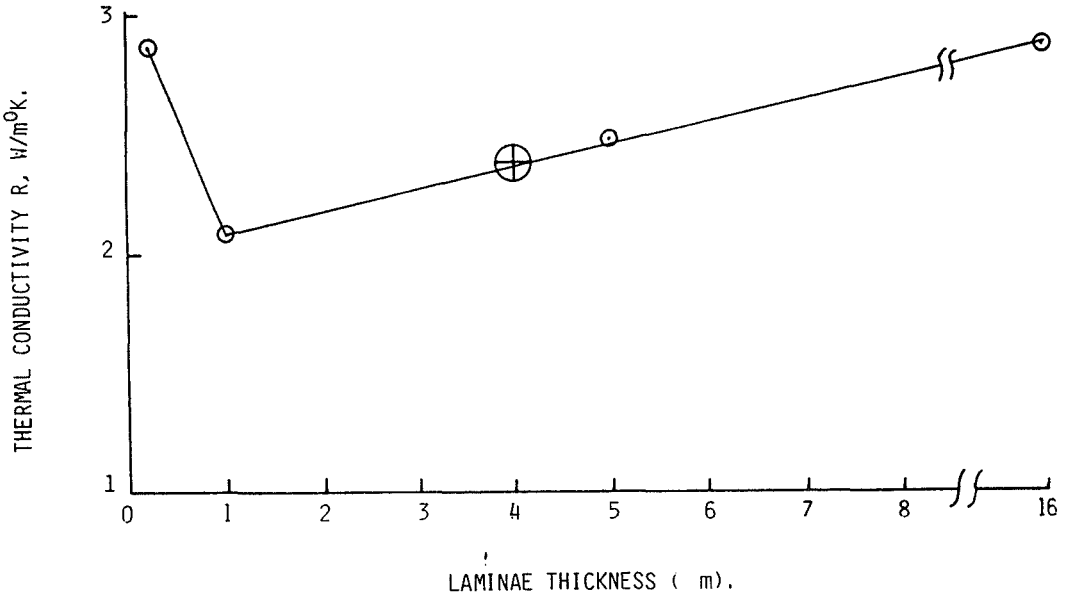

Thermal Conductivity (direction $\perp$ to laminae plane) vs. laminae thickness for MCrAlY - αAl_2O_3 microlaminates.

In practice 15 mils of ZrO_2 coating is used as thermal barrier coating. For 15 mil thickness and 1μm laminae thickness the number of interfaces would be 224. The thermal conductivity of a laminate with these many interfaces would be equal to 2.38-2.4 w/mk. This value is comparable to the thermal conductivity of pure ZrO_2 coating which is 3 w/mk.

These simple calculations therefore indicate that microlaminate composites offer as excellent potential as thermal barrier coatings.

PROPOSED FABRICATION TECHNIQUE

Electron beam evaporation/deposition alternately from two sources onto superalloy substrates (see Figure). This is compatible with current MCrAlY deposition methodology.

PROPERTIES TO BE MEASURED

Thermal Conductivity

Fracture Toughness - Using an indentation method (Evans et al., J. A. P. 53, 312, 1982).

Properties to be measured as deposited and after thermal cycling.

CONCLUSIONS

Microlaminate composites offer the potential to be a low thermal conductivity high fracture toughness material to be used as a thermal barrier coating on superalloy blades and vanes as an alternate to monolithic ceramic coatings.

HIGH TIME SERVICE EVALUATION OF THERMAL BARRIER COATINGS ON THE ROLLS-ROYCE RB211 ENGINE

F. Chris Toriz
Rolls-Royce Inc.
Atlanta, Georgia

One of the main concerns of airline operators for the use of thermal barrier coatings (TBC) in the turbine is that the coating will spall and cause a pre-mature engine removal. Even though much cyclic data is available on TBC's, high time data is much harder and expensive to come by. The typical 150 hour type test used to qualify new hardware, or modifications, falls far short of the 5-10,000 hour experience desired.

One way to obtain data demonstrating the longevity of TBC's is through a service evaluation program on a commercial engine. For a meaningful evaluation of the TBC system it must be applied to a component which operates in a typical hot end environment. In addition the component performance should not suffer if the coating is lost. For these reasons Rolls-Royce chose to coat the IP turbine nozzle guide vanes, and run these in an RB211 engine.

Two ceramic top coats and several different bond coats were tested in a rainbow fashion on several engines. Three layer Magnesium Zirconate was used as a base line. Various Yttria stabilized Zirconia ceramics were used a top MCrAlY bond coats which were applied by various techniques. Some of the coated vanes have now accumulated over 5000 hours. This report presents the results from the first 2 sets with 2500 and 4200 hours of service respectively.

1. Compare various TBC systems in the turbine environment (compare to Mag Zirc).

2. Determine effects of long time exposure (and of cycles).

3. Correlate Carousel rig testing vs. engine data.

4. Identify new coating systems worth testing.

Figure 1. - Thermal barrier coating (TBC's) service evaluation goals.

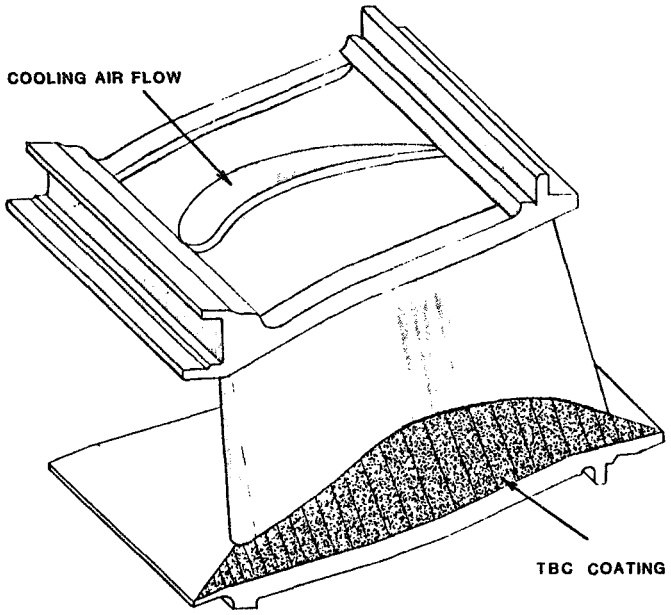

Figure 2. - RB-211 intermediate-pressure (IP) turbine nozzle guide vane (NGV) with thermal barrier coating for service evaluation.

IDENT	BOND	CERAMIC	BOND COAT METHOD	ON ENGINES	TOTAL VANES
A	443+441	210 MZ	Plasma	1234	22
B	443	210 MZ	Plasma	12	12
C	443	YSZ	Plasma	1234	22
D	NiCoCrAlY	YSZ	LPPS	1a234	20
E	NiCoCrAlY	YSZ	Ar Shrouded	1234	21
G	NiCoCrAlY	YSZ	Air Sprayed	34	10
Uncoated Vanes					5
TOTALS					114

Figure 3. - RB-211 service evaluation of intermediate-pressure turbine nozzle guide vanes with thermal barrier coatings.

ENGINE BUILD	ENGINE No.	FLIGHT HOURS	INSPECTED at-hours
1	10676	5068	4160
2	10575	5250	2539
3	10650	3818	3818
4	10398	4272	--

Figure 4. - Thermal barrier coating intermediate-pressure turbine nozzle guide vane service evaluation as of March 1985.

BUILD 1			BUILD 2		
	Coating	Position		Coating	Position
A	M443+441+210MZ	6:00	A	M443+441+210MZ	3:30
B	M443 + 210MZ	3:00	B	M443 + 210MZ	1:30
C	M443 + YSZ	12:00	C	M443 + YSZ	11:00
E	NiCoCrAlY[1] + YSZ	9:00	D	NiCoCrAlY[2] + YSZ	9:00
			E	NiCoCrAlY[1] + YSZ	6:00

M=Metco, MZ=Mag Zirc
YSZ=Yttria stabilized Zirconia

1=Ar Shrouded, 2=LPPS

Figure 5. - RB-211 service evaluation of intermediate-pressure turbine nozzle guide vanes with thermal barrier coatings.

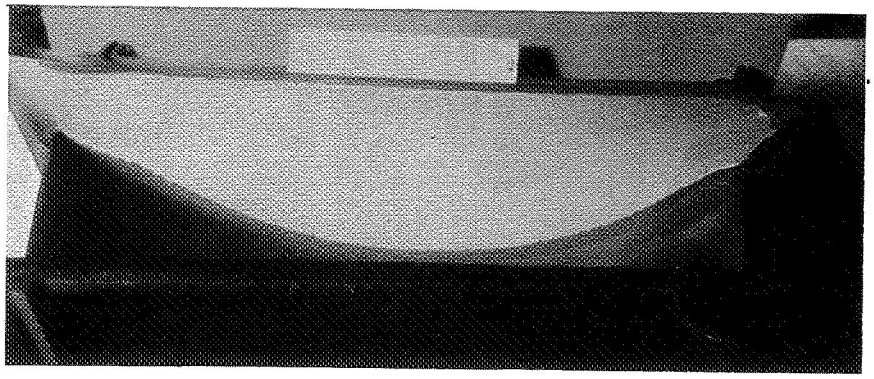

3 Layer Mag. Zirc (Typical)

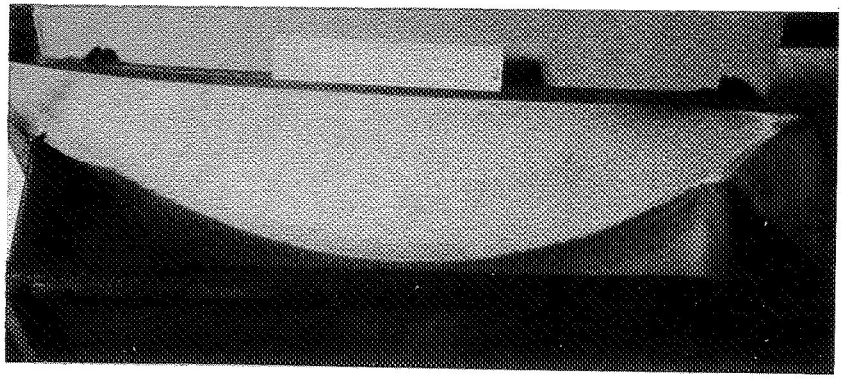

2 Layer Mag. Zirc (Typical)

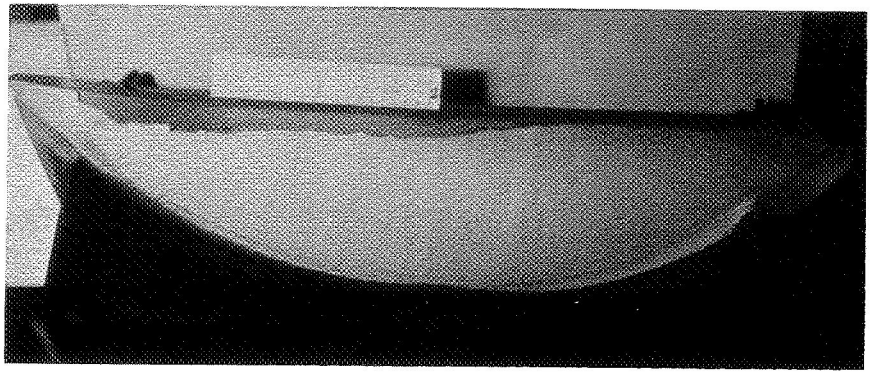

3 Layer Mag. Zirc (Worst)

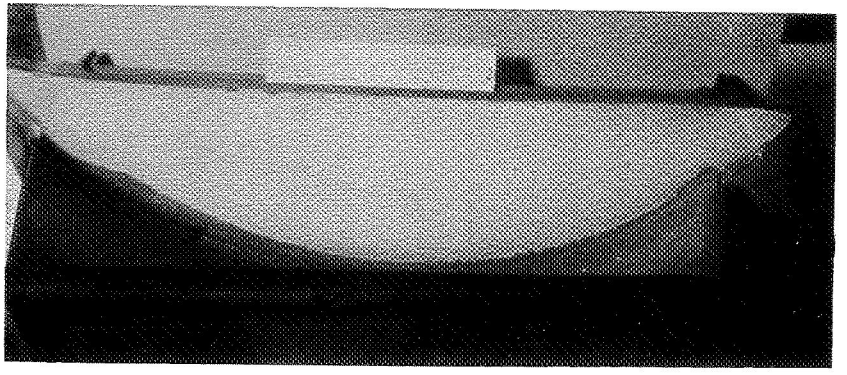

2 Layer Mag. Zirc (Worst)

Figure 6. - RB-211 service evaluation of engine build no. 2 with 2539 hr/1353 cycles.

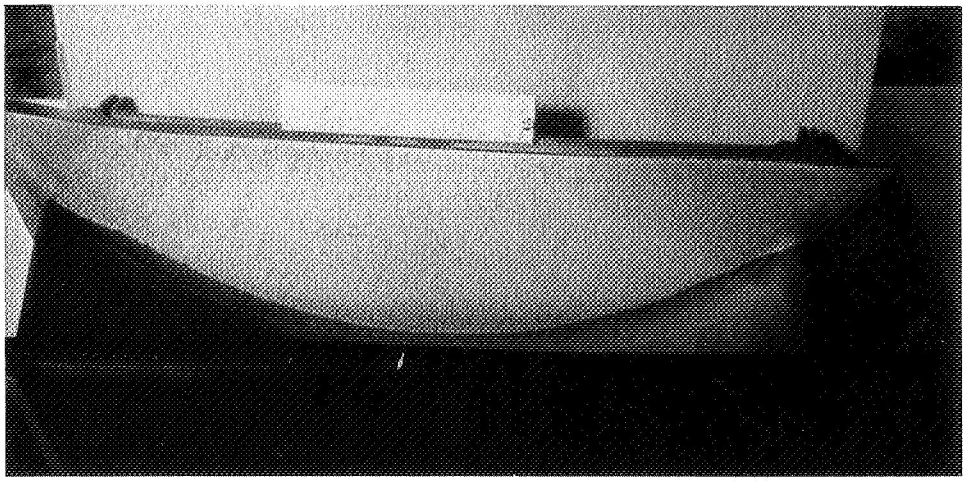

METCO 443 + YSZ (Typical)

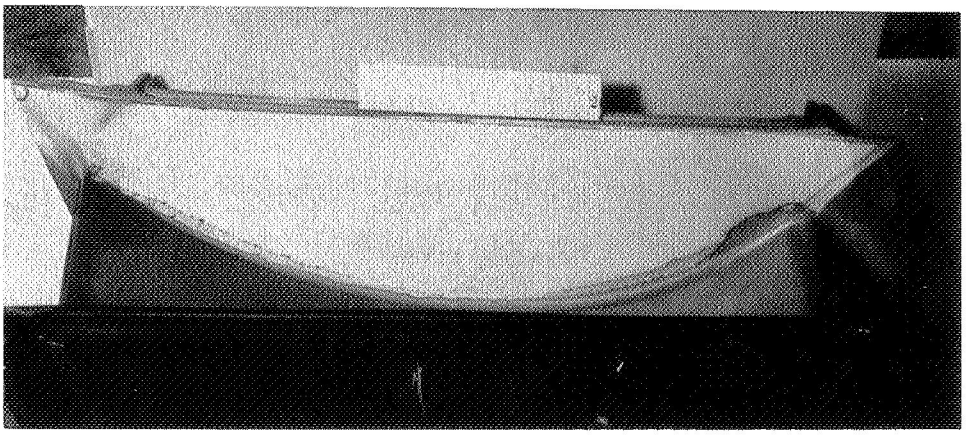

LPPS MCrAlY + YSZ (Typical)

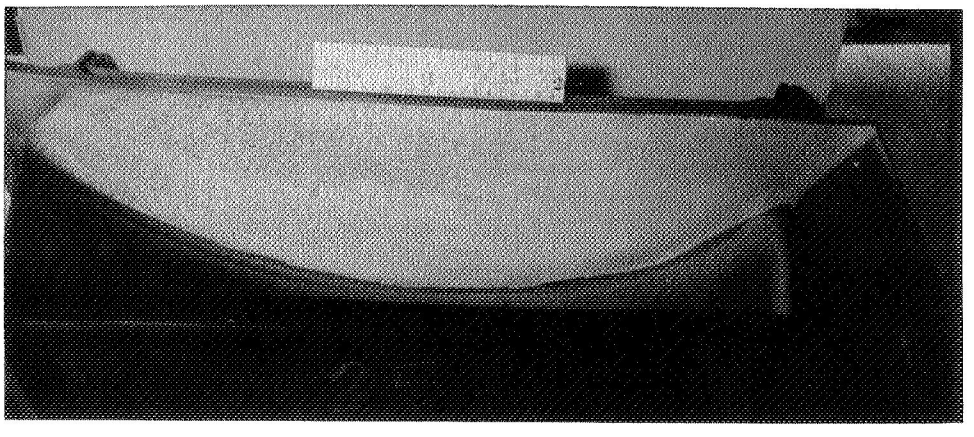

Argon Shrouded MCrAlY + YSZ (Typical)

Figure 6. - Concluded.

BUILD 1			BUILD 2		
	Coating	Position		Coating	Position
A	M443+441+210MZ	6:00	A	M443+441+210MZ	3:30
B	M443 + 210MZ	3:00	B	M443 + 210MZ	1:30
C	M443 + YSZ	12:00	C	M443 + YSZ	11:00
E	NiCoCrAlY[1] + YSZ	9:00	D	NiCoCrAlY[2] + YSZ	9:00
			E	NiCoCrAlY[1] + YSZ	6:00

M=Metco, MZ=Mag Zirc
YSZ=Yttria stabilized Zirconia

1=Ar Shrouded, 2=LPPS

Figure 7. - RB-211 service evaluation of intermediate-pressure turbine nozzle guide vanes with thermal barrier coatings.

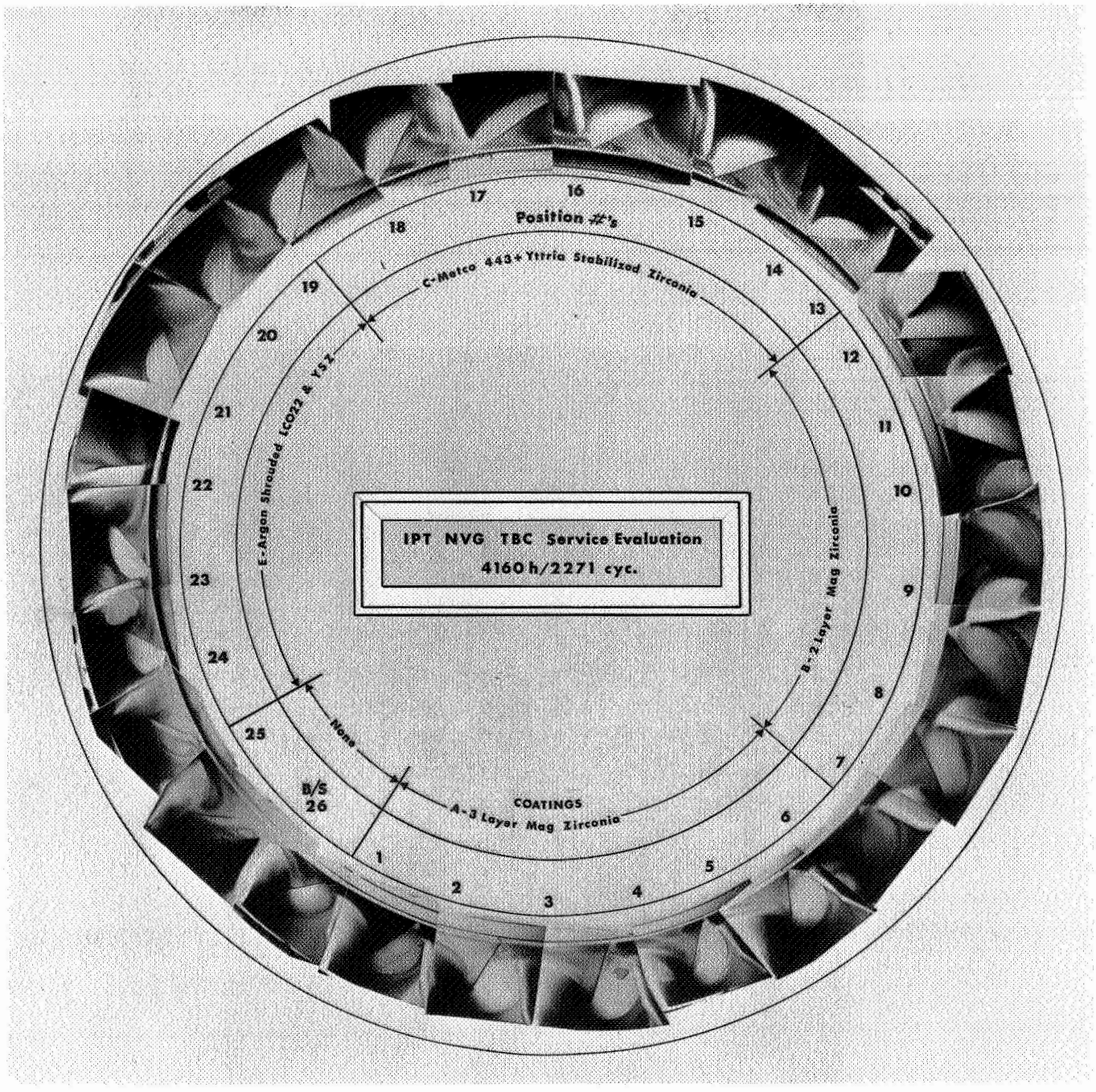

Figure 8. - RB-211 service evaluation.

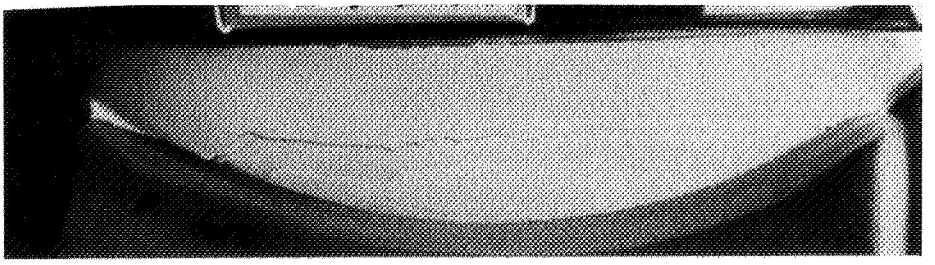

3 Layer Mag. Zirc

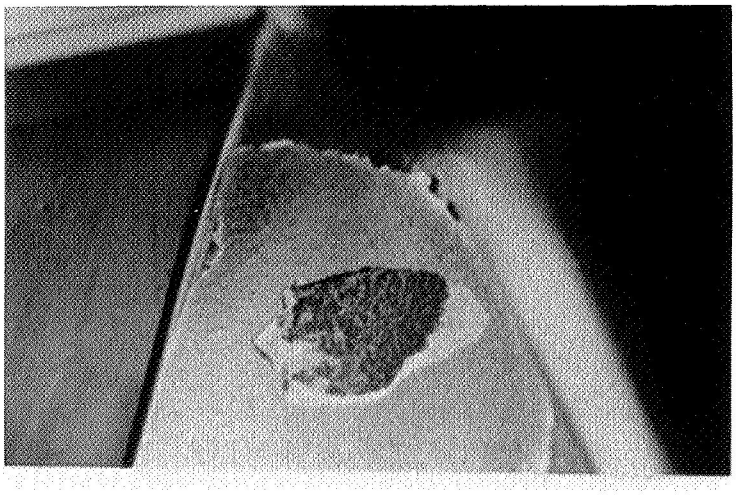

3 Layer Mag. Zirc

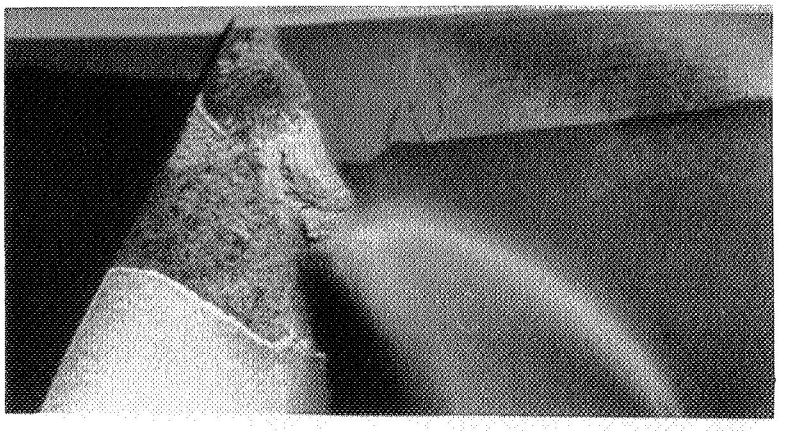

2 Layer Mag. Zirc (Worst)

Figure 9. - RB-211 service evaluation of engine build no. 1 with 4106 hr/2271 cycles

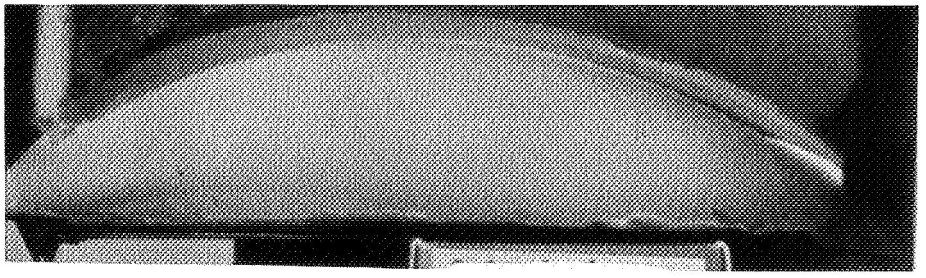

2 Layer Mag. Zirc (Typical)

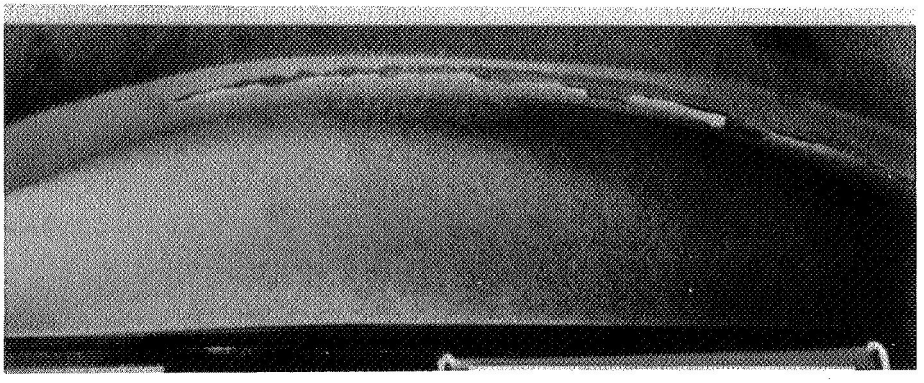

METCO 443 (Worst) + YSZ (Typical)

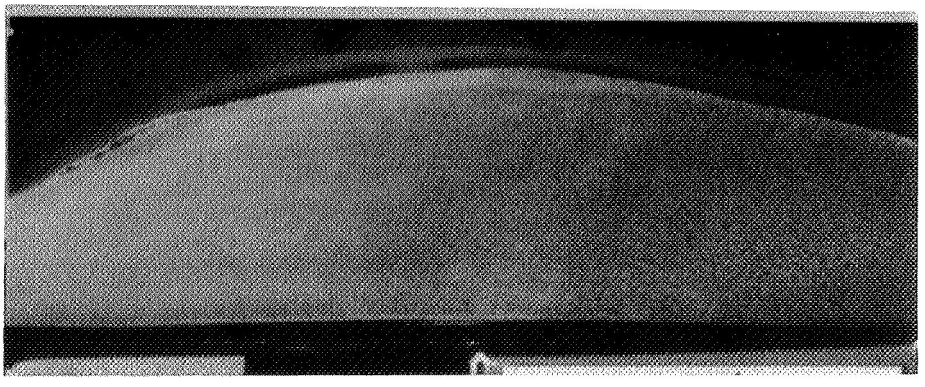

Argon Shrouded MCrAlY + YSZ (Worst)

Figure 9. - Concluded.

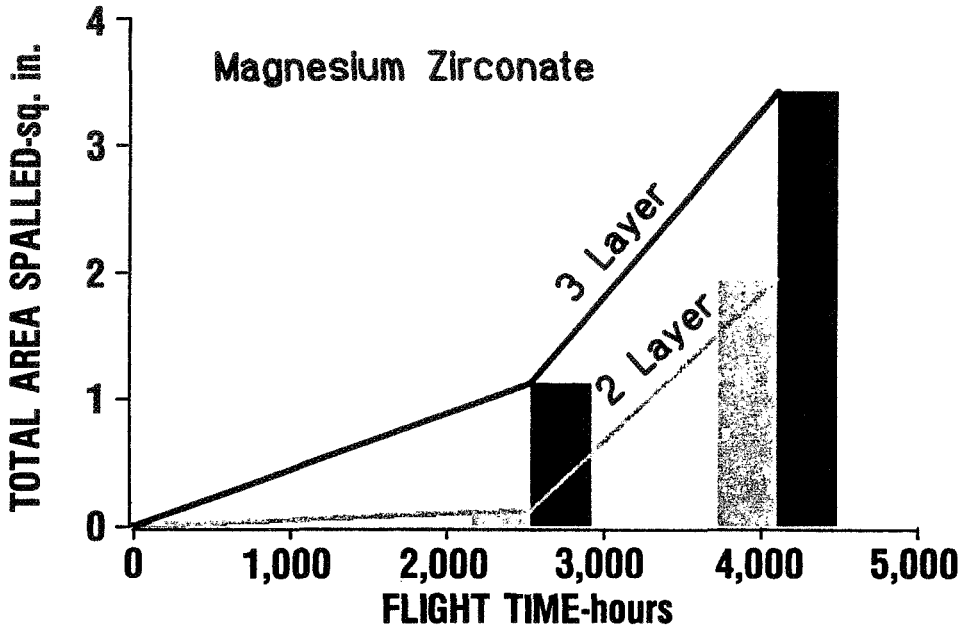

Figure 10. - Service evaluation of thermal barrier coatings on intermediate-pressure turbine nozzle guide vanes.

1. Mag Zirc is not adequate in the turbine.

2. Two layer Mag Zirc will out last 3 layer MZ.

3. Yttria stabilized Zirconia should do the job.

4. To date the Argon Shrouded bond coat looks best.

Figure 11. - Thermal barrier coating service evaluation conclusions.

THERMAL BARRIER COATINGS FOR THE SPACE SHUTTLE MAIN ENGINE TURBINE BLADES

B. N. Bhat, H. L. Gilmore and R. R. Holmes
Materials and Processes Laboratory
National Aeronautics and Space Administration
Marshall Space Flight Center, AL 35812

The Space Shuttle Main Engine (SSME) turbopump turbine blades experience extremely severe thermal shocks during start-up and shut-down. For instance, the high pressure fuel turbopump turbine which burns liquid hydrogen operates at approximately 1500°F, but is shut down fuel rich with turbine blades quenched in liquid hydrogen (-423°F). This thermal shock is a major contributor to blade cracking. The same thermal shock causes the protective ZrO_2 thermal barrier coatings to spall or flake off, leaving only the NiCrAly bond coating which provides only a minimum thermal protection. The turbine blades are therefore life limited to about 3000 sec. for want of a good thermal barrier coating.

NASA-MSFC is active in developing a suitable thermal barrier coating (TBC) for the SSME turbine blades. Various TBCs developed for the gas turbine engines were tested in a specially built turbine blade tester (also called thermal cycling tester or burner rig, Figure 1). This tester subjects the coated blades to thermal and pressure cycles similar to those during actual operation of the turbine (Figures 2, 3). The coatings were applied using a plasma spraying technique, both under atmospheric conditions and in vacuum. Results are given in Table 1. In general vacuum plasma sprayed coatings performed much better than those sprayed under atmospheric conditions A 50-50 blend of Cr_2O_3 and NiCrAly, vacuum plasma sprayed on SSME turbopump turbine blades appear to provide significant improvements in coating durability and thermal protection.

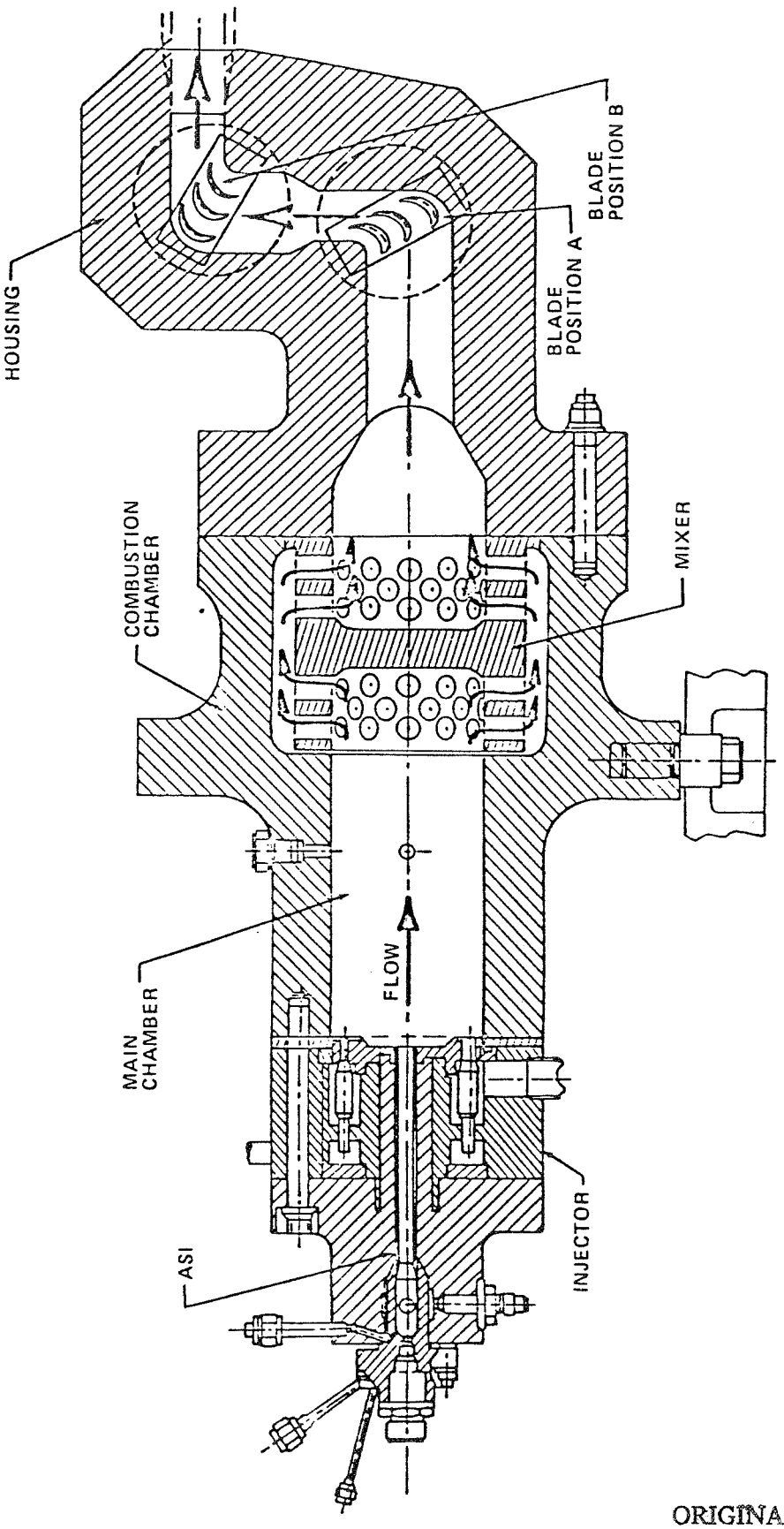

R-TEST 338

FIGURE 1. THERMAL CYCLING TESTER

ORIGINAL PAGE IS
OF POOR QUALITY

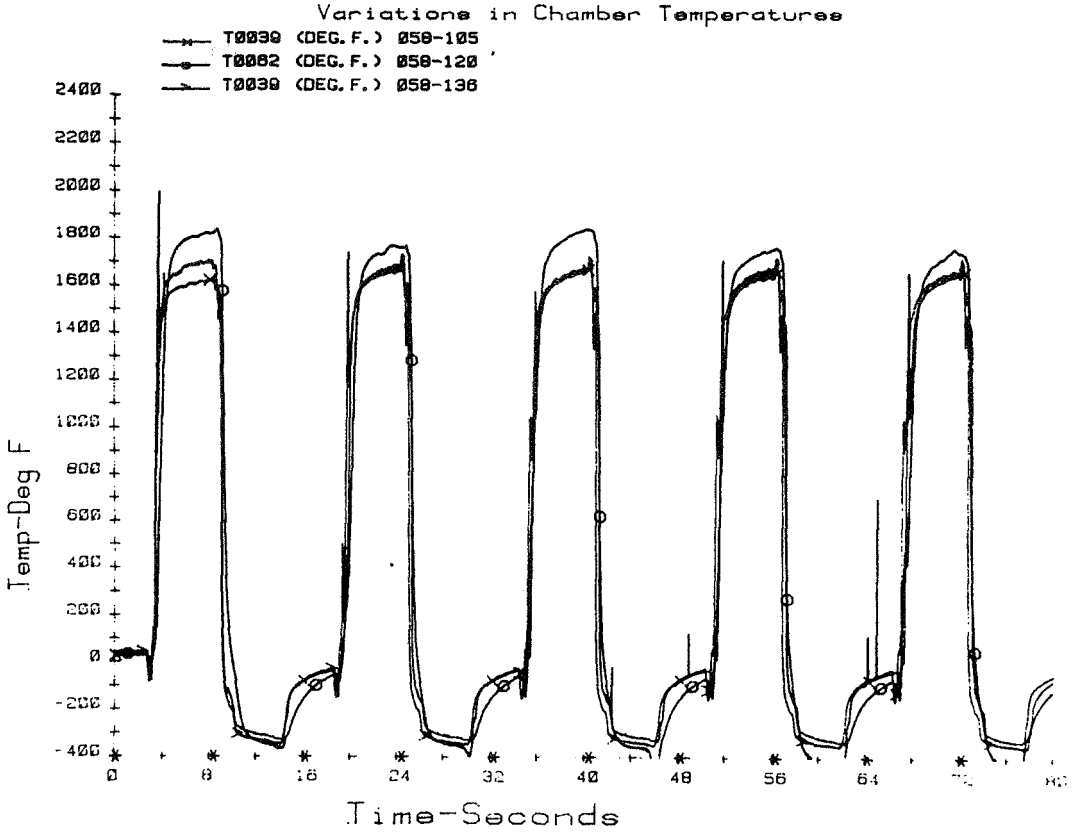

FIGURE 2

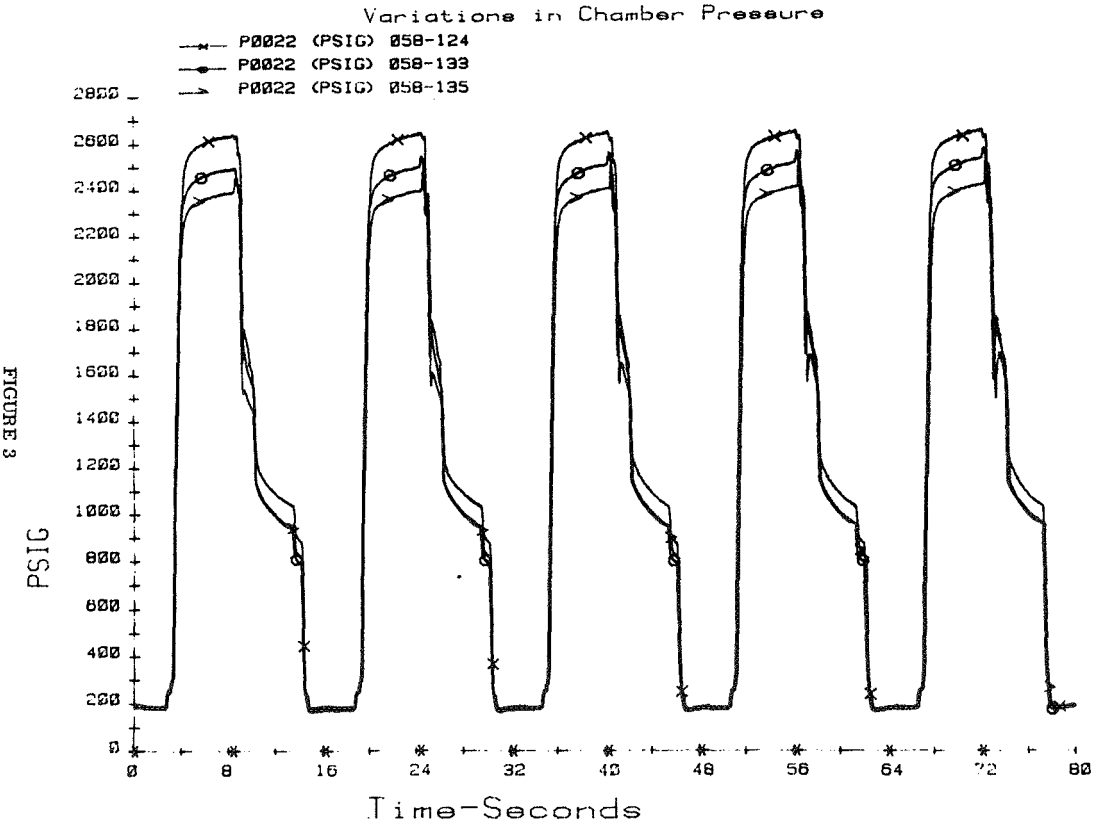

FIGURE 3

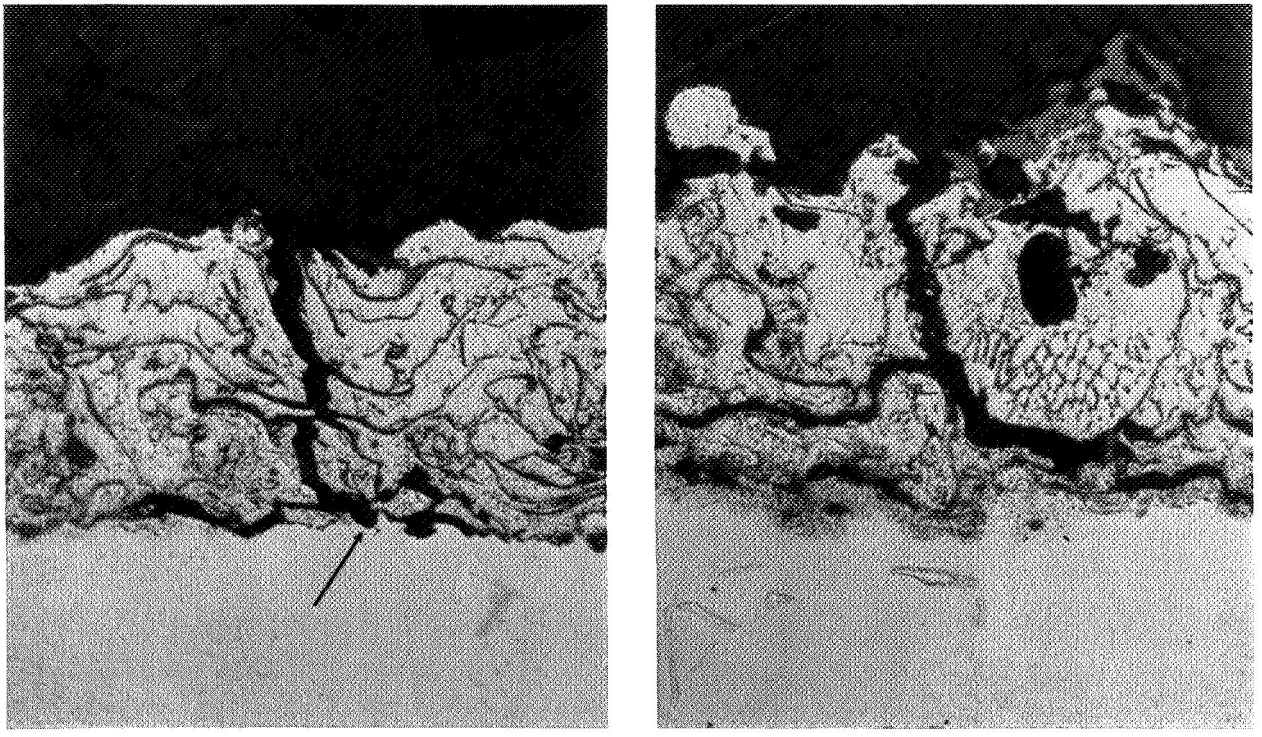

A B

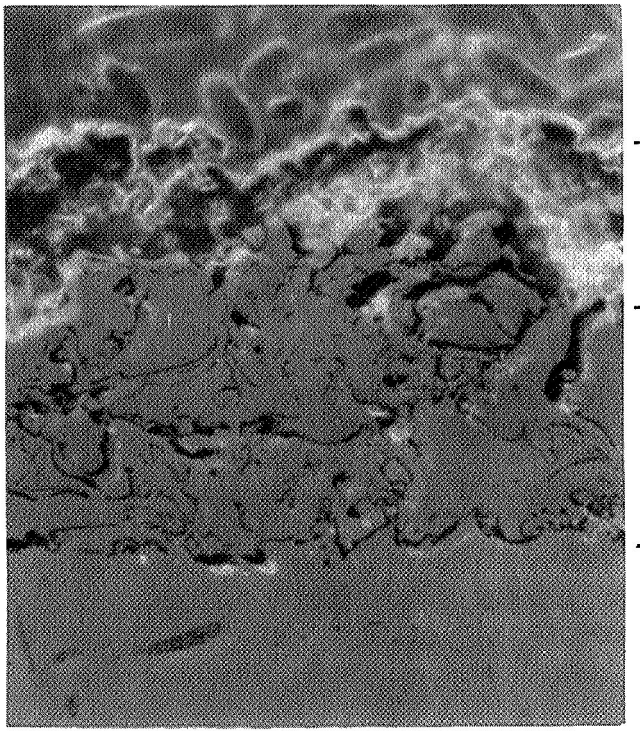

C

Figure 4 - NiCrAlY Airfoil Leading Edge Cracking on Blade 9Z13 From HPFTP 9005 (A&B) and Thin Layer of Zirconia on NiCrAlY (C). Mag. 400X

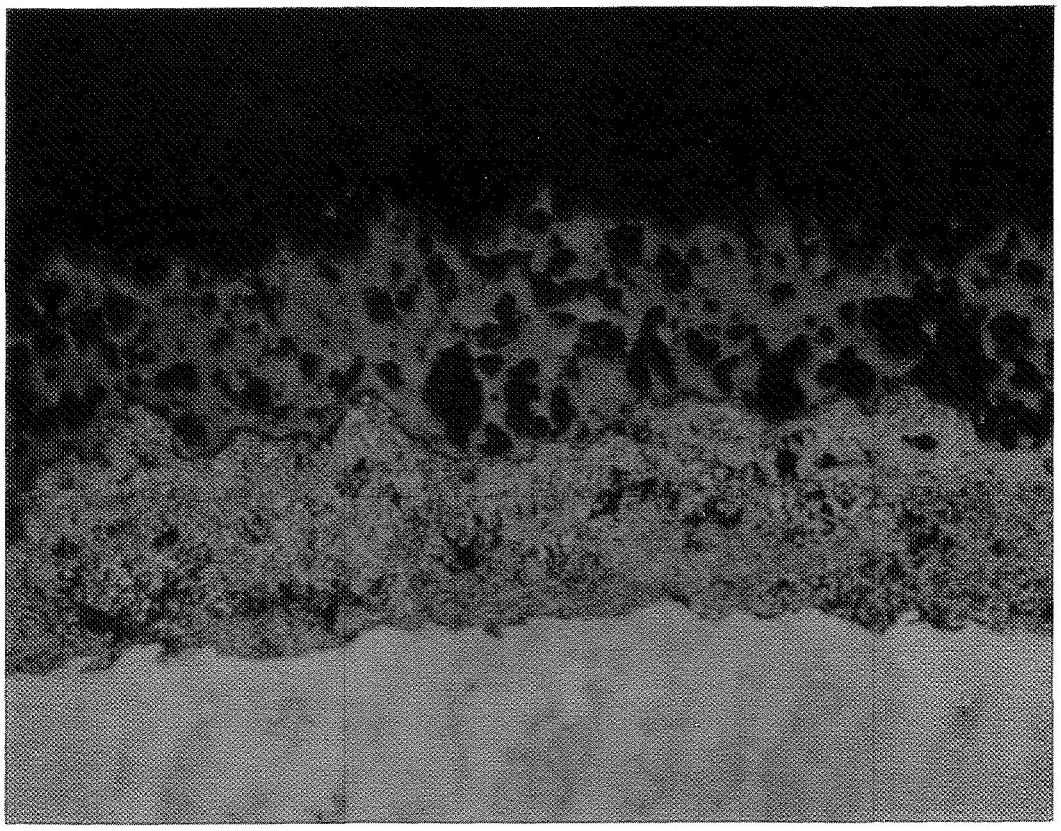

Figure 5 - NiCrAly Airfoil Leading Edge Applied by low Pressure Plasma Flame Spray Showing Improvements: (1) No cracks in NiCrAly bond coating. (2) No oxide layers in NiCrAly bond coating

Mag. 200X

TABLE 1

PLASMA COATED TURBINE BLADES

BURNER RIG CYCLIC THERMAL TESTING

25 CYCLES (1700°F TO -350°F

VACUUM SPRAY POWER MESH	BOND COATING*	THERMAL BARRIER COATING (4 MIL)	RATING** 100=PERFECT	COMMENTS
-200/+325	NiCrAlY	–	95	NO SPALLING
-400	CoCrAlY	–	94	NO SPALLING
-400	NiCrAlY	–	93	NO SPALLING
-200/+325	NiCrAlY	Cr_2O_3.50 NiCrAlY	94	NO SPALLING
-400	CoCrAlY	Cr_2O_3.50 CoCrAlY	94	NO SPALLING
-400	NiCrAlY	Cr_2O_3.50 NiCrAlY	93	NO SPALLING
-200/+325	NiCoCrAlY	–	25	SPALLING
ATMOSPHERIC SPRAY SSME BASELINE				
-200/+325	NiCrAlY	–	35	SPALLING

* BOND COATING ONLY : 6 MIL THICKNESS
BOND COATING BEFORE ADDING THERMAL BARRIER COATING: 3 MIL THICKNESS

** 3 BLADES EACH SAMPLE

CYCLIC STRESS ANALYSIS OF CERAMIC COATED GAS TURBINE SEALS

Joe Padovan
University of Akron
Akron, Ohio 44325

Dan Dougherty
General Tire and Rubber Co.
Akron, Ohio

Bob Hendricks
NASA Lewis Research Center
Cleveland, Ohio 44135

Through the use of the Finite Element Method, the cyclic thermomechanical response of ceramic coated gas turbine parts is considered. The analysis includes temperature dependent elastic-plastic-creep material properties and cyclic thermal loads. To demonstrate the cyclic thermomechanical response, a ceramic coated outer gas path seal is studied. The analysis will estimate the significant residual stress field created by the cyclic thermal loads.

*Work supported by NASA Lewis Research Center under Grant NAG3-265.

TABLE I.

% YSZ/CoCrAlY:		100/0	85/15	70/30	40/60	MAR-M-50
material set #:		1	2	3	4	5
property	temperature(°F)					
density(lb/in^3)	all	.155	.180	.205	.254	.320
poisson ratio	all	.25	.26	.27	.28	.30
thermal cond. (BTU/min-in-°F) ($X\ 10^{-4}$)	0	4.09	4.09	4.09	4.09	422.98
	200	4.09	4.09	4.09	4.09	"
	500	4.09	4.66	4.98	5.38	"
	1000	4.33	6.26	7.46	8.35	"
	1500	4.74	8.51	10.60	12.20	"
	2000	5.70	11.64	14.85	17.66	"
	2500	8.11	16.30	20.95	25.52	"
specific heat (BTU/lb-°F)($X\ 10^{-2}$)	0	.126	.121	.116	.107	.097
	2500	.161	.161	.161	.158	.155
coef of expansion (in/in-°F) ($X\ 10^{-6}$)	0	4.08	3.28	3.36	3.64	6.40
	2500	4.83	7.70	8.38	9.52	12.20
Young's modulus (lb/in^2)($X\ 10^6$)	0	6.90	3.80	5.15	8.30	34.70
	2500	2.00	2.00	8.00	17.75	15.60
tensile strength (lb/in^2)($X\ 10^3$)	0	4.25	6.00	8.10	33.25	40.0
	2500	3.30	7.25	11.75	1.00	40.0

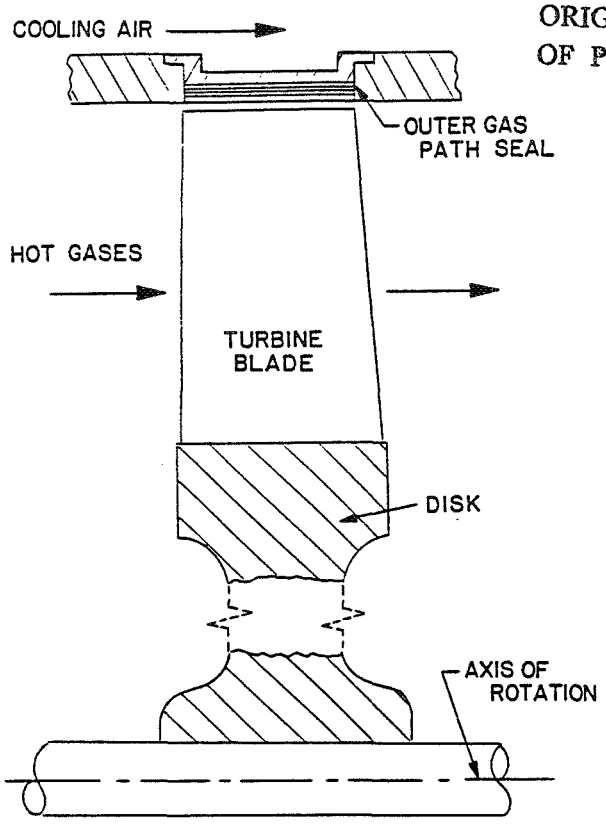

Figure 1.

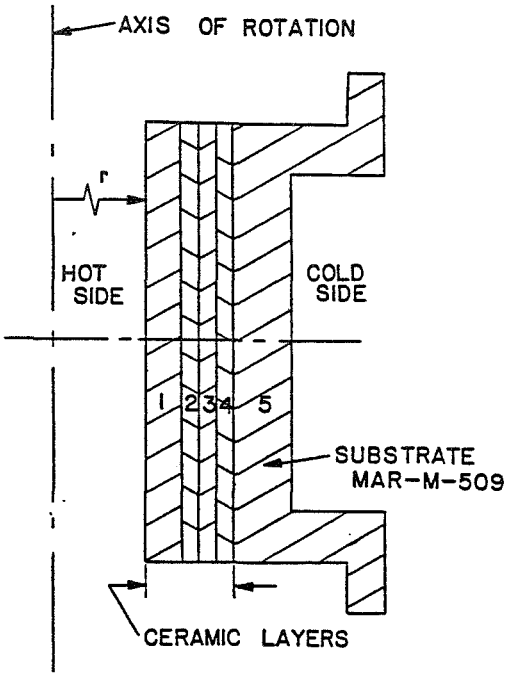

Figure 2.

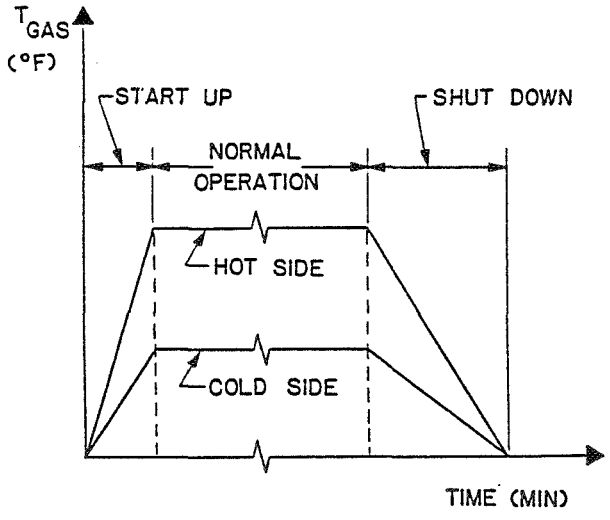

Figure 3.

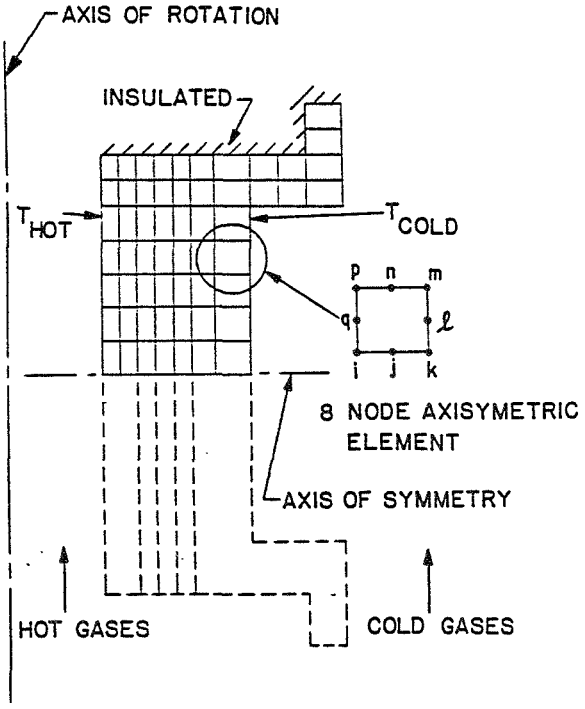

Figure 4.

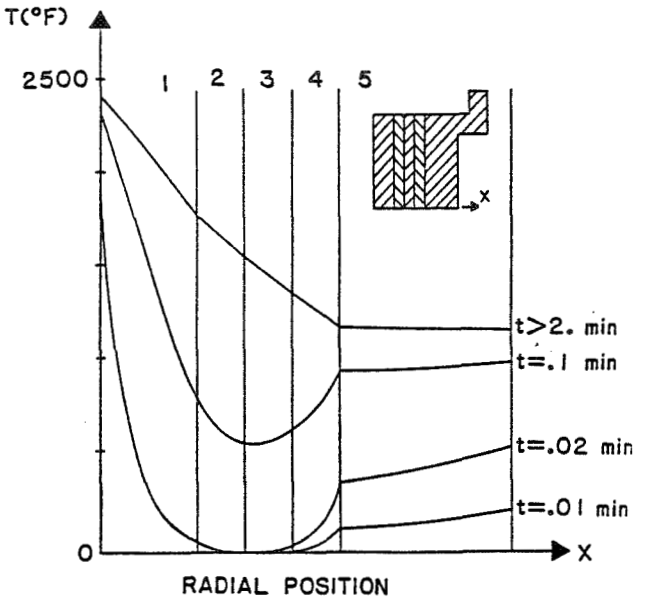

Figure 5.

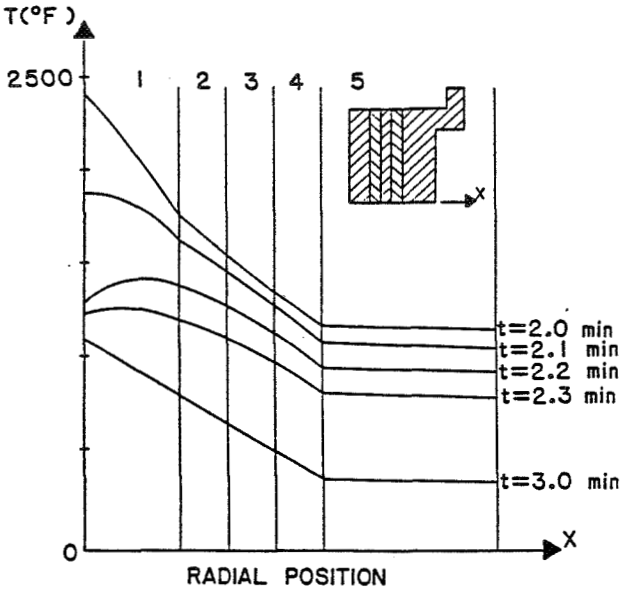

Figure 6.

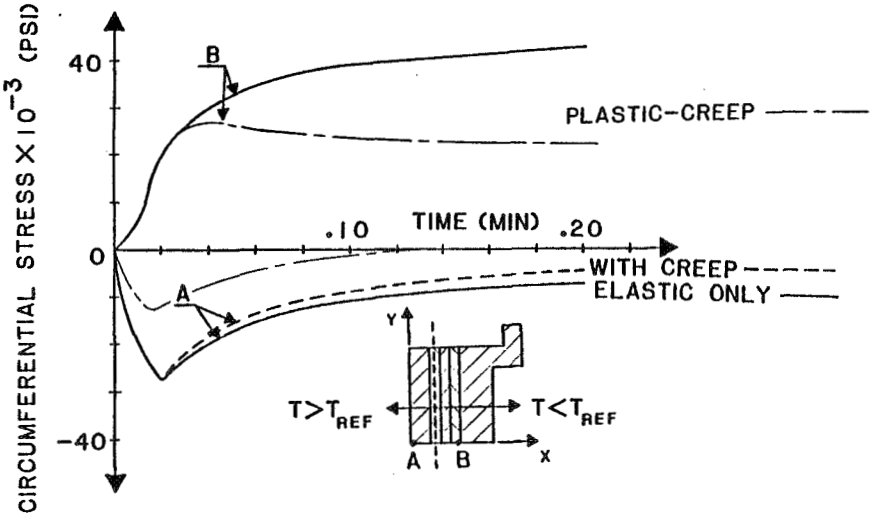

Figure 7.

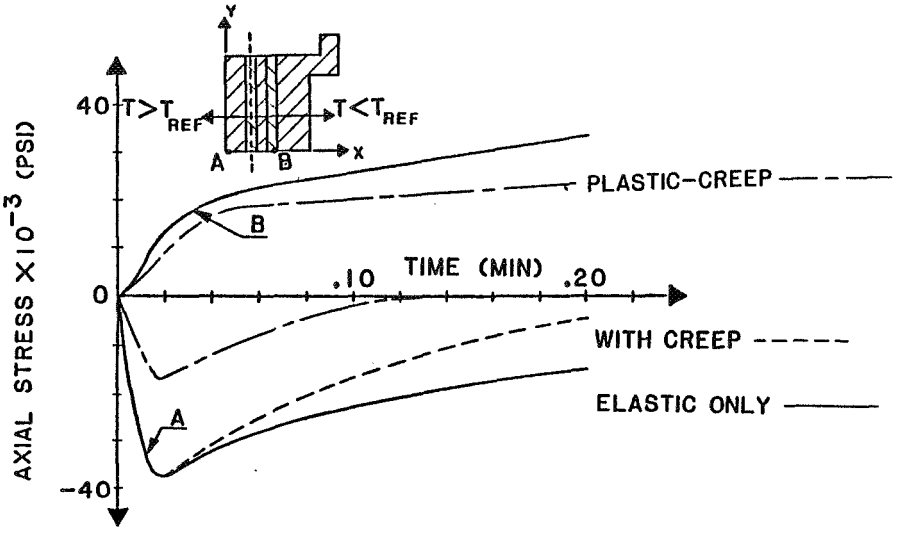

Figure 8.

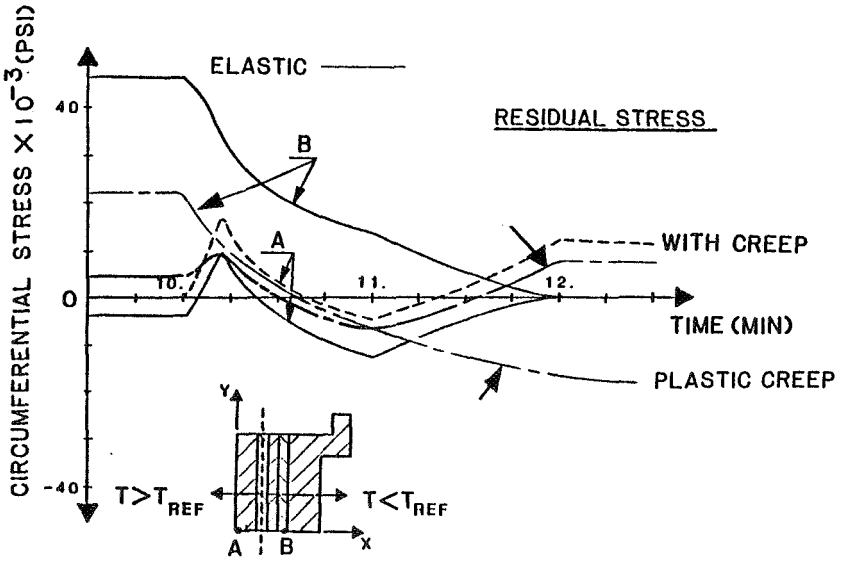

Figure 9.

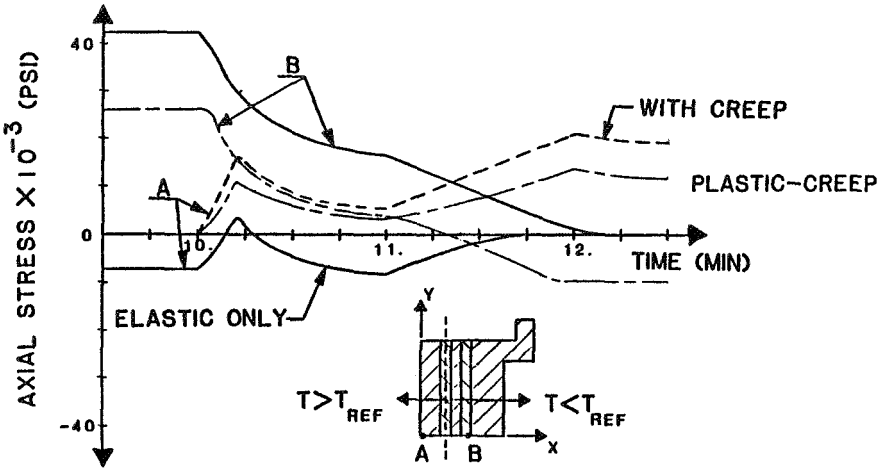

Figure 10.

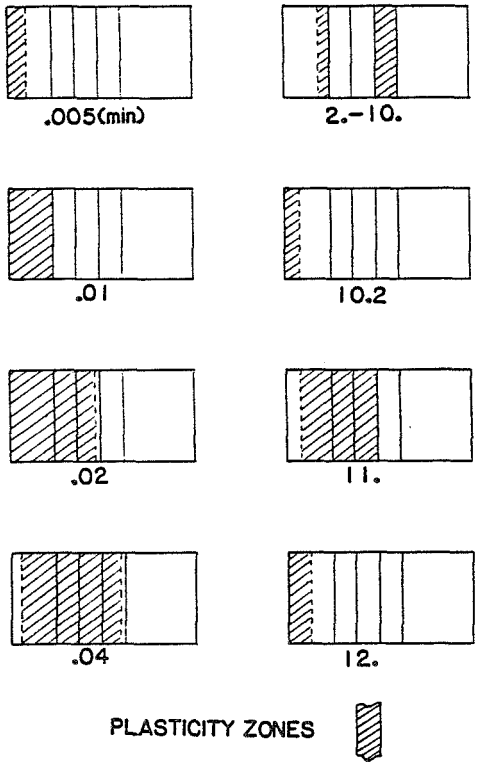

Figure 11.

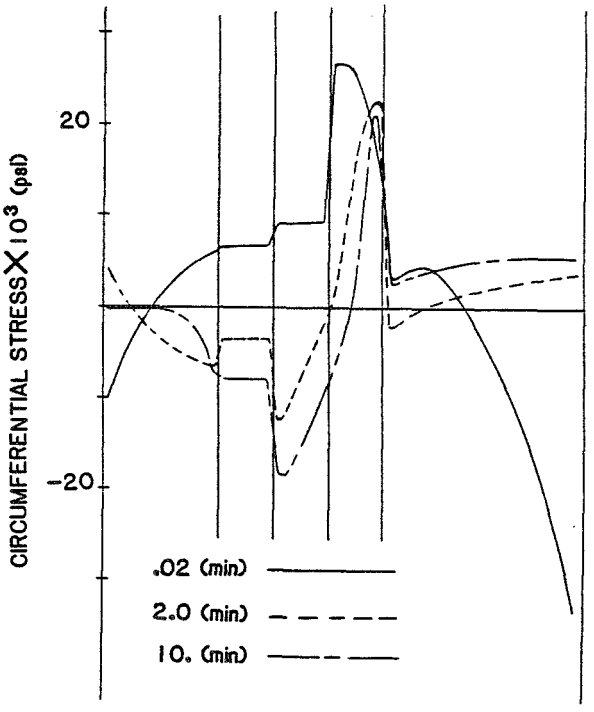

Figure 12.

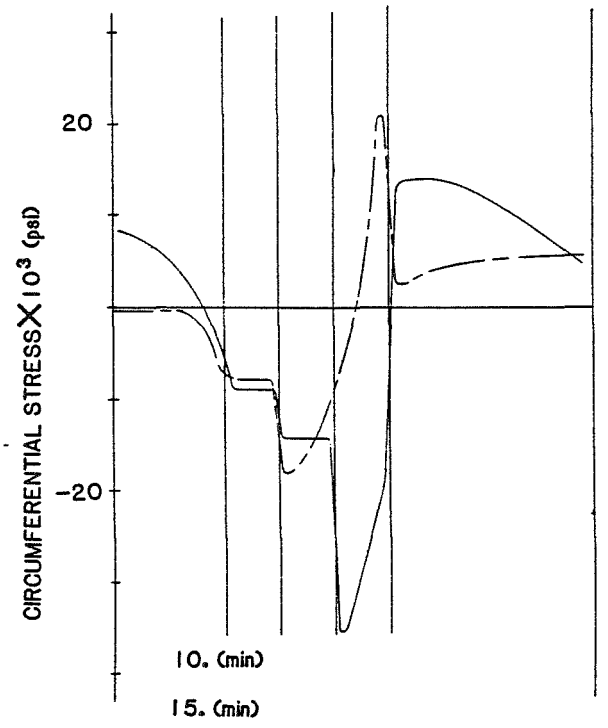

Figure 13.

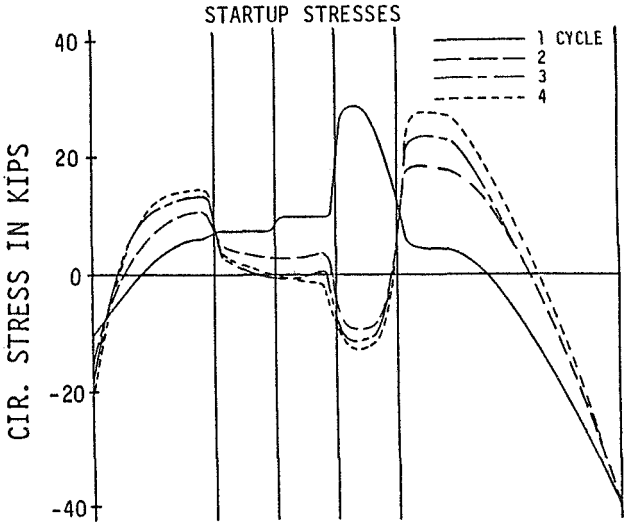

Figure 14.

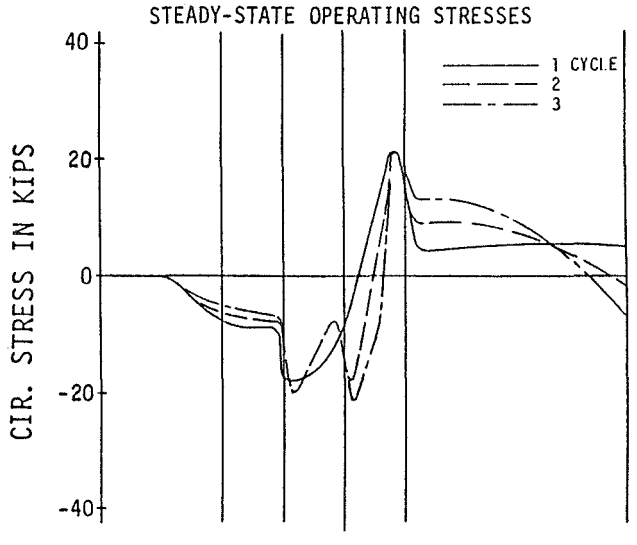

Figure 15.

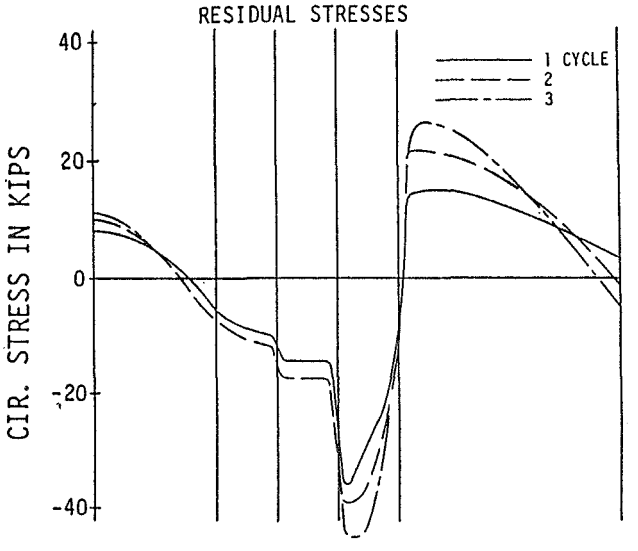

Figure 16.

N89-13663

FABRICATION OF STRAIN-ISOLATED CERAMIC COATED COMBUSTOR COMPONENTS

S. Rutter
Avco Lycoming Division
Stratford, Connecticut 06497

Avco is investigating the use of strain-isolated ceramic coated material to produce an AGT1500 combustor scroll-shaped transition duct which requires no air for film cooling. The scroll receives the exhaust of the can-style combustor liner and turns it into the annular inlet of the high pressure gas producer turbine nozzle.

Strain-isolation of plasma sprayed thermal barrier coating is achieved by placing a compliant pad between the structural base metal and the ceramic coating. The compliant pad is brazed to the metal structure. In order to achieve a good braze bond, the strain-isolating compliant pad and base metal must be closely matched in shape and tightly fixtured for joining. The complex geometry of the AGT1500 scroll makes it impractical to attach pads to the supporting structure in its finished shape. Instead the pads are brazed to flat stock and post-formed into scroll sections.

While test samples were successfully post-formed, plasma sprayed, and subjected to cyclic heating, the forming of full scale parts by normal methods resulted in tearing of the Hastelloy-X base metal because of embrittlement by the braze material. Several solutions were explored which finally resulted in the successful forming of full scale scroll parts.

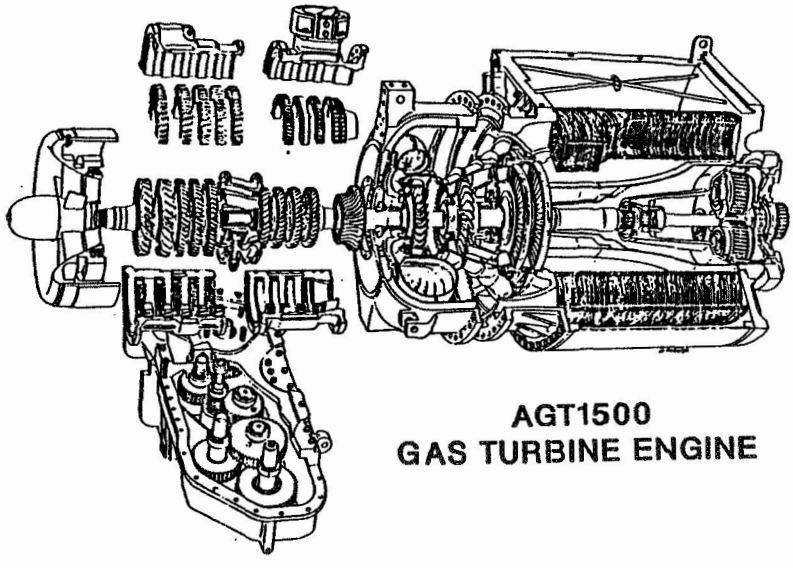

Figure 1.

FILM-COOLED PRODUCTION AGT1500 SCROLL

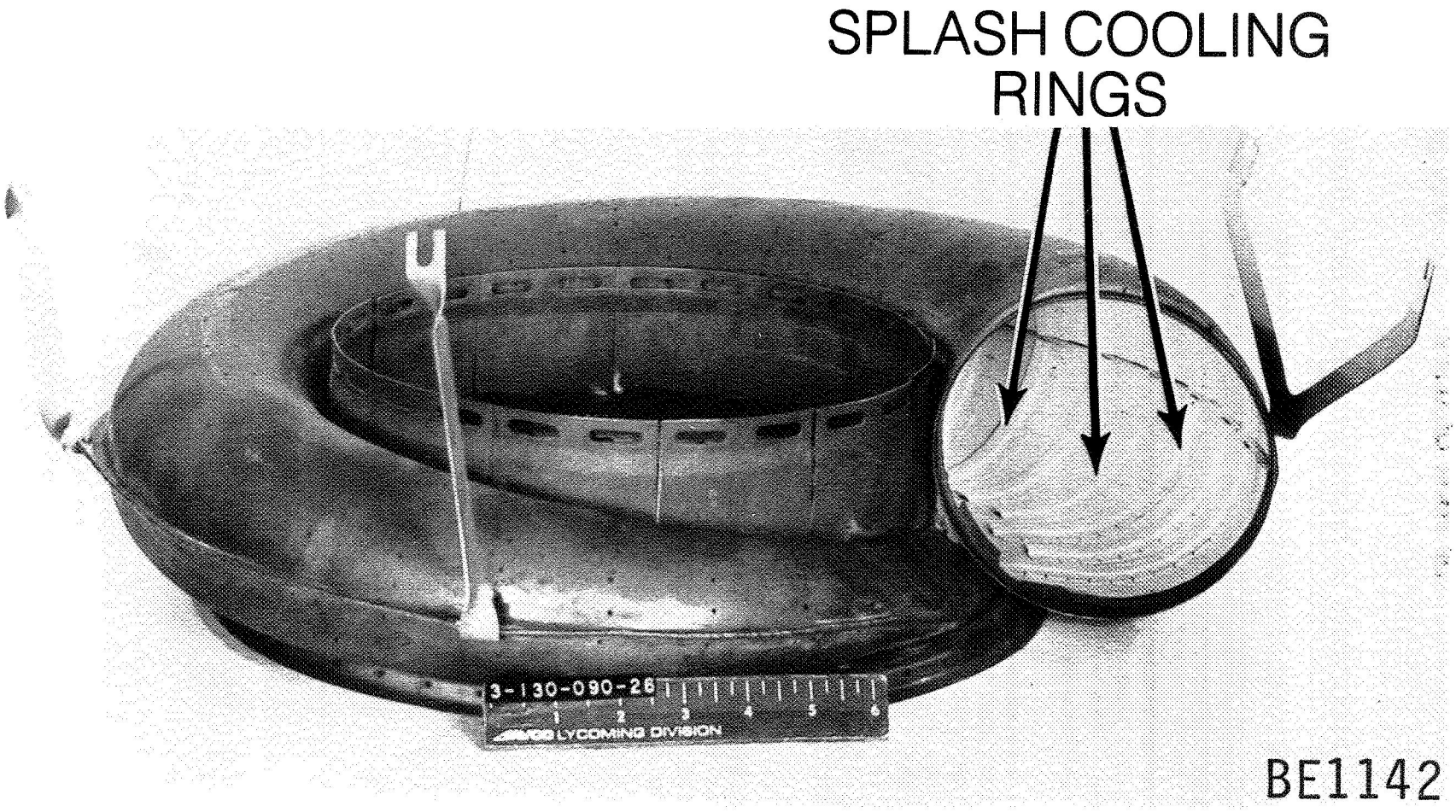

Figure 2.

SCHEMATIC OF STRAIN-ISOLATED CERAMIC COATING SYSTEM

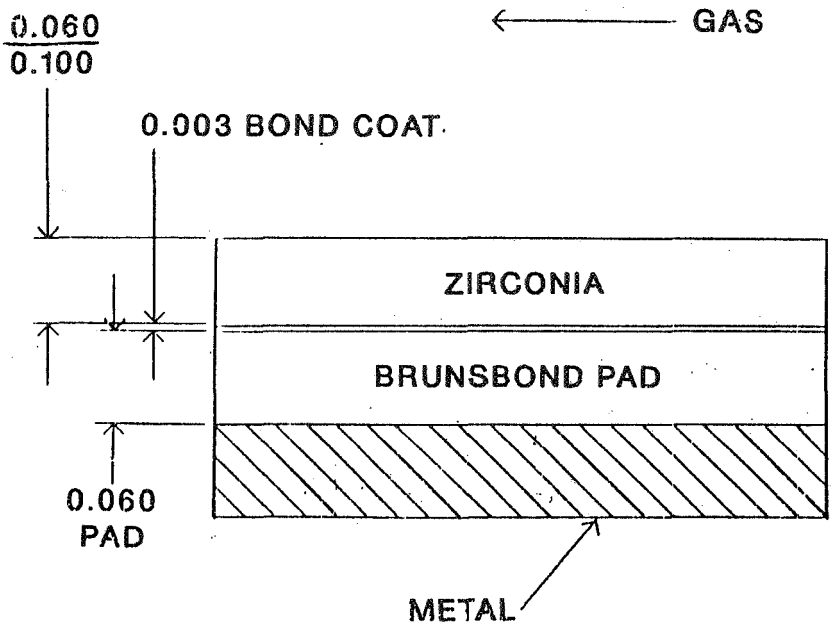

Figure 3.

THERMAL ANALYSIS

- Objective
  - Determine if the BRUNSBOND scroll can replace the existing scroll
  - Find if combustor exhaust temperatures can be increased by the use of BRUNSBOND
- Result
  - BRUNSBOND scroll saves 27% of combustor inlet air
  - Combustor exhaust temperature increase of 200 degrees F possible

Figure 4.

FABRICATION

- Problem
  - Scroll is complex shape
  - BRUNSBOND pad and substrate shape must be matched and tightly fixtured for brazing
- Solution
  - Apply BRUNSBOND to flat stock
  - Post form to final dimension
  - Apply TBC afterward

Figure 5.

FULL SCALE PARTS

Scroll formed from 2 halves

Each half made from 2 parts

One part die formed; the other part hydroformed

Die formed parts

Tore in high stretch areas

Base metal embrittled by braze

Flat stock trimmed to minimize stretch

Parts successfully formed

Figure 6.

TESTING

- Test panels fabricated
  - BRUNSBOND samples of 35% density laid over 2" by 2" Hastalloy-X
  - Post formed over a 1 inch steel ball
  - Pad compressed to 48% density
- Thermal cyclic testing
  - Alternate heating and cooling to develop 1400 degree F gradient
  - 500 cycles completed, 1800 F to 400 F

Figure 7.

SCHEMATIC OF THE BRUNSBOND TEST PIECE

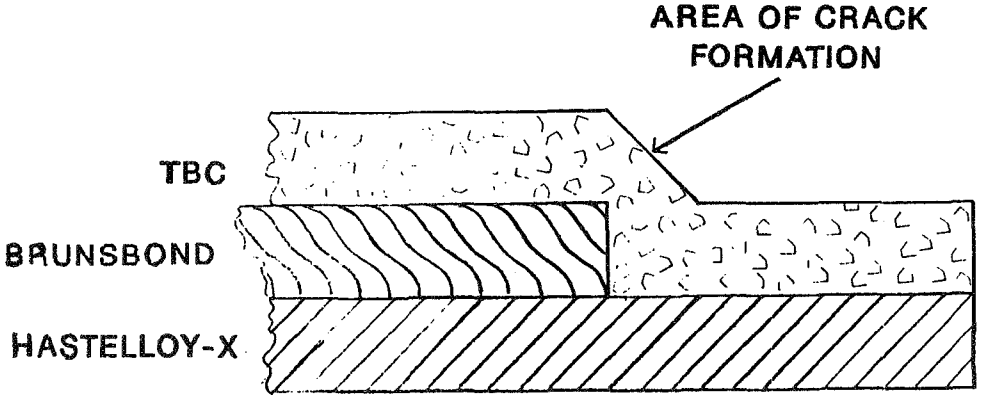

Figure 8.

DIE FORMED BRUNSBOND SCROLL SEGMENT

1 in.

BK1386

HYDROFORMING

- One scroll half successfully formed
  - Improved ductility material developed
- One half not yet made
  - Improved ductility material not sufficient
  - Formability study initiated

Figure 10.

STATUS

- Formability
  - Establish draw limits with 8 inch diameter test discs

    Form to limit followed by heat treat
- Testing
  - Full scale parts to be subjected to rig test to validate thermal analysis
  - Engine durability test to follow

Figure 11.

STRAIN ISOLATED CERAMIC COATINGS

R.P. Tolokan, J.B. Brady, and G.P. Jarrabet
Brunswick Technetics
Deland, Florida 32724

Plasma sprayed ceramic coatings are used in gas turbine engines to improve component temperature capability and cooling air efficiency. A compliant metal fiber strain isolator between a plasma sprayed ceramic coating and a metal substrate improves ceramic durability while allowing thicker coatings for better insulation. The low modulus strain isolator moves elastically to accommodate differential expansion of ceramic and metal to reduce the stress transmitted to the ceramic. A typical ceramic-strain isolator-backing system consists of .060-.100" of plasma sprayed zirconia (YSZ) applied to .060" fiber metal strain isolator. The strain isolator improves coating performance by: partially decoupling coating and backing, providing insulation to protect the metal backing from heat deformation, allowing thicker ceramic coatings for improved insulation, widening the operating boundaries of the coating system, and improving cooling and substrate protection by flowing air through the strain isolator. Strain isolated coating applications include ceramic seals, combustors, scrolls, vanes and internal combustion engines.

Development of strain isolated coatings has been concentrated on design and fabrication of coatings and coating evaluation via thermal shock testing. Coating design requires interactive matching of coating, strain isolator and backing for effective performance. Coating design is determined by material properties, component geometry and engine operating conditions. In thermal shock testing, five types of failure are possible: buckling failure in compression on heat up, bimetal type failure (see below), isothermal expansion mismatch failure, mudflat cracking during cool down, and long term fatigue. Preventing heat up and cool down failure require conflicting design approaches. Strain isolation allows a middle ground approach than can tolerate both types of cycles. Isothermal failure is atypical with proper cooling and data on long term fatigue is very limited at present.

A primary failure mode for thermally cycled coatings is what we have designated bimetal type failure. Bimetal type failure is tensile failure in the ceramic near the ceramic-metal interface (it occurs in both ceramic-metal and strain isolated coatings). A ceramic-metal coating can be viewed as a composite beam with a centroid or null point at which zero stress occurs. The centroid is the transition between compression and tension. Typically a plasma sprayed coating is a buildup of multiple thin layers on a cool backing. This produces a coating in compression with centroid location in the metal. Heat work on the metal substrate in plasma spraying or operation can reduce the metal modulus and allow plastic deformation of the metal substrate. As metal deformation occurs, the centroid moves into the ceramic creating a zone where the ceramic is in tension between the ceramic-metal interface and the centroid. Bimetal type tensile failure in the ceramic occurs due to thermal cycling after the centroid has moved into the ceramic. One of the significant benefits of the strain isolator is as an insulating layer protecting the metal substrate from heat deformation and thereby preventing bimetal type failure.

Substantial thermal shock testing has demonstrated the value of strain isolation as shown in the figures. Temperature, thermal loads, heating and cooling rates and steady-state holds in thermal shock testing should approximate engine operating conditions. Sample and test design have been found to be very important. Coating performance in thermal shock testing can be compromised by sample cutting, welding, cold work, attachment method, cooling method and inappropriate backing alloy or thickness.

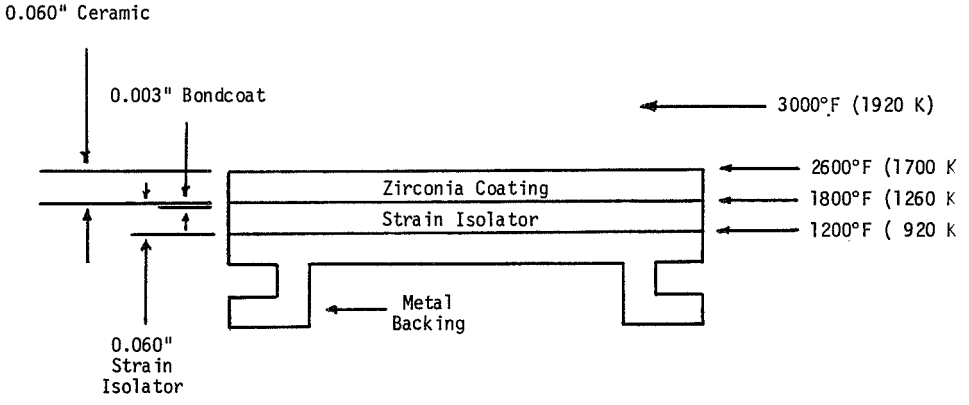

FIGURE 1
CROSS-SECTION VIEW OF A TYPICAL STRAIN ISOLATED CERAMIC COATING. THE STRAIN ISOLATOR IS BRAZED TO THE METAL BACKING. THE STRAIN ISOLATOR SURFACE IS GRIT BLASTED AND LIGHTLY BOND COATED (.001-.003" THICK BY WEIGHT) BEFORE PLASMA SPRAY APPLICATION OF THE ZIRCONIA COATING.

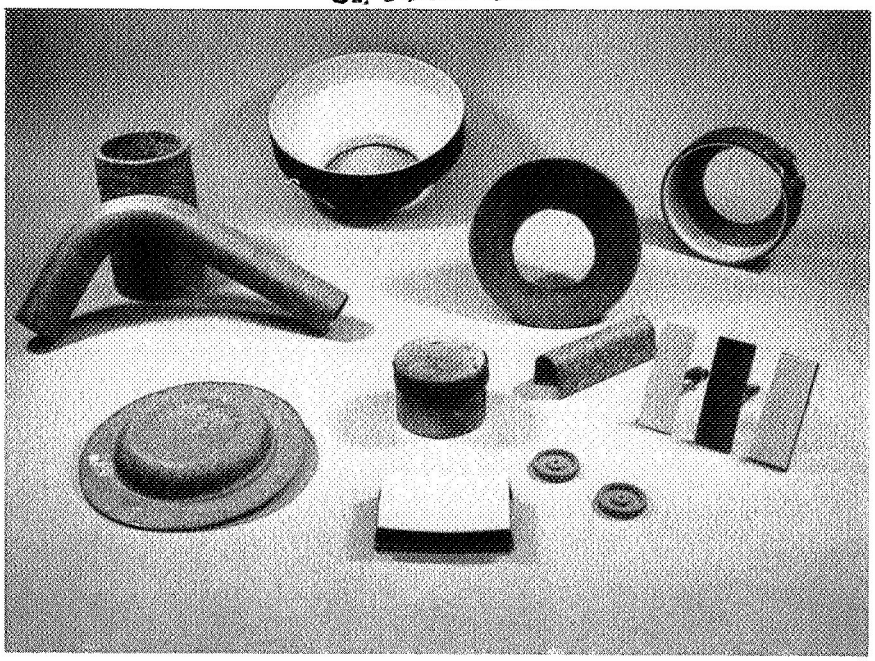

FIGURE 2
STRAIN ISOLATOR COMPONENTS WITH
AND WITHOUT CERAMIC COATINGS

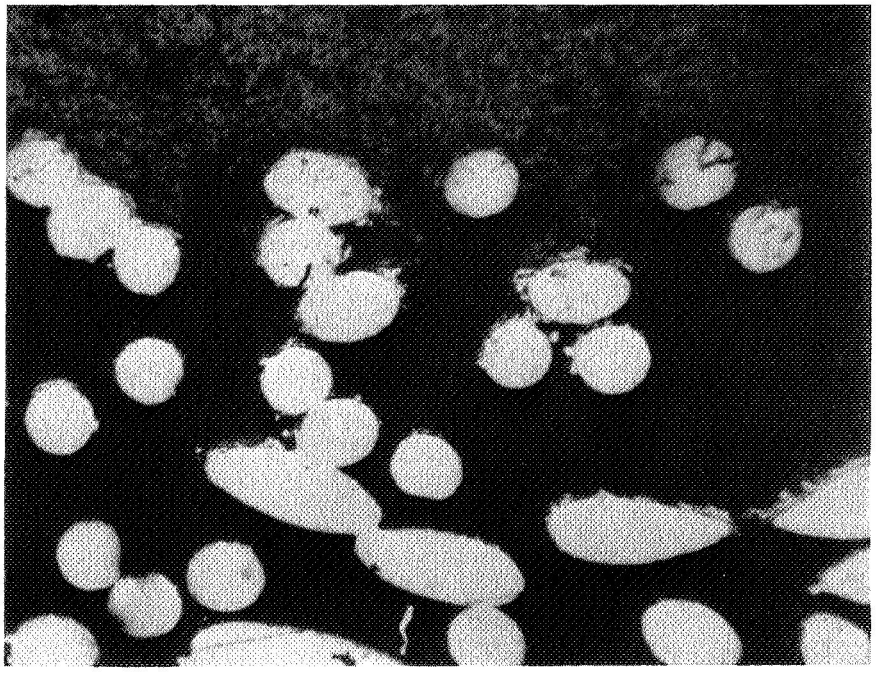

FIGURE 3
CROSS SECTION VIEW OF THE
CERAMIC-STRAIN ISOLATOR INTERFACE.
PENETRATION AND INTERLOCKING OF THE CERAMIC
COATING WITH THE POROUS STRAIN ISOLATOR IS ILLUSTRATED.

FIGURE 4
TYPICAL STRAIN ISOLATOR PROPERTIES

- HOSKINS 875 (FeCrAl) FIBER .0056" DIAMETER
- 35% DENSITY (65% POROSITY)
- .060" THICK

  UTS - IN PLANE: 4800 PSI
  TRAVERSE: 1000 PSI

- ELASTIC MODULUS: 1.1×10^6 PSI
- THERMAL CONDUCTIVITY: .010 W/CM-K
- OXIDATION RESISTANCE: 1800°F CAPABILITY - 10,000 HOUR LIFE

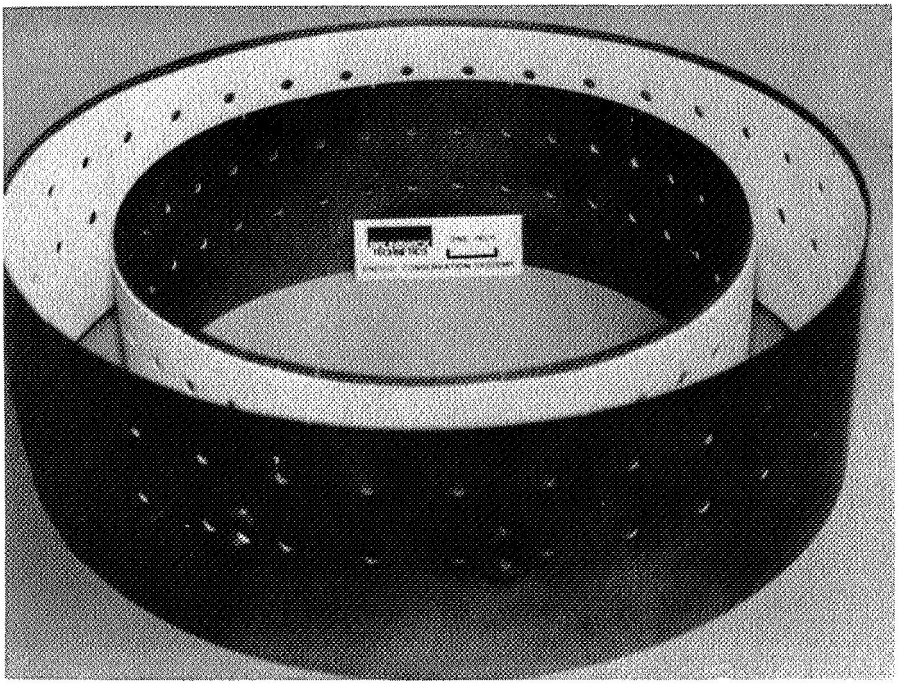

FIGURE 5
STRAIN ISOLATED ZIRCONIA
COATED COMBUSTOR SECTIONS

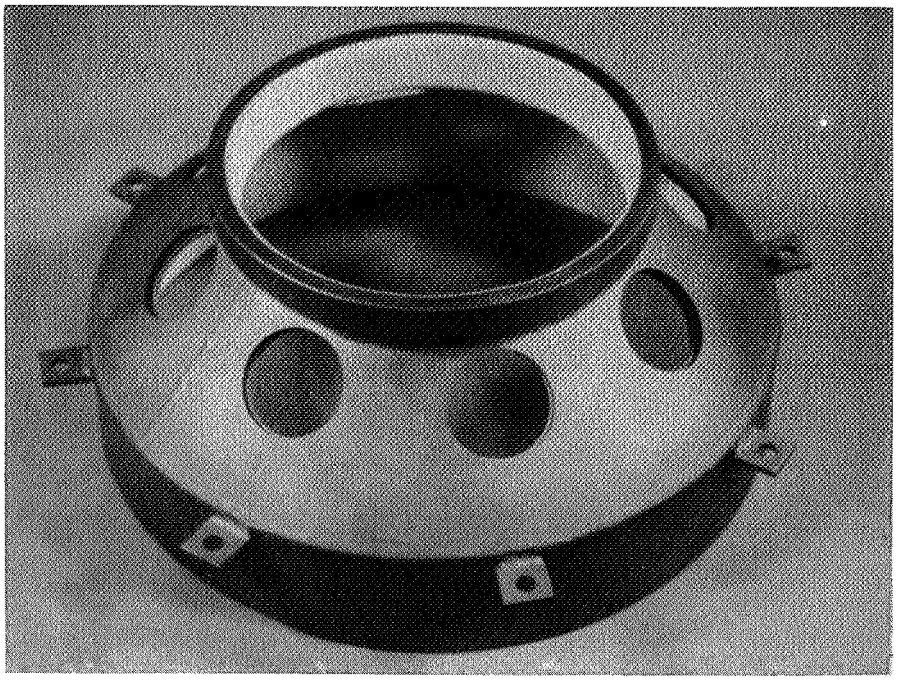

FIGURE 6
STRAIN ISOLATED ZIRCONIA
COATED COMBUSTOR SECTIONS

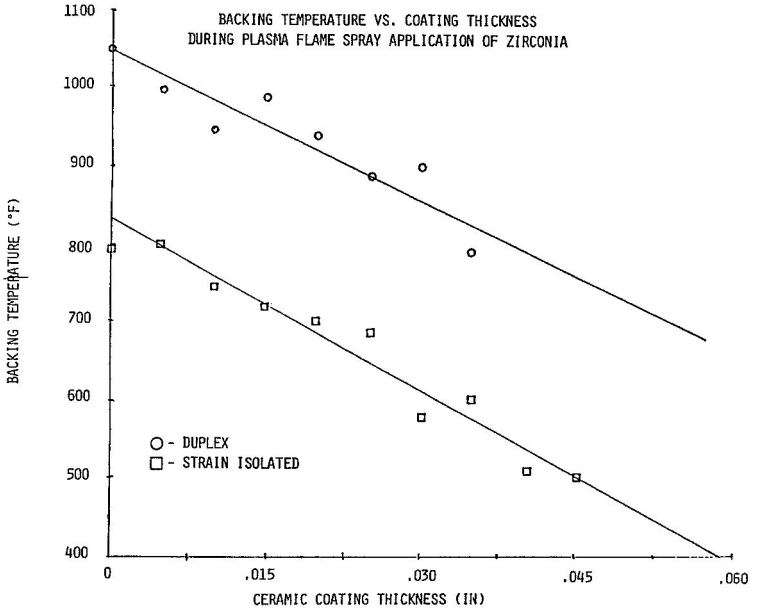

FIGURE 7
EFFECT OF STRAIN ISOLATION AND COATING
THICKNESS ON METAL BACKING TEMPERATURE

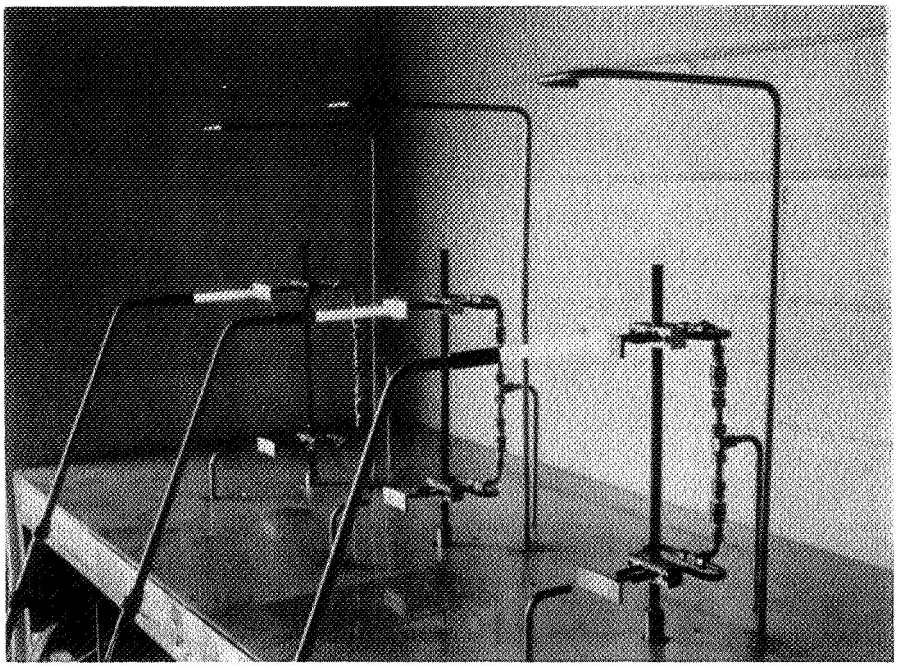

FIGURE 8
THERMAL SHOCK RIG

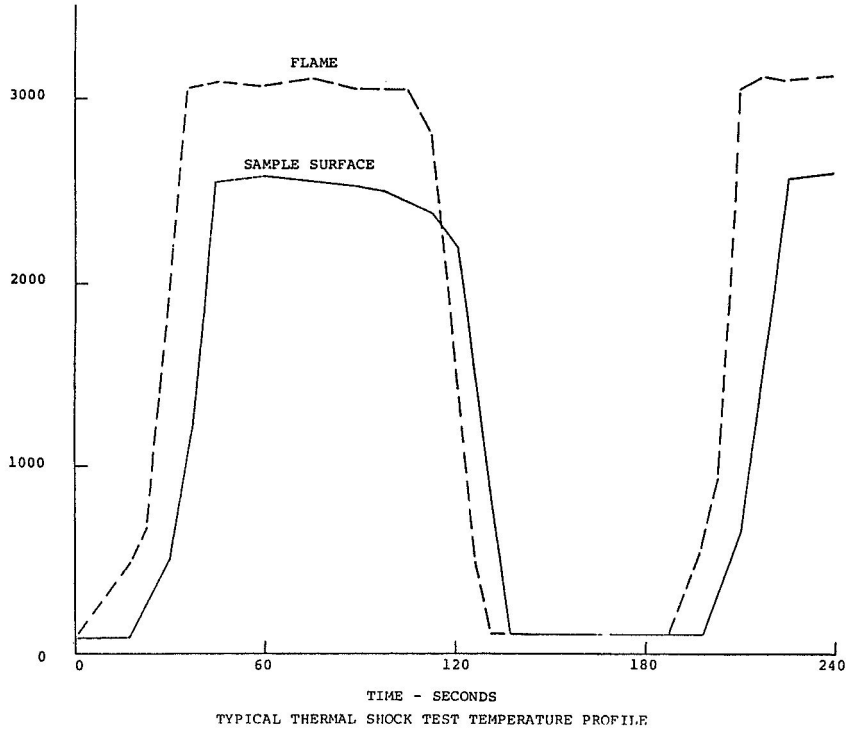

TYPICAL THERMAL SHOCK TEST TEMPERATURE PROFILE

FIGURE 9
TYPICAL THERMAL SHOCK
RIG TEMPERATURE CYCLE

FIGURE 10
THERMAL SHOCK TEST RESULTS
.060" THICK ZIRCONIA COATING

	AVG. CYCLES TO[1] LAMINAR CRACKING	AVG. CYCLES TO FAILURE
ZIRCONIA COATING[2] NO STRAIN ISOLATOR	125	1100
ZIRCONIA COATING STRAIN ISOLATED	1700	>5000[3]
IMPROVED ZIRCONIA COATING STRAIN ISOLATED	5300	>6600[3]

1. AVERAGE OF 3 SAMPLES
2. ZIRCONIA USED IS ZrO_2 - 20%Y_2O_3
3. SAMPLES DIDN'T FAIL; TEST WAS DISCONTINUED

NASA
National Aeronautics and Space Administration

Report Documentation Page

1. Report No.	2. Government Accession No.	3. Recipient's Catalog No.
NASA CP-10019		

4. Title and Subtitle	5. Report Date
Thermal Barrier Coatings Workshop	May 1985
	6. Performing Organization Code
7. Author(s)	8. Performing Organization Report No. E-4425
	10. Work Unit No. 505-63-01
9. Performing Organization Name and Address National Aeronautics and Space Administration Lewis Research Center Cleveland, Ohio 44135-3191	11. Contract or Grant No.
	13. Type of Report and Period Covered Conference Publication
12. Sponsoring Agency Name and Address National Aeronautics and Space Administration Washington, DC 20546-0001	14. Sponsoring Agency Code

15. Supplementary Notes

Abstracts and viewgraphs only.

16. Abstract

The Thermal Barrier Coatings Workshop was held May 21 and 22, 1985, at the NASA Lewis Research Center in Cleveland, Ohio. Six sessions covered Failure Mechanisms and Life Modeling, Effects of Oxidation and Creep, Phase Stability and Microstructural Aspects, Nondestructive and Analytical Assessment, Coating Development, and Alternative Applications.

17. Key Words (Suggested by Author(s))	18. Distribution Statement
Coatings Plasma spraying Thermal barriers	Unclassified - unlimited Subject Category 26

19. Security Classif. (of this report)	20. Security Classif. (of this page)	21. No of pages	22. Price*
Unclassified	Unclassified	227	A11

*For sale by the National Technical Information Service, Springfield, Virginia 22161